Velocity Mapping of Elementary Bimolecular Reactions

A thesis submitted for the degree of Doctor of Philosophy

by

Mark J. Bass

Jesus College, University of Oxford

Trinity Term, 2004

Velocity Mapping of Elementary Bimolecular Reactions

Mark J. Bass, Jesus College

A thesis submitted for the degree of Doctor of Philosophy

Trinity Term, 2004

Abstract

A new and flexible velocity-map ion imaging apparatus, designed for the study of photodissociation processes and photon-initiated bimolecular reactions in a single molecular beam, has been constructed, developed and characterised. An image Legendre moment fitting analysis was developed to allow recovery of centre-of-mass (CM) angular scattering and kinetic energy release distributions from velocity-map ion images of the products of photon-initiated bimolecular reactions.

The Legendre moment analysis methodology has been applied to images of the HCl($v' = 0, j' = 0$–6) products of the reactions of Cl($^2P_{3/2}$) atoms with ethane and *n*-butane at collision energies of 0.24 eV and 0.32 eV respectively. The Cl($^2P_{3/2}$) reactants were generated by polarised laser photodissociation of Cl_2 at 355 nm. For reaction with ethane, the CM angular scattering distributions show a steady trend from forward scattering at low j' to more isotropic, but backward peaking, scattering at high j'. An impact parameter-based mechanism is proposed to account for the observed dynamics. Abstraction of a hydrogen atom from a primary carbon site in *n*-butane is seen to produce rotationally very cold HCl products that are forward scattered, whereas H atom abstraction from a secondary carbon site in *n*-butane yields more isotropically scattered HCl products formed with higher rotational excitation. A peripheral mechanism is proposed to operate for the primary abstraction channel, whilst a more rebound type mechanism is seen to account for the dynamics of the secondary abstraction channel. Around 22% and 30% of the available energy is found in internal modes of the alkyl radical co-products of the Cl + C_2H_6 and Cl + *n*-C_4H_{10} reactions respectively. Possible sources of alkyl co-product excitation are discussed in each case.

The hydrogen or deuterium atom abstraction reactions of Cl($^2P_{3/2}$) with CH_4, CD_4 and CH_3D, have been studied at mean collision energies around 0.3 eV. Chlorine atom reactants were generated by polarised laser photodissociation of Cl_2 at 308 nm. The methyl radical products were detected using (2+1) resonance-enhanced multi-photon ionisation, coupled with velocity-map ion imaging. The laboratory frame speed distributions obtained from the images are in excellent agreement with previous work. The interpretation of the experiments is shown to be very sensitive to assumptions made about the reactant velocity distributions. If these are assumed to be narrow, the data are seen to suggest that a significant fraction of the product signal must arise from the reaction of Cl with vibrationally excited methane reactants. This conclusion is in agreement with previous photon-initiated reaction studies. However, by allowing for the spread in collision energies in the molecular beam, it is shown that it is possible to fit the data sensibly assuming reaction with vibrational ground state methane alone. CM angular scattering distributions thereby derived are presented for all three reactions.

Acknowledgements

I would like to begin by thanking my supervisor, Dr. Mark Brouard, for the unwavering support and guidance he has provided over the last three and a half years. Thanks must go to Dr. Claire Vallance with whom it was a pleasure to work and whose enthusiasm was a source of constant amazement, especially in the face of seemingly unsurmountable experimental difficulties. Also to all the other members of the group, past and present, who have shared with me the joys that the lab beholds: Dr. Patrick O'Keeffe, Dr. Denis Minayev, Joubin Moghaddam, Dave Ingham, Sarandis Marinakis, Andrew P. Clark, Dean Solaiman, Rob Davies, Patrick Tampkins, Dr. Luis Rubio, Dr. Raluca Cireasa, Fabio Quadrini and Tim Preston. I would also like to thank Prof. Bruno Martínez-Haya, despite the brevity of his visits to Oxford.

It is a pleasure to thank Prof. Theo Kitsopoulos, Dr. Rachel Toomes and all the people I met during my visit to Crete for making me so welcome.

These acknowledgements would not be complete with mentioning the HH—Lamb & Flag—new HH crowd: Thomas, Steve, Iain, Alex, Tom, Rachel, John, Mike and Charlie, to name but a few. Without your help I would have had far fewer hangovers and many more productive days. Cheers!

Special thanks must go to my long-suffering house mates, past and present: Ed,[1] Vicki, Paul-Ant and Brendon. You know you loved it really! I would also like to thank all the other people who have each contributed in their own special ways to my enjoyment of my time here: John, Jeanne, Emma, Harry, Ieuan, Dan, Izzy, Nicole, Ian, Sara and everyone else that space prevents me from mentioning. You're great friends and they were fun times.

Last, but certainly not least, I would like to thank my parents and my brother for their love and support throughout.

---

[1] Obligatory acknowledgement for 'helpful discussions'.

Contents

Chapter 1

Introduction

1.1 Motivation

Through the study of chemical reaction dynamics, one seeks to describe and understand fully at the most fundamental level possible the processes that take place when atoms and molecules interact and undergo chemical change. Our understanding of the intimate dynamics of a chemical reaction has, at its foundation, the concept of the potential energy surface (PES) [1]. In principle, the PES for any system may be constructed by *ab initio* quantum chemistry methods through solution of the Schrödinger equation for the electronic motion at all configurations of the system. Such calculations of PESs are subject to the Born–Oppenheimer approximation, in which it is assumed that nuclear motion may be decoupled from that of the electrons. In reality, however, calculations of this sort can be extremely complex and PESs are often constructed semi-empirically or even entirely empirically. There are cases in which the Born–Oppenheimer approximation cannot be applied, so that PESs for each of the accessible electronic states are required; such effects are termed non-adiabatic and accurate methods of calculating the couplings between surfaces are currently under development. The key goal of reaction dynamics is to understand the link between the PES and the properties of a reaction [2]. Once a PES has been calculated, quantum mechanical (QM) scattering [3] or quasi-classical trajectory (QCT) methods may be used to determine all the physical observables for the reaction described by the surface. The two types of calculations represent different methods of describing the evolution of the system from reagents to products. Within the QCT method, the system is defined in a precise 'quantum state' and then is evolved in time using classical mechanics only. The products are then assigned to 'quantum states' by an energy binning procedure [4]. This technique is frequently used as an alternative to QM methods which, while in principle more rigourous, are generally limited to simple three-atom systems by the rapid increase in complexity of solving the Schrödinger equation for the nuclear motion as the number and mass of the atoms involved increases.[1]

Physical observables sensitive to the nature of the PES include the product quantum state distribution, the product angular scattering distribution and the direction of product rotational motion. The results of calculations on a given PES may be compared with experimentally measured values, providing a very sensitive test of the accuracy of the PES used and of the ability to predict in detail the dynamical characteristics of reactions.

1.2 Angular Scattering Distributions

In 1939, Evans and Polanyi discovered that the topology of the PES for a reaction impacts upon the product quantum state distribution [5] and it is now accepted that the shape of the PES influences many aspects of the chemical process it describes. Experimentally determinable properties of a reaction are not limited to scalar, directionless characteristics such as the reaction rate constant or the product quantum state population distribution, but also incorporate properties directly associated with molecular motions during the reactive encounter, which are described by both magnitude and direction. Since the PES for a reaction is angular dependent, important information about the dynamics of the reaction may be obtained by investigating these vector properties of the reactants and products. One such

---

[1] For QM time-dependent and time-independent calculations the difficulty of the problem scales with n^3 and n^2 repspectively, where n is the number of atoms involved.

property is the differential cross-section (DCS), $\mathrm{d}\sigma_\mathrm{r}/\mathrm{d}\omega$, which characterises the dependence of the reaction cross-section, σ_r, on the angle between the reagent and product relative velocity vectors. Differential cross-sections (and the related angular scattering distributions) can provide a powerful means of probing the PES [6–9] and the experimental determination of differential cross-sections for elementary bimolecular reactions is therefore the principal purpose of the work presented in this thesis.

The relationship between the DCS and the reaction cross-section is given by

$$\sigma_\mathrm{r} = \int_0^{2\pi} \int_0^{\pi} \frac{\mathrm{d}\sigma_\mathrm{r}}{\mathrm{d}\omega} \sin\theta \, \mathrm{d}\theta \, \mathrm{d}\phi, \tag{1.1}$$

where $\mathrm{d}\omega$ is the solid angle $\sin\theta \, \mathrm{d}\theta \, \mathrm{d}\phi$. In the course of the work in this thesis, the angular scattering distributions, $(1/\sigma_\mathrm{r})(\mathrm{d}\sigma_\mathrm{r}/\mathrm{d}\omega)$, are measured; these distributions are normalised to unity and must be multiplied by the reaction cross-section to obtain the corresponding DCSs.

1.3 Experimental Techniques in Reaction Dynamics

The experimental methods that have been developed to probe the topology of the PES may be loosely divided into three categories:

Reactant quantum state selected experiments. These experiments provide information about the entrance region of the PES. Insight into the dynamics of a reaction is provided by preparing reactants in specific quantum states and analysing the dependence of the experimental observables on the initial state of the reagent prepared. Examples of such studies include work carried out on mode-specificity in the $\mathrm{H} + \mathrm{H_2O}$ (HOD) reactions by Crim and co-workers [10–14], Zare and co-workers [15, 16] and Smith and co-workers [17], in which the vibrationally excited O–H (O–D) bond was seen to react preferentially. The likelihood of fission of the excited bond was found to be significantly greater than for the unexcited bond.

Product quantum state selected experiments. These experiments probe the exit channel of the PES. The structure of the transition state and the forces operating on it in this region of the PES can be inferred by measurement of the various properties associated with the products. A typical observable is the distribution of the available energy between the various degrees of freedom in the products of a reaction, which can be a useful tool in revealing the nature of the transition state and product valley of the PES. The transition state may be probed indirectly by analysis of the results of state-to-state experiments, by establishing connections between the reactant and product quantum state population distributions [18–20]. These relationships can reveal how, in the transition state, chemical bonds are broken and new ones are formed. Qualitative information about the location of the barrier to reaction may be provided, for example, from the energy partitioning in the products using Polanyi's rules [20].

Transition state spectroscopy. These measurements are concerned with probing the reaction in and around the region of the transition state. Although these yield perhaps the most enlightening information about the PES in the interaction region, direct interrogation of the transition state is not possible for the vast majority of reactions. In a few specific cases, however, spectroscopic methods have been successful in overcoming this difficulty. Neumark and co-workers [21], for example, used anion photoelectron detachment spectroscopy to investigate the transition state of the F + H_2 reaction. The anion of the species of interest, FH_2^-, was formed by electron bombardment of a suitable mixture of precursor molecules in a free-jet expansion. The anions were then studied using conventional photoelectron spectroscopy. The resulting photoelectron spectrum was seen to consist of a series of transitions corresponding to excitation to vibrational 'states' of the FH_2 transition state. The FH_2 moi-

> ety was determined from *ab initio* calculations to be produced in a region on the reactant side of the reaction barrier. From this it was concluded that the technique should be a good probe both of the barrier height and of the bending potential in the transition state region of the F + H_2 PES. Indeed, the peaks in the photoelectron spectrum were later assigned to bending (hindered rotation) modes of the H_2 [22], which were excited by relaxation of the linear FH_2^- to the bent FH_2 on loss of the electron. Direct experimental evidence that the minimum energy path for the F + H_2 reaction passes through a bent FH_2 structure at the barrier was thus provided by the spectrum.
>
> An alternative approach to stabilising the reactant molecules in restricted geometries is through creation of van der Waals complexes by jet-cooling a mixture of the reagents in a supersonic expansion. This can subsequently be probed using conventional spectroscopy to investigate directly the relevant regions of the corresponding reactive PESs [23]. It should be mentioned here that van der Waals complexes present the only way in which bimolecular reactions can be investigated using femtochemistry techniques in real time, since they allow an accurate 'time zero' for the reactive process to be defined [24].

The work described in this thesis falls within the second category and involves preparation of the reagents of a bimolecular reaction in low rovibrational quantum states through cooling of the internal degrees of freedom in a supersonic expansion and detection of the products rovibrational quantum state selectively. In order to put the current work in context, a review of some of the experimental techniques that have been employed to explore the dynamics of gas-phase reactions is given in the remainder of this Section.

1.3.1 Crossed Molecular Beam Methods

One of the most historically important techniques developed in the field of experimental reaction dynamics is the crossed molecular beam method. The technique involves reaction at the intersection of two molecular beams of reactants, often coupled with time-of-flight mass spectrometric (TOF-MS) detection of the products. The method was initially developed in the 1950s by Herschbach, Lee and co-workers[2] [25] and has been used successfully to determine state-averaged DCSs for an extensive list of reactive and inelastic collisions. In addition, for a few benchmark reactions the crossed molecular beam method has also allowed some of the most detailed and accurate measurements of both state-resolved and state-to-state DCSs [26–28].

Molecular beams are generally generated in one of two ways, with the choice of which depending on the reactants to be employed. Early experiments used effusive atomic beams of alkali metal atoms, which were formed by heating the metal in an oven and then allowing the gas-phase atoms to escape through a pinhole into a high vacuum scattering chamber. Reactant beams of this type are characterised by broad speed distributions due to the temperature of the oven source. In contrast, stable molecular reactants are usually formed into supersonic beams by adiabatic expansion from very high pressures of the gas through a nozzle. By suitable choice of nozzle orifice diameter and backing pressure, a molecular beam with very high molecular speeds in the beam direction and very low speeds orthogonal to it may be produced. By using a pulsed nozzle, the total gas flow through an experiment can be minimised, which both reduces pumping requirements and also allows the use of greater backing pressures of the gas, thus resulting in colder and more intense molecular beams. Pulsed molecular beams are ideally suited to experiments in which the detection is also pulsed, as is frequently the case with laser based methods. In general, non-effusive methods have the advantage that the rotational and vibrational degrees of freedom of the reactant molecules are cooled by collisional relaxation in the expansion region directly in front of the nozzle. The extent of cooling may be increased by seeding the reagent in an inert carrier gas such as helium or argon. The collision energy of the reaction under study may thus be controlled by varying the carrier gas composition and source temperature, along with the angle at which the

---

[2] The pioneers of this area of research, Dudley R. Herschbach, Yuan T. Lee and John C. Polanyi, were awarded the 1986 Nobel prize in chemistry "for their contributions concerning the dynamics of chemical elementary processes".

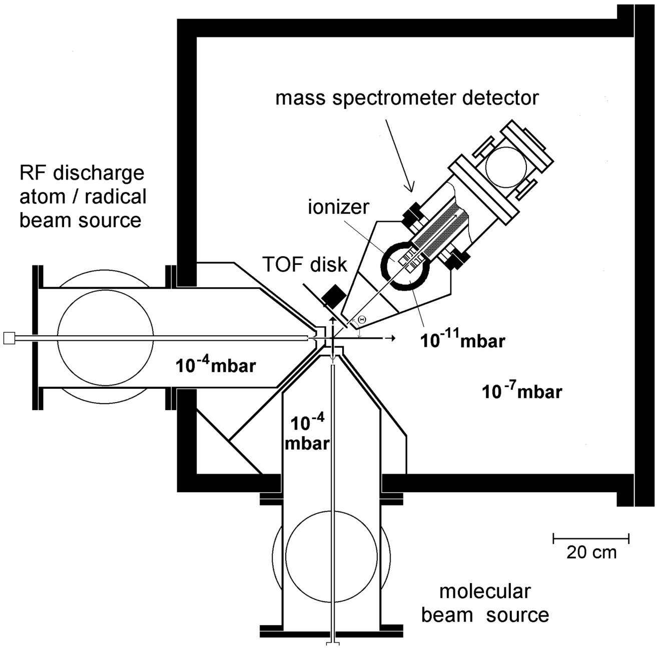

Figure 1.1: A schematic diagram of a 'universal' crossed molecular beam instrument with fixed effusive beam sources and rotating mass spectrometer TOF detector. Adapted from Ref. [26].

reactant beams intersect.

A number of techniques to form beams of aligned and oriented molecules using strong electric and laser fields have also been developed and used extensively in conjunction with the crossed molecular beam method. Comprehensive reviews of the most recent developments in experimental techniques and their application to dynamical stereochemistry may be found, for example, in Refs. [29–31].

'Universal' TOF-MS detection

In a typical 'universal' crossed molecular beam machine, time-of-flight (TOF) spectra of all reaction products are recorded as a function of the laboratory recoil angle for single and well-defined collision events using a rotatable electron-impact ionisation (or photoionisation) mass spectrometer detector and a pseudo-random TOF system. A schematic of a 'universal' crossed molecular beam instrument is shown in Figure 1.1. The advantage of the mass spectrometer lies in the fact that it is extremely flexible and allows the detection of almost any atomic or molecular fragment of interest.

The raw data from these experiments normally consist of the reaction product number density as a function of laboratory speed and scattering angle, Θ, which is usually defined relative to the propagation direction of one of the molecular beams. In order to obtain the differential cross-section and the relative speed of the reaction products, the measured data are first converted to product flux (by multiplication by the product speed) followed by transformation from the laboratory (LAB) frame to the centre-of-mass (CM) frame [32]. Owing to the finite resolution of the experimental conditions (the angular and velocity spread of the molecular beams and the angular resolution of the detector), this frame transformation of the experimental data is typically performed using a forward convolution procedure, in which trial CM frame distributions are iteratively adjusted and compared to the observed data. The resulting information is usually presented in the form of a product flux velocity-angle contour plot.

Although the crossed molecular beam technique can be tuned to provide well-defined reactant kinetic energies and the high angular resolution presents a convenient method with which to measure differential cross-sections and excitation functions (the collision energy dependence of the reaction cross-section), there remain some significant limitations of the conventional crossed molecular beams method. The most important and well-cited of these are:

- The time-of-flight resolution of a crossed molecular beams experiment is usually limited by the velocity spread in the molecular beams. The resulting product kinetic energy distribution is not therefore usually of sufficiently high resolution to allow different quantum states of the products to be resolved. One famous example of a crossed molecular beam experiment where favourable kinematics and product energy level spacings allowed vibrational state resolution of the DCS to be achieved is that carried out by Lee and co-workers on the F + H_2 reaction [33, 34]. Indeed, Toennies and co-workers have since reported resolution of the HF rotational levels in this system [35–38].

- The very low pressures required to create and maintain supersonic reactant molecular beams result in low product number densities and correspondingly poor signal-to-noise ratios. This limits the number of systems that may be investigated using this technique.
- The method is not well suited to studies at low collision energies, owing to the high translational energy of the reactants provided by the supersonic molecular beams employed. Note that this limitation may be overcome to a certain extent by judicious choice of the intersection angle of the molecular beams.

Some of these limitations have been addressed in recent years by combination of the crossed molecular beam method with laser spectroscopic detection methods. These new techniques are described in the following Sections.

Rydberg Atom TOF Spectroscopy

Representing a significant development of the crossed molecular beams method, the highly sensitive and extremely high resolution Rydberg 'tagging' technique was recently developed for the detection of hydrogen atoms by Welge and co-workers [39]. They applied the technique to the study of the

$$\mathrm{H} + \mathrm{D}_2 \longrightarrow \mathrm{HD}(v', j') + \mathrm{D} \tag{1.2}$$

reaction in a crossed molecular beam instrument [39–44]. A schematic diagram of the apparatus is shown in Figure 1.2. In these experiments, the nascent D atom products in the collision volume were 'tagged' with high selectivity and sensitivity using two laser photons to effect a double-resonant excitation to a long-lived Rydberg state with high principal quantum number ($n \sim 70$). The translational and angular distributions of the D atoms were monitored through field ionisation at the end of the TOF. By 'tagging' the deuterium atoms rather than ionising them, the possibility of velocity spread due to ionic repulsion is eliminated. In addition, since the D atoms are selected for detection spectroscopically, no mass analysis is required.

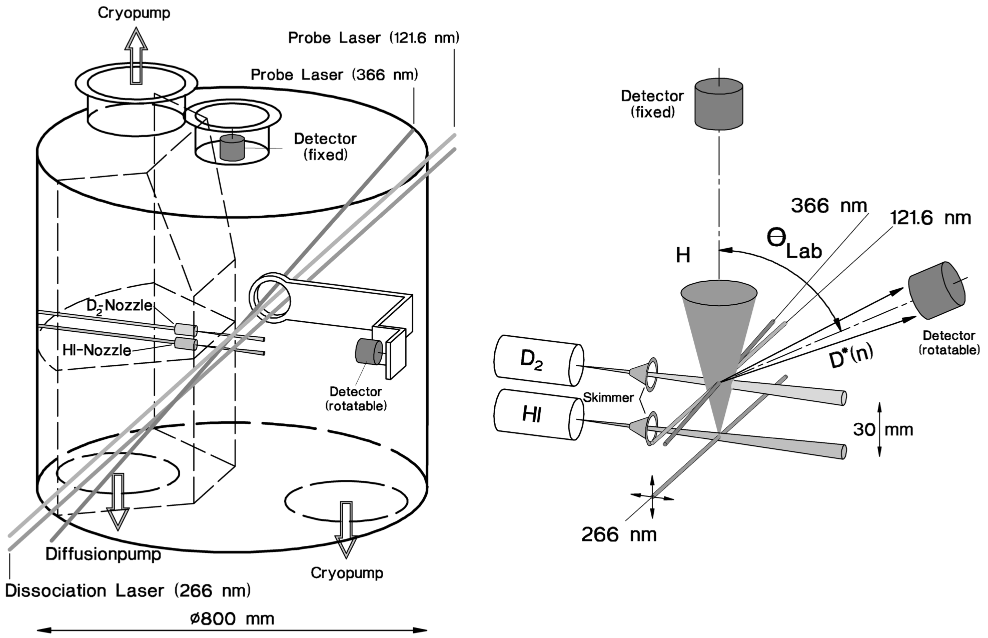

Figure 1.2: A schematic diagram of a crossed molecular beam instrument with H Rydberg atom TOF spectroscopy rotating detector (left). Also shown is a more detailed view of the scattering region and rotatable detector (right). Adapted from Ref. [39].

Most importantly of all, the technique is effectively background free, since the detector is sensitive only to the deuterium atoms that are initially moving towards the detector. From the conservation of momentum, Welge and co-workers were able use the technique to resolve all of the rovibrational levels of the HD co-product in the kinetic energy distribution of the D atom product of reaction 1.2. This was the first example of the derivation of state-to-state DCSs for a chemical reaction. Yang and co-workers have subsequently conducted a series of experiments on the $O(^1D_2) + H_2$ [45], D_2 [46], and HD [47] systems using this method, while Davis and co-workers have used the technique to investigate the $OH + D_2 \longrightarrow HOD + D$ reaction [48]. The resulting velocity-angle contour plot from the latter study is shown in Figure 1.3. It should be noted that this technique may represent the only method with which to obtain internal state distributions for the polyatomic co-fragment in reactions producing X + H/D when X is not amenable to laser based detection methods. A drawback to the technique, however, is that in order to achieve the

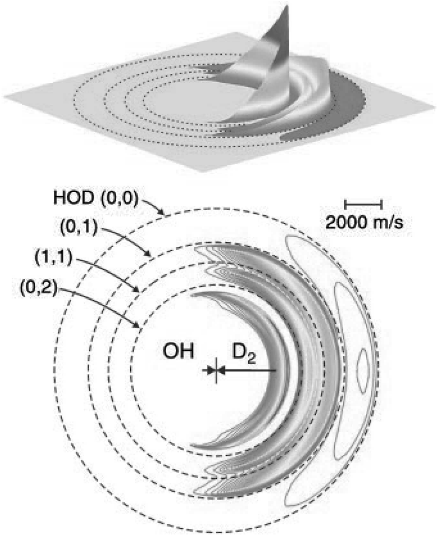

Figure 1.3: Velocity-angle contour plot obtained from a D atom Rydberg tagging experiment on the OH + D_2 $\longrightarrow$ HOD + D reaction. Taken from Ref. [48].

remarkably high kinetic energy resolution possible, the probe lasers are necessarily focussed, making the interaction volume significantly smaller than the molecular beam overlap volume. In order to obtain the desired DCSs, extensive modelling is therefore required [40]. Moreover, such ultra-high resolution can be fully realised only when the Rydberg H/D atom 'tagging' detection scheme is combined with very high translational energy molecular beams.

Doppler-Selected Time-of-Flight

The novel Doppler-selected TOF technique implemented by Liu and co-workers [49] represents a significant advance in the development of crossed molecular beam methods. The Doppler-shift and ion TOF techniques are combined in an orthogonal manner such that the three-dimensional (3D) velocity distribution of the reaction product is directly mapped out in a CM Cartesian coordinate. The versatility and power of the technique has been extensively demonstrated by its application to the investigations of the reactions O($^1D_2$) + HD [50–52], S($^1D_2$) + D_2 [53, 54], Cl(^2P) + H_2 [55] and CN + D_2 [56]. The H or D atom products were detected in each of these studies, so as to take advantage of their large recoil velocities and thus to maximise

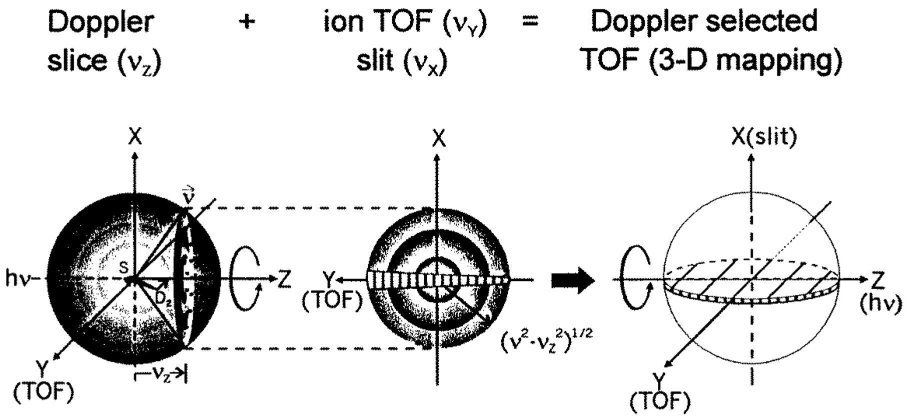

Figure 1.4: The basic concepts of the Doppler-selected TOF technique for mapping the 3D product distribution. The slice represents a Doppler-selected two-dimensional (2D) velocity distribution for a certain v_z. The strip on the 2D slice is the one-dimensional (1D) distribution measured by the TOF technique under the restriction of a slit. Adapted from Refs. [26, 49].

the TOF resolution. A schematic diagram of the method is shown in Figure 1.4. The H(D) atoms are probed *via* resonance-enhanced multi-photon ionisation (REMPI) in the collision region of the two pulsed molecular beams. The ionisation laser is arranged to propagate parallel to the relative velocity axis, z, in order to take advantage of the cylindrical symmetry of the scattering event along the relative velocity vector. Using the Doppler-shift, the laser frequency is tuned so that a subgroup of the products, with component v_z in the CM frame, are ionised. Rather than detecting the whole signal arising from the resulting 'slice' through the 3D scattering distribution as a single data point, as in the conventional approach, the ions are dispersed both spatially and temporally. A slit placed in front of the detector ensures that only those products with $v_x \approx 0$ are detected, so that a 1D sampling of the product velocity distribution is achieved. By recording TOF spectra at successive probe laser wavelengths over the product Doppler profile, it is possible to map out the entire 3D scattering distribution essentially in the CM frame in Cartesian coordinates. The resolution in this coordinate system is constant along each of the axes. When recast in the conventional product flux velocity-angle contour plot in polar coordinates, however, different speed resolutions along different CM scattering angles are obtained. The TOF resolution is highest for sideways scattering, while it is more limited in the forward and backward directions. Some co-product vibrational resolution was achieved in the study of the S(^{1}D$_2$) + D$_2$ reaction [53, 54].

Ion Imaging Techniques

A relatively new modification of the REMPI-TOF detection scheme involves direct measurement of the velocity distribution of the products of a scattering process on a position sensitive detector. In this way, the product angular and speed distributions can be measured simultaneously with, in principle, quantum state resolution. The technique was pioneered by Chandler and Houston [57] and was used initially for the product state selective investigation of photodissociation processes. Comprehensive reviews of the field of ion imaging may be found, for example, in Refs. [58–62]. In this method, the products are ionised *via* REMPI in an electric field and accelerated down a TOF tube where they impinge on a detector consisting of micro-channel plates (MCPs) coupled to a phosphor screen and a charge-coupled device (CCD) camera. When the ions strike the MCPs at a certain position, the stream of electrons produced results in a luminescence at the corresponding position on the phosphor screen that is subsequently captured by the CCD camera.[3] The ion image that is recorded is thus a 2D projection of the 3D scattering distribution. In general, the ion imaging technique is most suited to the detection of slow moving species. The ion imaging method was first used in conjunction with crossed molecular beams in studies of Ar + NO inelastic scattering by Houston and co-workers [63, 64]. Chandler and co-workers studied the reaction

$$\mathrm{H} + n\text{–}\mathrm{D}_2(v = 0, j = 0, 1) \longrightarrow \mathrm{HD}(v', j') + \mathrm{D} \tag{1.3}$$

by detecting the D atom [65]. A numerical procedure, the inverse Abel transform, was used to recover information about the speed and angular distributions of the products from the 2D projection. The images of the D atom provided the DCS of the

---

[3] A more comprehensive description of the prototypical ion imaging apparatus is given in Chapter 2.

The figure originally located here has been removed from this version of the thesis for copyright reasons

Figure 1.5: Left: Image for the hydroxyisopropyl radical products of the Cl + isopropanol reaction at a collision energy of 0.52 eV. Forward scattering (0°) corresponds to the isopropanol beam propagation direction. Right: The corresponding kinetic energy (top) and angular scattering (bottom) distributions. Adapted from Ref. [66].

reaction summed over all rovibrational states of the HD co-product. The different vibrational levels of the HD(v') co-product were resolved as separated rings in the transformed image, with the intensity distribution of each ring in the polar direction giving the vibrational state resolved angular distribution. The resolution in these experiments was limited by the finite interaction region of the ionisation laser with the molecular beam overlap volume and by inhomogeneities in the electric field around the grid wires in the mesh of the extractor electrode which led to deviation of the ion velocities.

More recently, the resolution of the ion imaging method has been dramatically improved with the advent of the velocity mapping scheme [67]. In this arrangement, the grid used for ion extraction in the early experiments is replaced by a simple three-plate ion lens with open electrodes. Using these velocity mapping optics, all ions with the same mass and velocity strike the same point on the detector at the same time, regardless of their point of formation. With the benefits of these improvements, Chandler, Houston and co-workers have compared the inelastic scattering of NO from He and H_2 [68], and have also studied the Ar + HCl [69] and Ne + CO [70]

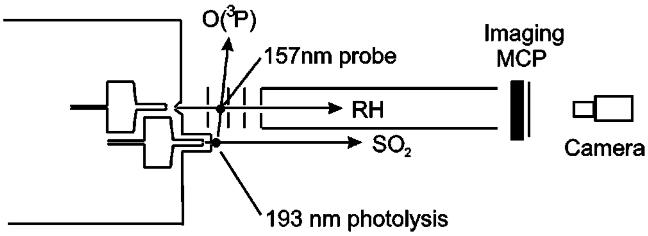

Figure 1.6: Schematic diagram of the 'crossed' parallel beam experiment of Suits and co-workers used to investigate the O + cyclohexane, *n*-butane, *i*-butane and *n*-pentane reactions. O(^{3}P) and O(^{1}D$_2$) atoms were produced by photolysis of SO$_2$ and N$_2$O respectively, at 193 nm. The alkyl products were detected *via* single photon ionisation using 157 nm laser radiation coupled with velocity-map ion imaging. Taken from Ref. [75].

inelastic scattering systems. A similar method was used by Chandler, Cline and co-workers to investigate orientation in the rotation of NO following inelastic scattering from Ar [71]. Very recently, crossed molecular beams have been used in conjunction with velocity-map ion imaging by Suits and co-workers to study the O(^{1}D$_2$) + D$_2$ reaction in which the D atom was detected [72], and the H atom abstraction reactions Cl + methanol, ethanol and isopropanol, in which the hydrocarbon radical products were detected non-state selectively *via* single photon ionisation using 157 nm laser radiation [66, 73]. An example image and the corresponding CM angular scattering and kinetic energy distributions are shown for the Cl + isopropanol reaction in Figure 1.5.

'Crossed' Parallel Beams

An interesting adaptation of the H Rydberg atom 'tagging' instrument of Welge and co-workers was reported recently by Suits and co-workers and used to study the O(^{3}P) + c-C$_6$D$_{12}$ [74, 75], O(^{3}P) + n-C$_4$H$_{10}$ [75], O(^{3}P) + i-C$_4$H$_{10}$ [75], O(^{3}P) + n-C$_5$H$_{12}$ [76] and O(^{1}D$_2$) + n-C$_5$H$_{12}$ [76] reactions. A schematic of the apparatus is shown in Figure 1.6. Two pulsed, skimmed, parallel molecular beams containing the alkane and the O atom precursor were generated a small distance apart, with the alkane beam propagating along the axis of the velocity mapping ion lens. O(^{3}P) and O(^{1}D$_2$) reactants were produced by 193 nm photodissociation of SO$_2$ and N$_2$O respectively. The fast moving O atoms thereby produced cross the alkane beam a small distance downstream from the photolysis region. The choice of photolysis region dictates the collision energy selected. The alkyl radical products are then detected non-state selectively *via* single photon ionisation using 157 nm laser radiation coupled with velocity-map ion imaging. It should be noted that the experiments are inherently more sensitive to products with low velocities that are backward scattered and, reflecting this fact, the resulting images were therefore analysed using a forward convolution technique.

The technique has also been used by Kitsopoulos and co-workers to investigate hydrogen atom abstraction from small organic molecules by chlorine atoms [77–79]. Cl($^2P_{3/2}$) atoms were produced using 355 nm radiation and the HCl reaction products detected using (2+1) REMPI. In this apparatus the two molecular beams were not skimmed, but free-jet expansions used instead. It was hoped that product number density would be increased without significant degradation in the quality of the images obtained. This was confirmed by comparison of the results obtained using this new apparatus [77] with those of the Cl + ethane and Cl + *n*-butane reactions presented in Chapters 4 and 5. Angular scattering and kinetic energy distributions were obtained by direct integration of the raw data over velocity and angle respectively. In the last few months, Orr-Ewing, Kitsopoulos and co-workers have also investigated the Cl + methanol and dimethyl ether [78] and Cl + CH_3Cl and CH_3Br [79] reactions using this technique.

Crossed Molecular Beam Time-Sliced Ion Velocity Imaging

A further recent development of imaging methods applied to the crossed molecular beam technique has been the time-sliced velocity imaging detection scheme of Liu and co-workers [80]. The method is essentially a variant of the slice imaging techniques developed previously for investigation of photolysis processes [81–85]. The reaction products are probed *via* REMPI in the intersection region of the two molecular beams. A weak d.c. extraction field is used to spread the ion arrival

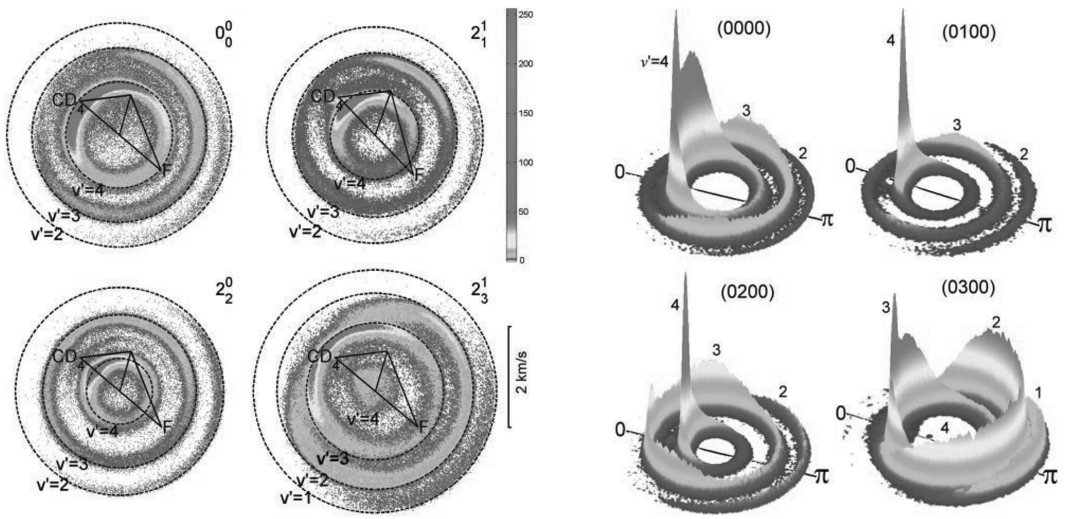

Figure 1.7: Left: Raw ion images of the state selected CD$_3$ from the F + CD$_4$ reaction at a collision energy of 0.23 eV. The successive rings on each image correspond to the labelled vibrational states of the DF co-product. Right: CD$_3$ product state resolved velocity-angle flux contour maps derived from the images. The intensities of the contours are not normalised to one another. Adapted from Ref. [86].

time over an interval of a few hundred nanoseconds, while maintaining conventional 2D mapping in the transverse directions. A slice through the 3D product Newton sphere is then recorded using a gated imaging detector. Typical gate widths used were ∼40 ns. The great advantage of the soft focus used to accelerate the nascent ions is that the ion trajectories are much less sensitive to the positions at which they were born. A large volume of products can therefore be ionised and extracted, with the focus condition of the ion lens very stable to laser alignment. There are, however, some problems inherent to the technique. The two molecular beams cross each other on the timescale of at least several microseconds. Within this crossing period, the products with high LAB speeds can escape the detection region, while slower moving products tend to accumulate. The ionisation probability of the slow moving products is therefore higher than for the products with higher velocities and a density-to-flux transformation is thus required to account for this non-uniform detection sensitivity. The density-to-flux transformation is achieved by multiplication of the raw image by a sensitivity matrix. It is also necessary to ensure that the detector gate is sufficiently narrow that slicing of the slowest products occurs. If this cannot be achieved (the narrowest gate on a typical intensified CCD camera is ~ 10 ns), some form of 2D to 3D transformation is required to account for the very slowest of these products. The corollary of narrowing the gate to obtain a thinner slice, however, is that fewer events are sampled by the detector and longer collection times are therefore required. Despite these difficulties, the technique has been demonstrated for the F + CD_4 and CH_4 reactions by Liu and co-workers [80, 86, 87], in which, through vibrational state selective detection of the methyl products, it was possible to determine information about the coincident DF(HF) co-products in a state-correlated manner (see Figure 1.7). In addition, the technique has been very recently used to investigate the Cl + CD_4 and CH_4 reactions [88]. These experiments are discussed further in Chapter 6.

1.3.2 Photon-Initiated Reactions

A distinct group of experiments are the quantum state selective techniques broadly classified as ‘laser based’. Whilst a large number of these methods may be used to measure scalar quantities, an important class of experiments have been developed to study the vector relationships involved in reactive systems.

In the 1960s Solomon and co-workers [89, 90] performed experiments which determined that the products of the photodissociation of a molecule with linearly polarised light were not distributed evenly through space.[4] It is possible to exploit the anisotropy exhibited in molecular photodissociation [91, 92] to determine the dynamics of gas phase chemical reactions. If a reaction is initiated with an anisotropic photodissociation step, the angular and linear momentum vectors of the reaction products will be correlated to those of the reactants derived from this photolysis; it is this principle upon which the work within this thesis is based. Simple trigonometric relationships exist between the reactant and product velocities which may be exploited, alongside certain constraints regarding the speeds and masses of the moieties involved, to relate the LAB frame speed distribution to the CM frame an-

---

[4] This is discussed in more detail in Chapter 3.

gular scattering distribution [93–97]. As will be shown in Chapter 3, in the simple case of a three-atom reaction, the product LAB velocity vector is directly related to the CM scattering angle through the law of cosines. This relationship between the LAB and CM frames led Zare and co-workers to coin the acronym ‘photoloc’ (photo law-of-cosines) to describe this technique [96]. The reaction scheme of such an experiment may be represented as

$$\begin{aligned} \mathrm{AX} + h\nu &\longrightarrow \mathrm{A} + \mathrm{X} \\ \mathrm{A} + \mathrm{BCD} &\longrightarrow \mathrm{AB}(v', j') + \mathrm{CD} \end{aligned} \tag{1.4}$$

where AX is a precursor molecule that is photolysed to produce reactive A moieties with well known speed and angular distributions. If the AX and BCD molecules are both entrained in a molecular beam or are held at low pressure in a ‘bulb’, the fast moving A species undergo reactive collisions with the BCD molecules. The nascent products are then detected using laser radiation. In order to probe the dynamics of such reactions, it is therefore necessary to employ detection techniques that are sensitive to the distribution of product velocities and angular momenta. Product quantum state selection, together with high detection sensitivity, is usually attained using either REMPI or laser-induced fluorescence (LIF). It should be emphasised here that these techniques, unlike the crossed molecular beam methods described in the previous Section, are fully product quantum state resolved and thus present a methodology for the measurement of state-to-state dynamical information.

Laser-Induced Fluorescence

The laser-induced fluorescence technique, when applied to the study of the dynamics of bimolecular reactions, involves Doppler-resolved optical detection of the scattered products at the collision zone. Products moving towards or away from the propagation direction of the detection laser experience a blue or red shift in their absorption spectra. The angle-resolved velocity distributions are therefore ‘encoded’ in the Doppler contours of the spectral lines. The strategy was pioneered in the late 1970s by Kinsey and co-workers [98] to investigate the H + NO_2 reaction and provided the first quantum state resolved product angular distributions for a bimolecular reaction. LIF studies are normally carried out at low pressures in a bulb, in order to maximise the intensity of the observed fluorescence.

By making measurements in a number of different experimental geometries (defined by the relative propagation directions and polarisation vectors of the photolysis and probe laser beams), sufficient information can be obtained to allow the full 3D scattering distribution to be reconstructed. In general, the contours of the Doppler-broadened product spectral lineshapes can be influenced by a range of factors, reflecting both the dynamical behaviour of the reactive system and the experimental conditions employed. The latter may include: (i) the velocity spreads in the precursor and molecular target; (ii) the quantum state population distribution in the molecular target; and, (iii) any spread in the collision energy distribution associated with the precursor photolysis step, which may occur, for example, if the precursor is polyatomic. All of these factors may be taken into account in the analysis of the experimental data, which involves a basis function fitting routine [94, 97, 99–106].

A wealth of information concerning the dynamics of bimolecular reactions has been obtained through the use of the photoloc technique coupled with LIF detection of the nascent products. Comprehensive reviews of the reaction systems investigated may be found, for example, in Refs. [99, 102, 106, 107].

REMPI Time-of-Flight

A very similar, though complementary, detection method to LIF is the REMPI-TOF technique. The reactant and photolysis precursor are normally entrained in a single molecular beam and reaction initiated by photodissociation of the precursor. Following quantum state selective ionisation of the products *via* REMPI, the ions are detected using a Wiley–McLaren time-of-flight mass spectrometer [108] and the ion time-of-arrival profile at the detector recorded. Analogously to the Doppler broadened product LIF spectral lineshapes, the ion time-of-arrival profiles are sensitive

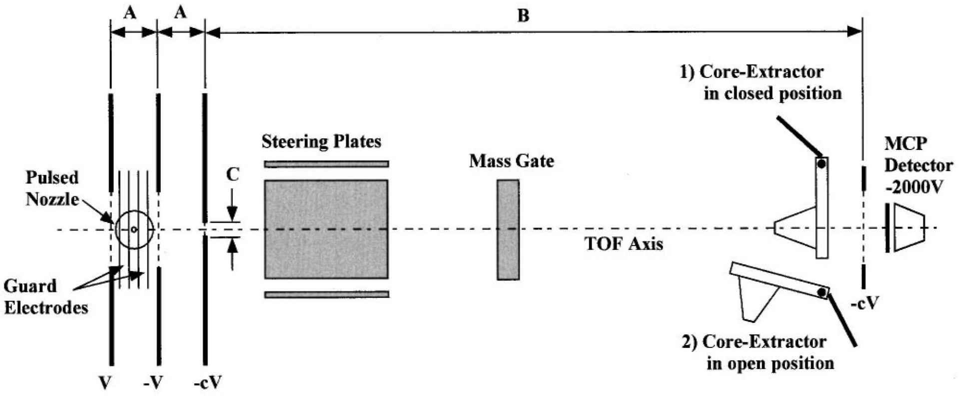

Figure 1.8: A schematic of the REMPI-TOF core-extraction apparatus of Zare and co-workers showing the extraction, acceleration and free-drift regions of the instrument. Adapted from Ref. [112].

to the velocity distribution of the reaction product. By recording time-of-arrival profiles for different geometries of the laser propagation directions and polarisation vectors, the full 3D scattering distribution may be reconstructed [109].

A major advance in the resolution of the REMPI-TOF technique was made by Zare and co-workers and named core extraction [110, 111]. A schematic of the apparatus is shown in Figure 1.8. In this method, a mask is placed in front of the detector to allow only ions with no speed component perpendicular to the TOF axis to impinge upon the detector. This technique thus converts a 1D projection of the product 3D velocity distribution into the 3D projection of the product velocity distribution in which both perpendicular velocities are zero. Note that similarly to the time-sliced ion velocity imaging of Liu and co-workers [80], products that are backward scattered or that are slow moving are more efficiently detected. In order to account for this inhomogeneous detection sensitivity and for an instrument resolution function, the ion time-of-arrival profiles are analysed using a basis function fitting routine.

The REMPI-TOF core-extraction apparatus was initially demonstrated by investigation of state-to-state

$$\mathrm{Cl} + \mathrm{CH_4}(\nu_3 = 1) \longrightarrow \mathrm{HCl}(v', j') + \mathrm{CH_3} \tag{1.5}$$

$$\mathrm{Cl} + \mathrm{CHD_3}(\nu_1 = 1) \longrightarrow \mathrm{HCl}(v', j') + \mathrm{CD_3} \tag{1.6}$$

reactions [111]. The technique has since been used to investigate a wide variety of reactions including an extensive study of the H + D_2 reaction at a wide range of collision energies [112–121]. In conjunction with theoretical calculations, this impressive series of experiments was able to show possible scattering resonances associated with a quasi-bound collision complex [114].

1.4 Outline of the Thesis

The work in this thesis is concerned with the application of the velocity-map ion imaging technique to the study of photon-initiated bimolecular reactions in a single molecular beam. A detailed description of the apparatus that was constructed and developed in order to perform these experiments is given in Chapter 2, together with the methods with which it was characterised. The various analysis methodologies used to extract dynamical information from the velocity-map ion images are addressed in Chapter 3. Detailed accounts of the hydrogen atom abstraction reactions of atomic chlorine with C_2H_6 and n-C_4H_{10} at collision energies of 0.24 eV and 0.32 eV are given in Chapters 4 and 5, while in Chapter 6 the issue of vibrational enhancement of the reaction cross-section in the Cl + CH_4 reaction is addressed through an in-depth investigation into the H and D atom abstraction reactions between chlorine atoms and CH_4, CH_3D and CD_4 at collision energies around 0.3 eV.

Chapter 2

Experimental Technique

2.1 Introduction

This Chapter is concerned with the work carried out to construct, develop and characterise a new and flexible velocity-map [67] ion imaging [57, 59] apparatus designed for studying the dynamics of both photodissociation processes and photon-initiated bimolecular reactions. A brief overview of the velocity-map ion imaging technique is given in the following Section, in order to put the subsequent Sections, which detail the various parts of the apparatus, into context. Experiments performed during a short visit to Crete to use the velocity-map ion imaging apparatus of Professor T.N. Kitsopoulos at the Institute for Electronic Structure and Laser are described in the final Section.

2.2 Overview of the Technique

A schematic diagram of the experiment is shown in Figure 2.1. A skimmed supersonic molecular beam containing the gas(es) under study and usually a carrier gas (e.g. helium) is intersected perpendicularly by two pulsed, counter-propagating laser beams mid-way between the repeller and extractor plates of the velocity mapping ion lens. In a typical photodissociation study, the first laser pulse (from the 'photolysis' laser) serves to photolyse the gas under study. After a short time delay of

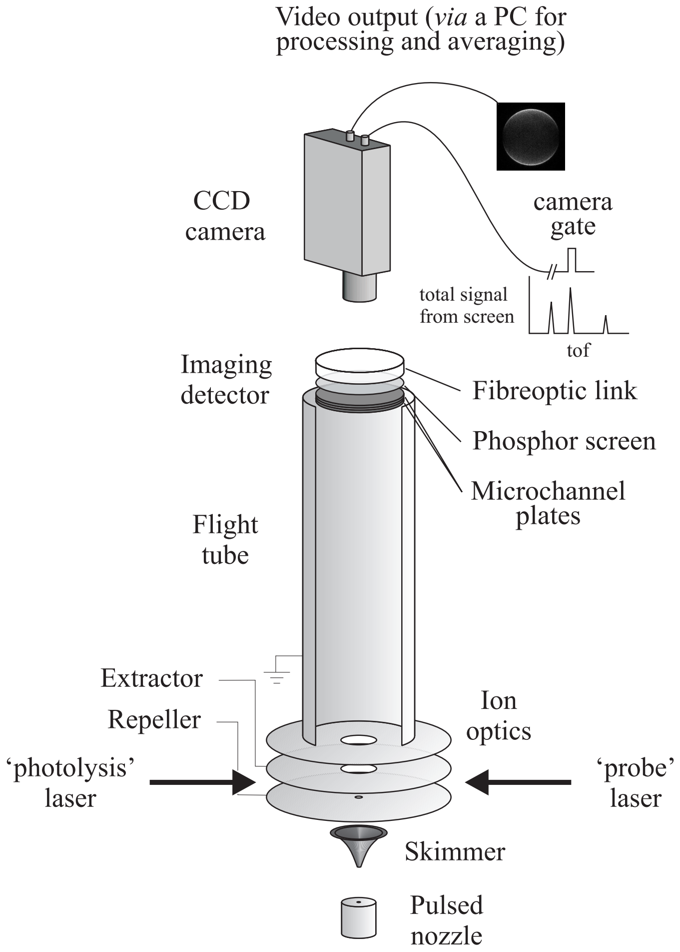

Figure 2.1: A schematic diagram of the velocity-map ion imaging experiment.

around 10–20 ns, the photofragment products are ionised quantum state-selectively *via* REMPI by a second laser pulse (from the 'probe' laser). In a typical photon-initiated *bimolecular* process, a slightly longer time delay between photodissociation of the precursor gas by the photolysis laser pulse and ionisation of the reaction products by the probe laser pulse is required. The delay is chosen to be long enough to allow sufficient product density to build up prior to the detection step, but also sufficiently short to ensure that the product distribution is nascent at the instant of detection and that no post-reactive collisions have occurred (i.e., under single collision conditions). The delay must also be short enough to ensure that products formed with the highest velocities do not escape the probe laser interaction region before they can be ionised (i.e., fly-out is avoided). Note that removal of an electron does not significantly alter the velocity of the molecules in the expanding product sphere and that the velocities of the detected ions therefore reflect those of the nascent molecules [122]. The repeller and extractor plates are held at potentials V_{R} and V_{E}, respectively, so that an electric field is maintained between them; this electric field accelerates the newly formed ions along the time-of-flight tube towards a position sensitive detector. By tuning the ratio of the voltages V_{R} and V_{E}, the lens can be made to guide simultaneously all ions with the same mass and velocity to the same point on the detector, irrespective of the initial distance of the ion from the axis of the ion lens (i.e., the voltages can be tuned to effect velocity mapping). Once this ratio has been found, the size of the image may be changed by varying V_{E} and V_{R} whilst keeping the ratio $V_{\mathrm{E}}/V_{\mathrm{R}}$ constant. The radial position at which an ion strikes the detector is proportional to its velocity at the point of ionisation. Calibration of the system using ions of known velocity permits determination of the proportionality constant. As the product ions travel through the ion lens, the acceleration along the time-of-flight axis flattens the 3D distribution of ions, so that a 2D 'pancake' of ions travels along the flight tube and strikes the detector. It should be noted that this 'pancaking' occurs for all ions, independent of mass. The resulting flight times for ions of a given mass thus have a very low spread, with $\Delta t/t \lesssim 1\%$. Good separation between the flight times of ions of different masses is therefore obtained, and the ions of interest can easily be detected separately from other ions by gating the detector (either the micro-channel plates (MCPs) or the camera) to the appropriate time-of-flight.

2.3 The Apparatus

2.3.1 The Vacuum System

In order to improve the efficiency of the pumping, the arrangement of the vacuum chambers and pumps was changed significantly over time. The two principal configurations that were used are outlined below. Arrangement 1 was used mainly for photodissociation studies, while the principal use of the apparatus in arrangement 2 was for the investigation of photon-initiated reactions.

Arrangement 1

A schematic of the apparatus in arrangement 1 is shown in Figure 2.2. This configuration consisted of a molecular beam source chamber separated by a skimmer from a differentially pumped scattering and detection chamber. The molecular beam source chamber was pumped by a 3700 l/s oil diffusion pump (Varian VHS-250) fitted with a liquid nitrogen-cooled baffle and backed by a mechanical pump (Edwards 40). Pumping of the scattering and detection chamber was achieved using a 700 l/s oil diffusion pump (Edwards Diffstak 160) fitted with a liquid nitrogen-cooled baffle and backed by a mechanical pump (Leybold Trivac D40V); the flight tube region of this chamber was additionally pumped by a 60 l/s turbo-molecular pump (Pfeiffer Vacuum TMU 071P). A gate valve allowed the flight tube and detector region to be isolated so that a vacuum could be maintained when the source and scattering chambers were not being pumped. The liquid nitrogen-cooled baffles prevented back-streaming of the silicone oil (Testbourne Silicone 4) from the diffusion pumps and also provided cryogenic pumping. A toroidal liquid nitrogen trap in the scattering region provided additional cryogenic pumping. The pressures in the two chambers were monitored using hot cathode ion gauges (Duniway gauge heads with an MKS Instruments SensaVac Series 919 hot cathode controller); in addition, a baratron capacitance manometer (MKS Instruments) was used to indicate pressures from 1–760 Torr in the scattering chamber during initial pumping down, while two Pirani gauges (Edwards Pirani 11) were used to monitor the fore-line pressures of the diffusion pumps. Typical base pressures in the two chambers were $\sim 1\times10^{-7}$ Torr.

The gas(es) under study and a carrier gas were premixed in a stainless steel tank at typical stagnation pressures of 1.0–2.0 bar, prior to being introduced into the expansion chamber *via* a pulsed solenoid nozzle (General Valve, Series 9) with a 500 μm diameter orifice. Alternative nozzle faceplates with 150 μm and 1 mm

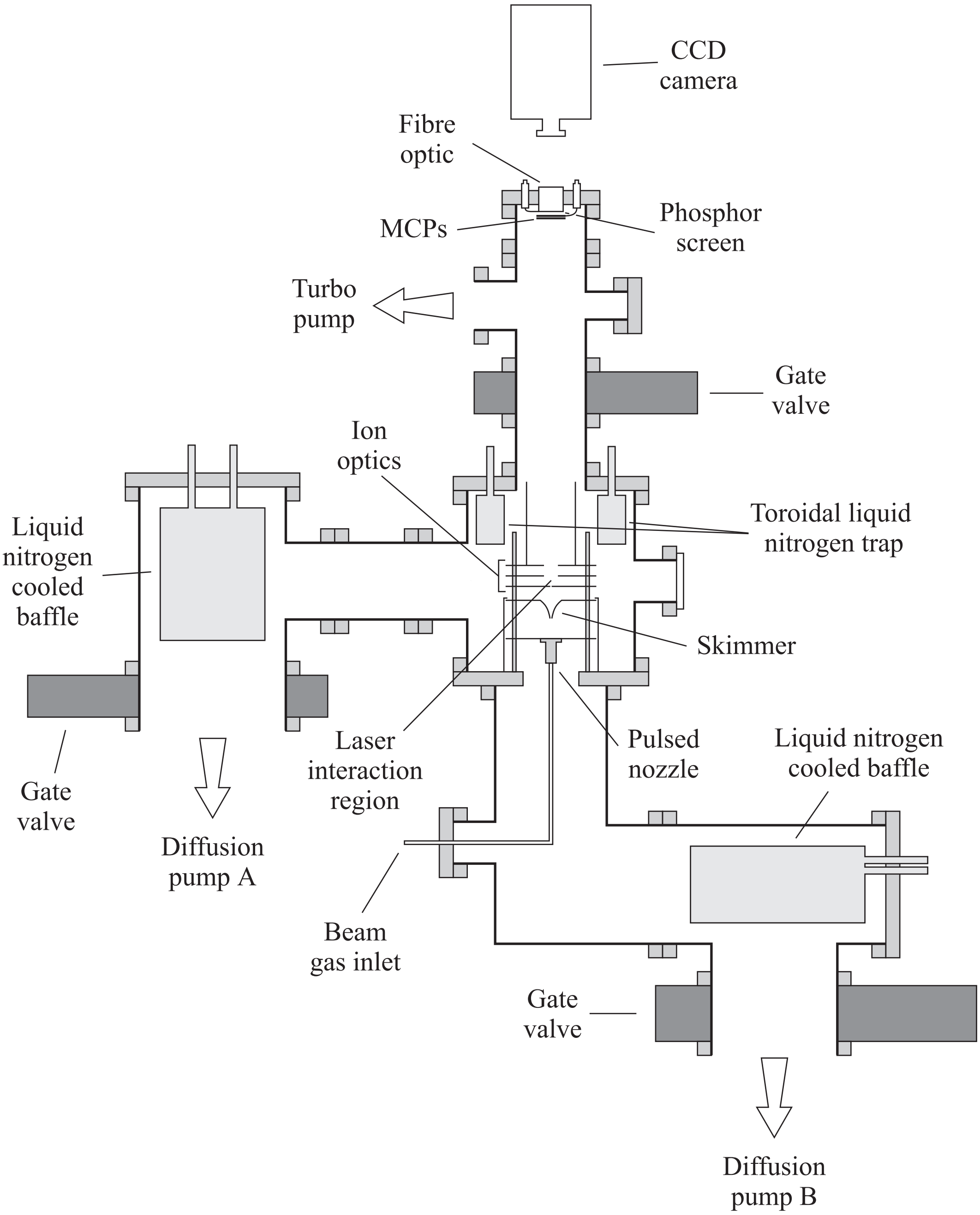

Figure 2.2: A schematic of the experimental apparatus in arrangement 1.

diameter orifices allowed the gas throughput of the molecular beam formed by this expansion to be decreased or increased, as required. A second pulsed solenoid nozzle (General Valve, Series 9) with an 800 μm diameter orifice was also used extensively. With the nozzle operating at 10–12 Hz, typical pressures in the source and scattering chambers were 1×10^{-5} Torr and 1×10^{-6} Torr respectively. The supersonic molecular beam was collimated using either a 0.98 mm or a 2.0 mm diameter nickel skimmer (Beam Dynamics Model 2) located approximately 50 mm downstream from the nozzle, prior to entering the scattering chamber. The ion optics were mounted on the base of the scattering chamber. A ‘top hat’ around the plate on which the skimmer was mounted separated the scattering and molecular beam source chambers. Four 10 mm thick fused silica windows were mounted on the end of short sidearms on the scattering chamber, providing $\sim 98\%$ transmission of the laser beams at the wavelengths used.

Arrangement 2

A schematic of the apparatus in arrangement 2 is shown in Figure 2.3. The main modifications relative to arrangement 1 were as follows: (i) the chamber with the right-angle bend to diffusion pump B was removed to bring the pump closer to the nozzle; (ii) the hole in the flange on the base of the scattering chamber was widened to improve the pumping efficiency around the molecular beam source; (iii) a set of conductively cooled baffles were added to the toroidal liquid nitrogen trap in the scattering chamber to prevent back-streaming of diffusion pump B; and, (iv) the ion optics were suspended from a flange on the top of the scattering chamber. Note that in this configuration the two chambers were no longer differentially pumped. A skimmer is not shown in Figure 2.3, however the ion optics mount was designed such that one could have easily been accommodated if desired. Base pressures in the two chambers were typically $\sim 1\times10^{-7}$ Torr, with the pressure rising to 2×10^{-6} Torr under normal operating conditions (the nozzle opening at 10 Hz with a 1 bar stagnation pressure).

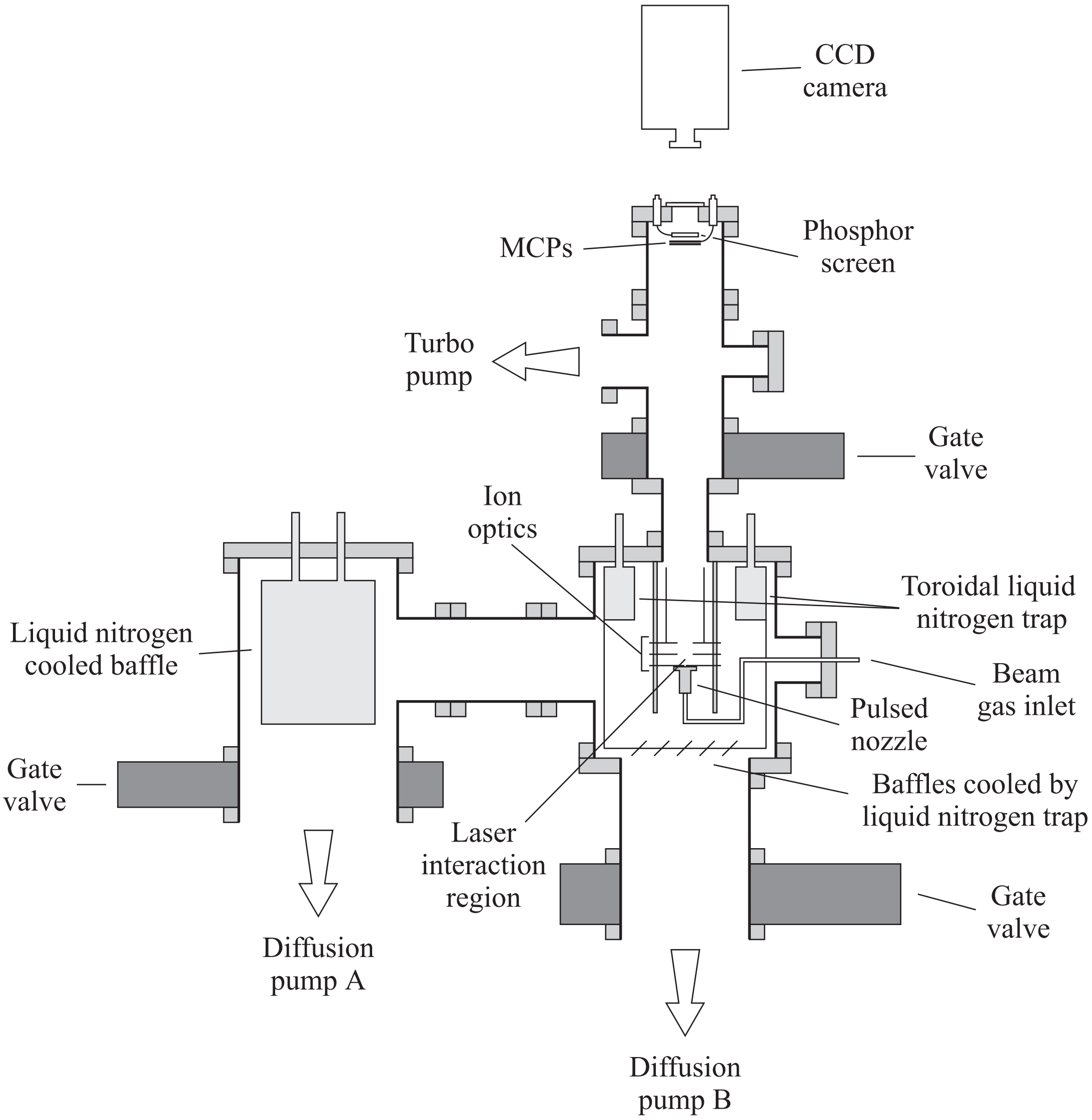

Figure 2.3: A schematic of the experimental apparatus in arrangement 2.

2.3.2 The Lasers

Photolysis Laser

Photodissociation of either the gas under study or the precursor gas for a reaction was achieved using the beam output from a rare-gas halide excimer laser (Lambda Physik EMG 103 MSC) with a nominal pulse duration of 25 ns and typical pulse energies of 180 mJ. The beam was narrowed using an iris and collimated using a 2 m lens before passing through a quartz Rochon polariser. This produced two divergent beams of opposite linear polarisation, one of which continued to travel in the direction of the incident beam and one of which was deviated. A second iris was used to block the deviated beam. Rotation of the polariser through 90° about the axis of the laser beam allowed either linear polarisation to be selected. Pulse energies measured at the entrance window were typically 5–10 mJ. If required, the photolysis laser beam was focussed into the interaction region using a 30 cm focal length fused silica lens.

Probe Lasers

REMPI of the products of photodissociation or reaction was effected using the linearly polarised output of a tunable dye laser (Lambda Physik LPD 3002) pumped with the 308 nm output of a XeCl excimer laser. The pump laser was either a Lambda Physik LPX 110i excimer laser or a Lambda Physik LPX 200 excimer laser, giving pulse energies of around 200 mJ and 400 mJ respectively. The dyes used were solutions of Coumarin 2 (Lambda Physik LC 4500, Exciton, Radiant) in methanol, Coumarin 102 (Lambda Physik LC 4800, Exciton, Radiant) in methanol, and *p*-terphenyl (Aldrich) in dioxane, which provided tunable output in the ranges 432–475 nm, 460–510 nm and 332–360 nm respectively. When using the Coumarin dye solutions, the output of the dye laser was frequency doubled using a BBO I crystal. The frequency doubled light was separated from the fundamental using a set of Pellin–Broca prisms. Typical pulse energies of the frequency doubled light using both Coumarin 2 and Coumarin 102 were around 2 mJ at wavelengths of 225 nm and 240 nm, respectively; the pulse energy of the fundamental at 333 nm using *p*-terphenyl was around 6 mJ. Owing to their low photostability, very frequent (almost daily) replacement of the Coumarin dye solutions was required. During image acquisition, the probe laser wavelength was scanned repeatedly over the Doppler linewidth of the chosen REMPI transition to ensure detection of all products.

2.3.3 The Ion Optics

Different ion optics assemblies were used in the two arrangements of the vacuum chambers; these are described separately below. Both designs closely resemble that of Eppink and Parker [67].

Ion Optics Assembly 1

Ion optics assembly 1 was mounted on the base flange of the scattering chamber in vacuum chamber arrangement 1. It consisted of three circular stainless steel field plates 1 mm thick and 130 mm in diameter. The plates were mounted on three posts, with the centres of the plates arranged collinearly. The repeller plate (the lowest plate) had a 2 mm hole in the centre through which the molecular beam passed, and was held at potential V_R. This could be replaced by an alternative repeller plate with a 4 mm hole in the centre (see Section 2.7.2). The remaining two plates had 20 mm holes in the centre through which the expanding cloud of product ions were extracted, with the upper plate additionally having a 120 mm tube attached on the top. The extractor plate (the middle plate), was maintained at potential V_E, while the upper plate was held at ground potential. The field plates were insulated from the mounting posts and one another by 15 mm long MACOR spacers. In the present system, the optimum ratio of potentials $V_\mathrm{E}/V_\mathrm{R}$ was found to be ~ 0.71 (see Section 2.7.1). The maximum voltage that could be applied to either the repeller or the extractor plate was 5 kV.

Ion Optics Assembly 2

This ion optics assembly was designed to be mounted on the top flange of the scattering chamber in vacuum chamber arrangement 2, in order to allow the diffusion pump to be attached below (see Figure 2.3). Owing to the stringent space constraints imposed by mounting the ion lens in this manner, field plates 93 mm in diameter were used. Four mounting posts were used instead of three to aid structural integrity. These additionally served to simplify alignment of the plates in the ion lens with the skimmer and nozzle, which were also mounted on the posts. The facility to add an additional plate and thus create an ion lens assembly suitable for direct current slice imaging [84] was also provided. Due to the smaller size of the plates in this ion lens, care was taken to avoid leakage of the electric field. Interference from the wires supplying the potentials was minimised by using high vacuum electrically shielded coaxial wires (Caburn-MDC Kapton® KAP5) and by routing the wires around the mounting posts.

2.3.4 The Detection Assembly

Owing to a breakdown of electrical insulation in the original detector, which caused catastrophic damage, two imaging detection assemblies have been used with the apparatus described in the previous Sections. The underlying design of both detectors (Photonic Science; DelMar Ventures) was very similar, and an overview of the operation of a general imaging detector is thus given here.

An imaging detector consists of a pair of resistance-matched MCPs arranged in a Chevron™ (Burle Technologies Inc.) configuration. Each MCP in the detector is a flat glass disc ~ 500 μm thick, containing millions of small pores 8–10 μm in diameter at an angle of 12° with respect to the surface. Upon impact of a charged particle on the front of the pair of MCPs, electrons are ejected from the walls of nearby channels. A potential difference maintained between the front and back faces of the MCPs forms an electric field along the channels through which these electrons are accelerated. Further collisions of the electrons with the walls of the channel produces a cascade of electrons, which is then emitted from the rear of the MCPs. The strength of the electric field along the channel governs the energy of the electrons incident upon the walls of the channels and therefore the number of electrons emitted by each impact. The gain is thus easily controlled by varying the potential maintained between the faces of the MCPs. For each ion striking the front of the pair of MCPs, a burst of $\sim 10^6$ electrons is typically emitted from the same location on the back face. The bursts of electrons are accelerated towards a P-47 phosphor screen by a further electric field formed by a potential difference between the back face of the MCPs and the screen, where the incident electrons excite the phosphor to produce a flash of light.

In the present experiments, the light flashes resulting from each set of ions (produced on each probe laser shot) were captured using a gateable intensified charge-coupled device (CCD) camera (Photonic Science, 576 × 768 pixels, 50 ns minimum gate width). The images were then transferred to a PC equipped with a frame grabber card (Euresys Picolo Pro 2) where they were summed and processed in real time. This real time processing comprised thresholding and ion counting [123], and was undertaken using a home-written program.

Thresholding

The pixel intensity seen on the camera arising from an ion impacting on the detector was usually much higher than any low-level background noise resulting from the camera intensifier or imperfect shielding of the camera from ambient light. Background noise was thus removed from the images by applying an equal threshold to each pixel in the image. Any pixel intensity which was lower than the chosen discrimination level was rejected as noise. For images collected with the system described above, where the maximum greyscale depth (i.e., the value assigned to the 'brightest' pixel) was 255, the best results were obtained using a threshold of 10.

Ion Counting

The ion counting technique was developed in 1998 by Houston and co-workers [123], and was found to significantly improve both the spatial resolution and the detection sensitivity of 2D ion imaging detectors.

Each ion striking the detector typically results in intensity seen over several pixels on the camera. Within the ion counting scheme, only the brightest pixel in each of these spots was counted towards the final accumulated image. The algorithm used to determine the location of the bright spots compared all pixel intensities with the four nearest neighbours. Pixels with intensity $p(x, y)$ were accepted subject to the following criteria:

$$\begin{aligned} &p(x-1, y) < p(x, y) \geq p(x+1, y), \\ &p(x, y-1) < p(x, y) \geq p(x, y+1). \end{aligned} \tag{2.1}$$

On satisfying all of the above relationships, the corresponding pixel in the final accumulated image was incremented by one (i.e., an ion signal was counted at that location). Each data value at point (x, y) in the final accumulated image thus represented the total number of ions that had struck that pixel over the entire experiment. Problems with the ion counting method can occur when a large number of ions are recorded with a relatively small spatial distribution, a condition called spatial congestion. In severe cases, the intensity distributions of neighbouring ions are combined and maxima can no longer be reliably located because the pixel intensities surrounding an ion spot may not decrease regularly in intensity. In such cases the ion counting method may miss entire clusters of detected ions. The effects of spatial congestion may be limited by attenuation of the probe laser power or the molecular beam intensity until all ions are seen to be counted. It should also be noted that the ion counting technique tends to result in 'grainy' images. As will be seen in Section 3.2.1, this can cause problems when using the Abel-inversion method to recover the full 3D scattering distribution from the 2D projection provided by the imaging experiments.

2.4 Ion Time-of-Flight Spectra

Measurement of the total current flow due to electrons emitted from the MCPs striking the phosphor screen allowed the ion arrival time-of-flight spectrum to be monitored. The current was amplified and converted to a voltage, and the resulting time-of-flight spectrum viewed together with the camera gate in real time on a two-channel digital oscilloscope (Tektronix TDS 220). The full-width-at-half-maximum

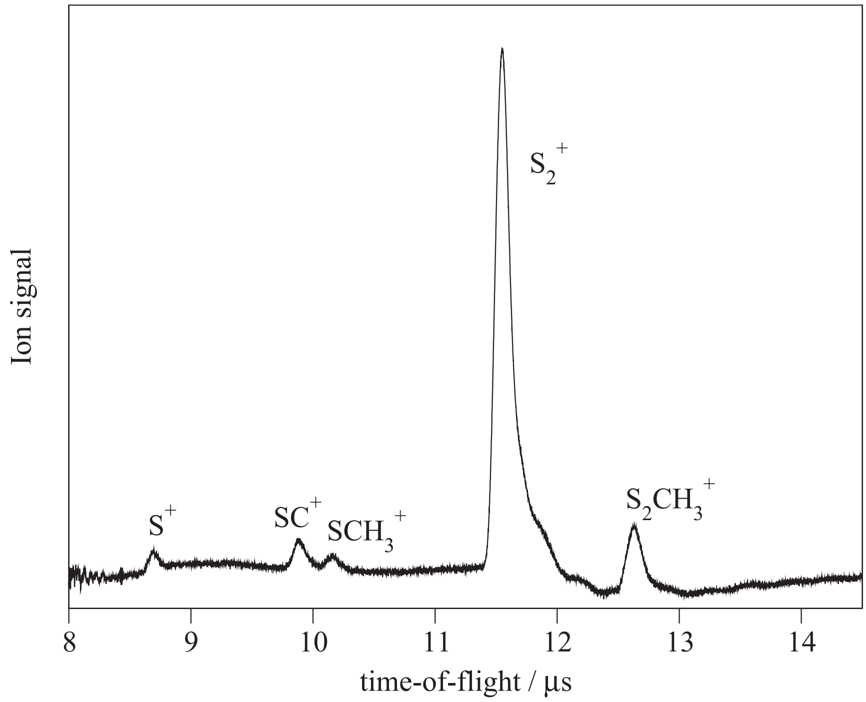

Figure 2.4: A typical time-of-flight spectrum for the products of photodissociation and multi-photon dissociative ionisation of $CH_3S_2CH_3$ at 193 nm [124], obtained by measuring the current flow due to electrons travelling from the MCPs to the phosphor screen.

(FWHM) of a peak was typically ~120 ns. A typical time-of-flight spectrum obtained for the products of photodissociation and multi-photon dissociative ionisation of dimethyl disulphide ($CH_3S_2CH_3$) at 193 nm [124], which was recorded in this way, is shown in Figure 2.4. In these experiments, a mixture of ~1% of dimethyl disulphide in helium was entrained in a skimmed molecular beam and photolysed using the 193 nm output of an ArF excimer laser (Lambda Physik EMG 103 MSC). The laser was linearly polarised in the plane of the detector using a Rochon polariser and focussed into the interaction region using a 30 cm focal length fused silica lens. Products of single-photon dissociation were detected *via* multi-photon ionisation; ionic products of two-photon dissociative ionisation were also detected [124].

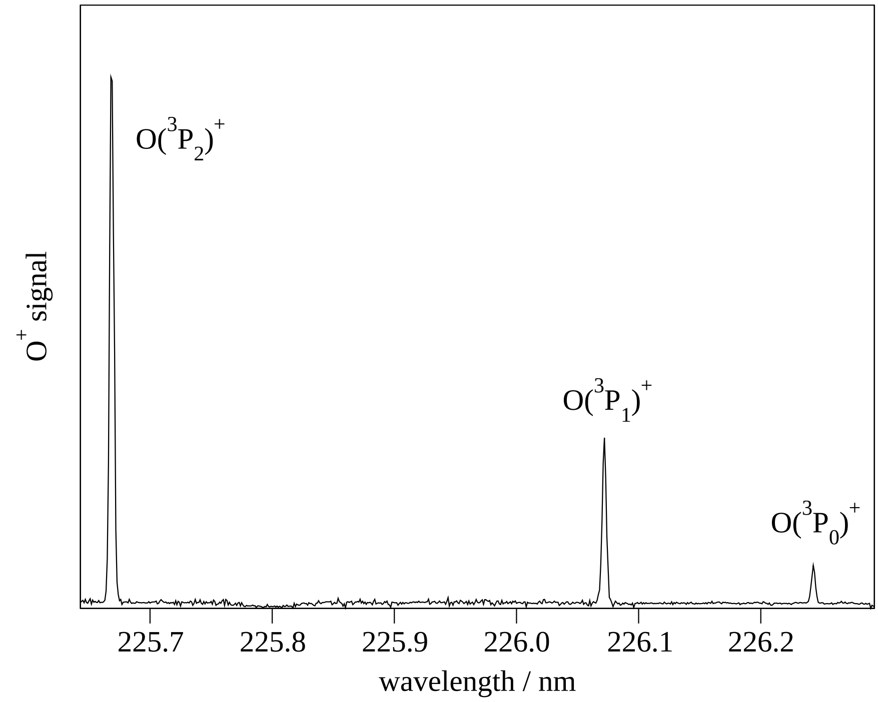

Figure 2.5: (2+1) REMPI spectrum of the O(^{3}P$_J$) products of NO_2 photodissociation at 308 nm.

2.5 REMPI Spectra

The total ion signal for a given mass peak in the time-of-flight spectrum could be measured using a gated boxcar integrator (Stanford Research Systems SRS250). By scanning the probe laser wavelength, it was possible to record the structure of the nascent product REMPI spectrum. Data were transferred to a PC for signal averaging (typically 20–40 shots per wavelength step) and storage. An example spectrum obtained in this way is shown for the O(^{3}P$_J$) products of photodissociation of NO_2 at 308 nm in Figure 2.5. The O(^{3}P$_J$) atoms were detected *via* the $3p\,^3\mathrm{P} \leftarrow {}^3\mathrm{P}_J$ (2+1) REMPI transitions at around 226 nm [125].

2.6 Molecular Beam Temperature

The rotational temperature of the molecular beam was determined by measuring the REMPI spectrum of NO molecules in the beam. These experiments were car-

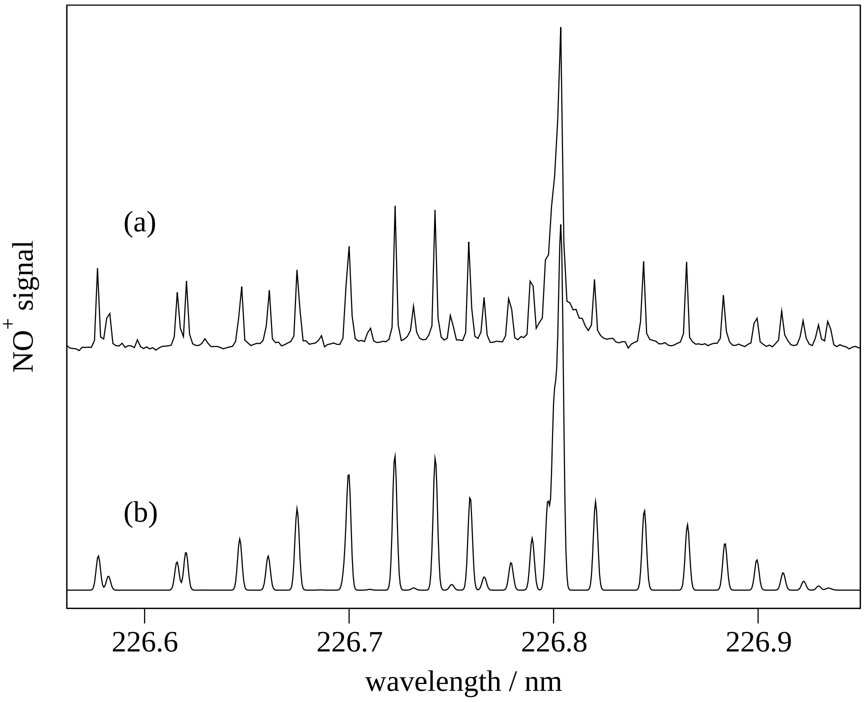

Figure 2.6: (1+1) REMPI spectrum of the NO(v = 0) molecules rovibrationally cooled in the molecular beam: (a) experimental spectrum, (b) simulated spectrum using a rotational temperature of 50 K [126]. Structure is seen for the (0,0)P_2, (0,0)P_{12}, (0,0)Q_2, (0,0)Q_{12}, (0,0)R_2 and (0,0)R_{12} rovibrational branches in both spectra.

ried out with the vacuum chambers in arrangement 2 (see Section 2.3.1); the nozzle and detection areas of the vacuum system were therefore not differentially pumped. The molecular beam was formed by expansion of a mixture of $< 1\%$ NO in argon through a nozzle with a 800 µm diameter orifice. A skimmer was not used, however collimation of the free-jet expansion was achieved using the hole in the repeller plate. Ground vibrational state NO molecules were probed state selectively *via* (1+1) REMPI on the (0,0)P_2, (0,0)P_{12}, (0,0)Q_2, (0,0)Q_{12}, (0,0)R_2 and (0,0)R_{12} rovibrational branches of the $A\,^2\Sigma^+ \leftarrow X\,^2\Pi_{1/2}$ electronic band at wavelengths between 226.5 and 227 nm [126]. Care was taken to avoid saturation of the resonant transitions. The resulting REMPI spectrum is shown in the upper panel of Figure 2.6. Also shown is a simulation of the experimental spectrum calculated using LIFBASE [126]. The best fit to the data was achieved when the rotational temperature was fixed to be 50 K. The rotational temperature of the molecular beam with the vacuum chambers in arrangement 2 is thus believed to be ~ 50 K. Several factors may have contributed to the relatively poor rotational cooling observed in the molecular beam. The main reason is believed to be that the distance between the nozzle orifice and the interaction region was insufficient for collisional cooling to be maximally effected. In addition, since the expansion was not skimmed, some of the molecules that were released early in the gas pulse and did not pass through the repeller plate may have been scattered into the molecular beam, thereby impeding the efficiency of the cooling in the most intense portions of the molecular beam.

2.7 Image Properties

Various factors that affect the quality of the velocity-map ion images obtained from the apparatus have been investigated and are detailed in this Section. Brief overviews of the experimental procedures employed in the photodissociation processes used in these investigations are given below.

Cl_2 photolysis

The experiments which employed Cl_2 photolysis were conducted using a beam of 5% Cl_2 in helium. Photolysis was effected at 308 nm using the focussed output of a XeCl excimer laser. Ground state $Cl(^2P_{3/2})$ atoms were detected on the $4p\,^4P_{3/2} \leftarrow {}^2P_{3/2}$ (2+1) REMPI transition at 240.46 nm [125]. The photolysis laser was linearly polarised in the plane of the detector using a Rochon polariser. Images were recorded with the electric vector of the photolysis laser in the plane of the detector, while the probe laser was polarised perpendicularly to the detector. From conservation of energy, the $Cl(^2P_{3/2})$ atoms are found to be travelling at the single speed of 2067 ms^{-1} following photolysis.[1]

---

[1] Calculated using $D_0^0(^{35}Cl_2) = 2.475$ eV [127, 128].

O_2 photolysis

The experiments employing O_2 photodissociation were carried out using a molecular beam comprising $\sim 10\%$ O_2 in helium. This was intersected by a single laser, used both to photolyse O_2 and to ionise the $O(^3P_2)$ products on the $3p\,^3P \leftarrow {}^3P_2$ (2+1) REMPI transition at 225.66 nm [125]. At this wavelength and with the pulse energies used, photodissociation of O_2 occurs by one-photon excitation into the Herzberg continuum and by two-photon excitation into the Schumann–Runge continuum (see, for example, Ref. [129] and references given therein), yielding two observable dissociation pathways:

$$O_2 + h\nu \longrightarrow O(^3P_2) + O(^3P_J) \tag{2.2}$$

$$O_2 + 2h\nu \longrightarrow O(^3P_2) + O(^1D_2). \tag{2.3}$$

By conservation of energy, the $O(^3P_2)$ products of pathways 2.2 and 2.3 are found to be travelling at the single speeds of 1583 ms^{-1} and 4875 ms^{-1}, respectively.[2]

2.7.1 Calibration of the Ion Optics

Focussing of the Ion Lens

As was mentioned in Section 2.1, the focus of the ion lens was adjusted by varying the potentials at which the repeller and extractor plates were maintained.[3] The optimum ratio of the repeller and extractor voltages was determined visually by fixing the potential on the repeller plate, V_R, and varying the potential on the extractor plate, V_E, until sharp images were obtained. A set of images collected at different values of V_E with a fixed value of V_R are shown in Figure 2.7 for the $Cl(^2P_{3/2})$ products of Cl_2 photodissociation at 308 nm. The effects of over- and under-focussing were easily recognised as a blurring of the images along the laser

---

[2] Calculated using $D_0^0(^{16}O_2) = 5.080$ eV [127].

[3] Note that the term 'focus' used here should be understood as a mapping of all charged particles that have the same initial velocity vector onto the same point in the focal plane, thus compensating for their initial position of creation.

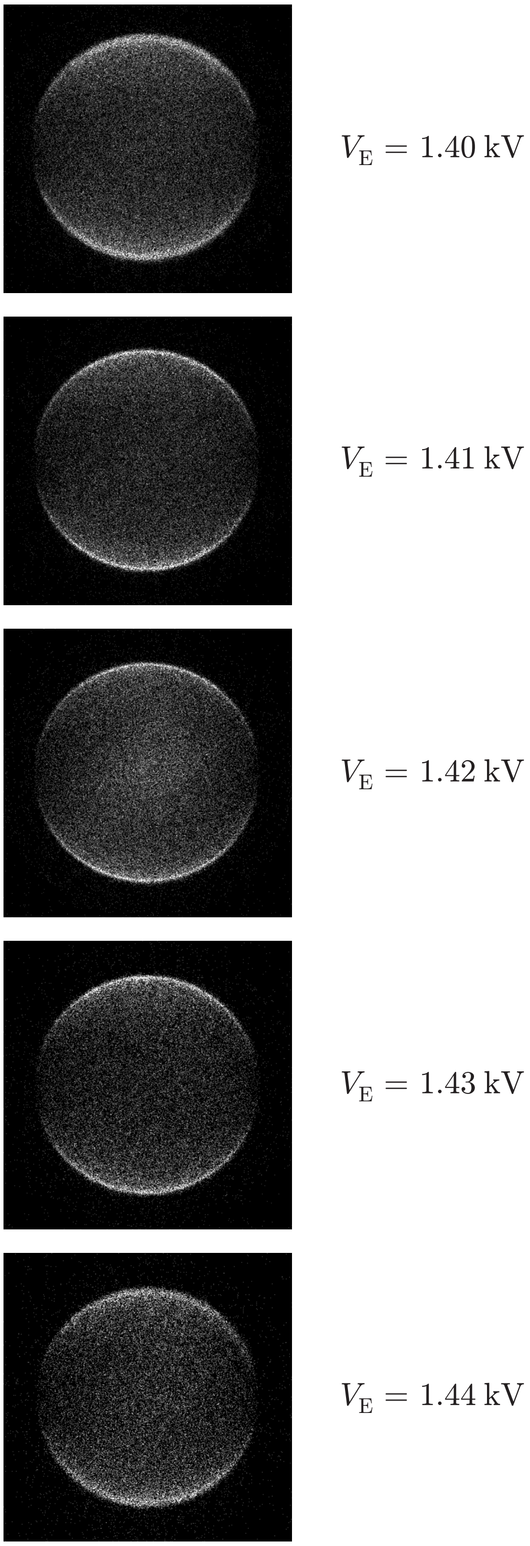

Figure 2.7: Raw ion images of the Cl($^2P_{3/2}$) atom products of photodissociation of Cl_2 at 308 nm. Images were acquired with the voltage on the repeller plate of the ion optics, V_R, held at 2.00 kV, with the various voltages applied to the extractor plate, V_E, shown. Optimum focus of the ion lens is seen with $V_E = 1.42$ kV, corresponding to $V_E/V_R = 0.71$. Images were accumulated over 5000 laser shots.

propagation direction (vertically in the images shown). The ion lens was seen to be optimally focussed when $V_{\mathrm{E}}/V_{\mathrm{R}} = 0.71$.

Pixel-to-Velocity Conversion Factor

The velocity of an ion of mass m and charge q accelerated by potential V along the time-of-flight axis is given by

$$v_{\mathrm{TOF}} = \sqrt{\frac{2qV}{m}}. \tag{2.4}$$

The time-of-flight, t, is thus given by

$$t = d\sqrt{\frac{m}{2qV}}, \tag{2.5}$$

where d is the length of the flight tube. The radial distance on the detector, r_{p}, travelled by the ion with initial radial speed, v_{p}, during its time-of-flight, is therefore given by

$$r_{\mathrm{p}} = N v_{\mathrm{p}} d\sqrt{\frac{m}{2qV}}, \tag{2.6}$$

where N is a magnification factor introduced by the ion lens [67]. For a given accelerating potential, the radial distances travelled by all ions with the same mass and charge are thus directly proportional to their initial speeds. The factor required to convert between distance and speed, $v_{\mathrm{p}}/r_{\mathrm{p}}$, can be determined experimentally for a particular value of V_{R},[4] by detecting ions of known mass and velocity. Once the conversion factor has been determined for an ion of known mass at a given value of V_{R}, the factor required for other masses may be evaluated using the relation $r_{\mathrm{p}} \propto v_{\mathrm{p}}\sqrt{(m/q)}$.

In the current experiments, the calibration factor required to convert the radial coordinate of the images into product velocity was determined as a function of repeller voltage using the atomic and diatomic products of photodissociation of diatomic and triatomic molecules, respectively, for which the photofragment velocities may be calculated exactly by conservation of energy. An example image obtained

---

[4] Note that by fixing the ratio $V_{\mathrm{R}}/V_{\mathrm{E}}$, the accelerating potential V is proportional to V_{R}.

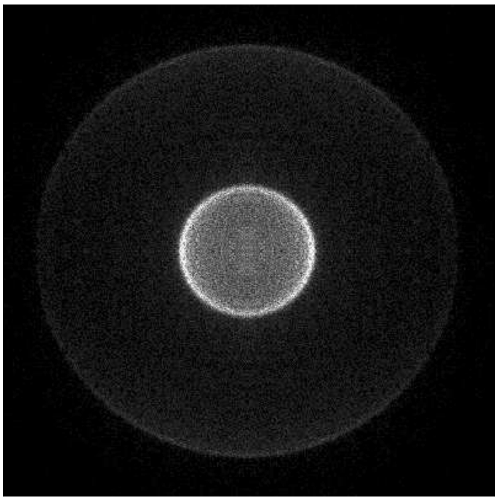

Figure 2.8: Symmetrised raw ion image of the O($^3P_2$) atom products of photodissociation of O_2 at 225.66 nm.

in order to determine this calibration factor at $V_R = 4.00$ kV is shown in Figure 2.8 for the O($^3P_2$) products of O_2 photodissociation at 225.66 nm. The inner and outer rings correspond to the O($^3P_2$) products of photolysis pathways 2.2 and 2.3, respectively. The pixel-to-velocity conversion factor was determined by inverse Abel transformation of the images, with the maxima in the radial coordinate of the resulting 'slice' through the 3D scattering distributions corresponding to the known velocities of the photofragments. Integration of the inverse Abel transform of the image shown in Figure 2.8 over angle returned the O atom speed distribution, $P(v_O)$, shown in Figure 2.9.

2.7.2 Skimmer and Repeller Plate Hole Sizes

The size of the molecular beam could be changed by using nozzle faceplates with different diameter orifices. For molecular beams created by expansion of the gas mixture from the nozzle using the faceplate with a 500 µm diameter orifice and collimated using the 1 mm skimmer, a repeller plate with a 2 mm hole in the centre was used. A larger collimated molecular beam was formed using a nozzle faceplate with a 1 mm diameter orifice and a 2 mm skimmer. A repeller plate with a 4 mm hole in the centre was required to allow this larger molecular beam to pass through

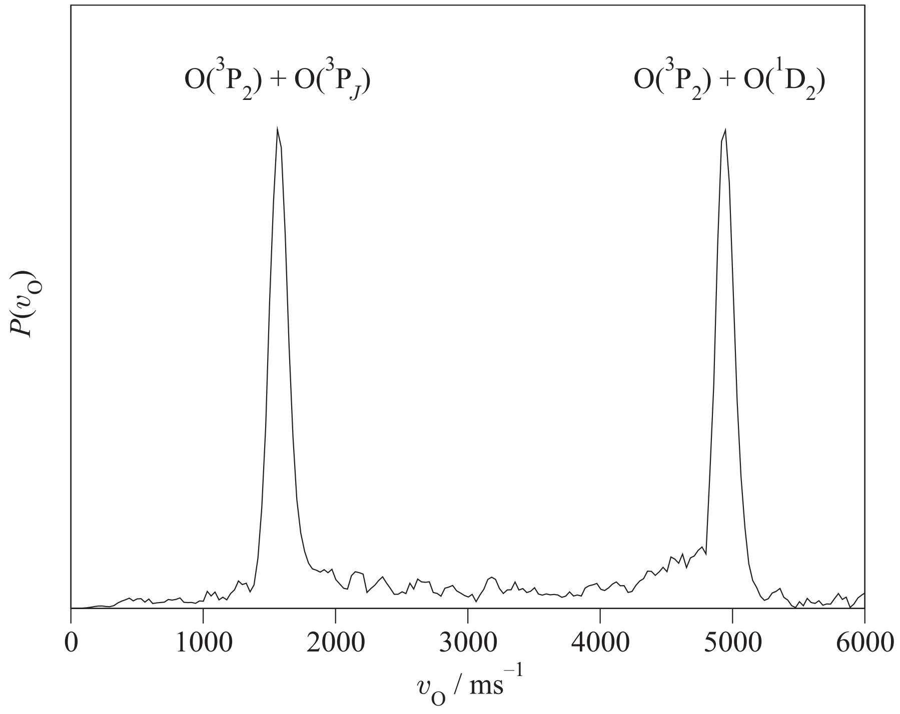

Figure 2.9: Speed distribution of the O($^3P_2$) atoms—obtained from an inverse Abel transformation of the image shown in Figure 2.8—used to calibrate the radial axis of the images.

unimpeded. The sensitivity of the focus of the ion lens to the ratio of the potentials at which the repeller and extractor voltages were maintained was greatly increased when using the repeller plate with the larger hole (acceptable errors were reduced to $\sim 0.2\%$ when using the plate with the 4 mm hole, compared to $\sim 1\%$ when using the plate with the 2 mm hole). Once the correct ratio had been determined, however, the speed resolution of the apparatus was seen to be only very slightly decreased by use of the larger molecular beam and repeller plate hole sizes, with $\Delta v/v$ found to deteriorate from 3.9% to just 4.2%. Cl atom speed distributions, $P(v_{\mathrm{Cl}})$, determined by integration of the inverse Abel transforms of the images of the Cl atom products of 308 nm photodissociation of Cl_2 over angle, are shown in Figure 2.10 for the two different sized molecular beams.

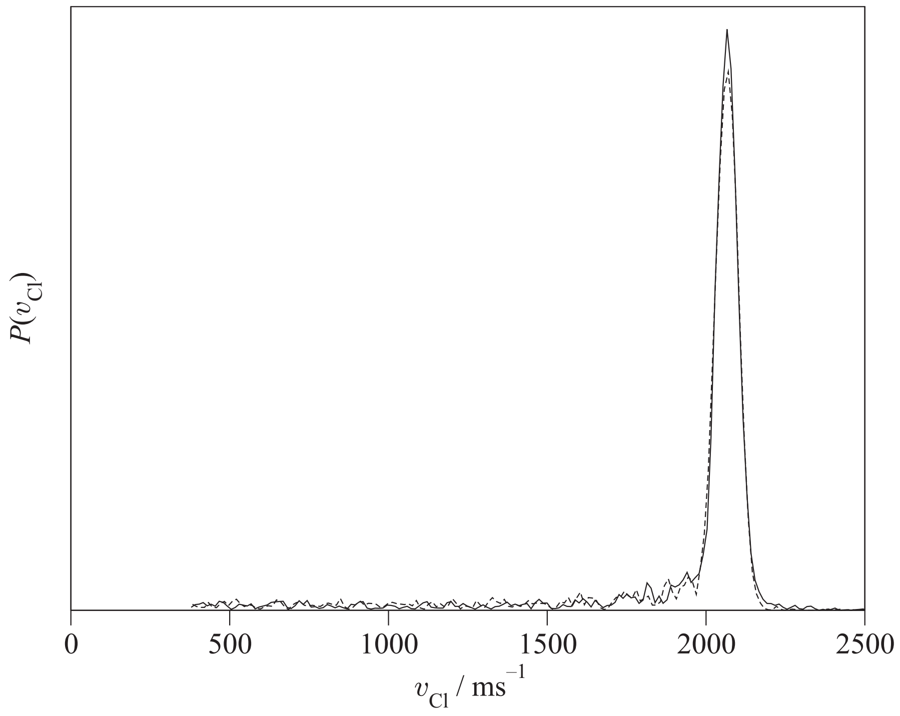

Figure 2.10: Speed distributions of the Cl(^{2}P$_{3/2}$) atom products of Cl$_2$ in molecular beams formed using a 1 mm skimmer with a 2 mm hole in the repeller plate (—) and using a 2 mm skimmer with a 4 mm hole in the repeller plate (- - -). $\Delta v/v$ was found to be 3.9% in the former configuration and 4.2% in the latter.

2.8 A Capillary

In an attempt to maximise the number density of reaction precursor and reactant molecules in the interaction region, a $\sim$1 mm internal diameter ceramic capillary was mounted on a plate attached to the front of the nozzle. A nozzle faceplate with a 800 μm diameter orifice was used. The nozzle orifice was chosen to be similar to the internal diameter of the capillary in an effort to effect a small degree of cooling in the expansion of the gas pulses at the end of the capillary. A similar arrangement has been used by Orr-Ewing and co-workers in their studies on the reactions of chlorine atoms with small organic molecules [130]. In these experiments, the Cl$_2$ precursor and organic reagent were expanded in parallel from different nozzles through Teflon tubing of a slightly narrower internal diameter than the nozzle orifice diameters to give a cooled molecular beam with a temperature of $\sim$60 K [130]. In the current experiments, the nozzle-capillary setup was arranged so that the end of the capillary protruded through the repeller plate to around 3 mm below the interaction region. Unfortunately, although electrical insulation was maintained under normal operating conditions without the lasers firing, on allowing either the photolysis or probe laser beams into the chamber, the production of ions caused a breakdown of the electrical insulation and arcing to occur between the repeller plate and the nozzle *via* the gas pulse in the capillary. Several attempts were made to eliminate this arcing by using shorter gas pulse durations and increasing the distance between the opening of the capillary and the repeller plate. None were successful, however, and the use of a capillary was therefore abandoned. It should be noted that these experiments on the use of a capillary were carried out prior to modifications made to allow the nozzle to be electrically floated at the same potential as the repeller plate (see Section 2.9.1); in light of these improvements, reinvestigation of the use of a capillary may be worthwhile in any further studies.

2.9 The Cl + CH_4 Reaction

Experiments on the Cl + CH_4, Cl + CD_4 and Cl + CH_3D reactions were carried out with the vacuum system in arrangement 2 (see Section 2.3.1) and using ion optics assembly 2 (see Section 2.3.3). The DelMar Ventures imaging detection assembly was used in these experiments. Further details on the experimental procedures employed are given below.

2.9.1 Experimental Details

In order to yield high reactant number density in the interaction region, the apparatus was arranged such that the pulsed solenoid nozzle was mounted directly behind the repeller plate of the velocity mapping ion optics assembly. This arrangement was originally proposed by Kitsopoulos and co-workers for a study on the Cl + C_2H_6 reaction [131]. In this arrangement both the nozzle and the nozzle mounting plate were required to be electrically floated at the same potential as the repeller plate, so as to avoid electrical discharge during the gas pulse.

A 1:4:5 mixture of Cl_2 (Aldrich, 99.5%), CH_4 (BOC, 99.99%) (CD_4 [Isotec Inc., 99%] or CH_3D [Isotec Inc., 98%]), and helium buffer gas was premixed in a stainless steel tank at a total stagnation pressure of 1.0 bar, prior to expansion through a 800 μm diameter orifice in the pulsed nozzle. High levels of unwanted side-reactions of the Cl_2 and methane gas mixtures in the gas manifold were seen to deplete the concentrations of reactant and photolysis precursor in the gas mixtures to unworkable levels very rapidly (typically over a period of $\sim$10 min). The HCl and DCl products of these reactions were also found to react with, and thus hinder operation of, the internal components of the pulsed nozzle. The side-reactions were believed to be surface-catalysed and accordingly, several attempts were made to reduce their rate, including the coating of the inside of the gas manifold with halocarbon wax (Halocarbon Products Corp. Series 1500), and separately, with a PTFE spray (RS Components Ltd.). The latter was found to extend the lifetime of the gas mixtures significantly. The free-jet expansion was intersected perpendicularly mid-way between the repeller and extractor plates of the ion lens by two counter-propagating linearly polarised laser beams. The Cl_2 precursor was photolysed by focussed 308 nm radiation polarised in the plane of the detector, to form two fast-moving $Cl(^2P_{3/2})$ atoms.

The methyl radical products were detected *via* (2+1) REMPI through the 0_0^0 band of the $3p_z\,^2A_2'' \leftarrow \tilde{X}\,^2A_2''$ Rydberg transition [132–136] using laser radiation polarised parallel to the time-of-flight axis at wavelengths around 333 nm. Both the photolysis and probe laser beams were focussed into the interaction region using 30 cm focal length fused silica lenses. A short delay of between 25 and 50 ns was maintained between the laser pulses to allow a sufficient number of reactive collisions to occur, while avoiding complications due to fly-out of either the Cl atom reactants or the methyl radical products from the probe laser interaction region. Images were summed over around 60,000 laser shots.

Chlorine atoms with sufficient energy to participate in the Cl + CH_4 reaction were also formed by photodissociation of Cl_2 at the wavelength of the probe laser, and the observed signal thus also contained a contribution from the methyl products of these reactions. By triggering the photolysis laser at half the frequency of the probe laser and summing the resulting probe-only and photolysis-probe images into separate buffers, the desired photolysis-probe image was recovered reliably by subtraction of the probe-only image from the photolysis-probe image. Errors in the subtraction introduced by experimental drift were minimised by the simultaneous acquisition of the two images in this way.

2.9.2 The Cl Atom Reactant

The photodissociation of Cl_2 using linearly polarised light at 308 nm has been reasonably well characterised [137–141]. At this wavelength more than 99% of the chlorine atoms are produced in their ground electronic state, $Cl(^2P_{3/2})$, with a translational anisotropy, β_0, of -1.0 ± 0.1 [138, 141]. As was noted in Section 2.7, conservation of energy dictates that the $Cl(^2P_{3/2})$ atoms are travelling at the single speed of 2067 ms^{-1} following photolysis. Assuming that the relative motion between the molecular chlorine precursor and methane is small, owing to efficient translational cooling in the jet expansion, the photolysis defines the relative motion of the chlorine atom and the methane molecule and thus the collision energy.

Images were obtained for the $Cl(^2P_{3/2})$ atoms formed in the photolysis step under very similar conditions to those described previously for the Cl + CH_4 (CD_4 or CH_3D) reactions. The probe laser beam was used both to photolyse Cl_2 and then to detect the $Cl(^2P_{3/2})$ atom products *via* the $4d\,^4D_{1/2} \leftarrow {}^2P_{3/2}$ (3+1) REMPI transition at 339.86 nm [125]. A typical image is shown in Figure 2.11. The known velocity of the Cl atoms produced at this wavelength (1798 ms^{-1}) provided a check for the velocity scaling of the images. Integration of the inverse Abel transform of this image over angle returned the Cl atom speed distribution, $P(v_{Cl})$, shown in Figure 2.12. The speed distribution of the Cl atoms provides information about the

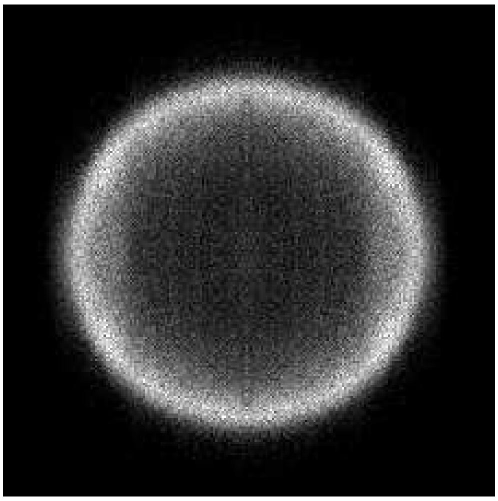

Figure 2.11: Symmetrised raw ion image of the Cl($^2P_{3/2}$) atom products of photodissociation of molecular chlorine at 339.86 nm.

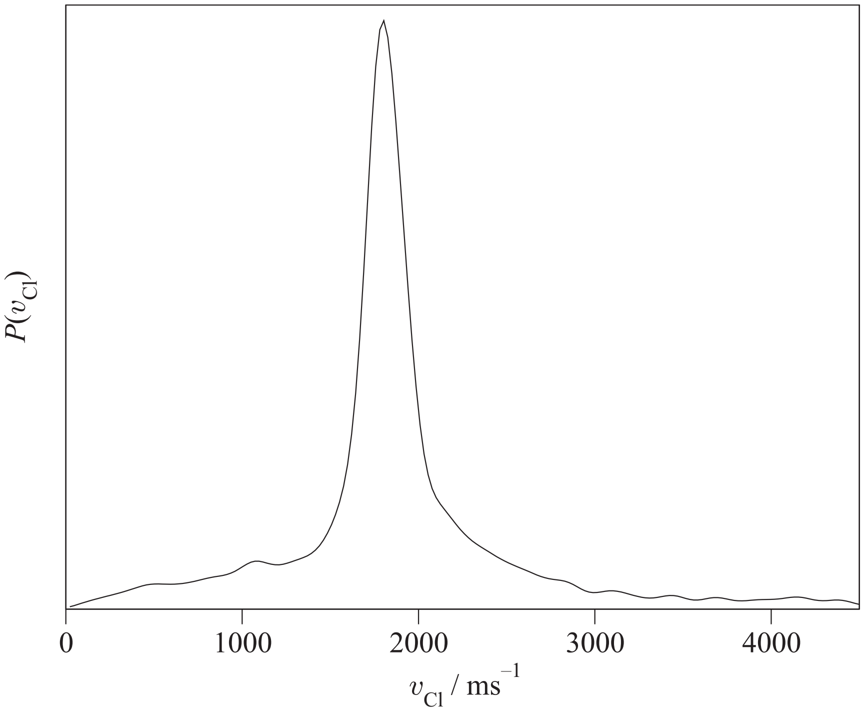

Figure 2.12: Speed distribution of the Cl($^2P_{3/2}$) atoms obtained from an inverse Abel transform of the image in Figure 2.11.

velocity resolution of the experiment, and also about the likely spread in collision energies; this aspect of the experiments and its relevance to the analysis procedures used is described more fully in Chapter 6. The Cl atom speed distribution is compared to that obtained for the Cl + C_2H_6 and Cl + n-C_4H_{10} reactions in Section 2.10.2.

2.9.3 Molecular Beam Number Density and Signal Levels

The number of molecules, N, contained in each gas pulse of the free-jet expansion was estimated to be $\sim 8 \times 10^{15}$ by measuring the drop in stagnation pressure behind the nozzle as a function of time and assuming ideal behaviour of the gas mixture. If the nozzle is assumed to emit a constant flow of gas per pulse, then the density at any point will be independent of time during the pulse. The number density in a free-jet expansion or molecular beam is known to fall as $1/r^2$, where r is the distance from the nozzle orifice [32]. Thus, if the angular dependence of the free-jet expansion is well approximated by a $\cos^2\theta$ distribution, where θ is the angle of deviation from the propagation direction of the molecular beam, then the number density at any point, $\rho(r,\theta)$, is given by

$$\rho(r,\theta) = \rho_0 \frac{\cos^2\theta}{r^2}, \tag{2.7}$$

where ρ_0 has units of molecules $\mathrm{m^{-1}\,sr^{-1}}$ and depends on the source stagnation number density. The total number of molecules emitted during the pulse is therefore given by

$$\begin{aligned} N &= \int_0^{2\pi}\int_0^{1}\int_0^{r_{\max}} \rho(r,\theta) r^2\,\mathrm{d}r\ \mathrm{d}\cos\theta\ \mathrm{d}\phi \\ &= \frac{2}{3}\pi\rho_0 r_{\max}, \end{aligned} \tag{2.8}$$

where $r_{\max} = vt$ is the maximum distance travelled by a molecule in the gas pulse, t is the duration of the gas pulse and v is the velocity of the molecular beam. In the current experiments $t \sim 300$ μs and v is estimated to be 1000 $\mathrm{ms^{-1}}$ [32]. Using Equation 2.8 to calculate ρ_0 from the estimated number of molecules in each gas pulse, the number density in the beam at the interaction region (7.5 mm from the nozzle orifice, along the axis of the molecular beam) is found, using Equation 2.7, to be $\simeq 2 \times 10^{14}$ molecules cm^{-3}.

As a crude check of the number density in the interaction region determined above, the value may be used to estimate the number of methyl products formed and detected by the photolysis and probe laser pulses. If Gaussian beam optics are assumed, the interaction volume, V, of the photolysis laser can be estimated using $V = \pi b w_0^2$, where

$$w_0 \approx \frac{f\lambda}{\pi w} \tag{2.9}$$

and

$$b = \frac{\pi w_0^2}{\lambda}. \tag{2.10}$$

In these equations w_0 is the radius of the laser beam waist at the focus, w is the radius of the beam at the lens, λ is the laser wavelength and b is the distance over which the beam radius spreads by a factor of $\sqrt{2}$ (giving a reasonable estimate of the 'depth of focus'). In the present experiments, $V \simeq 3 \times 10^{-5}$ cm^3. At the photolysis laser pulse energies employed in the current study ($\sim$5 mJ at the window on the chamber), all of the Cl_2 precursor molecules in the interaction region are found to be photolysed. The methyl radical number density, n_{CH_3}, is given by

$$n_{CH_3} = n_{Cl} \times V \times n_{CH_4} \times \sigma_{Cl+CH_4} \times \Delta t \times v_{Cl}, \tag{2.11}$$

where n_{Cl} is the number density of chlorine atoms, σ_{Cl+CH_4} is the reaction cross-section, Δt is the delay between photolysis and probe laser pulses and v_{Cl} is the velocity of the chlorine atoms. For a photolysis-probe delay of 25 ns and estimating the reaction cross-section to be $\sim 5 \times 10^{-20}$ cm^2, the methyl number density is calculated to be $\sim 5 \times 10^5$ radicals per pulse. Assuming a detection efficiency on the order of 1%, this gives around 5000 methyl ions formed for every laser pulse. Although slightly higher, this value is of a similar magnitude to that determined from the recorded images.

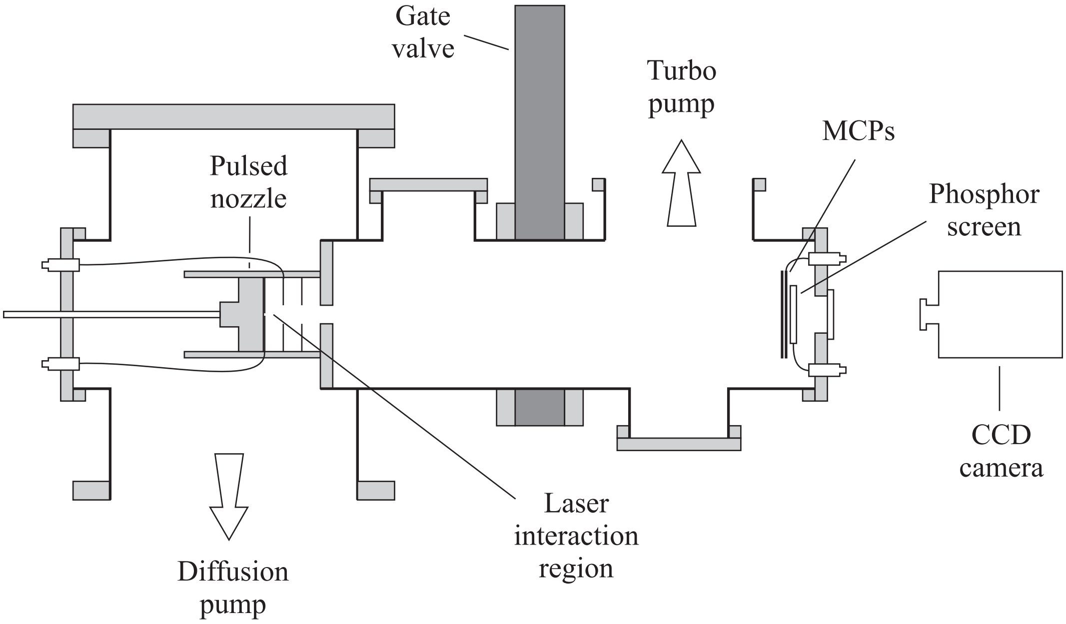

Figure 2.13: A schematic of the experimental apparatus.

2.10 Experiments Performed in Crete

Experiments on the Cl + C_2H_6 and Cl + n-C_4H_{10} reactions were performed using the velocity-map ion imaging apparatus at the Institute for Electronic Structure and Laser in Crete. The experimental work was carried out under the supervision of Professor Theofanis N. Kitsopoulos during a short visit to the institute.

2.10.1 The Machine

A schematic of the apparatus is shown in Figure 2.13. It consists of two regions: (i) the molecular beam source and reactive scattering region pumped by a mechanical pump backed 3000 l/s oil diffusion pump (Leybold, DI 3000) fitted with a water-cooled baffle and (ii) the detection region pumped by a 600 l/s turbo-molecular pump (Leybold, Turbovac 600). Owing to the separation of these two regions by a 15 mm hole, only a slight differential pumping between them was achieved. A 1:1 mixture of Cl_2 (Merck, 99.8%) and ethane (Aldrich, 99%), or n-butane (Aldrich 98%), stored in a glass bulb at a pressure of $\sim$600 Torr was co-expanded in a pulsed molecular beam using a homemade piezoelectrically actuated nozzle [142] with a

1 mm diameter orifice operating at 10 Hz. Typical operating pressures in the source and detection regions were 1×10^{-5} and 1×10^{-6} Torr respectively. Standard velocity mapping ion optics [67] were mounted directly in front of the nozzle, with the nozzle and the repeller plate maintained at the same voltage to avoid electrical discharge during the gas pulse. Midway between the repeller and extractor field plates the molecular beam was intersected perpendicularly by two counter-propagating laser beams. Photolysis of Cl_2 at 355 nm was effected using the third harmonic output of a Nd:YAG laser ($\sim$20 mJ per pulse).

The HCl($v' = 0$) products of both reactions were detected with rotational-state resolution *via* (2+1) REMPI, through the Q branch of the $E\ {}^1\Sigma^+$ state [143–145] for $j' = 0$–6, and additionally through the R branch of the $F\ {}^1\Delta_2$ state [143–145] for $j' = 1$, 3 and 6. The probe radiation was generated using the frequency-doubled output of a Nd:YAG-pumped optical parametric oscillator (Spectra-Physics Pro 250 MOPO) with a typical pulse energy of $\sim$1 mJ. For each transition the probe laser was scanned over the Doppler profile of the HCl product. Both photolysis and probe laser beams were linearly polarised in the plane of the detector and were focused using 25 cm focal length lenses. The timing of the experiment was controlled using digital delay pulse generators (SRS DG535). A short delay of between 120 ns and 150 ns between the photolysis and probe laser pulses allowed sufficient HCl product density to build up prior to detection. Owing to the narrow focus of both laser beams, care was taken to ensure that fly-out was avoided. Suitable electrostatic potentials applied to the repeller and extractor plates of the ion optics effected velocity mapping [67] of the ionised reaction products onto the detector (a pair of matched MCPs [Hamamatsu] coupled to a P46 phosphor anode [Proxitronic]) located approximately 45 cm from the interaction region. $H^{35}Cl^+$ ions were detected mass-selectively by pulsing the voltage applied to the MCPs from -1100 V to -1600 V at the appropriate time-of-flight. The resulting images were captured using a CCD camera (Cohu 4910) and sent to a PC for signal averaging (EyeSpy software by k-Space Associates).

2.10.2 The Cl Atom Reactant

The photodissociation of Cl_2 using linearly polarised light at 355 nm has been well characterised [82, 128, 137, 138, 146–150]. At this wavelength more than 98% of the chlorine atoms are produced in their ground electronic state, $Cl(^2P_{3/2})$, with a translational anisotropy, β_0, of -1.0 ± 0.1 [82, 128, 138]. Conservation of energy dictates that the $Cl(^2P_{3/2})$ atoms are therefore travelling at 1675 ms^{-1} following photolysis.[5] Assuming that the relative motion between the molecular chlorine precursor and the alkane is small, owing to efficient translational cooling in the jet expansion and that velocity slip [32] is negligible, the photolysis defines the relative motion of the chlorine atom and the alkane molecule, yielding a mean collision energy of 0.24 eV with a FWHM of 0.05 eV for the Cl + C_2H_6 reaction, and a mean collision energy of 0.32 eV with a FWHM of 0.06 eV for the Cl + n-C_4H_{10} reaction. The different mean collision energies arise solely from the differing masses of the C_2H_6 and n-C_4H_{10} molecules. The spread is due to residual thermal motion of the precursor and reagent and was calculated using an estimated translational temperature of 50 K based on probe-only images of background HCl [94] (see Section 2.10.4).

Direct detection of the $Cl(^2P_{3/2})$ atoms produced from 355 nm photolysis *via* the $4p\,^4P_{3/2} \leftarrow {}^2P_{3/2}$ (2+1) REMPI transition at 240.46 nm [125] allowed velocity calibration of the ion images of reaction products. These images were obtained under similar time delay and molecular beam intensity conditions to those used to study the bimolecular reaction. A typical image is shown in Figure 2.14. The pixel-to-velocity conversion factor was determined by inverse Abel transformation of the images, with the maximum in the radial coordinate of the resulting 'slice' through the 3D scattering distribution corresponding to the known single velocity of the Cl photofragment. Integration of the inverse Abel transforms over angle returned the Cl atom speed distribution, $P(v_{Cl})$, shown in Figure 2.15. The translational anisotropy parameter, β_0, also obtained from the inverse Abel transformed images, was found to be close to -1. This suggests that collisional scrambling of the Cl

---

[5] Calculated using $D_0^0(^{35}Cl_2) = 2.475$ eV [127, 128].

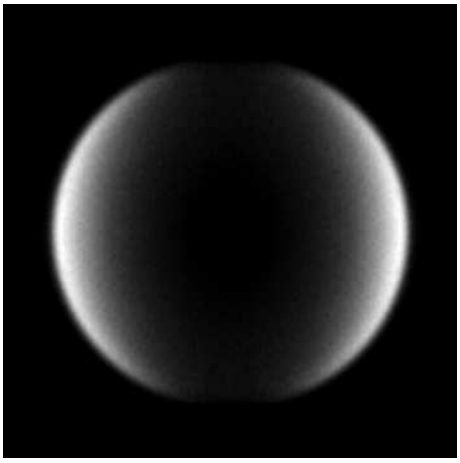

Figure 2.14: Raw ion image of the Cl($^2\mathrm{P}_{3/2}$) atom products of photodissociation of molecular chlorine at 355 nm.

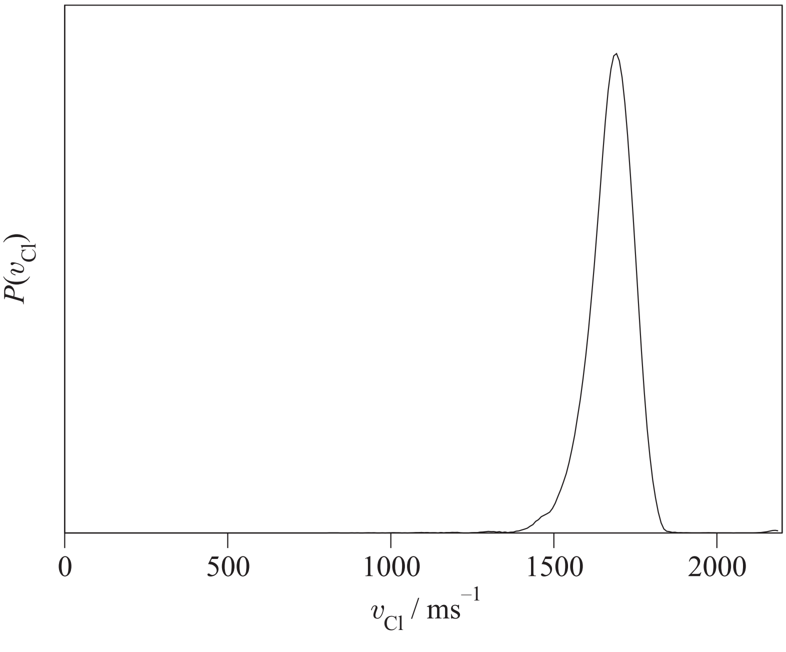

Figure 2.15: Speed distribution of the Cl($^2\mathrm{P}_{3/2}$) atoms—obtained from an inverse Abel transformed image—used to calibrate the radial axis of the images.

velocity distribution prior to reaction, which would lead to a lowering of β_0, was unlikely to be a problem in these experiments.

The Cl velocity distribution observed here for the reactions of chlorine with ethane and *n*-butane is more well-defined than that determined for the Cl atoms in the reaction of chlorine with methane (see Section 2.9.2). The difference is thought to arise as a result of several factors, including the different lasers, laser powers and nozzles used in the two different experimental rigs. The piezoelectrically actuated nozzle used in the experiments described here is believed to give a shorter and more directed gas pulse than the solenoid nozzle used in the Cl + CH_4 study. Also, owing to the lower cross-section for the Cl + CH_4 reaction than for either the Cl + C_2H_6 or Cl + *n*-C_4H_{10} reactions, and the somewhat lower power density of the laser pulses output by the excimer and excimer-pumped dye lasers compared to the Nd:YAG and Nd:YAG-pumped optical parametric oscillator lasers, rather higher laser intensities, resulting in a longer interaction region, were employed in the Cl + CH_4 experiments than in those described here. The combination of these factors means that a much smaller portion of the free-jet expansion is sampled in the present studies than in the investigation of the reaction of chlorine with methane, with the result that the chlorine atom speed distribution is correspondingly narrower.

2.10.3 Background HCl

Unwanted side-reactions of the Cl_2 with ethane and *n*-butane in the gas manifold, which produced translationally cold background HCl, complicated the acquisition of the ion images of reactively scattered HCl products. This background signal was observed as a bright spot in the centre of the HCl ion images. Attempts were made to minimise the background HCl by using a glass bulb reservoir to store the gas mixture and by using fresh gas mixtures every 2–3 hours. In addition, the bulb and gas lines were flushed with a mixture of $\sim 5\%$ NO in helium before introducing each new Cl_2/ethane or Cl_2/*n*-butane gas mixture. This procedure was observed to decrease the level of background HCl, although the reason for the success of this

Figure 2.16: From left to right, a raw ion image of HCl($v' = 0$,$j' = 1$) generated in a co-expanded mixture of Cl_2 and ethane, an image of the background HCl obtained without the photolysis laser firing, and the image obtained with the background subtracted.

procedure is unknown [131]. Probe-only images of the background HCl signal were obtained after collection of each reactive signal image and were subtracted from the signal images (see Figure 2.16). The background subtraction is imperfect due to near saturation of the detector in the centremost region of both the signal and background images (where the HCl intensity was concentrated), and thus the central portions of the images were not used in the data analysis.

Owing to the kinematics of the reaction of chlorine with ethane, the region obscured by the cold background signal in the images corresponds to extreme backward scattering of the HCl products with near maximum centre-of-mass kinetic energy. The grey circle in the collapsed[6] Newton diagram for the reaction shown in Figure 2.17 marks the region of scattering space to which the background subtraction renders the experiment insensitive. Only centre-of-mass scattering angles between 170°and 180°are seen to be affected. The two collapsed Newton diagrams for the two pathways in the reaction of chlorine with n-butane, namely abstraction of a hydrogen atom from either a primary or secondary carbon site, are shown in Figure 2.18. For both reaction channels, only HCl products scattered in the extreme backward direction with less than maximal kinetic energy releases are obscured by the background. A slightly wider range of angles and energy releases are therefore

---

[6] The term 'collapsed' refers to the assumption in these diagrams that the velocity of the alkane reactant, v_2, is zero and that the relative velocity of the reagents, k, is thus defined by the velocity of the hot atom, v_1. This assumption is reasonable in the current experiments, where $v_1 \gg v_2$, due to translational cooling of the alkanes in the molecular beam.

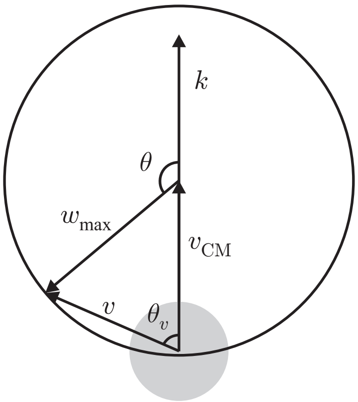

Figure 2.17: Collapsed Newton diagram for the Cl + C_2H_6 reaction (drawn to scale). k is the reagent relative velocity, v_{CM} is the velocity of the centre-of-mass, w and θ are the HCl CM frame speed and scattering angle, and v and θ_v are the LAB frame speed and scattering angle, respectively. The outer circle, of radius $w_{\max}$, represents the maximum speed of the HCl products in the CM frame. The grey circle represents the region of scattering space to which the experiments are insensitive due to background subtraction.

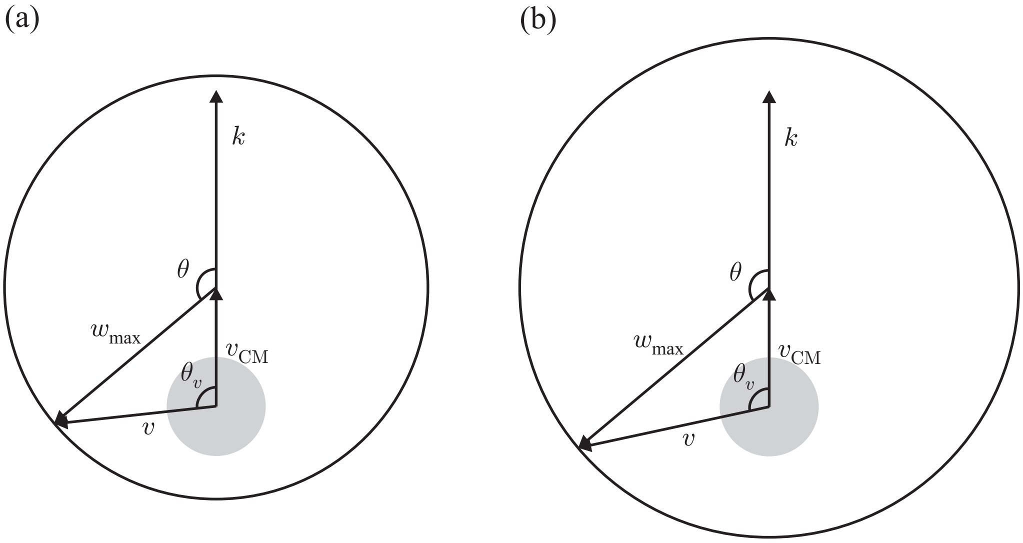

Figure 2.18: As for Figure 2.17, collapsed Newton diagrams for the abstraction of hydrogen atoms from (a) primary and (b) secondary carbon sites in the Cl + *n*-C_4H_{10} reaction; both drawn on the same scale as Figure 2.17.

affected in this reaction compared to the Cl + C_2H_6. Background subtraction does not, however, severely impair the analysis for either reaction system.

2.10.4 Speed Resolution and Molecular Beam Temperature

The speed resolution of the apparatus was estimated from images of Cl from Cl_2 photolysis. The images were obtained in a similar way to that described in Section 2.10.2, except that the delay between the photolysis and probe laser pulses was shortened to ∼25 ns, and a shorter gas pulse was used in order to effect maximal cooling of the jet expansion. Integration over angle of the inverse Abel transform of the images returned the Cl atom speed distribution, which was then fitted using a Gaussian of the form

$$y = A\,\mathrm{e}^{-(v-v_0)^2/2\sigma^2}\,, \tag{2.12}$$

where v_0 is the mean speed, σ is the standard deviation, and for which the FWHM, Δv_{res}, is given by

$$\Delta v_{\mathrm{res}} = \sigma 2\sqrt{2\ln 2}. \tag{2.13}$$

The speed resolution of the apparatus, $\Delta v_{\mathrm{res}}/v_0$, was determined from the fit to be ∼6%. The Cl atom speed distribution and the fit to it are shown in Figure 2.19.

The images of background HCl described in Section 2.10.3 were used to estimate the translational temperature of the molecular beam. A Gaussian of the form

$$y = \frac{A}{\sqrt{2\pi\sigma^2}}\,\mathrm{e}^{-v^2/2\sigma^2}\,, \tag{2.14}$$

for which the FWHM, Δv_{tot}, is given by

$$\Delta v_{\mathrm{tot}} = \sigma 2\sqrt{2\ln 2}, \tag{2.15}$$

was fitted to the central cross-section of the HCl spot. The speed distribution and the returned fit are shown in Figure 2.20. By equating the exponential term in

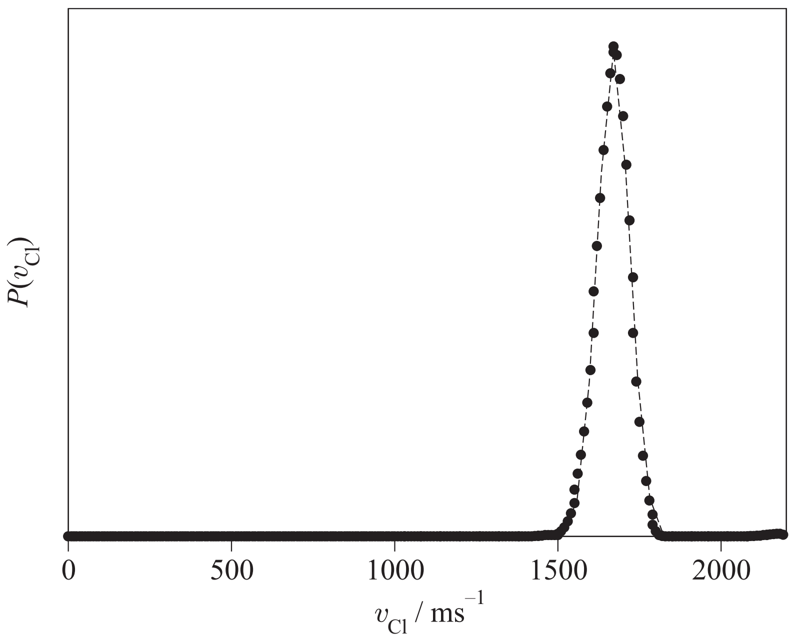

Figure 2.19: Speed distribution of the Cl(^{2}P$_{3/2}$) atoms (●) and Gaussian fit (- - -) used to determine the velocity resolution of the apparatus.

Equation 2.14 with that in the 1D Maxwell–Boltzmann speed distribution

$$f(v) = \left(\frac{m}{2\pi kT}\right)^{\frac{1}{2}} \mathrm{e}^{-mv^2/2kT}\,, \tag{2.16}$$

the total translational temperature in the Maxwell–Boltzmann distribution (i.e., that containing the contribution from both the translational temperature and the apparatus speed resolution), $T_{\rm tot}$, may be expressed in terms of $\Delta v_{\rm tot}$ as

$$T_{\rm tot} = \frac{(\Delta v_{\rm tot})^2 m}{8k \ln 2}. \tag{2.17}$$

Taking into account the broadening of the HCl speed distribution from the resolution of the apparatus, $\Delta v_{\rm res}$, using

$$(\Delta v_{\rm trans})^2 = (\Delta v_{\rm tot})^2 - (\Delta v_{\rm res})^2, \tag{2.18}$$

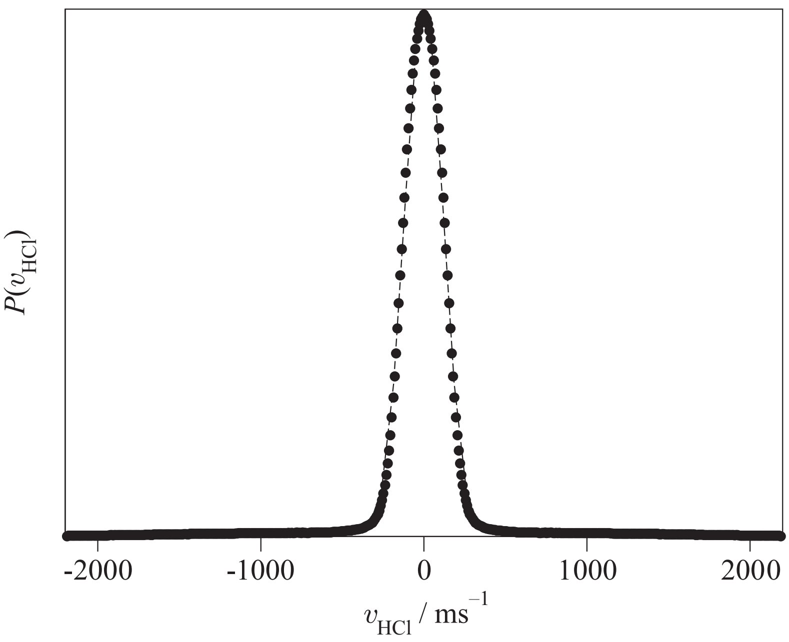

Figure 2.20: Speed distribution of the background HCl (●) and Gaussian fit (- - -) used to determine the translational temperature of the molecular beam.

the translational temperature, T, of the molecular beam is estimated to be 50 K. Good agreement between a simulation of the reactant Cl atom speed distribution and that determined experimentally in Section 2.10.2 can be seen in Figure 2.21. The simulated distribution was calculated [94] using the translational temperature of 50 K estimated above and was convoluted with an appropriate Gaussian to include the apparatus speed resolution.

2.10.5 Molecular Beam Number Density

The molecular number density in the interaction region of the free jet expansion can be estimated using

$$\frac{n}{n_0} = \left(1 + \frac{\gamma - 1}{2} M^2\right)^{-1/(\gamma-1)}, \tag{2.19}$$

assuming that the expansion is isentropic, the gases behave ideally, γ is constant and there is continuum flow [32]. In Equation 2.19, n is the number density, n_0 is

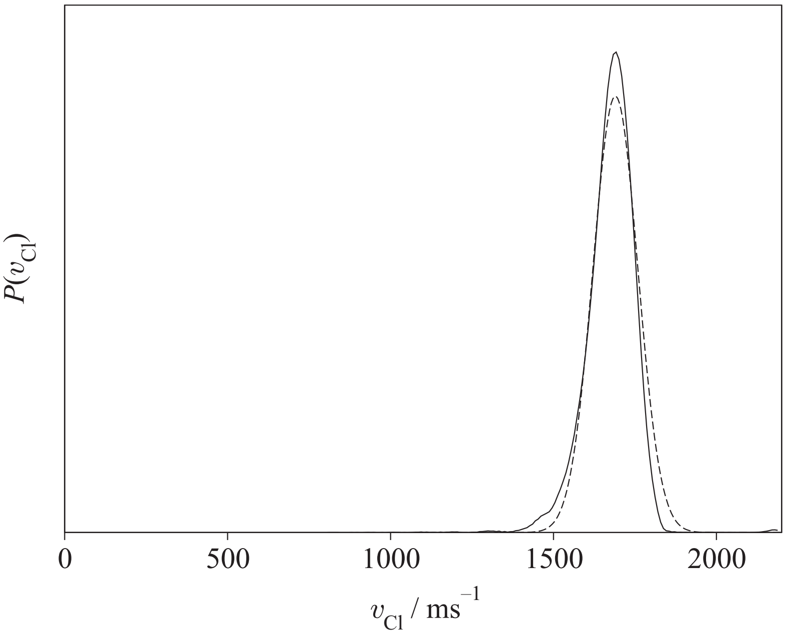

Figure 2.21: Experimental speed distribution of the reactant Cl($^2\mathrm{P}_{3/2}$) atoms (—) and simulated speed distribution (- - -) obtained using the determined speed resolution and translational temperature of the molecular beam.

the source stagnation number density and γ is the ratio of specific heat capacities ($C_\mathrm{p}/C_\mathrm{v}$). At small distances from the nozzle, as were used in the experiments described here, the centreline Mach number, M, is given by

$$M = \left(\frac{x}{d}\right)^{(\gamma-1)} \left[C_1 + \frac{C_2}{\left(\frac{x}{d}\right)} + \frac{C_3}{\left(\frac{x}{d}\right)^2} + \frac{C_4}{\left(\frac{x}{d}\right)^3} \right], \tag{2.20}$$

where x is the distance from the nozzle aperture, d is the diameter of the nozzle aperture, and C_1–C_4 are experimentally determined coefficients depending on γ and the expansion type. Using ideal gas heat capacities for the 1:1 mixtures of Cl_2 and alkanes used gives γ to be $\sim 7/5$. The currently accepted coefficients for an axisymmetric expansion for which $\gamma = 7/5$ are $C_1 = 3.606$, $C_2 = -1.742$, $C_3 = 0.9226$, and $C_4 = -0.2069$ [32]. Using Equations 2.19, 2.20 and the ideal gas law to calculate n_0, the number density, n, in the free jet expansion is thus estimated to be $\sim 10^{16}$ molecules cm^{-3} in the interaction region (7.5 mm downstream from the nozzle orifice). It should be noted that this is very much an upper limit on the number density, since non-ideal behaviour of both the expansion and the gases, and background gas scattering will attenuate the beam intensity in the interaction region [32]. The molecular beam number density is discussed further in Section 4.3.2 for the Cl + C_2H_6 reaction, where, by comparison of the raw data from the current experiments with previous work of Zare and co-workers [151, 152], secondary collisions of reactants or products are found to be insignificant. Secondary collisions are therefore also expected to be of minor importance in the Cl + n-C_4H_{10} reaction.

Chapter 3

Data Analysis

3.1 Introduction

The various analysis methods used to obtain the results presented later in this thesis are explained here.

The two most important frames of reference employed in the interpretation of the velocity-map image data obtained from the experiments described in Chapter 2 are the laboratory (LAB) frame and the centre-of-mass (CM) frame. The LAB frame is the most intuitive and may be defined, for example, with reference to the polarisation direction of the light used for molecular excitation (i.e., the direction of the electric vector of the photolysis light, $\boldsymbol{\epsilon}_{\mathrm{p}}$). All of the experimental data are measured in this reference frame. In order to describe the dynamics of a reaction or a photodissociation process, however, it is more useful to reference the relative positions and momenta of atoms with respect to the centre-of-mass, that is, in the CM frame. The different approaches that have been taken in the analysis of the velocity-map ion images, including the methods that have been used to convert the experimental LAB frame measurements into the CM frame angular scattering and speed distributions of interest, and to generate from these the product flux (velocity-angle) contour maps, are explained here.

Methods to reconstruct the full 3D scattering distribution from the 2D projection provided by the velocity-map ion imaging technique are outlined in the following

Section. These reconstruction methods yield a ‘slice’ through the full 3D scattering distribution, which for images of the products of photolysis processes, provides the CM scattering distributions directly. In the case of the products of bimolecular reactions, however, the ‘slice’ returned by reconstruction of the images provides only the LAB frame scattering distributions, which must then be converted into the CM frame. Simple inversion analyses to achieve this transformation are presented in Section 3.3, while the more complete Legendre moment fitting analysis is described in Section 3.4.

3.2 Image Reconstruction

Experiments employing velocity-map ion imaging allow the direct measurement of a 2D projection of the velocity distribution of a photofragment or reaction product. In order to take full advantage of the technique, reliable methods are required for the reconstruction of the 3D scattering distribution, and thus extraction of the dynamical quantities of interest, from the 2D images. A comprehensive survey of reconstruction methods is given in Chapter 3 of Ref. [153]. The two main approaches used to date, however, have been the inverse Abel transform and forward convolution methods, and these are described here.

3.2.1 The Inverse Abel Transform

The inverse Abel transform [59, 154, 155] is a direct mathematical transform that returns a ‘slice’ through the centre of the 3D velocity distribution for systems containing an axis of cylindrical symmetry. The transform is thus ideally suited to studies of photolysis processes and photon-initiated reactions that yield products with no angular momentum alignment. In both types of system, products are scattered with cylindrical symmetry about the electric vector of linearly polarised photolysis radiation. The 3D velocity distribution of the scattered products in Cartesian coordinates, $I(x, y, z)$, may therefore be written in terms of just two cylindrical coordinates, $I = I(r, z)$, where $r = \sqrt{x^2 + y^2}$. If the y axis is defined to be parallel to the time-of-flight axis, the 2D projection of $I(r, z)$ in the detection plane, the (x, z) plane, may then be written as $P(x, z)$, where the two functions are related by the Abel integral,

$$P(x, z) = 2 \int_x^\infty \frac{r I(r, z)}{\sqrt{r^2 - x^2}} \, \mathrm{d}r. \tag{3.1}$$

The inverse transform can be found by applying the Fourier transform convolution theorem [156] and is given by

$$I(r, z) = -\frac{1}{\pi} \int_r^\infty \frac{P'(x, z)}{\sqrt{x^2 - r^2}} \, \mathrm{d}x, \tag{3.2}$$

where $P'(x, z) = \mathrm{d}P(x, z)/\mathrm{d}x$. Solving Equation 3.2 is numerically impractical due to the singularity at $r^2 = x^2$ and because it requires the derivative of the projection data to be calculated at discrete sample points (the pixels); the derivative in the integrand also tends to magnify any noise in the data [157]. Currently, the most commonly used method for calculating the inverse Abel transform in ion imaging applications is the Fourier–Hankel technique, proposed by Smith *et al.* [70, 158]. Consider a single row of the image taken along the x axis with $z = z_0$, so that $P(x, z_0) \equiv P(x)$ may be written as

$$P(x) = \int_{-\infty}^\infty s(x, y) \, \mathrm{d}y = 2 \int_0^\infty s(x, y) \, \mathrm{d}y, \tag{3.3}$$

where $s(x, y) = I(x, y, z_0)$ is a slice taken through the 3D distribution perpendicular to the symmetry axis at z_0. By taking the Fourier transform, $\mathcal{F}(\cdots)$, of Equation 3.3,

$$\mathcal{F}\{P(x)\} = \int_{-\infty}^\infty \int_{-\infty}^\infty s(\sqrt{x^2 + y^2}) \, \mathrm{e}^{-i2\pi xq} \, \mathrm{d}x \, \mathrm{d}y, \tag{3.4}$$

and changing from Cartesian to polar coordinates, it can be shown that

$$\mathcal{F}\{P(x)\} = 2\pi \int_0^\infty s(r) J_0(2\pi rq) r \, \mathrm{d}r, \tag{3.5}$$

where $J_0(\cdots)$, the zero-order Bessel function of the first kind, is given by

$$J_0(z) = \frac{1}{2\pi} \int_0^{2\pi} \mathrm{e}^{-iz\cos\theta}\, \mathrm{d}\theta. \tag{3.6}$$

As noted by Smith *et al.* [158] and Castleman [155], the right hand side of Equation 3.5 is the zero-order Hankel transform, $H(\cdots)$, of $s(r)$. Since the inverse Hankel transform is identical in form to the forward transform, the original distribution $s(r)$ can then be recovered by taking the Hankel transform of the Fourier transform of the projected intensity:

$$\begin{aligned} s(r) &= H\Big[\mathcal{F}\{P(x)\}\Big] \\ &= 2\pi \int_0^{\infty} q J_0(2\pi r q) \int_{-\infty}^{\infty} P(x)\, \mathrm{e}^{-i2\pi x q}\, \mathrm{d}x\, \mathrm{d}q. \end{aligned} \tag{3.7}$$

From a computational point of view, the inversion formula given in Equation 3.7 has several advantages over the Abel inversion integral of Equation 3.2: (i) the difficulty associated with the singularity at the lower limit of integration is avoided; (ii) following the Fourier transform of $P(x)$, filters may be applied directly to the frequency domain to reduce noise and thus smooth the data in a systematic manner; and, (iii) Equation 3.7 can be numerically approximated with discrete fast Fourier transform (FFT) algorithms. In practice this is achieved using the Cooley–Tukey FFT algorithm [159] on each line in the image and then computing the Bessel function convolution by direct summation. Note that although the Fourier–Hankel formulation of the image reconstruction algorithm reduces the problems associated with any noise in the image, it does not completely eliminate them. In particular, because the Bessel function oscillates rapidly close to the origin, 'wide-sense stationary' noise (i.e., noise of zero mean and with constant variance) present in the image data appears as 'non-stationary' noise in the inverse Abel transform with variance inversely proportional to the distance from the centreline (the axis of cylindrical symmetry in the system) [160].

Inverse Abel transformation of the images obtained from the experiments described in this thesis was achieved using a FORTRAN 77 adaptation of the Fourier–Hankel C code written by Whitaker [70].

As was mentioned in Section 2.3.4, use of the ion counting method to enhance spatial resolution and detector sensitivity tends to produce ‘grainy’ images; the high sensitivity of the inverse Abel transform to this noise thus poses a problem for inversion of such data using this technique. A common method used to reduce the centreline noise generated by the inverse Abel transformation of ion counted images is to first convolute the original image with a 3×3 Gaussian kernel. Blurring of the experimental images in this way prior to calculation of the inverse Abel transform overcomes the noise problem to some extent, but also leads to a small loss in speed resolution. Note that care should be taken when performing this procedure, however, because smoothing of sharp features in the 2D projection of the 3D scattering distribution is not equivalent to complete sampling of the entire 3D scattering space, which is a requisite for use of the inverse Abel transform [82]. An alternative procedure for smoothing images acquired using the ion counting technique, which avoids this problem and does not entail any loss in speed resolution, was recently proposed by Bass *et al.* [161] and is discussed further in Section 3.4.2.

3.2.2 Forward Convolution Methods

An alternative approach to the inverse Abel transform involves forward convolution of the image, whereby images are simulated based on a trial scattering distribution and compared with the experimental data. The trial distribution is then adjusted iteratively until satisfactory agreement is obtained. Note that, in general, forward convolution methods are not limited to cylindrically symmetric distributions, and may be used to analyse images obtained from experiments on processes which form products with aligned angular momenta. In a variation on the forward convolution technique, a set of ‘basis images’ is simulated and fitted to the experimental image to extract the parameters of interest. Two such approaches that have been shown to be particularly successful for inversion of cylindrically symmetric systems [153] are the iterative inversion method of Vrakking [162] and the basis set expansion method of Reisler and co-workers [163]; these are described in more detail below.

In the iterative inversion method, use is made of the similarities that exist for cylindrically symmetric systems between the form of the angular and radial distributions of the 3D scattering distribution and of the corresponding 2D projection. First, a trial 3D scattering distribution based on the radial and angular distributions in the experimental image is assumed and the 2D projection calculated. The differences between the experimental image and this calculated projection are then evaluated and used to apply a correction to the 3D scattering distribution. The process is then repeated until the differences between the experimental data and the calculated 2D projection are acceptably small. A suitable level of convergence is usually achieved over 10–20 iterations. Since this method uses the radial distribution to perform the inversion, any noise in the experimental image is projected towards the centre-point of the returned 'slice' through the 3D scattering distribution and not, as is the case with other methods, along the centreline.

The basis set expansion (BASEX) method is based on expanding the 2D experimental projected image in a basis set of functions that are analytical projections of known well-behaved functions. The experimental 3D scattering distribution can then be reconstructed as a linear combination of these unprojected well-behaved functions, using the same expansion coefficients. The basis set functions in 3D scattering space are chosen such that they have analytical solutions to the Abel transform, and therefore give smooth functions in the 2D projection. The ill-posed inverse Abel transform is thus converted into the simple problem of determining the expansion coefficients, which is achieved purely by matrix multiplication.

There are two significant advantages of the BASEX method over other inversion methods used to reconstruct the 3D scattering distribution from the 2D projection for cylindrically symmetric systems. The first is that noise in the reconstructed distribution appears only when it exists in the 2D projection and is not generated by the inversion procedure. Note, however, that each point in the original 3D scattering distribution, located at a distance r from the axis of cylindrical symmetry, contributes only to points with $x \leq r$ in the projection. The projection therefore contains less information about regions of the 3D scattering distribution closer to the symmetry axis compared to those farther from the axis. Since the noise in the experimental images is ‘wide-sense stationary’, the signal-to-noise ratio in the reconstructed 3D scattering distribution therefore decreases towards the centreline. The BASEX method significantly reduces the effect of this lower signal-to-noise ratio along the centreline, without impacting on the quality of the reconstruction. The second advantage of the BASEX method lies in the analytical expression returned for the reconstructed 3D scattering distribution, which allows the speed and anisotropy distributions to be calculated analytically. The resolution of the distributions are therefore higher than those obtained from the discrete ‘slice’ through the 3D scattering distribution returned by other methods.

3.3 Photon-Initiated Reactions

Brief overviews of the photon-initiated reaction scheme and the photolysis step are given at the beginning of this Section, prior to discussion of the two closely related inversion methods that have been used to obtain the CM angular scattering distribution from the product LAB frame speed, $P(v)$, and speed-dependent translational anisotropy, $\beta(v)$, distributions. These LAB frame distributions are readily obtained from experimental images by integration over the angular coordinate of the ‘slice’ though the 3D product velocity distribution returned by the inverse Abel transform. The LAB frame is defined here such that the z axis lies parallel to the electric vector of the photolysis radiation, $\boldsymbol{\epsilon}_{\mathrm{p}}$.

3.3.1 Overview of the Photon-Initiated Reaction Scheme

The experiments carried out to determine the dynamics of bimolecular reactions presented in this thesis employ the laser pump-probe technique. This method may be represented by the following reaction scheme:

$$\begin{aligned} \mathrm{AX} + h\nu &\longrightarrow \mathrm{A} + \mathrm{X} \\ \mathrm{A} + \mathrm{BC} &\longrightarrow \mathrm{AB}(v', j') + \mathrm{C} \end{aligned} \tag{3.8}$$

Molecular photodissociation in the pump step is used to generate fast moving (generally atomic) reactants, A, with well-defined velocities. These then react with the target molecules, represented here as BC. The AB(v',j') (or C) products of the reaction are probed quantum state selectively at pump-probe delay times sufficiently short to ensure single collision conditions.

The choice of photolysis as the initiation step for the reaction has several advantages: (i) the use of a laser pulse allows the timing between reaction initiation and probing of the products to be chosen precisely; (ii) the reaction collision energy is defined by the wavelength of the light used; and, (iii) photodissociation is often an anisotropic process. If the precursor is photolysed using polarised light, the velocity vector of the photofragments will be linked to the direction of the electric vector of the photolysis light, providing a reference axis against which the measured product spatial distributions may be correlated.

3.3.2 The Anisotropy of the Photodissociation Step

The classical probability that a molecule will be dissociated through an electric dipole transition by absorption of one photon of linearly polarised light, P_{diss}, depends on the angle, θ_{m}, between the transition dipole moment, $\boldsymbol{\mu}$, and the electric vector of the photolysis radiation $\boldsymbol{\epsilon}_{\mathrm{p}}$:

$$P_{\mathrm{diss}} \propto |\boldsymbol{\mu}.\boldsymbol{\epsilon}_{\mathrm{p}}|^2 \propto \cos^2\theta_{\mathrm{m}}. \tag{3.9}$$

Radiation will therefore be preferentially absorbed by those molecules with $\boldsymbol{\mu}$ aligned parallel to $\boldsymbol{\epsilon}_{\mathrm{p}}$. For a single recoil velocity, the LAB frame photofragment angular distribution of A formed by photodissociation of AX, $I(\vartheta)$, is given by [91, 92]

$$I(\vartheta) = \frac{1}{4\pi} \left[1 + \beta_0 P_2(\cos\vartheta)\right], \tag{3.10}$$

where ϑ is the angle between the recoil velocity, $\mathbf{v}_\mathrm{A}$, and $\boldsymbol{\epsilon}_\mathrm{p}$, β_0 is the anisotropy parameter, and $P_2(x) = \frac{1}{2}(3x^2 - 1)$ is the second Legendre polynomial. The anisotropy parameter may therefore be expressed classically in terms of Legendre moments [91, 164] as

$$\beta_0 = 5\langle P_2(\hat{\boldsymbol{\epsilon}}_\mathrm{p}.\hat{\mathbf{v}}_\mathrm{A})\rangle, \tag{3.11}$$

where $\langle \cdots \rangle$ denotes an average over the recoil distribution. The azimuthally averaged addition theorem [165, 166] allows the factorisation

$$\beta_0 = 5\langle P_2(\hat{\boldsymbol{\epsilon}}_\mathrm{p}.\hat{\boldsymbol{\mu}})\rangle\langle P_2(\hat{\boldsymbol{\mu}}.\hat{\mathbf{v}}_\mathrm{A})\rangle, \tag{3.12}$$

where $\langle P_2(\hat{\boldsymbol{\epsilon}}_\mathrm{p}.\hat{\boldsymbol{\mu}})\rangle$ accounts for the LAB to molecule fixed frame transformation and is equal to 2/5. The anisotropy parameter is therefore given by

$$\beta_0 = 2\langle P_2(\hat{\boldsymbol{\mu}}.\hat{\mathbf{v}}_\mathrm{A})\rangle. \tag{3.13}$$

The value of β_0 thus ranges from -1 (a $\sin^2\vartheta$ distribution) to $+2$ (a $\cos^2\vartheta$ distribution). $\beta_0 = 0$ corresponds to an isotropic distribution. The angular distributions for these three cases are shown in Figure 3.1.

Simple limiting cases occur for a diatomic molecule when dissociation occurs on a single repulsive surface sufficiently promptly that the fragments have the same final direction as the orientation of the bond when the dissociative transition occurred (the axial recoil approximation). $\boldsymbol{\mu}$ must then either lie along the internuclear axis (a parallel type transition, $\Delta\Omega = 0$) where $\beta_0 = +2$, or lie in a plane at right angles to the internuclear axis (a perpendicular transition, $\Delta\Omega = \pm 1$) where $\beta_0 = -1$. Information about the symmetry of the ground and excited states of the electronic transition may therefore be deduced from measurements of the angular distributions

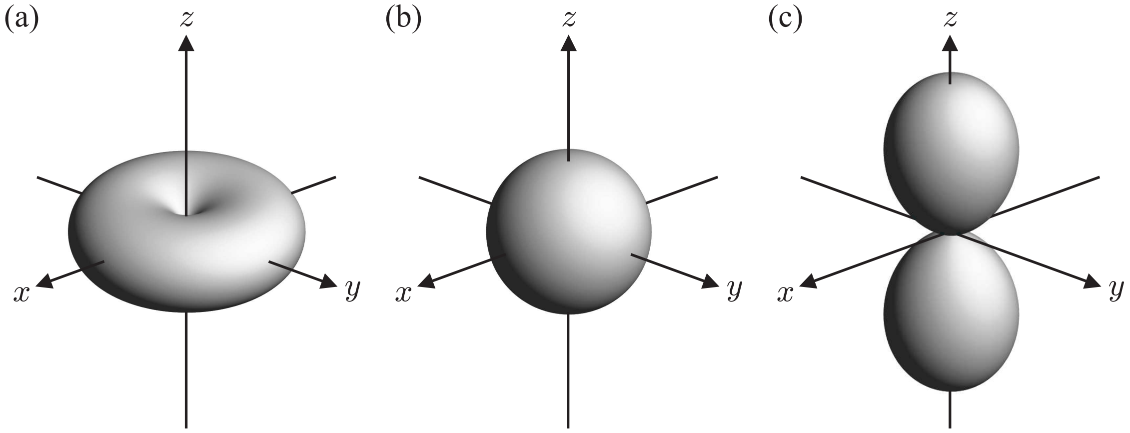

Figure 3.1: Surfaces representing the angular distribution of the velocities of products of photolysis by one photon of linearly polarised laser light, where the translational anisotropy, β_0, is (a) −1, (b) 0 and (c) +2. The z axis is defined to lie parallel to the electric vector of the photolysis radiation.

of the recoiling photofragments. Note that in general, however, even for a diatomic molecule the anisotropy parameter can be reduced from these limiting values by molecular rotation after excitation and prior to dissociation, or rotation during the dissociation process itself. Theoretical treatments of these effects have been given in detail elsewhere [167, 168]. Further complications can arise if multiple electronic states are excited coherently.

Initiation of a bimolecular reaction *via* the photolysis of a precursor, whose LAB and CM frame scattering distributions can be described accurately, therefore allows the reaction product momenta to be measured relative to the photodissociation recoil direction and thus relates the LAB frame observables to the CM frame distributions of interest.

3.3.3 Triatomic Reactions: A Simple Treatment

In order to simplify discussion of the product angular scattering distribution, it is useful to make some initial assumptions: (i) by co-expansion of the AX photolysis precursor and BC reactant gases into a vacuum to form a molecular beam, the limit of zero relative speed is approached (see Chapter 2); the precursor and target molecules are therefore assumed to be stationary with respect to each other (see

Section 3.4.1); (ii) photodissociation of the precursor using linearly polarised light occurs by a single channel to give a well-defined anisotropy and speed distribution; and, (iii) the reaction co-product C is structureless and has no energetically accessible excited states, so that the speed of the AB(v',j') product is constrained by conservation of energy.

The translational energy of photofragment A, E_{A}, is given by

$$E_{\mathrm{A}} = \left(\frac{m_{\mathrm{X}}}{m_{\mathrm{AX}}}\right) \cdot \left(h\nu - D_0^0(\mathrm{A{-}X})\right), \tag{3.14}$$

where m_{i} is the mass of moiety i, $h\nu$ is the photon energy and $D_0^0(\mathrm{A{-}X})$ is the dissociation energy of AX. Since the AX and BC molecules in the molecular beam are assumed to have the same LAB frame speed, the relative speed of the A and BC reactants, k, is equal to the speed of the hot atom, A. The collision energy, E_{t}, is therefore given by

$$\begin{aligned} E_{\mathrm{t}} &= \frac{1}{2}\mu k^2 \\ &= \frac{m_{\mathrm{BC}}}{M} E_{\mathrm{A}}, \end{aligned} \tag{3.15}$$

where $\mu = \frac{m_{\mathrm{A}} m_{\mathrm{BC}}}{m_{\mathrm{A}} + m_{\mathrm{BC}}}$ is the reduced mass of the reactants and $M = m_{\mathrm{A}} + m_{\mathrm{BC}} = m_{\mathrm{AB}} + m_{\mathrm{C}}$. The speed of the centre-of-mass, v_{CM}, is given by

$$\begin{aligned} v_{\mathrm{CM}} &= \left(\frac{m_{\mathrm{A}}}{M}\right) v_{\mathrm{A}} + \left(\frac{m_{\mathrm{BC}}}{M}\right) v_{\mathrm{BC}} \\ &= \frac{\left(2 m_{\mathrm{A}} E_{\mathrm{A}}\right)^{1/2}}{M}. \end{aligned} \tag{3.16}$$

Since the internal states of the reagents and products of this idealised reaction are uniquely defined, the speed of the AB products in the CM frame, w, is fixed by the kinematics to be

$$w = \left(\frac{2 m_{\mathrm{C}} E'_{\mathrm{t}}}{m_{\mathrm{AB}} M}\right)^{1/2}, \tag{3.17}$$

where E'_{t} is the translational energy of the products and can be calculated exactly

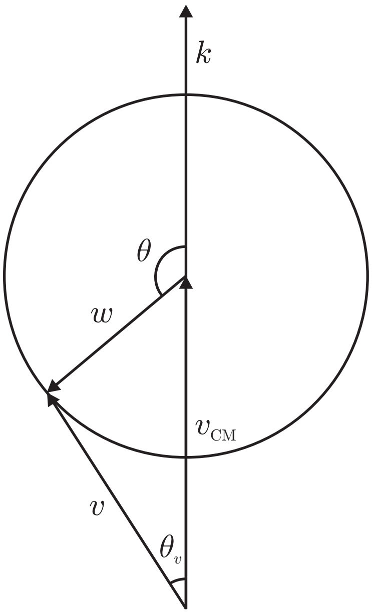

Figure 3.2: Newton diagram for a triatomic reaction. The probed product is constrained to a fixed CM speed, w, by conservation of energy; the LAB speed, v, is related to the CM scattering angle, θ, simply by the cosine rule.

using

$$E'_{\mathrm{t}} = \frac{1}{2}\mu' k'^2 \tag{3.18}$$

$$= E'_{\mathrm{AVL}} - E'_{\mathrm{INT}}, \tag{3.19}$$

where $\mu' = \frac{m_{\mathrm{AB}} m_{\mathrm{C}}}{m_{\mathrm{AB}} + m_{\mathrm{C}}}$ is the reduced mass of the products, k' is the relative speed of the AB and C products, E'_{INT} is the total internal energy of the products and E'_{AVL} is the total energy available to the products. E'_{AVL} is given by

$$E'_{\mathrm{AVL}} = E_{\mathrm{t}} + E_{\mathrm{INT}} - \Delta_{\mathrm{r}} H_0^{\ominus}, \tag{3.20}$$

where E_{INT} is the internal energy of the reactants, and $\Delta_{\mathrm{r}} H_0^{\ominus}$ is the enthalpy change of the reaction at 0 K. The only variable needed to determine the speed of AB in the LAB frame is therefore the CM scattering angle, θ (see Figure 3.2). The law of cosines may be used to relate the LAB frame to the CM frame [94–96, 109]. In terms of v_{CM}, w, and the LAB speed of the AB products, v, one may write

$$v^2 = w^2 + v_{\mathrm{CM}}^2 + 2wv_{\mathrm{CM}}\cos\theta \tag{3.21}$$

and

$$w^2 = v^2 + v_{\mathrm{CM}}^2 - 2vv_{\mathrm{CM}}\cos\theta_v, \tag{3.22}$$

where

$$\cos\theta_v = \hat{\mathbf{k}}.\hat{\mathbf{v}}, \quad \cos\theta = \hat{\mathbf{k}}.\hat{\mathbf{w}} \equiv \hat{\mathbf{k}}.\hat{\mathbf{k}}', \tag{3.23}$$

$\mathbf{k}$ ($= \mathbf{v}_{\mathrm{A}}$) is the reagent relative velocity vector, which lies parallel to v_{CM}, $\mathbf{v}$ is the AB product LAB frame velocity and $\mathbf{k}'$ ($\parallel \mathbf{w}$) is the product relative velocity vector. The simple law of cosines relationship between v and θ given in Equation 3.21 led Zare and co-workers to coin the acronym 'photoloc' (photo law-of-cosines) [96] to describe the photon-initiated reaction technique.

3.3.4 The LAB Frame Scattering Distribution

It has been shown previously [93–97] that, neglecting product polarisation effects, the product LAB frame scattering distribution takes the same functional form as that for the molecular photodissociation step used to generate the fast moving reactants (see also Section 3.4):

$$P(v,\Theta_v) = \frac{P(v)}{4\pi}\Big[1 + \beta(v)P_2(\cos\Theta_v)\Big], \tag{3.24}$$

where $P(v)$ is the product LAB frame speed distribution, $\beta(v)$ is the speed-dependent translational anisotropy parameter, and Θ_v is the angle between $\mathbf{v}$ and the electric vector of the precursor photolysis light, $\boldsymbol{\epsilon}_{\mathrm{p}}$. Analogously to molecular photodissociation, and again using the azimuthally averaged addition theorem [165, 166] to allow factorisation, it follows that $\beta(v)$ may be written as

$$\begin{aligned}\beta(v) &= 5\langle P_2(\hat{\boldsymbol{\epsilon}}_{\mathrm{p}}.\hat{\mathbf{v}})\rangle \\ &= 5\langle P_2(\hat{\boldsymbol{\epsilon}}_{\mathrm{p}}.\hat{\mathbf{v}}_{\mathrm{A}})\rangle\langle P_2(\hat{\mathbf{v}}_{\mathrm{A}}.\hat{\mathbf{v}})\rangle \\ &= \beta_0\langle P_2(\hat{\mathbf{v}}_{\mathrm{A}}.\hat{\mathbf{v}})\rangle, \qquad (3.25)\end{aligned}$$

where β_0 is the translational anisotropy of the products of the precursor photodissociation. In the present case, since $\hat{\mathbf{v}}_{\mathrm{A}}$ is parallel to $\mathbf{k}$,

$$\beta(v) = \beta_0\langle P_2(\hat{\mathbf{k}}.\hat{\mathbf{v}})\rangle. \qquad (3.26)$$

The speed-dependent translational anisotropy, $\beta(v)$, thus lies in the range

$$-\frac{\beta_0}{2} \leq \beta(v) \leq \beta_0. \qquad (3.27)$$

3.3.5 Simple Inversion Analysis

The simple inversion analysis procedure follows that developed by Zare and co-workers [109–111, 151], in which the LAB frame product speed distribution is directly transformed into the CM angular scattering distribution. For any reaction in which the products are detected quantum state selectively, by neglecting any spread in the velocity of either the reactant atom or the target molecule and by assuming the co-product is formed with zero or fixed internal energy, the dynamics of the system reduce to those of a triatomic reaction, for which the equations presented in Section 3.3.3 apply. It thus follows from Equation 3.21 that the CM angular scattering distribution, $P(\cos\theta)$, is related to the measured LAB frame speed distribution, $P(v)$, by a simple Jacobian:

$$\begin{aligned}P(\cos\theta) &= P(v)\left|\frac{\mathrm{d}v}{\mathrm{d}\cos\theta}\right| \\ &= P(v)\frac{wv_{\mathrm{CM}}}{v}, \qquad (3.28)\end{aligned}$$

where the distribution functions are normalised such that

$$\int_{-1}^{1} P(\cos\theta)\,\mathrm{d}\cos\theta = \int_{v_{\min}}^{v_{\max}} P(v)\,\mathrm{d}v = 1, \tag{3.29}$$

the velocity of the centre-of-mass, v_{CM}, is given by Equation 3.16 and, for a particular quantum state of the detected reaction product, the CM frame product speed, w, is given by Equation 3.17. Since all the required speeds may be calculated, the measured LAB speed distribution to CM angular scattering distribution transformation may be performed.

3.3.6 Polyatomic Reactions

Consider the case that A reacts with a polyatomic target molecule, BCD. The reaction scheme can now be represented by

$$\begin{aligned} \mathrm{AX} + h\nu &\longrightarrow \mathrm{A} + \mathrm{X} \\ \mathrm{A} + \mathrm{BCD} &\longrightarrow \mathrm{AB}(v',j') + \mathrm{CD}(v'',j'') \end{aligned} \tag{3.30}$$

Here the quantum state selectively detected $\mathrm{AB}(v',j')$ products are partnered by molecular co-products, $\mathrm{CD}(v'',j'')$, that may be formed in a range of quantum states. The AB products can now have a range of CM speeds, each corresponding to a particular internal state of the partner fragment, and the direct correspondence between the AB product LAB frame speed and CM scattering angle given by Equation 3.28 no longer holds. This situation is illustrated in Figure 3.3. In the polyatomic case it is therefore necessary to measure the LAB angular distribution, $P(\Theta_v)$, as well as the LAB speed distribution in order to determine the dynamically significant CM speed and angular distributions. This is discussed more fully in Section 3.4.

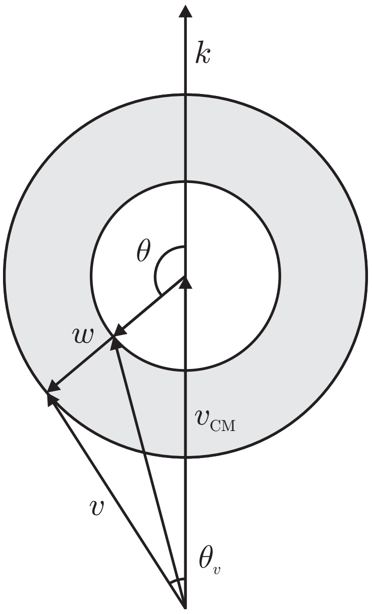

Figure 3.3: As for Figure 3.2, Newton diagram for a polyatomic reaction. The distribution of internal energies in the co-fragment results in a range of product CM speeds, w (shown as the grey ring). There is no direct correspondence between CM scattering angle and LAB speed.

3.3.7 Refined Inversion Analysis

The simple inversion analysis considered in Section 3.3.5 can be extended in an attempt to account for the distribution of product CM speeds in polyatomic reactions, by using the speed-dependent translational anisotropy, $\beta(v)$, to estimate the internal energy of the reaction co-product [151, 152]. Using Equation 3.23 and the definition of $\beta(v)$ given in Equation 3.26, the speed-dependent translational anisotropy may be written as

$$\begin{aligned}\beta(v) &= \beta_0 \langle P_2(\cos\theta_v)\rangle \\ &\simeq \beta_0 P_2(\cos\theta_v^i),\end{aligned} \tag{3.31}$$

where θ_v^i is the value of θ_v estimated assuming a single reaction product speed, w. Rearrangement of Equation 3.31 allows θ_v^i to be estimated as a function of LAB speed, v, from the speed-dependent translational anisotropy distribution using

$$\cos\theta_v^i = \left(\frac{2\beta(v)+\beta_0}{3\beta_0}\right)^{1/2}. \tag{3.32}$$

Since all the reactant speeds are known, this then allows the product CM speed, w (and hence the fractional kinetic energy release), to be determined as a function of v using Equation 3.22. Once all the relevant reactant and product speeds are known, the CM scattering angle corresponding to a particular LAB speed can be determined using Equation 3.21.

It must be emphasized, however, that the simplifying approximation in Equation 3.31 is that the CM recoil velocity of the products is fixed. A unique value of θ_v, that is, θ_v^i, and hence the CM product speed w and scattering angle θ, can therefore only be obtained from Equation 3.31 if the kinetic energy release distribution is a delta function. The implications of this approximation are further discussed, with reference to the Cl + C_2H_6 reaction, in Chapter 4.

3.3.8 Kinematic Constraints

For an experiment in which the product velocity distribution is measured in the LAB frame and where the analysis aims to relate this to the product velocity distribution in the CM frame, it is first useful to examine the expected sensitivity of the former observable to the latter. This has been discussed in detail by Shafer *et al.* [95] and only a brief overview is given here.

The speed of the AB product in the LAB frame, v, falls in the range

$$|v_{\mathrm{CM}} - w| \leq v \leq |v_{\mathrm{CM}} + w|, \tag{3.33}$$

where $|v_{\mathrm{CM}} - w|$ and $|v_{\mathrm{CM}} + w|$ are the LAB frame speeds of products which are backward and forward scattered in the CM frame, respectively. Experiments to determine the CM angular scattering distribution by measuring the product LAB frame speed distribution will thus be most sensitive when the range described by

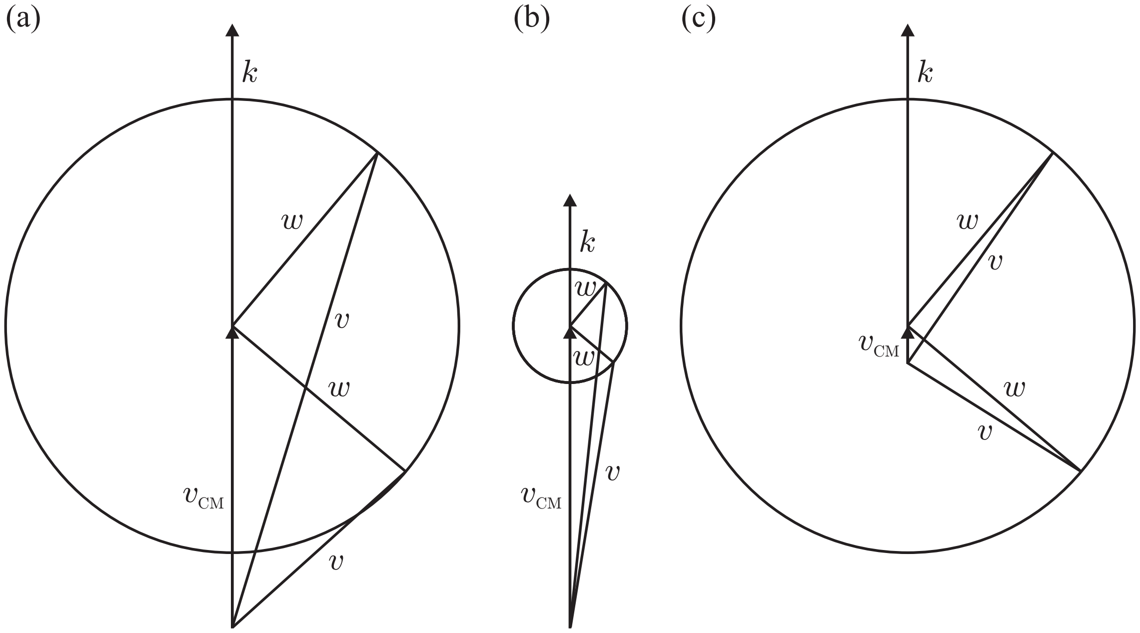

Figure 3.4: Newton diagrams illustrating the three limiting cases for the reaction kinematics. In the ideal case, (a), w is comparable in magnitude to v_{CM} so that the range of values taken by the product LAB velocity, v, is maximised and there is thus the greatest sensitivity to the scattering angle. In (b) v_{CM} dominates v, and the difference in magnitude of v for forward and backwards scattering is small. In (c) w is very much larger than v_{CM} and the range of values taken by v is therefore again very small.

Equation 3.33 is maximised. Three limiting cases for the relative magnitudes of v_{CM} and w are shown in Figure 3.4. If w is much smaller than v_{CM}, the difference in v between forward and backward scattered products will be very small and little about the angular scattering can be deduced from the distribution of v. Similarly, if v is dominated by w, the range of product speeds will be very limited and the only dynamically significant component to the product velocity is the angular anisotropy. For photon-initiated reactions this angular anisotropy is limited by the angular anisotropy of the reactant A, and only the zero and second order moments of the angular scattering distribution can therefore be determined. The widest range of values of v, and therefore the greatest sensitivity of the distribution of v to the CM scattering angle, is taken when w and v_{CM} are comparable in magnitude.

In the case of a triatomic system, in which the products are detected quantum state selectively, w is known precisely and the experimental sensitivity to the scattering distribution can be predicted confidently. In the polyatomic case, however, where the co-product is formed in a range of internal states and w can therefore take a range of values, it is more difficult to predict the experimental sensitivity. The Cl + CH_4 (CH_3D and CD_4), Cl + C_2H_6 and Cl + n-C_4H_{10} reactions described in this thesis are all light atom transfer reactions with low exothermicities, for which the maximum product CM speed, $w_{\max}$, is $\sim v_{\rm CM}$. The lowest and highest attainable LAB speeds are therefore roughly zero and k respectively. Thus, in the limit of zero internal excitation of the alkyl co-product, the kinematics are close to ideal for all of the reactions and the product LAB speeds are sensitive to the CM scattering angle.

3.4 Legendre Moment Fitting Analysis for Photon-Initiated Reactions

A new Legendre moment fitting analysis was developed [169] in order to avoid the problems associated with reconstruction of the 3D scattering distribution outlined in Section 3.2, and to allow for a *distribution* of product CM velocities arising from population of different quantum states in the reaction co-product. The methodology closely follows that developed to fit the Doppler-resolved laser induced fluorescence profiles of the products generated in photon-initiated reactions [94, 97, 99–106] and relies on fitting Legendre moments of the image with a set of suitably chosen basis functions. The general approach has recently been demonstrated by Brouard and co-workers, by applying a similar moment analysis to that used here for reactions to photofragment ion images [124, 141, 161, 170, 171]. The method has also been illustrated and tested using simulated ion images of reaction products (see Section 3.4.8) [106, 161].

The aim of the analysis is to extract the joint probability density function $P(\theta, w)$ for reaction products scattered at angle θ with speed w in the CM frame from the experimentally determined velocity-map ion images. The methodology involves (i) extraction of low order Legendre moments from the images; (ii) construction of a basis function set by simulating image Legendre moments over the full range of possible CM scattering angles and speeds; (iii) a fit of the basis set to the experimental image Legendre moments to determine the moments of the $P(\theta, w)$ distribution; and, (iv) error analysis and estimation of the confidence limits.

The Legendre moment analysis is described in this Section with reference to the generalised polyatomic reaction scheme represented by

$$\begin{aligned} \mathrm{AX} + h\nu &\longrightarrow \mathrm{A} + \mathrm{X} \\ \mathrm{A} + \mathrm{BCD} &\longrightarrow \mathrm{AB}(v', j') + \mathrm{CD}(v'', j'') \end{aligned} \tag{3.34}$$

where the $\mathrm{AB}(v',j')$ products are detected quantum state selectively and the $\mathrm{CD}(v'',j'')$ products are born in a range of internal states.

3.4.1 Angular Scattering and Kinetic Energy Release Distributions

The CM joint probability density function is defined as

$$P(\theta, w) \equiv \frac{2\pi}{\sigma_\mathrm{r}} \frac{\mathrm{d}^2\sigma_\mathrm{r}}{\mathrm{d}\omega\,\mathrm{d}w}, \tag{3.35}$$

where σ_r is the reaction cross-section, w is the product CM speed and ω represents the polar scattering angles θ and ϕ. Replacing w by the fraction of the available energy channelled into product translation, f_t [101, 103–105, 172], gives

$$P(\theta, w) \equiv P(\theta, f_\mathrm{t}) \left| \frac{\mathrm{d}f_\mathrm{t}}{\mathrm{d}w} \right|, \tag{3.36}$$

with

$$\left| \frac{\mathrm{d}f_\mathrm{t}}{\mathrm{d}w} \right| = M \frac{m_\mathrm{AB}}{m_\mathrm{CD}} \frac{w}{E'_\mathrm{t,max}}, \tag{3.37}$$

where $E'_{\mathrm{t,max}}$, the maximum possible kinetic energy release, is given by

$$E'_{\mathrm{t,max}} = -\Delta_{\mathrm{r}} H_0^{\ominus} + E_{\mathrm{t}} + E_{\mathrm{BCD}} - E_{\mathrm{AB}}. \tag{3.38}$$

In these equations m_{i} is the mass of moiety i, $M = m_{\mathrm{A}} + m_{\mathrm{BCD}} = m_{\mathrm{AB}} + m_{\mathrm{CD}}$, E_{t} is the collision energy, and E_{BCD} and E_{AB} are the average internal energy of the BCD reactant (taken to be zero) and the *fixed* internal energy of the probed AB quantum state respectively. Defining the rescaled parameter, f'_{t}, as

$$f'_{\mathrm{t}} = (2f_{\mathrm{t}} - 1), \tag{3.39}$$

to ensure orthonormality of the Legendre moments of the $P(f_{\mathrm{t}})$ distribution, the joint CM distribution may be expressed as a double expansion of Legendre polynomials

$$P(\theta, w) = \frac{1}{4} \sum_{n,m} a_{nm} P_n(\cos\theta) P_m(f'_{\mathrm{t}}) \left| \frac{\mathrm{d}f'_{\mathrm{t}}}{\mathrm{d}w} \right|, \tag{3.40}$$

where $P_i(\cdots)$ is the i^{th} order Legendre polynomial and the moments of the CM distribution are assumed to be independent of the comparatively narrow spread of reactant relative speeds, k. Integration of Equations 3.35 and 3.40 over the speed, w, and the fractional kinetic energy release, f'_{t}, respectively, produces the CM angular scattering distribution, i.e., the differential cross-section (DCS),

$$\frac{1}{\sigma} \frac{\mathrm{d}\sigma}{\mathrm{d}\cos\theta} \equiv P(\theta) = \frac{1}{2} \sum_{n} a_{n0} P_n(\cos\theta), \tag{3.41}$$

whereas integration over the scattering angle, θ, produces the CM speed distribution, or equivalently, the kinetic energy release distribution,

$$P(f_{\mathrm{t}}) = \sum_{m} a_{0m} P_m(f'_{\mathrm{t}}). \tag{3.42}$$

For a reaction initiated by linearly polarised photolysis radiation, the corresponding LAB frame velocity distribution takes a particularly simple form. The

LAB frame is defined with the z axis parallel to the photolysis polarisation vector, $\boldsymbol{\epsilon}_{\mathrm{p}}$, and the x axis along the photolysis propagation vector. Note that the photolysis propagation and electric vectors both lie in the plane of the detector (i.e., the xz plane) for all of the reaction systems studied in this thesis. It has been shown [93–97] that integration of the joint CM scattering distribution of Equation 3.40 over the reagent and precursor velocities leads to the LAB velocity distribution

$$P(v,\Theta_v) = \sum_L B_L(v) P_L(\cos\Theta_v) \tag{3.43}$$

with $L = 0$ and 2, and where Θ_v is the angle between the photolysis polarisation vector, $\boldsymbol{\epsilon}_{\mathrm{p}}$, and the AB LAB velocity vector, $\mathbf{v}$. Explicit expressions for $B_L(v)$, which are proportional to the bipolar moments $\overline{b_0^L(L,0;v)}$ averaged over all reagent velocities, have been presented previously in the context of Doppler profile analysis [94, 97]. $B_0(v) \equiv P(v)$ is the product LAB speed distribution and the LAB frame speed-dependent translational anisotropy is $\beta(v) = B_2(v)/B_0(v)$ (*cf.* Equation 3.24 of the inversion analysis in Section 3.3, where the reagent and precursor velocities were not taken into account).

Since the measured images are simply 2D projections of the LAB frame scattering distribution, analytical expressions for the images, $I(v_{\mathrm{p}},\phi)$, may be obtained by integration of Equation 3.43 over v_y, the velocity component along the time-of-flight axis. This yields the expression

$$I(v_{\mathrm{p}},\phi) = \sum_L M_L(v_{\mathrm{p}}) P_L(\cos\phi), \tag{3.44}$$

where v_{p} and ϕ are the radial and angular coordinates of the image, respectively, and the non-zero moments, $M_L(v_{\mathrm{p}})$, are given by

$$M_0(v_{\mathrm{p}}) = \int_0^\infty \left[2B_0(v) + \left(\frac{v_{\mathrm{p}}^2}{v^2} - 1\right) B_2(v)\right] \left(\frac{v^2}{v^2 - v_{\mathrm{p}}^2}\right)^{1/2} \mathrm{d}v \tag{3.45}$$

and

$$M_2(v_\mathrm{p}) = 2\int_0^\infty \left(\frac{v_\mathrm{p}^2}{v^2}\right) B_2(v) \left(\frac{v^2}{v^2 - v_\mathrm{p}^2}\right)^{1/2} \mathrm{d}v. \tag{3.46}$$

Note that Equation 3.44 can be used to simulate images for known CM angular scattering and kinetic energy release distributions. In the present approach, however, Equations 3.45 and 3.46 are used to generate sets of basis functions, $b_L(n, m; v_\mathrm{p})$ that are then fitted to the experimental data.

3.4.2 Experimental Legendre Moments

The experimentally derived Legendre moments, $\mathcal{M}_L(v_\mathrm{p})$, can be extracted from the experimental images, $\mathcal{I}(\cdots)$, by integration over the angular coordinate of the image, ϕ:

$$\mathcal{M}_L(v_\mathrm{p}) = \frac{1}{2}\int_{-1}^{1} \mathcal{I}(v_x, v_z)(2L+1)P_L(\cos\phi)v_\mathrm{p}\,\mathrm{d}\cos\phi \tag{3.47}$$

where $\mathcal{I}(v_\mathrm{p}, \phi) \equiv \mathcal{I}(v_x, v_z)v_\mathrm{p}$, and v_x and v_z are the appropriate projections of the LAB velocity in the image plane (proportional to the pixel coordinates of the image). Recall that in the experiments described in this thesis the only non-zero moments of the images are those with $L = 0$ and 2. The advantage of using moments of the image is that, while they contain the same information as the complete image, the reduction in dimensionality means that they can be fitted much more efficiently.

Image Centring

In order to evaluate the integral in Equation 3.47 and to extract the Legendre moments accurately, it is imperative to determine the centre of the experimental image precisely. Centring of the images was achieved in practice by fitting projections along v_x and v_z of the experimental image, $\mathcal{I}(v_x, v_z)$, with functions similar in form to simple harmonic oscillator wavefunctions. The centre thereby determined was then systematically checked, and if necessary, adjusted, by comparison of the left and right, and top and bottom, portions of the image. The accuracy of the algorithms used to carry out these procedures was extensively tested using both simulated images and experimental images of photolysis products.

Moment Smoothing of Images

As was discussed in Section 3.2.1, a common problem encountered when using the ion counting method is that the 'grainy' quality of the images obtained tends to preclude use of the inverse Abel transform due to the high levels of centreline noise that it would generate. A procedure to smooth images without incurring any loss in resolution was developed [161], which takes advantage of the fact that a velocity-map ion image may always be expressed as a Legendre (or Fourier [161]) moment expansion in the angular coordinate of the image. In the case of Legendre moments, these can be extracted from the image using Equation 3.47 and may then be used to reconstruct the image using Equation 3.44. An example of this smoothing method and its effect on the inverse Abel transform is shown in Figure 3.5 for an image of the Cl(^{2}P$_{1/2}$) products (detected on the $4p\,^4\mathrm{D}_{3/2} \leftarrow\, ^2\mathrm{P}_{1/2}$ (2+1) REMPI transition) of NOCl photolysis at 240.17 nm. There is a marked improvement in the inverse Abel transformed image following the smoothing procedure, with a significant reduction in the centreline noise. The reduction of the 'graininess' in the moment-smoothed image relative to the raw image is also reflected in the inverse Abel transforms of the two images. Although similar results may be achieved using the forward convolution methods of Vrakking [162] and Reisler and co-workers [163] discussed in Section 3.2.2, the moment smoothing procedure is thought to be simpler to implement.

3.4.3 Legendre Moment Basis Functions

Each basis function of order (n,m), $b_L(n, m; v_\mathrm{p})$, used in the fitting of the experimental data corresponds to a Legendre moment simulated for a single (n,m) term in the joint CM scattering distribution given by Equation 3.40. A Monte Carlo integration of the relevant terms in the CM scattering distribution over the velocity distributions of the precursor and reactant molecules, the velocity distribution of the reactive photofragment and, where necessary, the excitation function (the collision

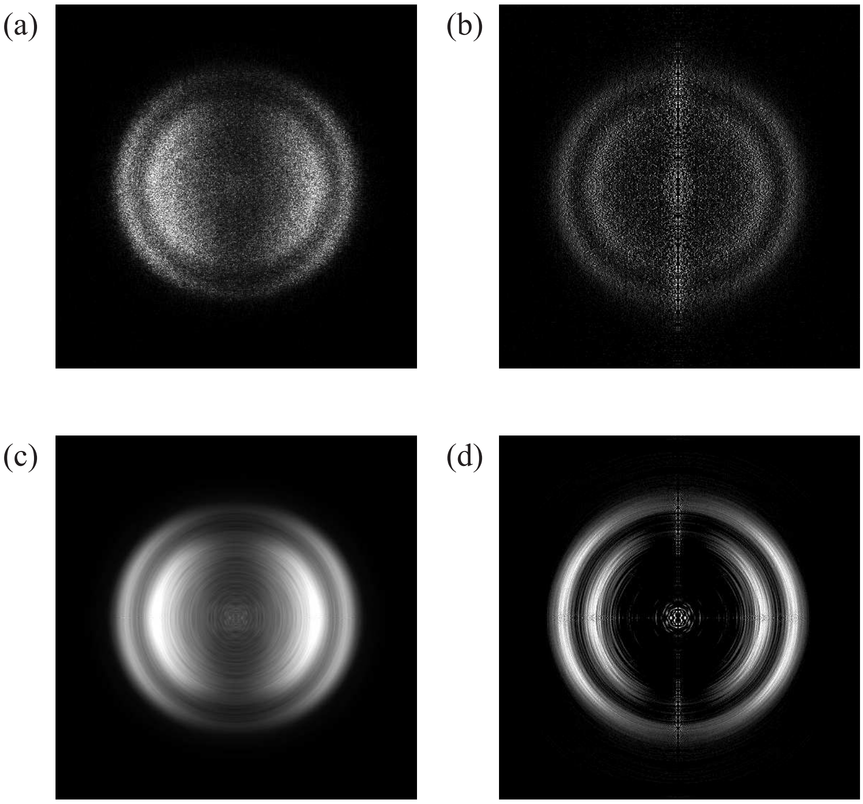

Figure 3.5: Moment smoothing: (a) raw image; (b) inverse Abel transform of the raw image in (a); (c) Moment smoothed image; and, (d) inverse Abel transform of the smoothed image in (c).

energy dependence of the reaction cross-section) for the reaction, $\sigma_{\mathrm{r}}(E_{\mathrm{t}})$, is used to simulate the $B_L(v)$ Legendre moments of the product LAB velocity distribution (see Equation 3.43). The basis functions, which are effectively the Legendre moments of the projection along v_y of this simulated LAB velocity distribution (i.e., the Legendre moments of the image one would obtain from the simulated LAB velocity distribution), are then evaluated from the $B_L(v)$ Legendre moments using Equations 3.45 and 3.46. The forms of these functions are illustrated in Figure 3.6. For the Monte Carlo sampling to be performed correctly, it is important that sufficient iterations are used for the resulting basis functions to be converged (i.e., the magnitude and functional form of the basis functions are invariant when the number of iterations used in the sampling procedure is increased). In practice, around 10^9 iterations are required for each low order basis function. If higher order polynomials in either the

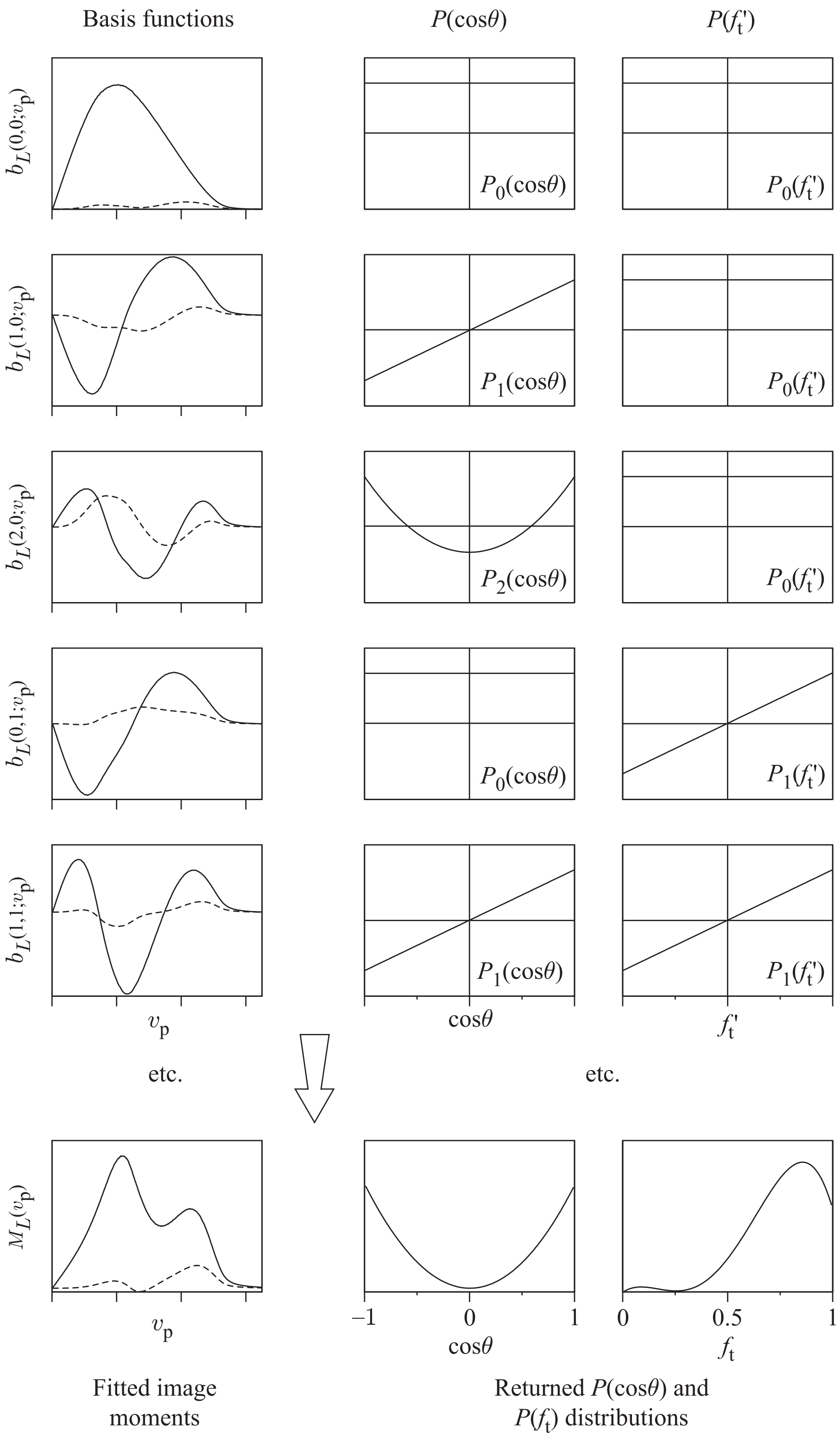

Figure 3.6: Top: low order $b_0(n,m;v_\mathrm{p})$ (—) and $b_2(n,m;v_\mathrm{p})$ (- - -) basis functions (left) and the corresponding $\cos\theta$ and f_t' Legendre polynomials used in their generation (right). Bottom: fitted moments and the returned $P(\cos\theta)$ and $P(f_\mathrm{t})$ distributions are shown in the bottom panels.

$P(\cos\theta)$ or $P(f_{\mathrm{t}})$ distributions are required to fit the data, however, the number of iterations needed to converge the corresponding basis functions may be significantly higher.

3.4.4 Constraints on the Fits

Certain constraints exist both on the values of the coefficients of the expansion of the joint CM scattering distribution given in Equation 3.40, and on the distribution itself [173]. Since the joint CM scattering distribution is a probability density function, it cannot take negative values and the constraints placed on the distribution thus arise on purely physical grounds:

$$\frac{1}{4}\sum_{n,m} a_{nm} P_n(\cos\theta) P_m(f'_{\mathrm{t}}) \left|\frac{\mathrm{d}f'_{\mathrm{t}}}{\mathrm{d}w}\right| \geq 0 \qquad (3.48)$$

for all θ and f_{t}. The limits on the expansion coefficients may be evaluated directly, by consideration of the polynomials used in the expansion. By expression of a probability density function, $f(x)$, as a sum of orthonormal polynomials, $\phi_n(x)$,

$$f(x) = \sum_n c_n \phi_n(x), \qquad (3.49)$$

each coefficient, c_n, of the expansion may be determined using

$$c_n = \int \phi_n(x) f(x)\,\mathrm{d}x. \qquad (3.50)$$

If $f(x)$ is a delta function where $\phi_n(x)$ takes either its maximum or minimum value, c_n will be equal to that value of $\phi_n(x)$. The limits on the expansion coefficients of the CM scattering distribution are therefore equal to the maximum and minimum values of the corresponding Legendre polynomials.

3.4.5 Separability

The joint CM scattering distribution expresses the probability of the product being scattered at a particular CM speed w (or with fractional kinetic energy release, f_t) and angle θ. Experimentally, the interdependence of $P(f_\mathrm{t})$ and $P(\theta)$ may not always be detectable, and in these cases the joint CM scattering distribution given by Equation 3.40 may be written in the separable form:

$$\begin{aligned} P(\theta, f_\mathrm{t}) &= P(\theta)P(f_\mathrm{t}) \\ &= \frac{1}{4}\left[\sum_n a_n P_n(\cos\theta)\right]\left[\sum_m d_m P_m(f'_\mathrm{t})\right]. \end{aligned} \tag{3.51}$$

By separating the two distributions in this way, the total number of coefficients that needs to be determined from the fitting routine is reduced from $n \times m$ to $n + m$, and the complexity of the analysis simplified accordingly. For each of the Cl + CH_4/CH_3D/CD_4, Cl + C_2H_6 and Cl + n-C_4H_{10} reactions described in this thesis, it was found that satisfactory fits to the data could be obtained assuming the separable form of the joint CM scattering distribution.

3.4.6 Fitting of the Image Moments

The coefficients of the joint CM scattering distribution, a_{nm} (or $a_n d_m$ for a separable distribution), are obtained by simultaneously fitting the basis functions, $b_L(n, m; v_\mathrm{p})$, to both experimental image moments, $\mathcal{M}_0(v_\mathrm{p})$ and $\mathcal{M}_2(v_\mathrm{p})$. The process involves minimisation of the χ^2 function

$$\chi^2 = \sum_{L=0,2} \sum_{i=1}^{N} \Big[\mathcal{M}_L(v_\mathrm{p}^i) - M_L(v_\mathrm{p}^i)\Big]^2, \tag{3.52}$$

where

$$M_L(v_\mathrm{p}^i) = \sum_{n,m} a_{nm} b_L(n, m; v_\mathrm{p}^i) \tag{3.53}$$

and N is the number of data points in the experimental image moments [103–105]. For the fit to be meaningful, the number of a_{nm} coefficients that may be determined is limited by the number of points in the experimental image moments, $n \times m \leq N$. For the systems studied in this thesis, the maximum number of Legendre polynomials in either the angular scattering or kinetic energy release distributions was generally restricted to five. This aspect of the fitting depends heavily on the data being fitted, however, and is discussed more fully in Chapters 4, 5 and 6.

The minimisation of χ^2 was achieved using a genetic algorithm routine [174].[1] This routine involves first randomly sampling sets of trial fitting coefficients and then evaluating χ^2 for each set. The coefficients in each set are chosen such that they lie within their physical limits (see Section 3.4.4). The set with the lowest value of χ^2 is retained. The sets are then sorted in order of increasing χ^2 and systematically modified using a 'cross-over' operator. The effect of the 'cross-over' operator is to combine the coefficients in two chosen sets to produce two new, different sets. At this stage a small number of the coefficients in the new sets are randomly selected and replaced by randomly sampled coefficients, in order to avoid stagnation of the fitting procedure. The χ^2 values for this next generation of sets are once again evaluated and the procedure is repeated until a specified number of iterations have been completed, or the value of χ^2 drops below some chosen threshold value.

There are two principal advantages of the genetic algorithm over other minimisation routines. The first is that the topography of the coefficient space is well sampled, with the result that convergence to false minima, which is a common problem with steepest-descent methods, is unlikely. The second advantage is that it is relatively straightforward to impose constraints on the returned distributions. For most other non-linear fitting algorithms, constraints of this type are non-trivial to impose on the coefficients directly. To prevent the returned joint CM scattering

---

[1] The genetic algorithm derives its name by analogy to biological systems, with the sets of coefficients equivalent to *chromosomes*, the position of the coefficient within a set equivalent to a *gene* and the value taken by the coefficient equivalent to an *allele*. The 'cross-over' operator may be compared to mating of chromosomes, while the randomised alteration of coefficients within sets corresponds to biological mutation of alleles.

distribution, $P(\theta, f_{\rm t})$, from becoming negative at any point (see Section 3.4.4), the χ^2 value evaluated for each set of coefficients is penalised [103–105] according to the equation

$$\chi^2_{\rm tot} = \chi^2 + \chi^2_{\rm pen}, \tag{3.54}$$

where

$$\chi^2_{\rm pen} = \iint\limits_{P(\theta, f_{\rm t})<0} \left|P(\theta, f_{\rm t})\right|^2 {\rm d}\cos\theta \, {\rm d}f_{\rm t}, \tag{3.55}$$

and the integral in Equation 3.55 only applies in the regions for which $P(\theta, f_{\rm t})$ is negative.

It should be noted, however, that using the genetic algorithm to perform fits to the data is computationally expensive. This is because it is necessary to evaluate χ^2 for each set of coefficients on every iteration, and large numbers of sets of coefficients and iterations are frequently required.

3.4.7 Error Analysis

A detailed error analysis employing a 'brute force' Monte Carlo procedure [159] was performed in order to determine the error limits on the CM angular scattering and kinetic energy release distributions returned from the fits [101, 103–105]. Within this error analysis procedure, sets of coefficients were chosen at random and the χ^2 value for each calculated. Those sets of coefficients which yielded χ^2 values below a predetermined threshold were then used to generate the corresponding CM scattering distributions, a large ensemble of which were used to provide the error limits for the distributions obtained from the best fit. The threshold value for χ^2 was chosen such that the distribution of fits encompassed the noise in the experimental data. An example set of fits to experimental image moments is given in Figure 3.7.

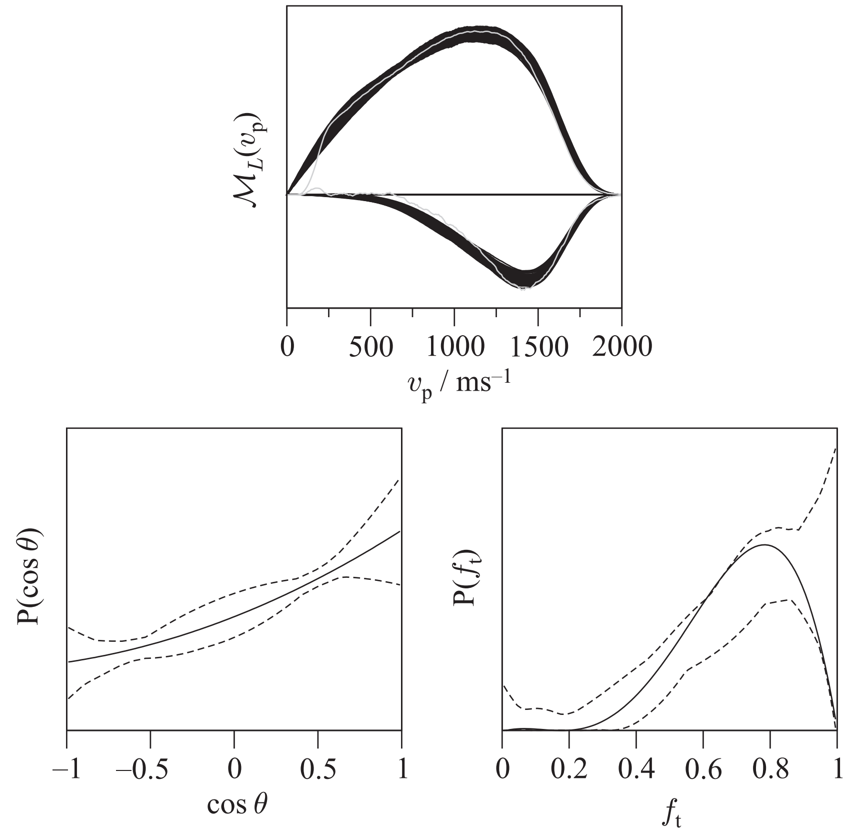

Figure 3.7: Error analysis for the HCl($v' = 0$,$j' = 0$) products of the reaction of chlorine with ethane. The distribution of acceptable fits is shown in the top panel. The CM angular scattering and kinetic energy release distributions returned by the best fit (—), along with the error limit envelopes determined from the error analysis (- - -), are shown in the bottom panels.

3.4.8 Image Simulation and Fitting: The H + D$_2$ Reaction

In order to test the sensitivity of the Legendre moment fitting methodology, images were simulated for the HD(v',j') products of the H + D$_2$ reaction [161].[2] The simulations were based on differential cross-sections derived from quantum scattering calculations carried out by Aoiz, Bañares and Castillo [176] at a collision energy of 1.49 eV. The model differential cross-sections were used as an input to a Monte Carlo simulation of $B_L(v)$ in Equation 3.43, using the equations developed in Ref. [97]

---

[2] In practice, the HD(v',j') products could be detected quantum state selectively using the $E,F\,^1\Sigma_g^+ \leftarrow X\,^1\Sigma_g^+$ (2+1) REMPI transitions at around 210 nm [175].

and assuming a molecular beam temperature of 10 K. Equation 3.43 was then used to construct the 3D LAB frame scattering distribution, from which simulated 2D velocity-map ion images were obtained by numerical integration over v_y, the velocity component along the time-of-flight axis. This approach was taken instead of using the calculated $B_L(v)$ functions in conjunction with Equations 3.45 and 3.46 to generate the image moments directly, in order for the methods used in generating the simulated images and in performing the analysis to be independent. In this way, fitting of the simulated data thus provided a stringent test of the performance of the Legendre moment analysis method. Random noise was added to the images to assess the effect it has on the CM scattering distributions returned from the fit.

With quantum state resolved 'detection' of the molecular products of the triatomic H + D_2 reaction, the CM speed of the HD(v',j') products had a single, well-defined value. The fixed collision energy used in the simulations therefore meant that the product LAB speed and the CM scattering angle were simply related by the law of cosines (see Sections 3.3.3 and 3.3.5). Fluctuations in the image intensity along the radial coordinate of the image thus directly reflect oscillations in the CM angular scattering distribution.

For comparison, simulations were performed for the HD($v' = 0$,$j' = 0$) and HD($v' = 0$,$j' = 9$) products, chosen for the markedly different CM angular scattering distributions associated with each product rotational state. Images, Legendre moments, the input CM angular scattering distributions and the CM angular scattering distributions returned from the fitting procedure are shown in Figure 3.8. The peaks in the CM angular scattering distributions are clearly visible as separate rings in the corresponding images. The simulations and the fits to the Legendre moments obtained from them demonstrate that using the Legendre moment analysis it is possible to extract even fairly complicated structure in the CM angular scattering distribution from velocity-map ion images with a high degree of accuracy. The high angular resolution obtainable using this method is illustrated by the sensitivity to the very sharp forward and backward peaks in the $j' = 0$ CM angular scattering

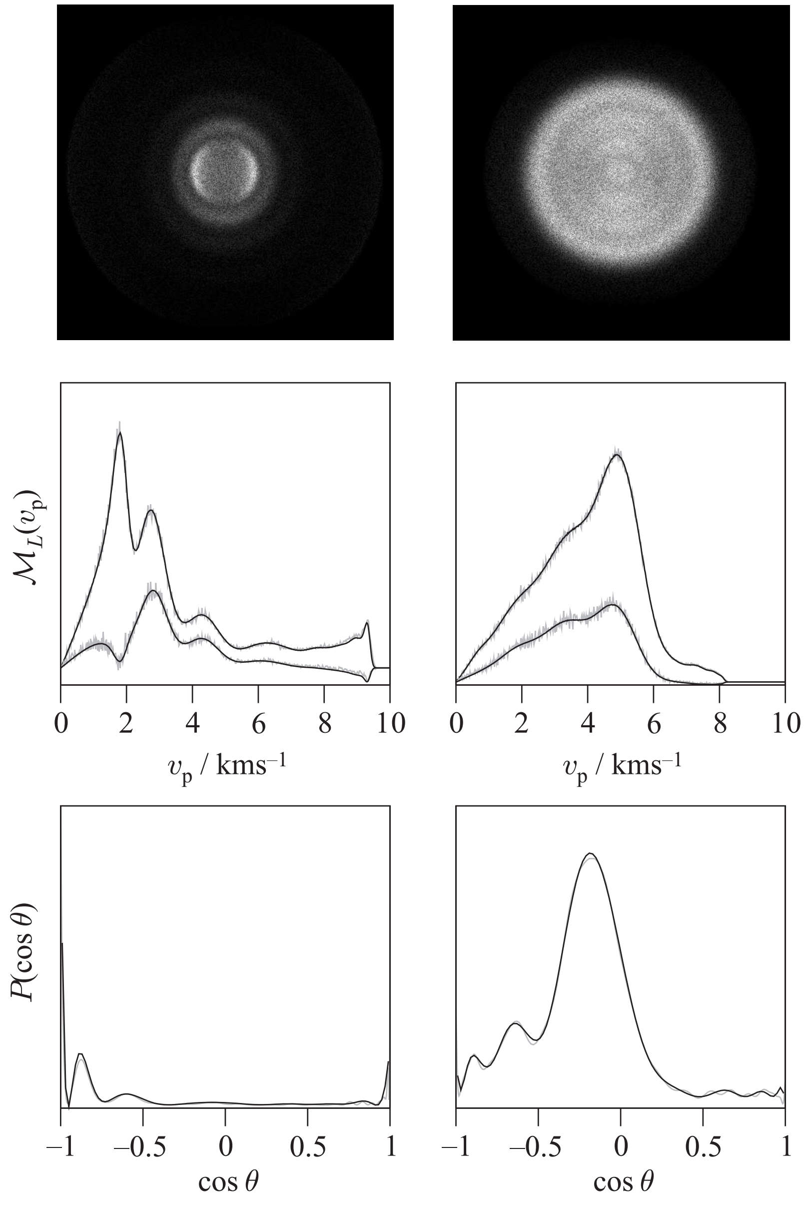

Figure 3.8: Top: simulated images for the HD($v' = 0$,$j' = 0$) (left) and HD($v' = 0$,$j' = 9$) (right) product quantum states of the H + D_2 reaction at a collision energy of 1.49 eV. Middle: the corresponding Legendre moments (grey lines) and fits (black lines). Bottom: the input CM angular scattering distributions from quantum scattering theory (grey lines), and the functions returned from the Legendre moment analysis (black lines).

distribution. The moment fitting method is also seen to be robust to added noise on the simulated data, with the returned CM angular scattering distribution faithfully reproducing the input data for even very grainy images.

Chapter 4

The Dynamics of the Cl + C_2H_6 Reaction at 0.24 eV

4.1 Introduction

The hydrogen atom abstraction reaction of atomic chlorine with ethane[1]

$$\mathrm{Cl} + \mathrm{C_2H_6} \longrightarrow \mathrm{HCl}(v', j') + \mathrm{C_2H_5} \qquad \Delta_\mathrm{r} H_0^\ominus = -11.6 \pm 2.1\,\mathrm{kJ\,mol^{-1}} \tag{4.1}$$

lends itself as a test system for velocity-map ion imaging of reactions using the photoloc technique for a variety of reasons: (i) the reactive cross-section is relatively large, so that the probability of reaction, and therefore production of detectable products, is high; (ii) the dynamics of the reaction have been reasonably well investigated previously using a range of experimental techniques; and, (iii) few rovibrational quantum states of the HCl products are populated. Two direct results of this final point are that few quantum state resolved measurements are required to fully characterise the reaction and that signal levels in these measurements should be high.

With the aim of preparing for the discussion and comparisons of the current results with earlier work, an overview of the previous experimental and theoretical

---

[1] Enthalpy of reaction calculated using D_0^0(H–Cl) = 427.64 ± 0.02 kJ mol^{-1} [177, 178] and D_0^0(H–C_2H_5) = 416.0 ± 2.1 kJ mol^{-1} [179].

studies carried out on the Cl + C_2H_6 reaction is provided in the following Section.

4.2 Previous Work on the Cl + C_2H_6 Reaction

4.2.1 Kinetics Studies

The reaction of atomic chlorine with ethane has long been used as a reference reaction in kinetic studies of reactions of chlorine with larger hydrocarbons [180–184]. A great deal of effort has therefore been made to determine accurate values for the rate coefficients for this reaction. Work carried out to date spans the wide temperature range of 203−1400 K and has utilised a variety of both direct and indirect techniques. Direct methods for the measurement of the absolute rate constant include microwave discharge photolysis of Cl_2 in a helium flow coupled with resonance fluorescence detection of the Cl atoms at around 134 nm and pulsed laser photolysis of chlorinated precursors (e.g. Cl_2 at 308 nm, and HCl or CF_2Cl_2 at 193 nm) followed either by infrared absorption of the HCl products or by vacuum ultraviolet laser-induced fluorescence of the Cl atoms. The results of these studies and those determined using relative rate methods are in general agreement with one another (see, for example, Refs. [185–194]). Recent reviews of the data recommend the value of the absolute rate coefficient, k, to be (5.7–5.9) $\times$ 10^{-11} $\mathrm{cm}^3\,\mathrm{molecule}^{-1}\,\mathrm{s}^{-1}$ at 298 K [195–197]. The rate constant exhibits a positive temperature dependence, displaying significant non-Arrhenius behaviour at high temperatures. Even greater deviation from Arrhenius behaviour has been seen in the Cl + CH_4 reaction at high temperatures. Factors proposed to account for this include quantum mechanical tunnelling [198, 199], and the population and enhanced reactivity of either spin-orbit excited Cl atoms [200], or vibrationally excited methane molecules [198]. All of these factors could also be relevant in the Cl + C_2H_6 reaction, although, due to the low activation barrier in this reaction, the effect of spin-orbit excited Cl($^2P_{1/2}$) atoms is not thought to be significant [190]. Very recently Bryukov *et al.* [193] combined new experimental rate constants for the reaction of chlorine with ethane, measured using the discharge flow/resonance fluorescence technique over the temperature range 299–1002 K, with those determined in earlier studies. They achieved a good fit to the resulting data set using the modified Arrhenius expression

$$k = (7.3 \times 10^{-13})\, T^{0.7}\, \mathrm{e}^{+117/T}\ \ \mathrm{cm}^3\,\mathrm{molecule}^{-1}\,\mathrm{s}^{-1}\ (203\text{–}1400\,\mathrm{K}). \qquad (4.2)$$

At temperatures below 600 K, however, the experimental data are well reproduced by the simple Arrhenius expression, $k = A\,\mathrm{e}^{-E_\mathrm{a}/RT}$, with a pre-exponential factor, $A = (8.3 \pm 1.2) \times 10^{-11}\ \mathrm{cm}^3\,\mathrm{molecule}^{-1}\,\mathrm{s}^{-1}$, and an activation energy of $E_\mathrm{a}/R = 100\,(\pm 100)\,\mathrm{K}$ [195].

Transition-state theory kinetics calculations, which include the zero-curvature approximation for tunnelling and use the zero-order interpolation (IVTST-0) approach [201] have been performed by Roberto-Neto and Machado [202]. More recently, Fernández-Ramos *et al.* [203] have calculated an *ab initio* potential energy surface at the Møller–Plesset second-order perturbation level with the augmented correlation-consistent double-zeta basis set (MP2/apDZ). Thermal rate constants were calculated on this surface using microcanonical variational transition-state theory (μVTST) with multi-dimensional corrections for tunnelling. The transition state was found to be almost linear in both calculations ($\angle$(Cl–H–C) = 175.6–177.2°, depending on the level of theory employed), in accord with the work of Bottoni and Poggi [204] and Rudić *et al.* [130, 205]. The rate constants obtained in both studies are in good agreement with experimental values at low temperatures, but are too large at higher temperatures. This is thought to be a result of the neglect of anharmonicity along the reaction path [203]. Fernández-Ramos *et al.* report that tunnelling effects are negligible in the reactivity of the system, in stark disagreement with the findings of Roberto-Neto and Machado, who state that tunnelling effects *are* important. This difference is claimed by Fernández-Ramos *et al.* to originate from the different potential energy surfaces and the level of the calculations employed in the two studies: Fernández-Ramos *et al.* performed high-level dynamics calculations on a high-level *ab initio* potential energy surface, whereas Roberto-Neto and Machado used dual-level dynamics on a lower level surface that has a higher, but narrower barrier. This higher reaction barrier leads to a localised transition state, in contradiction to the 'loose' transition state suggested from previous experimental work [151, 206] and the broader barrier determined by Fernández-Ramos *et al.*

4.2.2 Dynamical Studies

Product Rotational Population Distributions

Zare and co-workers measured the nascent rotational population distribution of HCl($v' = 0$) using REMPI coupled with linear time-of-flight (TOF) mass spectrometry [151]. A mixture of Cl_2 and ethane seeded in helium was co-expanded in a pulsed molecular beam. Reaction was initiated by photolysis of Cl_2 using 355 nm laser radiation to produce monoenergetic Cl($^2P_{3/2}$) atoms and to provide a well-defined collision energy of 0.24 ± 0.03 eV. The HCl($v' = 0$) products were allowed to accumulate for 50–100 ns before detection *via* (2+1) REMPI at around 240 nm. Empirical linestrength factors derived from spectra of thermal HCl were then used to obtain the product HCl rotational population distribution shown in Figure 4.1. HCl($v' = 0,j'$) was seen to be produced rotationally very cold, with the $j' = 1$ state maximally populated. HCl products formed in $v' = 1$ were also observed in these experiments due to the collision energy spread, but it was estimated that these constituted only $\sim 0.3\%$ of the total [151].

The results of a later study at the same collision energy by Orr-Ewing and co-workers are also shown in Figure 4.1 [207]. They also employed REMPI-TOF detection of the HCl products, but introduced the Cl_2 and ethane through separate nozzles in order to limit the production of background HCl. The molecular beam produced in this way was cooled only modestly to ~ 200 K, compared to the 15 K reported by Zare and co-workers; this gave a broader collision energy distribution and is believed to be the origin of the slightly hotter HCl product rotational distribution observed.

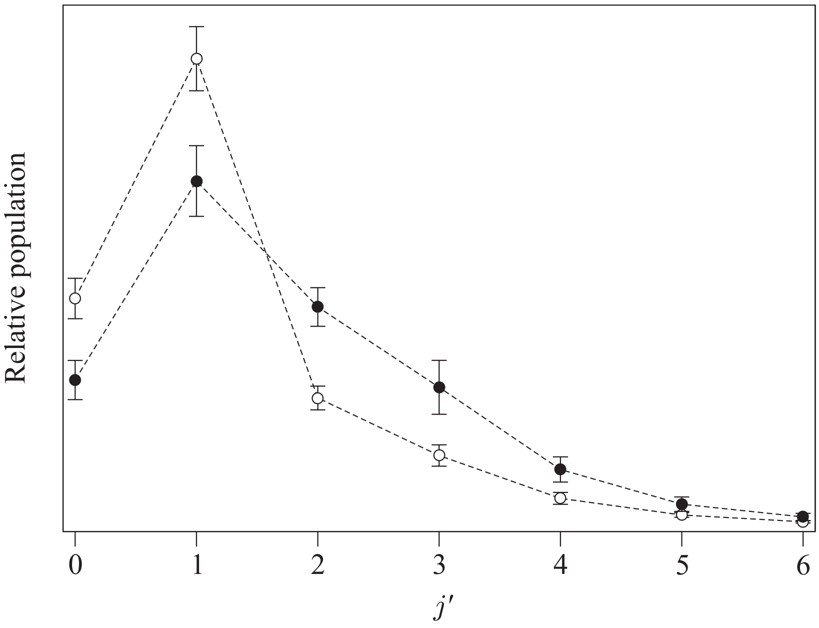

Figure 4.1: A comparison of the experimental nascent rotational quantum state population distributions for HCl($v' = 0$,j') from the reaction of Cl with C_2H_6 obtained by Zare and co-workers (--○--) [151] and by Orr-Ewing and co-workers (--●--) [207]. The error bars represent 1σ confidence limits; the distributions have been normalised in the j' range shown.

Angular Scattering Distributions

In addition to measuring the HCl($v' = 0$) nascent product rotational population distribution, Zare and co-workers also obtained rotational state-specific CM angular scattering distributions for HCl($v' = 0$,$j' = 1$, 3, 6 and 8) [151]. In these experiments, the Wiley–McLaren mass spectrometer used for REMPI-TOF detection was modified to operate under space-focusing and velocity-sensitive conditions, and a mask was placed in front of the detector to effect core-extraction [110] of the 3D product velocity distribution. The time-of-flight profiles obtained using this method were analysed on the assumption that there is zero internal excitation of the ethyl co-product. This assumption was supported by measurements of the speed-dependent translational anisotropy parameter, $\beta(v)$, which suggested that *on average* the ethyl radicals were born internally cold (200 ± 120 cm^{-1} of internal energy in the C_2H_5

moiety) [151]. Broad sideways scattering was observed for the HCl products formed in low rotational states, whilst the more rotationally excited HCl products were seen to be predominantly backward scattered. These results were rationalised using the line-of-centres model (see, for example, Ref. [2]) combined with the hard-sphere relationship between impact parameter and scattering angle. The resulting qualitative model predicts a CM angular scattering distribution that is constant between the angles $\cos\theta = -1$ (back-scattering) and a maximal scattering projection, $\cos\theta_{\mathrm{max}}$, which depends on the reagent translational energy [208]. For the Cl + ethane reaction, the maximum scattering angle was calculated to be $\cos\theta_{\mathrm{max}} = 0.93$, consistent with the nearly isotropic scattering observed [151]. Note that a more sophisticated model that includes a dependence of the barrier on Cl–H–C transition state angle, as presented by Smith [209], would provide a more realistic CM angular scattering distribution than this step-function.

In a very similar experiment, Zare and co-workers probed the LAB velocity distribution of the ethyl products *non*-state-selectively using multi-photon ionisation at 242 nm [206]. The data obtained from this experiment were analysed using the speed-dependent translational anisotropy parameter, $\beta(v)$, to estimate the centre-of-mass speed (and therefore the internal excitation) of the ethyl fragment. The CM angular scattering distribution obtained in this way is consistent with those derived from the state-resolved HCl experiments when the latter are reanalysed using the same procedure.

The reaction of atomic chlorine with perdeuterated ethane, C_2D_6, has been studied at a collision energy of 0.25 eV by Zare and co-workers [151, 210]. The reaction is very nearly thermoneutral, with $\Delta_{\mathrm{r}}H^{\ominus} = -1.05\ \mathrm{kJ\,mol^{-1}}$ [211]. DCl($v' = 0, j'$) products were detected using core-extraction REMPI-TOF [110] and were observed to be formed in higher rotational states than the HCl produced in the analogous Cl + C_2H_6 reaction, though the average rotational energy was found to be very similar for the two cases.[2] The CM angular scattering distributions obtained for

---

[2] The rotational constants of the two molecules are very different: B_e(H–Cl) = 10.59 cm^{-1}, whereas B_e(D–Cl) = 5.45 cm^{-1} [127].

the DCl products of the Cl + C_2D_6 reaction were seen to be very similar to those obtained for HCl from Cl + C_2H_6 and also followed the trend of increasing backward scattering with increasing rotational excitation [151]. Stationary target frame polarisation-dependent moments of the differential cross-section were also obtained for DCl($v' = 0$,$j' = 1$) products [210, 212]. These measurements indicated that the DCl rotational angular momentum vector, $\mathbf{J}_{\mathrm{DCl}}$, was aligned in the plane perpendicular to the line of centres for scattering in the sideways and backwards directions, while for scattering in the forward direction $\mathbf{J}_{\mathrm{DCl}}$ was aligned in the plane perpendicular to an axis between the line of centres and the relative velocity vector. Assuming that the DCl rotational angular momentum alignment arises purely from motion during the transfer of the D atom, these measurements are consistent with the reaction proceeding through an early transition state [210]. The data were analysed assuming that no energy is deposited in internal modes of the ethyl product, so that there is an unambiguous relationship between the product LAB speed and LAB scattering angle. It should be noted, however, that the expressions for the polarisation parameters determined from this analysis depend strongly on the LAB scattering angle [212], and therefore the returned values for the polarisation parameters are very sensitive to the validity of the assumption made about the energy disposal [210, 212].

Kitsopoulos and co-workers investigated the reaction of Cl with ethane using a single, unskimmed molecular beam containing both Cl_2 and ethane, and employing velocity-map ion imaging detection of the HCl($v' = 0$,$j' = 1$) products *via* (2+1) REMPI [131]. Reaction was initiated using 308 nm laser radiation to give a collision energy of ~0.36 eV. The product speed distribution and the speed-dependent translational anisotropy parameter were obtained from the resulting image using the inverse Abel transform, which returns a 'slice' through the 3D scattering distribution. The CM angular scattering distribution was then determined assuming zero internal excitation of the ethyl co-fragment. The HCl($v' = 0$,$j' = 1$) products were observed to be forward scattered.[3] The large difference in collision energy (approximately 1.5 times greater), however, precluded a direct comparison with the earlier results of Zare and co-workers [151, 206].

Despite the considerable experimental effort expended in studying the dynamics of the reaction of atomic chlorine with ethane, very few theoretical calculations have been carried out to determine product angular scattering distributions for the system. In 1998 Xu *et al.* [213] performed a three-atom quasi-classical trajectory calculation on a London–Eyring–Polanyi–Sato surface computed for the collinear Cl–H–C configuration. They obtained CM angular scattering distributions for HCl($v' = 0, j' = 1$, 3, 6 and 8), all of which are in agreement with the experimental results of Zare and co-workers [151, 206]. The HCl product rotational population distribution returned from the calculations was, however, seen to be much hotter than those determined experimentally. In addition to their kinetics calculations, Fernández-Ramos *et al.* [203] also performed quasi-classical trajectory calculations on a reduced dimensionality (2D, $r_{\mathrm{C-H}}$, $r_{\mathrm{H-Cl}}$) parameterized *ab initio* potential energy surface to obtain the HCl relative velocity distribution.[4]

4.2.3 Summary

The previous work on the Cl + C_2H_6 reaction at 0.24 eV can be summarised as follows: (i) *ab initio* calculations suggest that the transition state of the reaction is close to linear; (ii) the HCl products are found experimentally to be formed in very low rotational states of the ground vibrational state, with the rotational population distribution peaking at $j' = 1$; (iii) experimental and theoretical treatments of the dynamics of the reaction have assumed that the system may be approximated to a three-body reaction, where internal modes of the ethyl radical are not excited; and, (iv) within this approximation, the HCl products formed in low rotational levels are

---

[3] Inspection of the data does not support this assertion: the products are actually seen to be strongly sideways scattered.

[4] The calculated HCl relative velocity distribution was shown to be in good agreement with experimental data. However, the experimental data presented were product *LAB*, rather than CM, velocity distributions [151, 206], and the agreement is entirely fortuitous.

observed to be broadly sideways scattered, moving to more backwards scattering with increasing rotational excitation.

4.3 Results

4.3.1 Images and Legendre Moments

Velocity-map ion images and the corresponding zeroth, second and fourth order Legendre moments are shown in Figure 4.2 for HCl($v' = 0$,$j' = 0$, 2 and 6). The images have been background-subtracted and quadrant-averaged for clarity; the Legendre moments were obtained from the raw images as described in Chapter 3. It can be seen clearly in the images, and especially in the zeroth order moments, that the intensity is shifted towards the centre of the images with increasing HCl rotational state. This trend is qualitatively consistent with the observations of Zare and co-workers, who had found previously that higher HCl rotational states were more backward scattered [151]. It should also be noted that, within the experimental signal-to-noise ratio of the data, the 4th order Legendre moments are very close to zero.

4.3.2 Inversion Analyses

When using the photoloc method to investigate reactions with two molecular products, a major issue concerns the ability to extract the full product flux distribution in both CM speed, w, and scattering angle, θ. As was discussed in Section 4.2.2, previous studies on the Cl + C_2H_6 reaction employing the photoloc technique determined CM angular scattering distributions by neglecting the internal excitation of the co-product entirely [151]; this approach has also been taken for the analysis of data obtained for other Cl + alkane reactions [214–216]. Information about the kinetic energy release of the reaction is, however, contained in the LAB frame speed distribution, $P(v)$, and the speed-dependent translational anisotropy, $\beta(v)$. A variety of methods have been proposed in order to obtain the CM angular scatter-

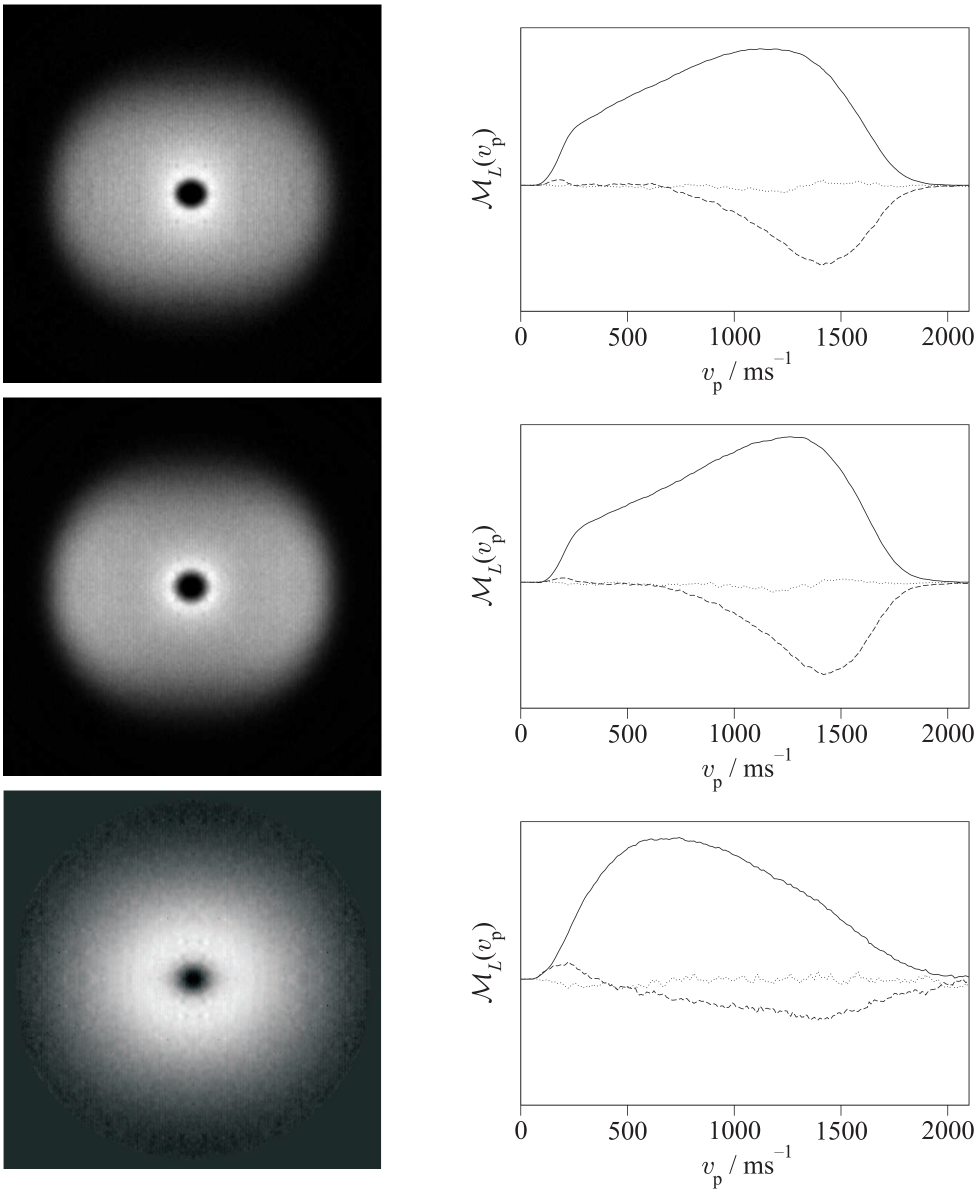

Figure 4.2: Background subtracted images and Legendre moments of order 0 (—), 2 (- - -) and 4 ($\cdots$) for HCl($v' = 0$,$j' = 0$ (top), 2 (middle) and 6 (bottom)).

ing distribution from the LAB distributions, relying either on inversion of the LAB speed distribution and speed-dependent translational anisotropy, or on fitting the experimental data using basis functions that accommodate a distribution of product speeds or fractional kinetic energy releases. In this Section, inversion methods that have previously been used to investigate the Cl + C_2H_6 reaction are critically assessed in light of the velocity-map ion imaging data presented in the preceding Section.

The LAB Frame Speed Distribution

In order to make meaningful comparisons with the previous experimental work of Zare and co-workers [151, 206], it is essential to establish that there is good agreement between the raw data presented from the REMPI-TOF core-extraction experiments and those collected in the present work. In addition, the potentially high molecular beam density in the current work ($\lesssim 10^{16}$ cm^{-3}, see Section 2.10.5) is approximately an order of magnitude greater than that used by Zare and co-workers (when estimated in a similar way), and so such a comparison of the raw data is also useful in determining that the HCl products are detected under single collision conditions in both experiments.

The most direct comparison between the two studies that can be made is with the derived LAB frame speed distributions. In Figure 4.3, the HCl($v' = 0$,$j' = 1$) LAB speed distributions, $P(v)$, and LAB speed-dependent translational anisotropies, $\beta(v)$, obtained from the two experiments are compared. The distributions from the current experiments were extracted by inverse Abel transformation of the background subtracted images followed by appropriate integration of the resulting ‘slice’ through the 3D velocity distribution. The very good agreement between the two sets of experimental results supports the view that both experiments probe nascent HCl products and that the potentially high molecular beam density in the current study does not adversely affect the quality of the ion images recorded. It also suggests that the ion imaging data are not significantly perturbed by fly-out of Cl reactants or

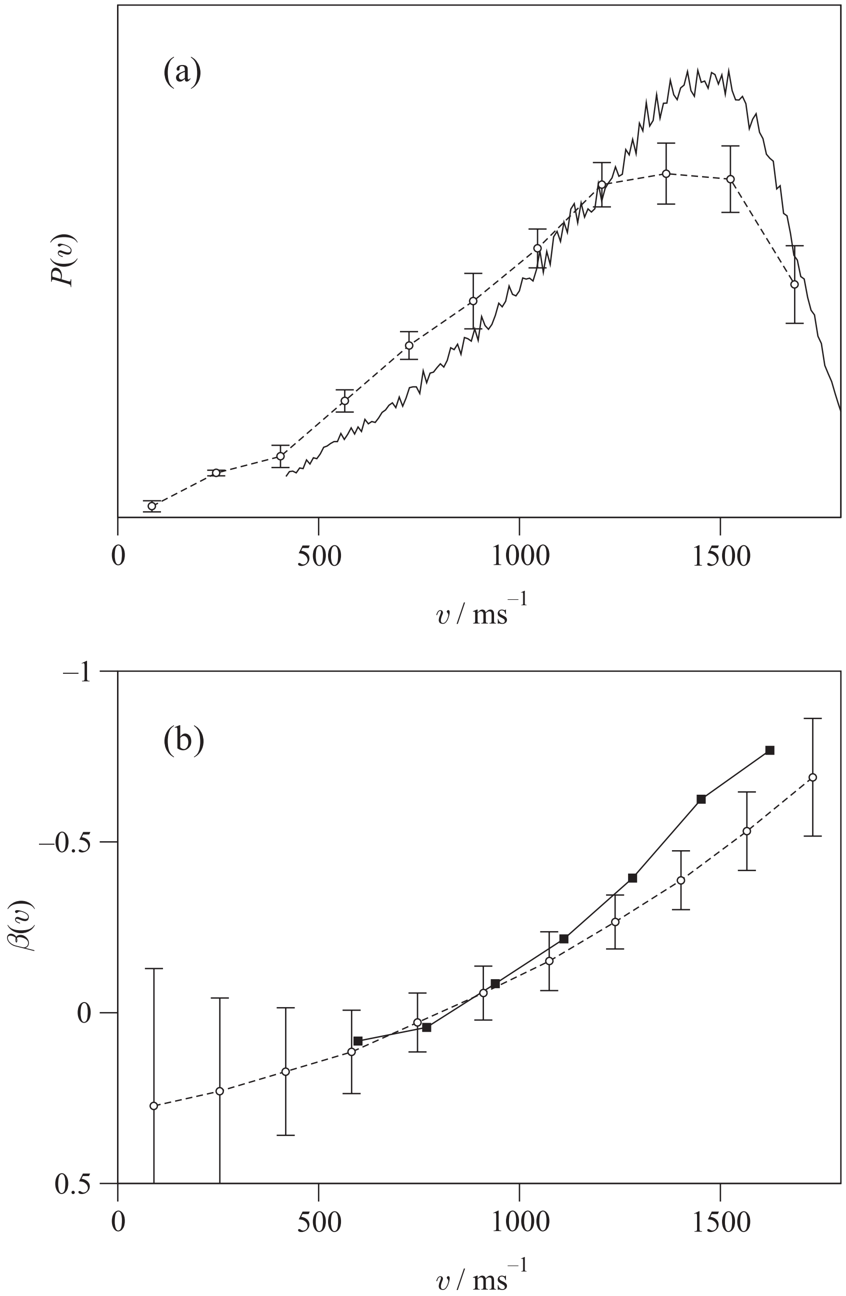

Figure 4.3: (a) The LAB speed distribution and (b) the speed-dependent translational anisotropy parameter, $\beta(v)$, obtained in the present study by direct inverse Abel transformation of the ion images (— in (a) and ■ in (b)), and in the REMPI-TOF core-extraction data of Zare and co-workers (- - ○ - -) [151]. Both sets of data are for HCl($v' = 0, j' = 1$).

HCl products from the probe region during the delay between photolysis and probe laser pulses. In the present study, fly-out would occur preferentially perpendicular to the photolysis laser propagation direction. This would be manifested as a decreased intensity in the ion image away from the laser propagation direction and would thus lead to a distortion of the LAB angular distribution obtained. A further indication that the ion imaging data are not notably affected by fly-out comes from the fact that the 4th and higher order Legendre moments of the image are zero within experimental precision, which is consistent with Equations 3.43 and 3.44 used to describe reactive scattering and the associated Legendre moments.

These considerations, together with the Cl ion images discussed in Section 2.10.2, and the direct comparison with previous work by Zare and co-workers, confirm that the data from the ion imaging experiments truly reflect the nascent HCl LAB frame velocity distribution, and that secondary collisions involving either the Cl atom reactants or the HCl products are of minor importance.

Simple Inversion Analysis

This analysis assumes that the ethyl radical is formed with zero internal energy. In this limit the CM angular scattering distribution is returned by direct transformation of the LAB speed distribution obtained by Abel-inversion using Equation 3.28 (see Chapter 3). The transformed image data are shown, along with analogous results from the HCl REMPI-TOF core-extraction experiments of Zare and co-workers [151], in Figure 4.4. The agreement between the two studies is excellent, as would be expected from the nearly identical LAB speed distributions. Also shown in Figure 4.4 are the CM angular scattering distributions obtained from a fit to *only* the zeroth Legendre moment extracted from the images. The fit was performed using the basis function method (see Chapter 3), where the basis functions in CM scattering angle were generated assuming no energy is deposited into internal modes in the ethyl co-product. To allow full comparison with the inversion results, the instrument resolution function was omitted from the basis functions and a reduced molecular

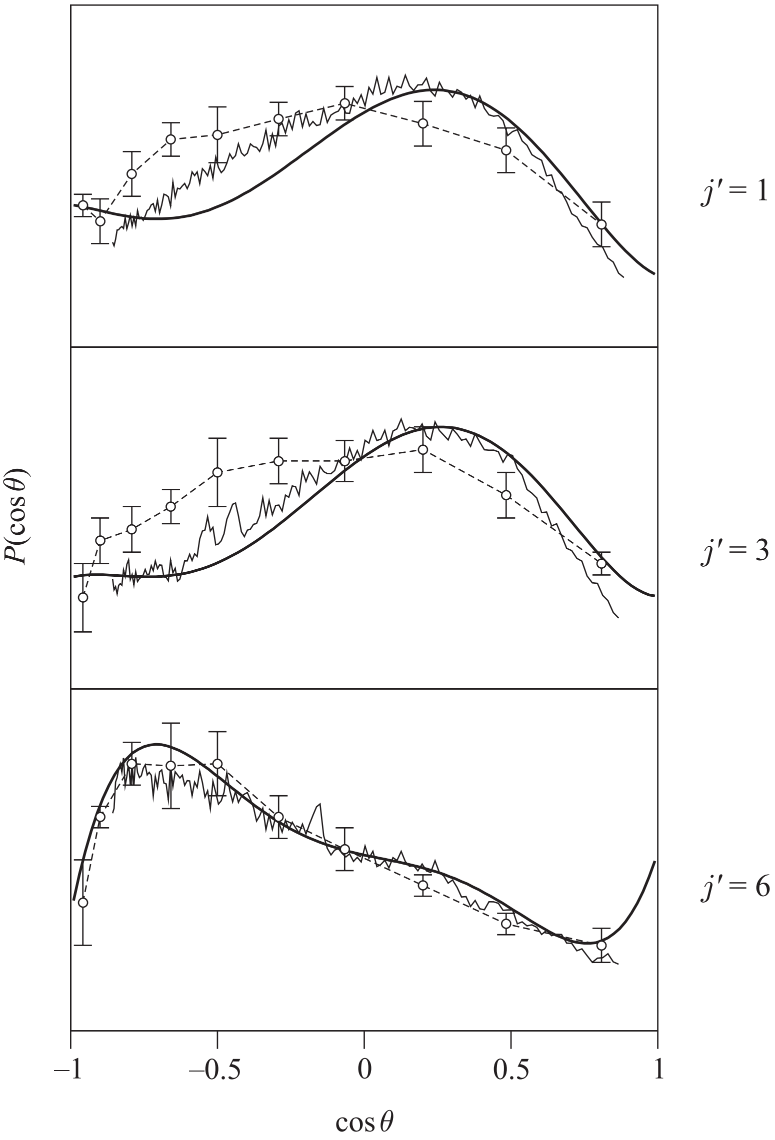

Figure 4.4: Comparison between the CM angular scattering distributions for HCl ($v' = 0$,$j' = 1$, 3 and 6) obtained assuming the ethyl co-products are born internally cold. The present results of inverse Abel transformation are shown as fine lines. Dashed lines with open points are the results of Zare and co-workers [151]. Dark lines are the result of fits to the zeroth Legendre moments, with basis functions generated assuming that $f_{\mathrm{t}} = 1$. The basis functions used in this latter case also take no account of the finite speed resolution of the experiment, and the finite molecular beam temperature.

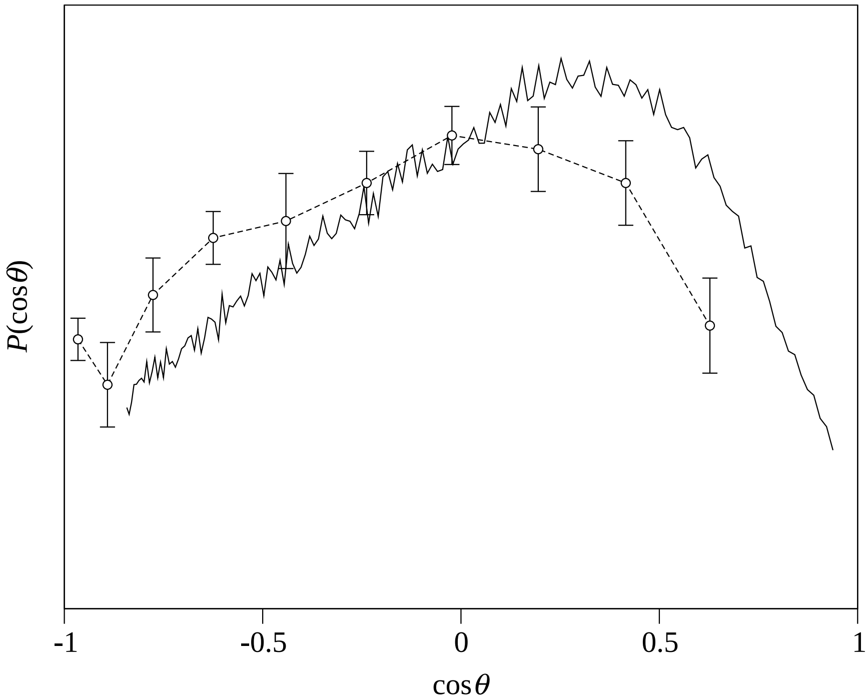

Figure 4.5: Comparison between the CM angular scattering distribution obtained using the refined inversion method (—) and that obtained previously by Zare and co-workers [151, 206] (- - ○ - -).

beam temperature of 10 K was employed. The results of the fits with these basis functions are again very similar to previous work [151], and to the results obtained from the inversion method. These comparisons therefore serve both to validate the raw ion imaging data, and to preclude errors in the basis function generation and fitting procedures.

Refined Inversion Analysis

As discussed in Chapter 3, the simple inversion analysis used in Section 4.3.2 may be refined by using the speed dependence of the translational anisotropy, $\beta(v)$, to estimate the HCl CM recoil speed, w [151, 206]. The CM angular scattering distribution obtained using this method is compared with the HCl($v' = 0$,$j' = 1$) data from Ref. [206] in Figure 4.5. This analysis yields very similar CM angular scattering distributions to those obtained assuming that the ethyl radical is formed internally cold, even though on average the method predicts a significant internal

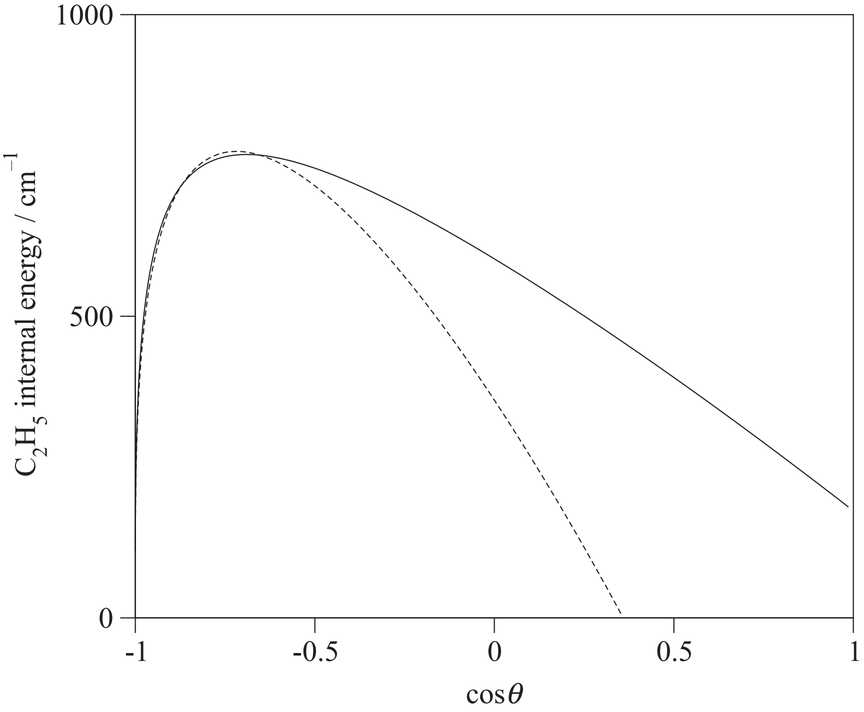

Figure 4.6: Comparison between the internal excitation of the ethyl co-products derived from the refined inversion method (—) and that obtained previously by Zare and co-workers (- - -). The latter data are taken from Figure 8(b) of Ref. [151], but are plotted here as a function of $\cos\theta$.

excitation in the ethyl co-products of $\sim 500\ \mathrm{cm}^{-1}$ (see Figure 4.6).

There are, however, inherent problems with this inversion method, as illustrated in Figure 4.7. Products travelling at the highest LAB speed, $v_{\max}$, must correspond to those in the CM frame that are scattered forwards with the highest possible CM kinetic energy release (see Figure 4.7(a)). These products are necessarily accompanied by co-products with low internal excitation and possess a $\beta(v)$ parameter close to the limiting value of -1.0, determined by the anisotropy of the Cl_2 precursor photolysis (see Figure 4.3(b)). Products formed with slightly lower LAB speeds, however, can be associated with either those formed with slightly lower CM kinetic energy release (and therefore more internally excited co-products), or those scattered at angles away from the forward direction, as illustrated in Figure 4.7(b). Within the present analysis procedure the kinetic energy release distribution is assumed to

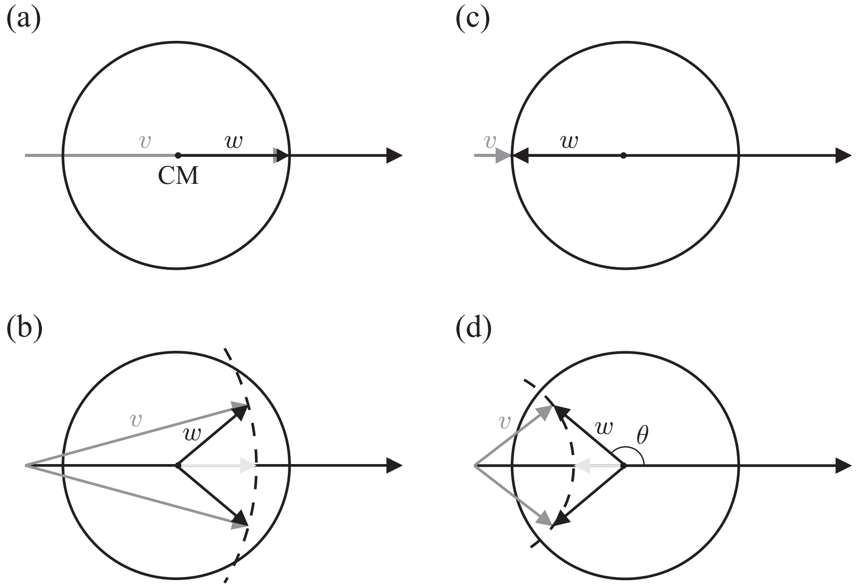

Figure 4.7: Collapsed Newton diagrams showing the effect of assuming a single CM scattering velocity, w, for each LAB speed, v, on the CM scattering angle, θ, obtained. The lightest grey arrows in (b) and (d) show CM scattering velocities consistent with the LAB speed shown; these correspond to products accompanied by internally excited ethyl radicals and are not included in the CM angular scattering distribution returned by the inversion procedure.

be a delta function, so that the speed-dependent translational anisotropy is linked to a *single* LAB scattering angle, θ_v, and thus CM speed, w, using Equations 3.32, 3.22 and 3.21. Products with less than maximal LAB speeds are therefore exclusively assigned to CM scattering angles, θ, away from the forward direction. A similar situation arises for the products generated with the lowest LAB speeds. These products necessarily correspond to backward scattering, with the co-products born in low internal quantum states (see Figure 4.7(c)). Products formed with slightly higher LAB speeds will once more be exclusively assigned to CM scattering angles away from the extreme backward direction, even though those LAB velocities may correspond to backward scattered products accompanied by internally excited ethyl radicals (see Figure 4.7(d)). This inversion procedure therefore inherently biases the CM angular scattering distribution away from the forwards and backwards directions, and artificially enhances the importance of sideways scattering. The inversion procedure also yields a false dependence of the excitation of the internal modes of the co-product on the CM scattering angle (or LAB speed). More internal excitation of the co-product is observed in the sideways direction than in the extreme forwards and backwards directions, as is clearly seen in the inverted ethyl internal energy data shown in Figure 4.6, which is plotted as a function of CM scattering angle. Similar behaviour was observed previously using this analysis method by Zare and co-workers [151, 206], as also shown in Figure 4.6.

In summary, the inversion analysis has the following limitations: (i) the assumption of a delta function in the kinetic energy release distribution is generally unrealistic; (ii) the returned CM angular scattering distributions are biased away from the extreme forward and backward directions; and, (iii) the internal energy of the co-product exhibits an artificial dependence on scattering angle.

Legendre Moment Fitting Using a Fixed f_{t}

Fitting of the Legendre moments extracted from the images using basis functions obtained assuming a delta function in the fractional kinetic energy release, f_{t}, allows some of the problems with the direct inversion analysis to be overcome. In these fits, it is assumed that the fixed f_{t} value is independent of scattering angle. Fits to the experimental data and the returned CM angular scattering distributions are shown in Figure 4.8 for f_{t} values ranging from 1.0 to 0.6. These data are compared to the full analysis, shown in the bottom panels of the figure, where a *distribution* in kinetic energy release values is allowed. The basis functions used in all the fits allow for the finite instrument resolution and molecular beam temperature; the fits are performed simultaneously to both the $L = 0$ and $L = 2$ Legendre moments of the ion image. It should be noted that the CM angular scattering distribution returned from the fit where $f_{\mathrm{t}} = 1.0$ is very similar to that obtained using the inversion method in Section 4.3.2. This suggests that the inclusion of the molecular beam temperature and the instrument resolution function in the basis set generation is not critical to the correct analysis.

As can be seen from Figure 4.8, a significantly better fit to the data is produced

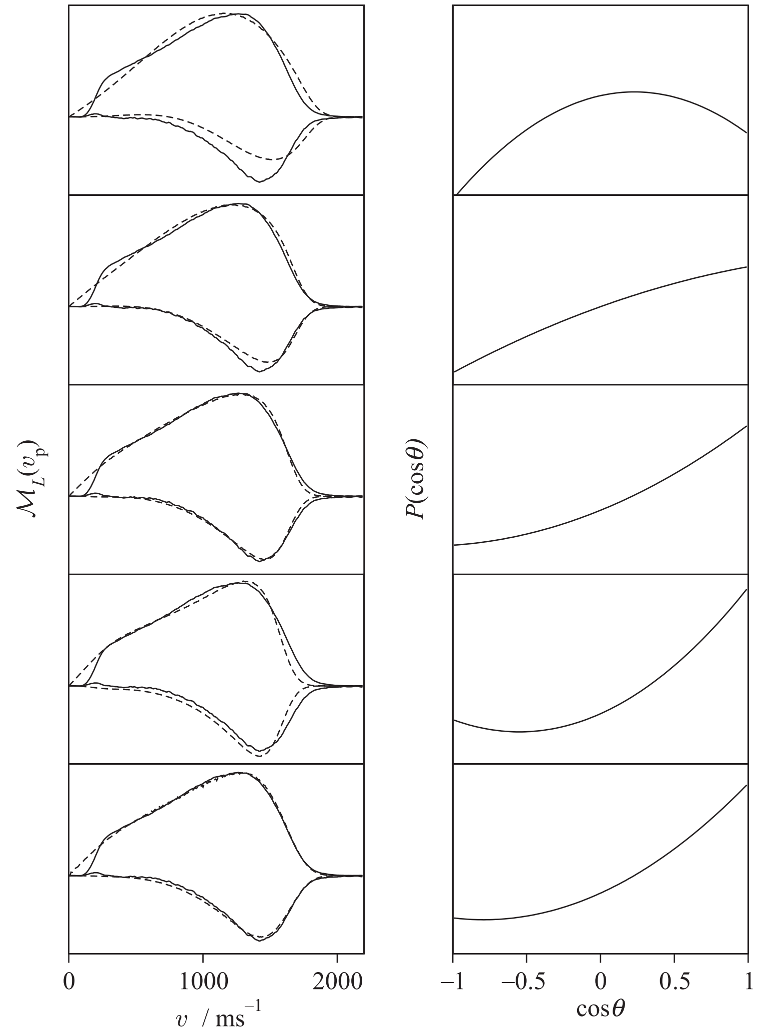

Figure 4.8: Dependence of the fits to the Legendre moments (left) and the returned CM angular scattering distributions (right) on the fixed single value for f_t (top four pairs of panels). From the top the fixed f_t values used were 1.0, 0.8, 0.7 and 0.6 and the returned relative χ^2 values were 30, 5, 2 and 12, respectively. The χ^2 values have been normalised to that obtained in the bottom row, which shows the fit and CM angular scattering distribution obtained when the data were analysed allowing a distribution of f_t values. In this case, the mean fractional kinetic energy release was $\langle f_t \rangle = 0.69$ (see Table 4.1). For all sets of data, the basis functions used in the fits allowed for the speed resolution of the apparatus, and employed a beam temperature of 50 K. The data are for HCl($v' = 0, j' = 2$).

from the full analysis than when fixed f_t values are used. Relative χ^2 values for each of the fits are given in the figure caption. When f_t is fixed to a single value, the best fit to the data is found when $f_t \approx 0.7$. This is very close to the mean kinetic energy release, $\langle f_t \rangle = 0.69$, obtained from the full analysis of the data. The CM angular scattering distributions obtained in these two cases are almost indistinguishable, demonstrating that although the best fits to the data are obtained using a distribution of kinetic energy releases, the CM angular scattering distribution can be returned reliably in this case by optimization of the fixed value of f_t employed in generating the basis functions.

4.3.3 Full Legendre Moment Fitting Analysis

The Legendre moment fitting analysis used in this Section allows for the *distribution* of product CM velocities arising from population of different internal quantum states in the undetected ethyl co-product. This analysis relies on fitting the Legendre moments of the experimental images using a set of basis functions generated in moments of both the CM angular scattering and kinetic energy release distributions.

The Number of Moments

An important issue when fitting the Legendre moments of the images is the number of moments in CM scattering angle and kinetic energy release used, since this dictates the overall angular and energy resolution of the experiment. The dependence of the CM angular scattering and kinetic energy release distributions obtained from the full analysis on the number of moments used for each distribution is shown in Figure 4.9. The error bars shown on the data are the result of the Monte Carlo analysis detailed in Section 3.4.7, and reflect generous uncertainties in the fitting procedure. The truncation point for the number of basis functions used is determined by observing the dependence of χ^2 on the number of fitting coefficients employed. In the present case, χ^2 did not decrease by a significant amount with inclusion of more than three moments in the CM angular scattering distribution or with more than five moments

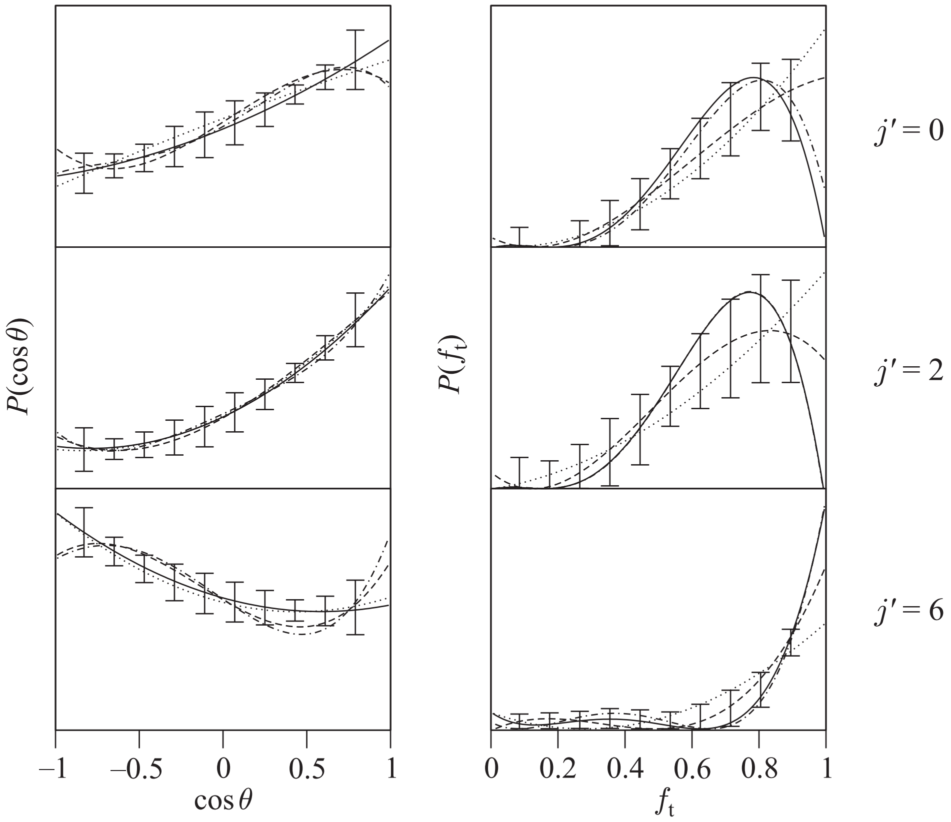

Figure 4.9: The dependence of the returned CM angular scattering (left) and kinetic energy release (right) distributions on the number of moments employed. From the top, the data are for HCl ($v' = 0$,$j' = 0$, 2 and 6). The solid lines represent fits to the data using 3 moments in the CM angular scattering distribution and 5 moments in the kinetic energy release distribution. The other lines are fits with basis sets of dimension (n,m)=(3,3) ($\cdots$), (4,4) (- - -) and (5,5) ($- \cdot - \cdot$) (see Equation 3.51).

in the kinetic energy release distribution. The returned distributions are, however, remarkably consistent as the number of moments used is varied. The fact that the returned fits to the data are not significantly improved when the number of moments is increased above these values demonstrates that the experiment is not sensitive to features with more structure than those which can be generated using three or five moments. The resolution of the experiment is thus defined by the number of moments that can be extracted reliably from the data. Note that the assumption of a delta function in kinetic energy release used in the inversion analysis is not only physically unrealistic for this system, but also implies an infinite energy resolution.

Full Legendre Moment Fits

The zeroth and second order Legendre moments obtained for each HCl($v' = 0$) rotational quantum state investigated, and the fits to those moments using the full Legendre moment analysis, are shown in Figure 4.10. The complete set of CM angular scattering and kinetic energy release distributions returned from the fits are shown in Figure 4.11. A steady trend from forwards scattering of low HCl rotational states, to more isotropic, but backwards peaking, scattering of high rotational states can be seen in the CM angular scattering distributions (left-hand panels). This shift towards backwards scattering with increasing HCl rotational excitation is in agreement with the previous work of Zare and co-workers [151], although with the present analysis, all of the CM angular distributions are more forward scattered than those previously reported (*cf.* Figures 4.11 and 4.4). The kinetic energy release distributions are shown in the right-hand panels of Figure 4.11. There is an overall trend towards higher kinetic energy release with higher HCl rotational states, but the returned kinetic energy release distributions are remarkably consistent. The f_{t} values shown on the x axes in Figure 4.11 refer to the fractional energy release for the specific HCl quantum state in question. The mean values obtained from these data, $\langle f_{\mathrm{t}} \rangle$, corrected for the HCl($v' = 0$,$j'$) rotational energy, are shown in Table 4.1. The mean internal energy in the ethyl fragment decreases slightly with increasing HCl rotational state. A weighted mean over all populated HCl rotational quantum states gives an overall average fraction of available energy in internal excitation of the ethyl, $\overline{\langle f_{\mathrm{int}}(\mathrm{C_2H_5}) \rangle}$, to be ~ 0.22. The weights for each quantum state used in calculating this average were taken from the HCl($v' = 0$,j') rotational populations determined previously by Zare and co-workers [151] (see Figure 4.1). Average energy disposal data obtained from on-the-fly *ab initio* trajectory calculations by Rudić *et al.* [205] are also given in Table 4.1, and are in excellent agreement with the current results.

A 2D contour map and the corresponding 3D 'wireframe' plot of the total product flux as a function of CM scattering angle and HCl speed, $P(w, \theta_{\mathrm{t}})$, are shown in

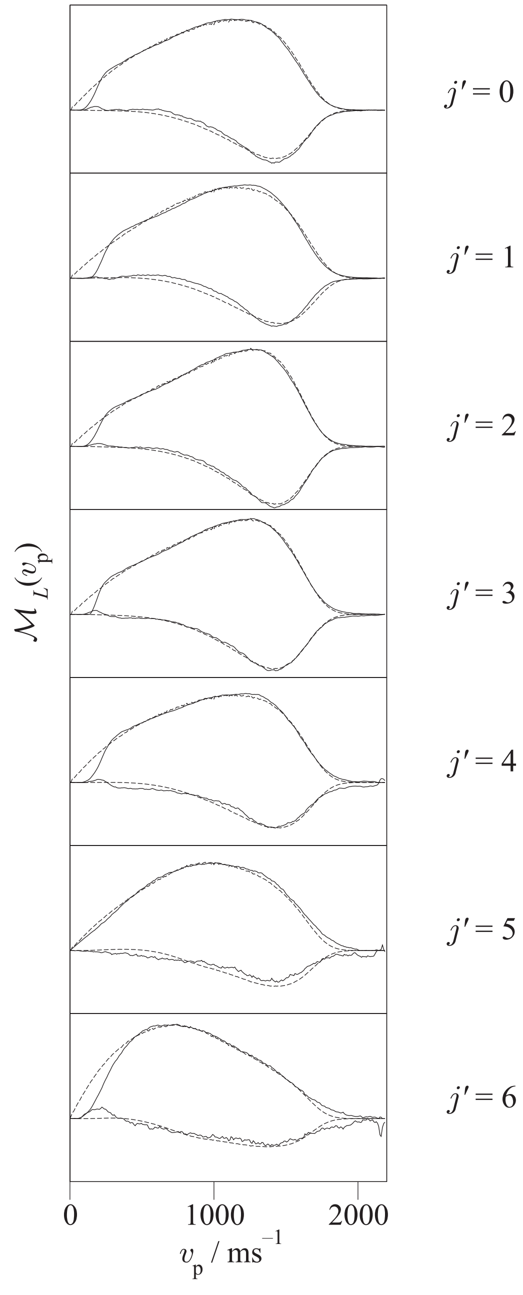

Figure 4.10: Zeroth and second order Legendre moments (—), and fits to those moments (- - -) for HCl($v' = 0$,$j' = 0$) (top) through to HCl($v' = 0$,$j' = 6$) (bottom). The fits were performed using basis function sets with three moments in the CM angular scattering distribution and five moments in the kinetic energy release distribution. The very low speed section of the moments ($v_p < 255\,\text{ms}^{-1}$) was not included in the fits, as discussed in Section 2.10.3.

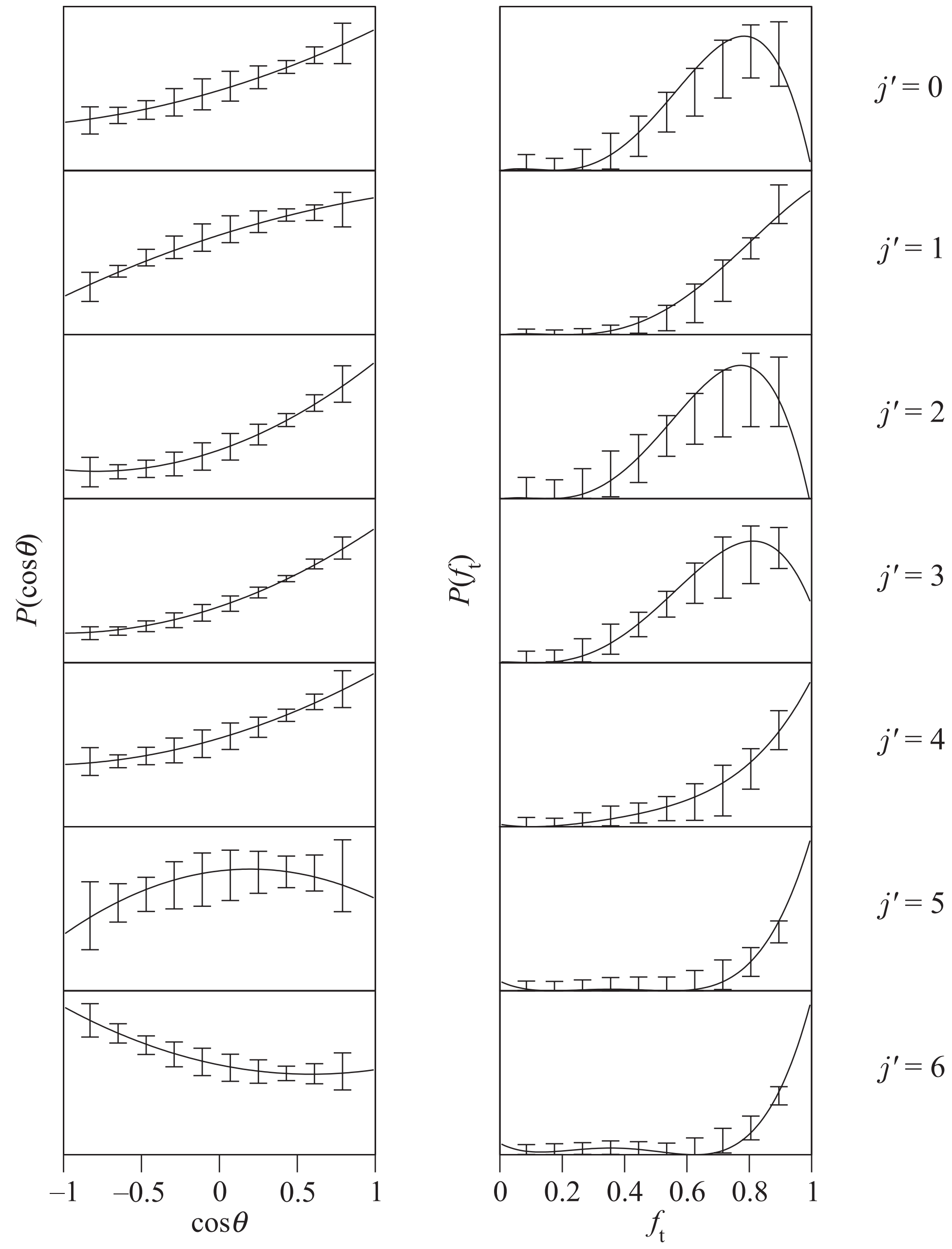

Figure 4.11: Returned CM angular scattering (left) and kinetic energy release (right) distributions for HCl($v' = 0$,$j' = 0$) (top) through to HCl($v' = 0$,$j' = 6$) (bottom). Error bars represent 2σ errors resulting from statistical errors in the fits. Note that in the right-hand panels, the f_t scale refers to the state-specific fractional kinetic energy release, which does not include the rotational energy in the HCl product (see Table 4.1).

Table 4.1: HCl($v' = 0, j'$) state-resolved, and state-averaged energy disposal data for the Cl + C_2H_6 reaction. The data have been obtained assuming a mean available energy of 2875 cm^{-1}. The errors on the state-resolved $\langle f_t \rangle$ values are typically ±0.05. The averaging over rotational state was performed using the HCl($v' = 0$) rotational population distribution obtained by Zare and co-workers [151]. HCl($v' = 1$), which is only just energetically accessible, has been shown previously to be produced in negligible quantities [151]. The data are compared to the theoretical fractional energy partitioning calculated by Rudić *et al.* [205] for the system with 2695 cm^{-1} available energy.

HCl($v' = 0, j'$)	f_{rot}(HCl)	f_{vib}(HCl)	$\langle f_{\mathrm{t}} \rangle$	$\langle f_{\mathrm{int}}(\mathrm{C_2H_5}) \rangle$
0	0.00	—	0.72	0.28
1	0.01	—	0.80	0.19
2	0.02	—	0.69	0.29
3	0.04	—	0.70	0.26
4	0.07	—	0.75	0.18
5	0.11	—	0.79	0.10
6	0.15	—	0.70	0.15
Average	0.02	—	0.76	0.22
Theory[a]	0.03	−0.03[b]	0.78	0.21

[a] Ref. [205]

[b] This negative value arises from the classically computed vibrational energy being slightly lower than the quantum mechanical zero point energy associated with the HCl molecule.

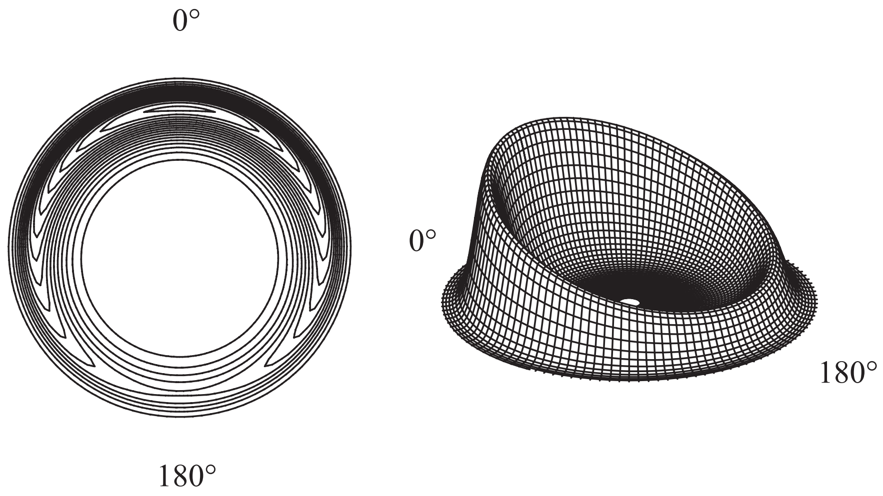

Figure 4.12: Contour map and 'wireframe' plot of the total product velocity-angle flux averaged over HCl rotational state using the rotational populations reported by Zare and co-workers [151]. The plots were obtained using the results shown in Figure 4.11.

Figure 4.12. These plots were generated using the CM angular scattering and kinetic energy release distributions shown in Figure 4.11, using the same contribution from each HCl rotational quantum state as above. The contour map therefore mimics the data that would be obtained from a crossed molecular beam experiment without product quantum state resolution.

4.4 Discussion

The results of new velocity-map ion imaging photoloc experiments were reported in the previous Section for the reaction of Cl atoms with ethane. Product rotational state resolved CM angular scattering distributions and kinetic energy release distributions were obtained for HCl($v' = 0$,$j' = 0$–6) using a basis function fitting analysis of the Legendre moments of the ion images.

4.4.1 Angular Scattering Distributions

The CM angular scattering distributions obtained from the ion images show a clear dependence on the HCl rotational quantum state probed: HCl products formed in the lowest rotational levels are predominantly forward scattered, with a shift towards isotropic scattering for intermediate rotational excitation of the HCl, and more backward peaked scattering for the HCl products formed in the highest rotational quantum states.

Subsequent to completion of the work presented here, Toomes and Kitsopoulos reported the extension of the technique of ‘crossed’ parallel beams [39, 217] combined with velocity-map ion imaging, previously used by Suits and co-workers to study the reactions of O(^{3}P) with alkanes [75], to the rotational state resolved detection of the HCl($v' = 0$,j') products of the reaction of Cl with ethane at 0.24 eV [77, 78]. In these experiments, ethane and Cl_2 were entrained in two separate, unskimmed parallel molecular beams, with the former beam located on the ion imaging TOF axis and the latter beam located slightly off the TOF axis. Both nozzles were mounted on the repeller plate of the velocity mapping ion optics. A small percentage of the Cl atoms produced by 355 nm photolysis of Cl_2 in the off-axis molecular beam travelled towards, and intersected, the on-axis ethane beam. The HCl($v' = 0$,$j' = 1$–5) products of the ensuing reaction were then detected *via* (2+1) REMPI at ∼ 240 nm and velocity-map imaged. Note that, due to the nature of the chlorine atom ‘beam’ produced in these experiments, the energy and angular resolutions are relatively low compared to those achievable using single beam photoloc or crossed molecular beam experiments. CM angular scattering distributions were extracted from the resulting images by direct integration of the raw data over velocity. It should be stressed that this simple method includes no density-to-flux transformation, and thus does not take into account the differing sensitivities to forward and backward scattered products or the speed distribution of the Cl atoms; for these factors to be allowed for requires the use of forward convolution methods [75].

The CM angular scattering distributions returned from the ‘crossed’ parallel beam experiments described above [77, 218] are compared with the results of the present work in Figure 4.13. The excellent agreement between the CM angular scattering distributions returned from the two studies strongly supports the reliability

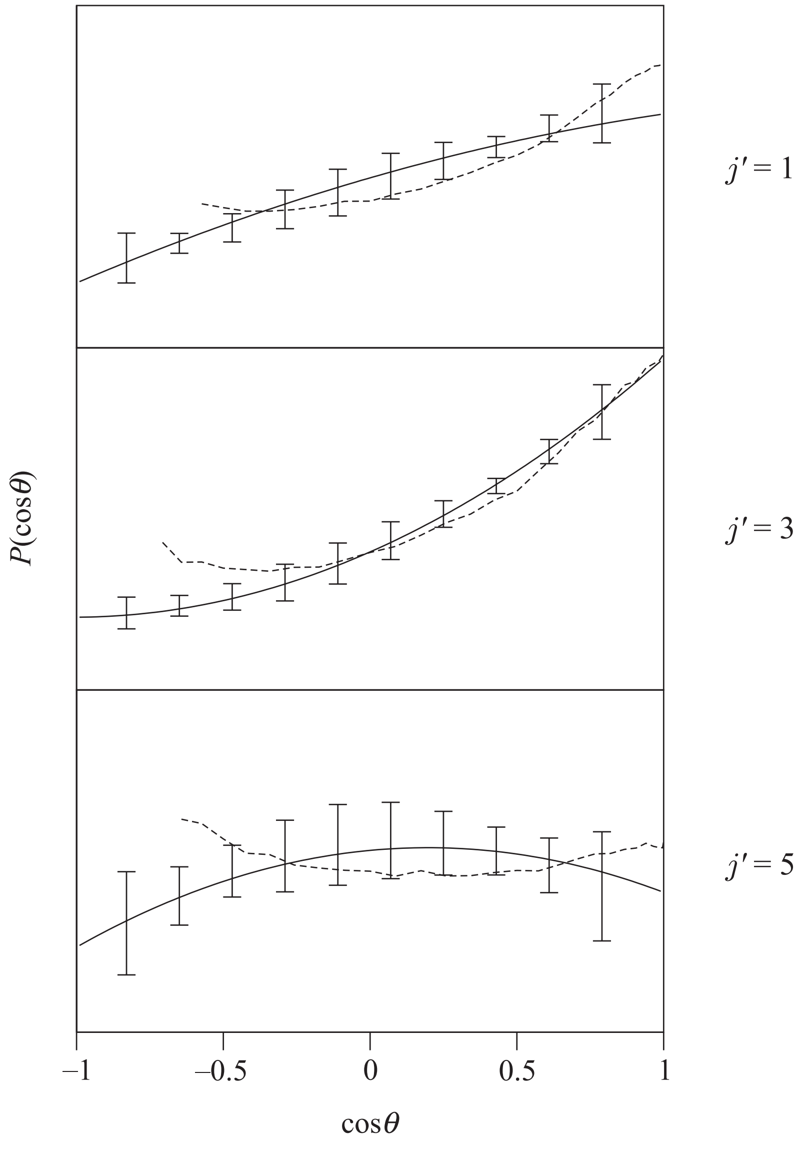

Figure 4.13: Comparison between the CM angular scattering distributions obtained in the present study (—) and those obtained from the 'crossed' parallel beam experiments of Toomes and Kitsopoulos (- - -) [77, 218]. From top to bottom, data are shown for HCl($v' = 0$,$j' = 1$, 3 and 5).

of both sets of results. Moreover, Toomes and Kitsopoulos also concluded that a significant fraction of the available energy is deposited into internal excitation of the ethyl radical [77], which is also in excellent accord with the present findings.

The observed CM angular scattering distributions and the very cold HCl rotational population distribution measured by Zare and co-workers [151] and Orr-Ewing and co-workers [207] may be explained using an impact parameter-based model. *Ab inito* calculations show that the transition state adopts a near-linear Cl–H–C configuration with an energy slightly below that of the reactants [130, 202–205], and that there are shallow van der Waals wells in both the entrance and exit channels [203, 205]. Notwithstanding the decisive role played by the shallow van der Waals well in the reactant channel of the related Cl + H_2/HD reactions [219], the very shallow van der Waals well in the entrance channel of the Cl + C_2H_6 reaction is not anticipated to impact upon the dynamics, and the reaction should therefore be direct [205]. For products of a direct reaction to be forward scattered, as observed in the Cl + C_2H_6 reaction, they must be formed in high impact parameter collisions. These high impact parameter collisions may be indicative of a mechanism with a loosely constrained transition state or of the reaction taking place *via* a more peripheral mechanism [220]. The degree of constraint on the transition state geometry relates to the magnitude of the internal angle of the cone of acceptance for attack of the Cl atom on the C–H bond, which depends on the barrier height and its variation with Cl–H–C angle. Deviations of the Cl–H–C framework from 180° depend upon the steepness of the bending potential of the transition state; the vibrational frequencies of the transition state bending modes thus indicate the ease of deformation from linearity. Calculated bending mode frequencies for the Cl–H–C_2H_5 transition state are ~ 125 cm^{-1} and ~ 175 cm^{-1} [130, 202]. These values are relatively low, consistent with a broad bending potential, and an open cone of acceptance for the reaction with regards to the bending coordinate. The high thermal rate constant for the reaction (discussed in Section 4.2.1) is in accordance with an open cone of acceptance and also with the predominantly forward scattering observed. However, the high thermal rate constant is also consistent with the reaction taking place *via* a peripheral mechanism [220]. This mechanism is characterised by a preferred reactivity for collisions that are not along the lines of the centre-of-masses of the approaching reactants (i.e., the opacity function of the reaction peaks at large impact parameters), and that yield products that are forward scattered. That the hydrogen atoms in ethane are all located away from the centre-of-mass, the transition state is calculated to be nearly collinear along Cl–H–C, and the HCl products are seen to be forward scattered, are all supporting factors for a peripheral mechanism for the Cl + C_2H_6 reaction.

If product formation is associated with a low impulsive release of energy into the HCl products and there is either a weak steric restriction on the approach of the Cl atom to H–C bond or a more peripheral-type mechanism with a collinear transition state, the observed dynamics of the Cl + C_2H_6 reaction can be rationalised in terms of the opacity function of the reaction (see Figure 4.14) [111, 151, 206, 221]. Non-impulsive reactions at high impact parameters give rotationally cold HCl products scattered in the forwards and sideways directions. Backwards scattered products are formed in reactions with lower impact parameters, which could be associated with a more impulsive-type mechanism, giving higher HCl rotational excitation.

4.4.2 Energy Partitioning

The kinetic energy release distributions returned from the basis function fitting analysis show that on average 22% of the available energy is channelled into the internal modes of the ethyl radical. Based on measurements of the speed-dependent translational anisotropy parameter, the fraction of available energy in internal modes of the ethyl radical was previously estimated by Zare and co-workers to be 7 ± 4% [151]; this value is significantly lower than that found in the present study. The very low internal excitation of the ethyl product determined by Zare and co-workers forms the basis of their argument that the ethyl fragment is essentially a spectator in the reaction, and provides the justification for their data analysis method, which

Figure 4.14: Proposed model for the mechanism of the reaction of Cl with C_2H_6. Reaction occurring at a range of impact parameters is indicated by the 'target'. Low, medium and high impact parameter collisions result in forward, sideways and backwards scattering of the HCl products, respectively. Adapted from Refs. [111, 221]. Note that the shown orientation of the C_2H_6 molecule is arbitrary; in order to maintain the preferred collinearity of Cl–H–C in the transition state, the precise orientation may be different for the three types of collision.

is based on the assumption that the reaction is well approximated as a 'three-atom' system.

Following publication of the results of the current investigation, Rudić *et al.* reported their results of a quasi-classical trajectory study on the Cl + C_2H_6 reaction. *Ab initio* potential energies and gradients were computed on-the-fly using restricted and restricted-open-shell Hartree–Fock (HF) self-consistent field wavefunctions with the 6-31G basis set (HF/6-31G) at the geometries through which the trajectories passed. Trajectories were started from the transition state with $\sim$0.35 eV available energy (approximately the total energy available in the present study) and were propagated to separated products. The transition state was chosen to have zero-point level excitation of the vibrational modes transverse to the reaction coordinate, with random initial displacements and velocities in these modes. The remaining available energy was placed into kinetic energy along the reaction coordinate to-

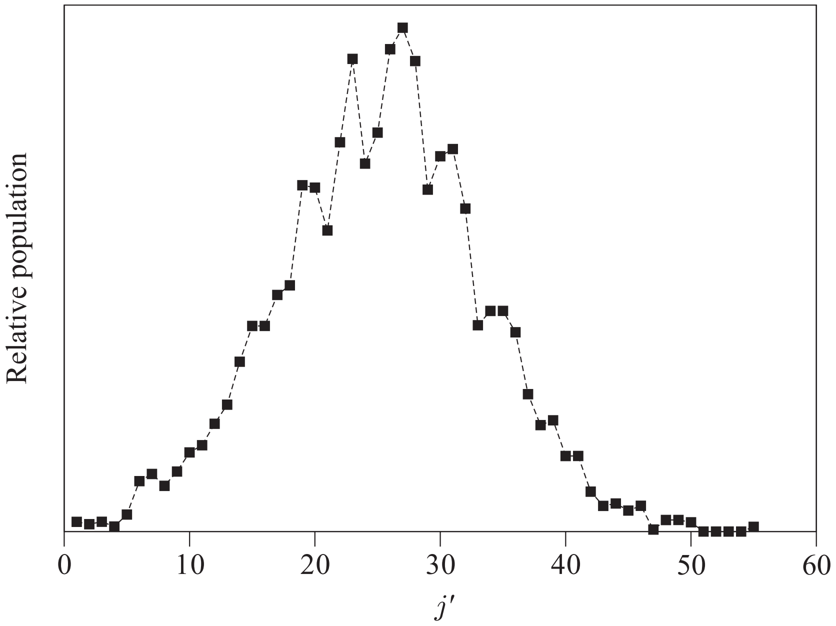

Figure 4.15: Nascent rotational state population distribution for ethyl products of the reaction of Cl with C_2H_6 returned from quasi-classical trajectory calculations by Rudić *et al.* [205].

wards products. It should be noted that this choice of initial conditions samples only the outcome of low impact parameter, low orbital angular momentum collisions, and thus the calculations are not fully representative of the experiments. The HCl rotational population distribution obtained using this on-the-fly approach was seen to be hotter than those determined experimentally (see Figure 4.1): the theoretical distribution peaked broadly at $j' = 2$, with a long tail of low population in high j' levels. The calculations also yielded the ethyl radical rotational state population distribution shown in Figure 4.15. The distribution was obtained using an analysis that rejected HCl co-products formed in high rotational states ($j' > 6$) and is seen to be roughly Gaussian in shape, with the mean populated rotational state being $j' = 25$. This distribution corresponds to 21% of the available energy being channelled into internal energy of the C_2H_5 fragment [205], in excellent agreement with the results of the present study (see Table 4.1). The present findings are thus strongly supported by both the theoretical calculations of Rudić *et al.* [205] and the experimental results of Toomes and Kitsopoulos [77].

Crossed molecular beam studies on the reaction of chlorine with propane [222] and pentane [223] have been carried out by Suits and co-workers, and although direct comparison with the present data is not possible, it is noteworthy that these studies reveal significant internal excitation of the products. In the case of Cl + C_3H_8, it is known from the REMPI experiments of Koplitz and co-workers [224] and Varley and Dagdigian [214, 215] that the HCl products of this reaction carry away little internal excitation; the interpretation of the crossed molecular beam experiments must therefore be that the internal modes of the propyl products are excited.[5] This conclusion is in broad agreement with the present findings for the reaction of chlorine with ethane. Since the ethyl radical is produced with significant internal excitation, it must be concluded that it does not behave as a spectator.

The kinematics of the reaction are those of a light atom abstraction, which favour the transfer of kinetic energy from reactants to the products, and the release of the reaction exothermicity into the HCl internal degrees of freedom. The experimentally determined absence of internal excitation in the HCl products has been ascribed to a modest energy release from a collinear Cl–H–C_2H_5 transition state (i.e., non-impulsive transfer of the H atom) [151].

4.4.3 Internal Excitation of the Ethyl

Two limiting mechanisms can be considered for the excitation of the ethyl products, producing either predominantly rotationally, or predominantly vibrationally, excited ethyl radicals.

---

[5] As with the experiments on Cl + C_2H_6 by Zare and co-workers, the photoloc study by Varley and Dagdigian on the reaction of Cl with partially deuterated propane [215] assumed that the propyl co-products were formed internally cold. For this reason, the CM angular scattering distributions derived from that study were probably artificially biased in the backwards direction [215, 222].

Vibrationally Excited Ethyl

Energy release into vibrational modes of the ethyl radical may be associated with the relaxation of the –CH_2 moiety in the nascent ethyl radical from the pyramidal geometry adopted in the transition state [202–204], to the more planar geometry of the free ethyl radical [179, 202, 225, 226]. The extent of deformation from planarity of the –CH_2 in the C_2H_5 fragment is measured using the dihedral angle. This is defined as the angle between the plane containing the CH_2 and the plane containing the C–C bond parallel to a line between the two H atoms of the CH_2. The lowest energy conformation of the ethyl radical has a dihedral angle of $\sim 10°$, with the CH_3 in a 'staggered' conformation [225, 227, 228]; the dihedral angle in the collinear transition state is $\sim 58°$ [205]. The change in geometry on going from the transition state to the free ethyl could therefore give rise to excitation of the out-of-plane –CH_2 rocking mode. It is possible to estimate the maximum excitation generated by this relaxation from the Franck–Condon overlap between the bending wavefunctions of the transition state and the ethyl products. Approximating the rocking vibration to be a harmonic oscillator with potential energy

$$V(\phi) = \frac{1}{2}k\phi^2, \tag{4.3}$$

where ϕ is the dihedral angle in the ethyl fragment defined above and k is the vibrational force constant, gives a Hamiltonian of the form

$$\hat{H} = -\frac{\hbar^2}{2I}\frac{\mathrm{d}^2}{\mathrm{d}\phi^2} + \frac{1}{2}k\phi^2, \tag{4.4}$$

where I is the effective moment of inertia of the –CH_2 moiety. Solution of the Schrödinger equation associated with this Hamiltonian gives

$$E_v = (v + \tfrac{1}{2})h\omega \quad \text{where} \quad \omega = \frac{1}{2\pi}\sqrt{\frac{k}{I}} \quad ; \quad v = 0, 1, 2, \ldots \tag{4.5}$$

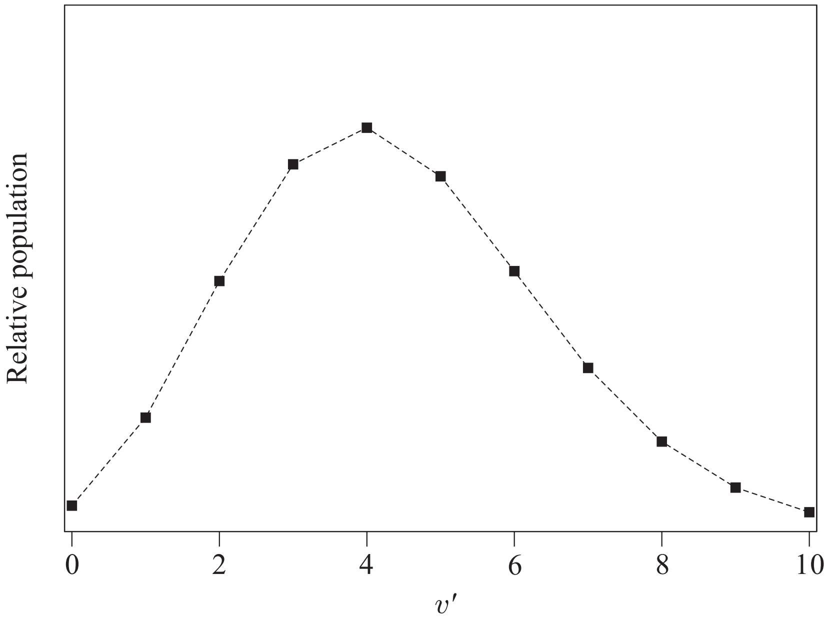

Figure 4.16: Ethyl vibrational population distribution predicted using the Franck–Condon overlap model.

From *ab initio* calculations by Johnson and Sears [228], the force constant, k, of the rocking vibration is estimated to be $\sim 9 \times 10^{-20}$ J rad^{-2}. The rocking vibrational frequency has been measured by Sears *et al.* to be 528.1 cm^{-1} [226, 229], from which the effective moment of inertia of the –CH_2 is estimated to be 9×10^{-48} kg m^2. If the rocking force constants are assumed to be similar in the transition state and the free ethyl radical, the Franck–Condon overlap model predicts significant vibrational excitation of the rocking mode of the –CH_2 unit. The vibrational state population distribution predicted using this model, shown in Figure 4.16, peaks broadly at $v = 4$. Since only ~ 630 cm^{-1} of the available energy is channelled into internal excitation of the ethyl radical, this predicted level of excitation is unrealistically high. However, lower levels of excitation could be generated if there was a more gradual relaxation of the geometry of the CH_2 moiety from the transition state to the products.

Rotationally Excited Ethyl

Consider now the possibility that the observed ethyl internal excitation is rotational in origin. Assuming the ethyl radical is a rigid asymmetric top with a rigid 'frame' (i.e., the C–CH_2 backbone is fixed—the rigid top–rigid frame approximation), the average rotational constant about the b and c axes, $\bar{B} = 0.5(B + C)$, is $\sim 0.729\ \text{cm}^{-1}$ [226, 230, 231]. The maximum rotational state accessible if all the observed available energy deposited into internal modes of the ethyl is found as end-over-end rotation is thus $j_{\text{C}_2\text{H}_5} \simeq 30$. This level of rotational excitation may be associated with impulsive release of the exothermicity of the reaction along the axis of the C–H bond in the transition state. Since this axis does not pass through the centre of mass of the ethyl fragment, such an impulse would lead to a torque on the nascent ethyl radical. The total angular momentum, $\mathbf{J}$, of the reaction is given by

$$\begin{aligned}\mathbf{J} &= \mathbf{j}_{\text{Cl}} + \mathbf{j}_{\text{C}_2\text{H}_6} + \mathbf{L} \\ &= \mathbf{j}_{\text{HCl}} + \mathbf{j}_{\text{C}_2\text{H}_5} + \mathbf{L}' + \mathbf{L}'_{\text{IMP}},\end{aligned} \tag{4.6}$$

where $\mathbf{j}_\text{X}$ is the total (rotational plus electronic) angular momentum of species X, $\mathbf{L}$ is the orbital angular momentum of the reactants, $\mathbf{L}'$ is the orbital angular momentum of the products and $\mathbf{L}'_{\text{IMP}}$ is the orbital angular momentum associated with the impulsive release of energy along the axis of the breaking C–H bond. Since the rotational angular momentum of the ethane is nearly zero due to collisional cooling in the molecular beam, the electronic angular momentum of $\text{Cl}(^2\text{P}_{3/2})$ ($\mathbf{j}_{\text{Cl}} = 3/2$) may be neglected, and the rotational angular momentum of the HCl products has been measured to be very low,

$$\mathbf{J} \simeq \mathbf{L} = \mathbf{j}_{\text{C}_2\text{H}_5} + \mathbf{L}' + \mathbf{L}'_{\text{IMP}}. \tag{4.7}$$

For the kinematics of a light atom transfer reaction, where $\mathbf{L} \to \mathbf{L}'$, this reduces to

$$\mathbf{j}_{\text{C}_2\text{H}_5} \simeq -\mathbf{L}'_{\text{IMP}}. \tag{4.8}$$

The magnitude of the rotational angular momentum of the ethyl radical, $j_{\mathrm{C_2H_5}}$, associated with an impulse release of the reaction exothermicity may thus be estimated from the magnitude of the orbital angular momentum, L', using

$$\begin{aligned} L' &= \mu' v' b' \\ &\simeq \hbar\sqrt{j_{\mathrm{C_2H_5}}(j_{\mathrm{C_2H_5}}+1)}, \end{aligned} \tag{4.9}$$

where μ' is the reduced mass of the products, v' is the velocity imparted to the –CH_2 end of the ethyl radical as a result of the impulse, and b' is the distance of the breaking C–H bond from the centre of mass of the ethyl product. Using the transition state geometry obtained from the recent *ab initio* calculations of Fernández-Ramos *et al.* [203], ethyl rotational angular momenta of $\sim 22\hbar$ can be generated from an impulsive release corresponding to the reaction exothermicity. The results of the on-the-fly *ab initio* trajectory calculations by Rudić *et al.* [205] suggest that the bulk of the ethyl internal excitation may be accounted for by rotation. The ethyl product rotational state population distribution computed is shown in Figure 4.15, and is seen to peak broadly at $j \sim 25$. In the limit of the total energy in ethyl rotation calculated from this distribution being found as rotation about the b and c axes of the ethyl radical only, approximately 96% of the energy observed to be channelled into internal excitation of the ethyl co-fragment is found as rotation. Although the considerations made here are mostly qualitative, they are in agreement with these recent theoretical predictions.

4.5 Summary

The HCl($v' = 0$) products of the reaction of Cl with ethane at 0.24 eV are formed rotationally cold, with the $j' = 1$ state maximally populated. Rotational state resolved angular scattering and kinetic energy release distributions have been determined from velocity-map ion images for HCl($v' = 0, j' = 0$–6) products using the Legendre moment analysis method. The angular scattering distributions show a steady trend from forward scattering at low j' to more isotropic, but backward peaking, scattering at high j'. The kinetic energy release distributions obtained show that around 22% of the available energy is channelled into internal excitation of the ethyl products, much more than that found in previous studies. Possible sources of this excitation have been discussed. Analyses previously used to extract angular scattering distributions for this, and similar Cl + alkane reactions, made the assumption that the alkyl radical plays only a spectator role in the reaction and carries away none of the available energy; this has been shown to be invalid in the case of the present reaction. It is thus suggested that caution should be exercised when making this assumption, in either reduced dimensionality dynamics calculations or in analysis of experimental results, for this type of reaction in the future.

Chapter 5

The Dynamics of the Cl + n-C_4H_{10} Reaction at 0.32 eV

5.1 Introduction

A key feature of the reactions of chlorine atoms with alkanes containing more than two carbon atoms is the availability of more than one reaction pathway, namely abstraction of a hydrogen atom from a primary (1°), secondary (2°) or tertiary (3°) carbon atom. It is therefore important to have a detailed understanding of the differing propensities for reaction at these sites and the dynamics associated with them. The reaction of atomic chlorine with n-butane can proceed *via* two pathways:

$$\begin{aligned} \mathrm{Cl} + \mathrm{CH_3CH_2CH_2CH_3} &\longrightarrow \mathrm{HCl} + \mathrm{\dot{C}H_2CH_2CH_2CH_3} \\ &\qquad \Delta_\mathrm{r}H_0^\ominus = -8.4 \pm 2.1\,\mathrm{kJ\,mol^{-1}} \qquad (5.1) \\ &\longrightarrow \mathrm{HCl} + \mathrm{CH_3\dot{C}HCH_2CH_3} \\ &\qquad \Delta_\mathrm{r}H_0^\ominus = -23.1 \pm 2.1\,\mathrm{kJ\,mol^{-1}} \qquad (5.2) \end{aligned}$$

The considerably different exothermicities[1] of reactions 5.1 and 5.2 suggest that the dynamics of the competing reaction pathways may be investigated by quantum state

---

[1] Enthalpies of reaction calculated using D_0^0(H–Cl) = 427.64 ± 0.02 kJ mol^{-1} [177, 178], D_0^0(H–n-C_4H_9) = 419.2 ± 2.1 kJ mol^{-1} [232, 233] and D_0^0(H–s-C_4H_9) = 404.6 ± 2.1 kJ mol^{-1} [234].

selective measurements of the scattering of the HCl(v',j') products.

Whilst a considerable amount of work has been carried out to determine the kinetics of the reaction of chlorine atoms with *n*-butane, to date the dynamics of the two reactive pathways have not been examined. Previous work on the kinetics of the title reaction, and dynamics studies carried out on the reactions of atomic chlorine with propane and heavier saturated hydrocarbons are discussed in the following Section.

5.2 Previous Work on the Cl + *n*-C_4H_{10} Reaction

5.2.1 Kinetics Studies

Structure activity relationships for the reaction of chlorine atoms with alkanes allow the prediction of reaction rates in systems for which no measurements are available, and can be calculated from known experimental kinetic data for large hydrocarbons. Many of the rate coefficients for the reactions of chlorine with these larger hydrocarbons have been measured relative to those for reaction with butane [182, 189, 235–241], resulting in the pursuit of increasingly accurate values for the absolute rate of the Cl + *n*-butane reaction. Direct measurements of the absolute rate constant employed similar techniques to those used in the kinetic studies of the Cl + C_2H_6 reaction outlined in Section 4.2.1. The results of the most recent of these studies [189, 191, 192, 242] are in good agreement with those determined using relative rate methods [184, 189, 191, 238]. The recommended value of the absolute rate coefficient, k, is $(2.05 \pm 0.07) \times 10^{-10}$ cm^3 molecule^{-1} s^{-1}, independent of temperature over the range 290–600 K [195]. In recent relative rate experiments using gas chromatographic product analysis, Sarzynski and Sztuba found a weak negative temperature dependence for abstraction of hydrogen atoms from a primary carbon atom, and a weak positive temperature dependence for abstraction from a secondary carbon atom over the temperature range of 295–470 K [184]. Fits to the data using the simple Arrhenius expression, $k = A\,\mathrm{e}^{-E_\mathrm{a}/RT}$, give pre-exponential factors

$A_\mathrm{p} = (7.3 \pm 0.2) \times 10^{-11}$ and $A_\mathrm{s} = (9.9 \pm 2.2) \times 10^{-11}\,\mathrm{cm}^3\,\mathrm{molecule}^{-1}\,\mathrm{s}^{-1}$ and activation energies of $(E_\mathrm{a}/R)_\mathrm{p} = 68\,(\pm 10)\,\mathrm{K}$ and $(E_\mathrm{a}/R)_\mathrm{s} = -106\,(\pm 75)\,\mathrm{K}$, where the subscript p and s refer to abstraction of primary and secondary hydrogens respectively. The differing temperature dependencies were proposed to arise from the formation of a weakly bound complex during abstraction of a secondary hydrogen atom. The overall rate coefficient at 298 K, determined as the sum of the rates for both reaction pathways, was found to be in good agreement with the recommended value [184].

A preference for abstraction of a hydrogen atom from secondary carbon atoms over primary carbon atoms was observed in the relative rate experiments carried out by Tyndall *et al.* [191] and Sarzynski and Sztuba [184]. In both experiments, 29% of the butyl products were found to result from abstraction of a primary hydrogen atom, and 71% from abstraction of a secondary hydrogen atom.

5.2.2 Transition States

The geometries of the transition states for the reaction of chlorine and bromine atoms with propane have been calculated by Bottoni and Poggi at the unrestricted Hartree–Fock and Møller–Plesset second-order perturbation (MP2) levels using the 6-31G* basis set [204]. The transition states were found to be nearly collinear for abstraction of either a primary or secondary hydrogen atom by both chlorine and bromine ($\angle$(X–H–C) = 177.1–179.8°, depending on the level of theory employed). In more recent calculations by Seetula at the MP2 level using the 6-31G(*d*,*p*) basis set and the frozen core approximation, the transition state for the abstraction of a primary hydrogen atom from *n*-butane by bromine was also found to be nearly collinear ($\angle$(Br–H–C)=173.5°) [243]. From the similarities in geometry of all five of these *ab initio* transition states, involving both chlorine and bromine, it seems likely that the abstraction of hydrogen atoms from primary and secondary carbon sites in *n*-butane by chlorine also proceed *via* nearly collinear transition states. The Cl + C_2H_6 reaction discussed in Chapter 4, in which the hydrogen atom may only be abstracted from a primary carbon site, has a similar exothermicity to that of the primary H atom abstraction pathway in the Cl + n-C_4H_{10} reaction and passes through a nearly collinear transition state. By virtue of these similarities between the two reactions, the dynamics of abstraction of a primary (and possibly secondary) hydrogen atom from n-butane are therefore anticipated to be closely related to those for H atom abstraction from ethane.

5.2.3 Dynamical Studies

Cl + C_3H_8

The two pathways available in the reaction of chlorine atoms with propane, and the associated exothermicities,[2] are shown below:

$$\mathrm{Cl} + \mathrm{CH_3CH_2CH_3} \longrightarrow \mathrm{HCl} + \dot{\mathrm{C}}\mathrm{H_2CH_2CH_3}$$
$$\Delta_r H_0^\ominus = -10.5 \pm 2.1\,\mathrm{kJ\,mol^{-1}} \tag{5.3}$$
$$\longrightarrow \mathrm{HCl} + \mathrm{CH_3}\dot{\mathrm{C}}\mathrm{HCH_3}$$
$$\Delta_r H_0^\ominus = -21.4 \pm 1.7\,\mathrm{kJ\,mol^{-1}} \tag{5.4}$$

Koplitz and co-workers investigated the site-specific chemistry of the Cl + propane reaction using the selectively deuterated propanes $CH_3CD_2CH_3$ and $CD_3CH_2CD_3$ [224]. Nascent product rotational spectra were obtained for the HCl and DCl using REMPI coupled with linear time-of-flight (TOF) mass spectrometry. A 1:1 mixture of Cl_2 and either $CH_3CD_2CH_3$ or $CD_3CH_2CD_3$ was co-expanded in a pulsed molecular beam. Reaction was initiated by photolysis of Cl_2 using 351 nm laser radiation to produce monoenergetic $Cl(^2P_{3/2})$ atoms and to give well-defined collision energies of 0.30 and 0.31 eV for reaction with $CH_3CD_2CH_3$ and $CD_3CH_2CD_3$ respectively. The $HCl(v' = 0)$ and $DCl(v' = 0)$ products were allowed to accumulate for 120 ns before detection *via* (2+1) REMPI at around 240 nm. For abstraction

---

[2] Enthalpies of reaction calculated using $D_0^0(\mathrm{H}\text{–}n\text{-}C_3H_7) = 417.1 \pm 2.1\,\mathrm{kJ\,mol^{-1}}$ [232, 233] and $D_0^0(\mathrm{H}\text{–}s\text{-}C_3H_7) = 406.3 \pm 1.7\,\mathrm{kJ\,mol^{-1}}$ [234].

of primary hydrogen atoms the observed HCl($v' = 0$) product rotational structure was reasonably well described using a Boltzmann distribution with a temperature of ∼ 70–100 K. HCl products arising from reaction at the secondary carbon atom were found to be slightly rotationally hotter. The yields of DCl products from abstraction of a primary or secondary D atom were found to be equal, despite the 3:1 ratio of available atoms (i.e., abstraction of a secondary D atom was seen to be three times as probable as abstraction of a primary D atom). The difference in reactivity was found to be lower for the HCl products, with 60% arising from abstraction of a primary H atom and 40% from abstraction of a secondary H atom (i.e., allowing for the statistical abundance of primary and secondary carbon sites, abstraction of a secondary H atom was seen to be twice as likely as abstraction of a primary H atom). Contrary to these findings, a kinetics study by Tyndall *et al.* on the Cl + C_3H_8 reaction at 298 K showed that 43 ± 3% of the products were observed to be produced from abstraction of H from a primary carbon atom and 57 ± 3% from the secondary carbon atom [191]. The opposing conclusions of the two studies were speculatively attributed to the differing kinetic energy distributions of the chlorine atoms employed: Cl_2 photolysis produced translationally 'hot' Cl atoms, whereas thermalized Cl atoms were used in the kinetic study. It should be noted, however, that abstraction by chlorine of H and D atoms from the different carbon sites in the $CH_3CD_2CH_3$ and $CD_3CH_2CD_3$ molecules have different exothermicities to those for abstraction from the fully deuterated or fully hydrogenated propanes; the conclusion drawn regarding the dynamics and relative reactivities of the primary and secondary carbon sites in the Cl + C_3H_8 reaction derived from this study should therefore be viewed with some caution.

Similar dynamics experiments have been carried out on the reaction of chlorine atoms with C_3H_8 and $CD_3CH_2CD_3$ by Varley and Dagdigian [214, 215]. In the case of reaction with undeuterated propane, Cl_2 and C_3H_8 were introduced into the interaction region of a linear TOF mass spectrometer through two pulsed valves mounted perpendicularly both to one other and to the time-of-flight axis. Owing to this configuration of the apparatus, initiation of the reaction by photolysis of the Cl_2 using 355 nm laser radiation resulted in a very broad, isotropic collision energy distribution that extended from 0.0 to 0.9 eV. Following a 100–200 ns delay, HCl($v' = 0$ and 1) products were detected *via* (2+1) REMPI in the wavelength range 238–247 nm. Rotational population distributions were obtained from the resulting spectra using linestrength factors determined experimentally by Rohlfing *et al.* [244] and Xie *et al.* [245]. The returned HCl($v' = 0$ and 1) rotational population distributions were seen to be cold, with the $j' = 1$ state maximally populated in both vibrational levels. From relative signal intensities, it was estimated that ~13% of the observed HCl products were formed in the $v' = 1$ vibrational state. As a result of the broad collision energy distribution, the two reaction pathways 5.3 and 5.4 could not be distinguished. Reduction of the intersection angle between the two pulsed valves from 90° to 20° yielded the much narrower collision energy distribution of 0.3 ± 0.15 eV for the Cl + $CD_3CH_2CD_3$ reaction [215, 216]. The energetics of this reaction are similar to those of the reaction with C_3H_8: $\Delta_r H_0^{\ominus} = -6\,\mathrm{kJ\,mol^{-1}}$ for abstraction of a D atom from a primary carbon atom of $CD_3CH_2CD_3$, whilst $\Delta_r H_0^{\ominus} = -22\,\mathrm{kJ\,mol^{-1}}$ for abstraction of an H atom from the secondary carbon atom [215]. HCl($v' = 1$) and DCl($v' = 1$) products were found to be formed in negligible quantities, reflecting the lower mean collision energy employed. The rotational population distributions obtained for the HCl($v' = 0$,j') and DCl($v' = 0$,j') products have been plotted as a function of rotational energy, E_{rot}, in Figure 5.1. Both distributions were found to be rotationally cold, although the HCl products of abstraction of the secondary H atoms were seen to be produced with higher rotational energies than the DCl products. From the relative populations of the $j' = 1$ rotational states, the ratio of the cross-sections for production of HCl($v' = 0$) and DCl($v' = 0$) was calculated to be 1.1 ± 0.2. Allowing for the 3:1 abundance of D versus H, abstraction of an atom in the secondary position was thus concluded to be favoured by a factor of 2.7 ± 0.5 over that for primary atoms. This was rationalised on the basis of a larger cone of acceptance about the linear Cl–H(D)–C transition state geometry for ab-

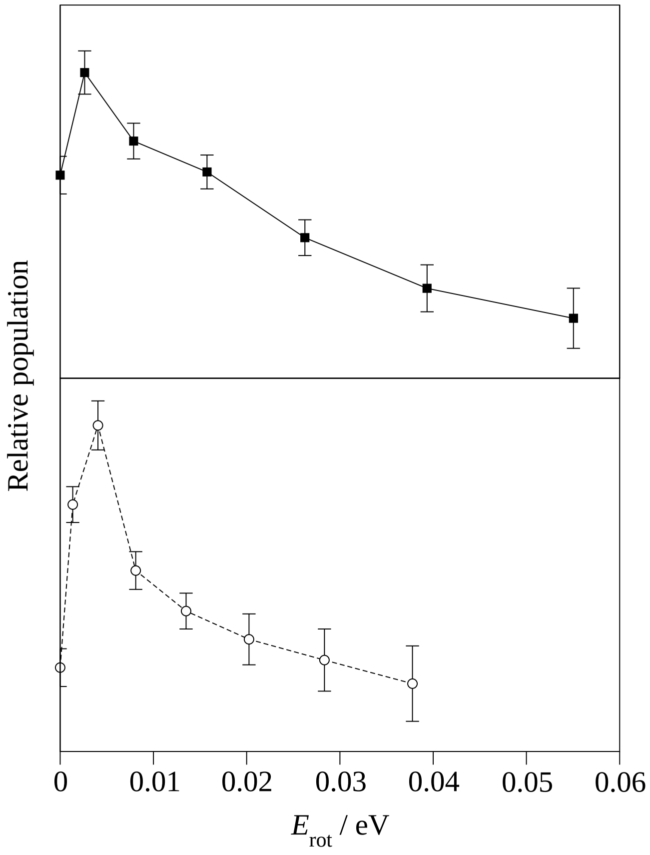

Figure 5.1: The nascent rotational population distributions obtained by Varley and Dagdigian for the HCl($v' = 0,j'$) (--■--) and DCl($v' = 0,j'$) (--○--) products of the reaction of Cl with $CD_3CH_2CD_3$ [215]. The distributions have been plotted as a function of rotational energy, E_{rot}, to aid comparison.

straction of a secondary atom than for abstraction of a primary atom. CM angular scattering distributions were extracted from the time-of-flight ion arrival profiles for the HCl($v' = 0,j' = 1$) and DCl($v' = 0,j' = 1$) products on the assumption of zero internal excitation of the alkyl co-product. Broad sideways scattering was thereby obtained for the DCl products arising from abstraction from a primary carbon atom, whereas the HCl products formed from abstraction from the secondary carbon atom were found to show more isotropic, but backward peaking scattering.[3]

Blank *et al.* have studied the reaction of chlorine with propane at a series of collision energies using a crossed molecular beam apparatus [222]. Cl atoms, produced

---

[3] As mentioned in Section 4.4.2, the CM angular scattering distributions derived in this study were probably artificially biased in the backwards direction as a result of the assumption that the propyl products are formed internally cold.

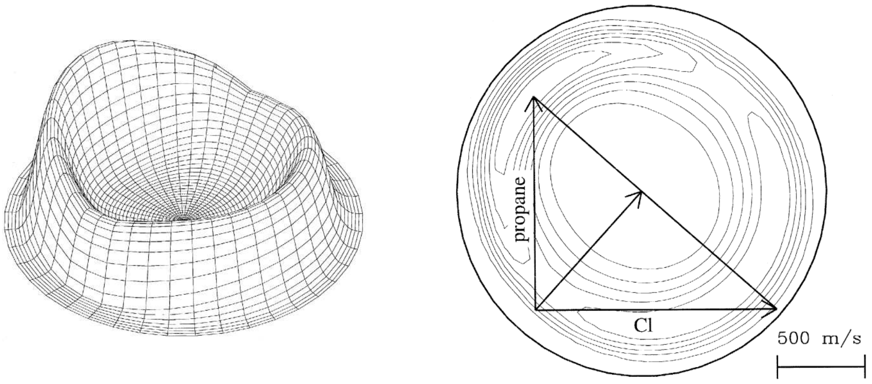

Figure 5.2: The total CM velocity flux map for the reaction of chlorine with propane at 0.35±0.04 eV obtained from the crossed molecular beam study by Blank *et al.*. Adapted from Ref. [222].

by thermal dissociation of Cl_2 at $\sim$1800 K, were diluted in rare gas mixtures and entrained in a continuous, double-skimmed molecular beam. This was crossed at 90° by a continuous beam of C_3H_8 diluted in rare gas, formed by skimming the expansion from a heatable nozzle source. By varying the gas mixtures and source temperatures used, collision energies of 0.35 ± 0.04, 0.50 ± 0.07 and 1.37 ± 0.22 eV were achieved. The scattered n-C_3H_7 and i-C_3H_7 products were detected simultaneously using 9.5 eV vacuum ultraviolet synchrotron radiation coupled with quadrupole TOF mass spectrometry of the resulting ions. CM angular scattering and translational energy release distributions were obtained from the resulting LAB angular distributions and TOF profiles using the forward convolution technique. At the lowest collision energy, 40–50% of the available energy was found to be partitioned into internal energy of the products. From the very small HCl internal energy measured by Varley and Dagdigian at a similar collision energy [215], it was concluded that most of the energy found in the products must be channelled into internal modes of the propyl radical products. The CM angular scattering distribution was seen to be nearly isotropic, with a peak in the forwards direction and a smaller peak in the backwards direction. The total CM velocity flux map obtained at the collision energy of 0.35 ± 0.04 eV is shown in Figure 5.2. The propyl products were found to be more forward and sideways scattered with increasing collision energy. From this observation and the lower activation energy associated with abstraction of a secondary H atom than for abstraction of a primary H atom [184, 246], the forward scattered products were tentatively assigned to be those associated with secondary H abstraction, whilst the backwards and sideways scattered products were thought to be linked with primary H abstraction.[4]

Cl + *i*-C_4H_{10}

The two available pathways for the reaction of chlorine atoms with isobutane, corresponding to abstraction of a hydrogen atom from a primary and tertiary carbon atom respectively, are shown below:[5]

$$\begin{aligned} \mathrm{Cl} + \mathrm{CH(CH_3)_3} &\longrightarrow \mathrm{HCl} + \dot{\mathrm{C}}\mathrm{H_2CH(CH_3)_2} \\ &\qquad \Delta_\mathrm{r}H_0^{\ominus} = -8.6 \pm 1.3\,\mathrm{kJ\,mol^{-1}} \qquad (5.5) \\ &\longrightarrow \mathrm{HCl} + \dot{\mathrm{C}}\mathrm{(CH_3)_3} \\ &\qquad \Delta_\mathrm{r}H_0^{\ominus} = -30.2 \pm 2.1\,\mathrm{kJ\,mol^{-1}} \qquad (5.6) \end{aligned}$$

Using the same experimental apparatus as for their study on the Cl + $CD_3CH_2CD_3$ reaction, Varley and Dagdigian investigated the dynamics of the reaction of Cl with $(CH_3)_3CD$ at a collision energy of 0.35 ± 0.25 eV [216]. $\Delta_\mathrm{r}H_0^{\ominus} = -11\,\mathrm{kJ\,mol^{-1}}$ for abstraction of an H atom from a primary carbon atom of $(CH_3)_3CD$, whilst $\Delta_\mathrm{r}H_0^{\ominus} = -26\,\mathrm{kJ\,mol^{-1}}$ for abstraction of the D atom from the tertiary carbon atom [216]; the energetics are thus similar to those of the reaction with *i*-C_4H_{10}. The rotational population distributions obtained for the HCl($v' = 0$) and DCl($v' = 0$) products are compared in Figure 5.3 as a function of rotational energy, E_rot. Although both rotational population distributions were found to be cold, abstraction from the tertiary carbon atom was seen to give more rotationally excited products than abstraction

---

[4] The recent results of Brouard and co-workers on the reaction of chlorine with ethane, where all products arise from abstraction of primary H atoms and are seen to be forward scattered, bring this assignment into question [169, 247].

[5] Enthalpies of reaction calculated using D_0^0(H–C$(CH_3)_3$) = 397.5± 2.5 kJ mol^{-1} [234] and D_0^0(H–$CH_2CH(CH_3)_2$) = 419.0 ± 2.1 kJ mol^{-1} [232, 233].

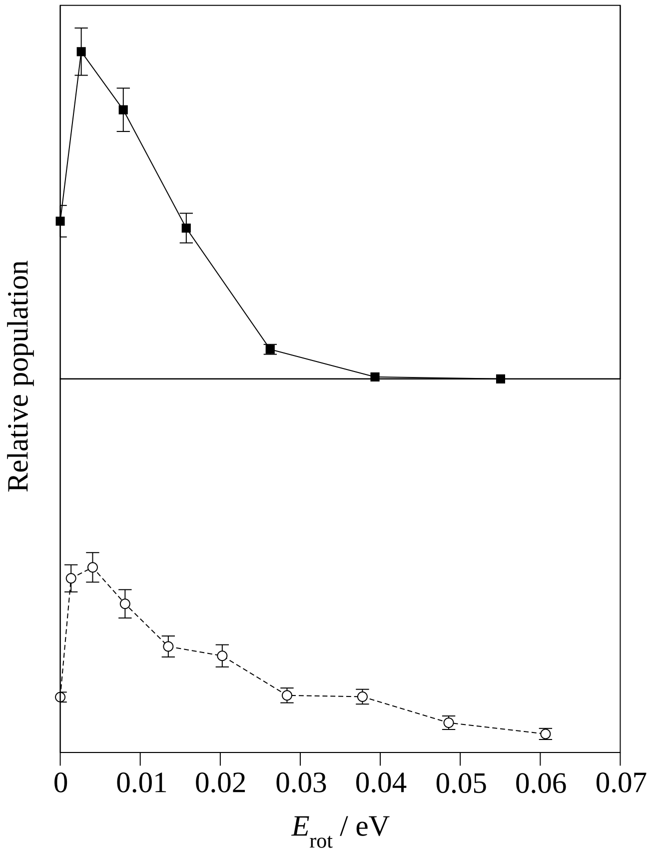

Figure 5.3: The nascent rotational population distributions obtained by Varley and Dagdigian for the HCl($v' = 0,j'$) (--■--) and DCl($v' = 0,j'$) (--○--) products of the reaction of Cl with $(CH_3)_3CD$ [216]. The distributions have been plotted as a function of rotational energy, E_{rot}, to aid comparison.

from one of the primary carbon sites, with on average double the energy being deposited into the DCl($v' = 0$) products compared to the HCl($v' = 0$) products. Negligible vibrational excitation had been observed for the HCl products of the reaction of chlorine with *i*-C_4H_{10}, thus HCl($v' = 1$) and DCl($v' = 1$) products of the Cl + $(CH_3)_3CD$ were not searched for. The ratio of cross-sections for production of HCl($v' = 0$) and DCl($v' = 0$) was calculated to be 3.3 ± 0.4, which, allowing for the 9:1 abundance of H versus D, corresponds to abstraction of the atom from the tertiary carbon site being favoured by a factor of 2.7 ± 0.3 over that of abstraction from a primary carbon site. CM angular scattering distributions were obtained from the TOF profiles for the HCl($v' = 0,j' = 0$) and DCl($v' = 0,j' = 0$) products on the assumption that none of the available energy was deposited into the internal modes of the butyl co-products. HCl($v' = 0$,$j' = 0$) products from reaction at a primary carbon site were seen to be broadly sideways scattered, whilst for the DCl($v' = 0$,$j' = 0$) products of abstraction from the tertiary carbon atom a strong propensity for backward scattering was observed. These dynamics were explained using an impact parameter based model, where the more forward scattered products of reaction at a primary site are attributed to a non-impulsive, large impact parameter, stripping-type mechanism, and the backwards scattering of the products from reaction at the tertiary site are formed from necessarily low impact parameter encounters with a more impulsive energy release.

Cl + *n*-C_5H_{12}

Three pathways exist for the reaction of chlorine with *n*-pentane, proceeding *via* abstraction of either primary or secondary hydrogen atoms:[6]

$$\mathrm{Cl} + \mathrm{CH_3CH_2CH_2CH_2CH_3} \longrightarrow \mathrm{HCl} + \dot{\mathrm{C}}\mathrm{H_2CH_2CH_2CH_2CH_3} \qquad \Delta_{\mathrm{r}}H_0^{\ominus} = -8.4\,\mathrm{kJ\,mol^{-1}} \tag{5.7}$$

$$\longrightarrow \mathrm{HCl} + \mathrm{CH_3}\dot{\mathrm{C}}\mathrm{HCH_2CH_2CH_3} \qquad \Delta_{\mathrm{r}}H_0^{\ominus} = -22.6 \pm 2.1\,\mathrm{kJ\,mol^{-1}} \tag{5.8}$$

$$\longrightarrow \mathrm{HCl} + \mathrm{CH_3CH_2}\dot{\mathrm{C}}\mathrm{HCH_2CH_3} \qquad \Delta_{\mathrm{r}}H_0^{\ominus} = -22.6 \pm 2.1\,\mathrm{kJ\,mol^{-1}} \tag{5.9}$$

Hemmi and Suits studied the reaction of chlorine with *n*-pentane using the crossed beam machine previously employed to investigate the reaction of chlorine with propane [223]. All three pentyl products of the reaction at 0.73 eV were simultaneously detected by photoionisation and TOF mass spectrometry using 9.5 eV synchrotron radiation. Reaction pathways 5.8 and 5.9, producing 2-pentyl (1-methylbutyl) and 3-pentyl (1-ethylpropyl) radicals respectively, were considered to-

---

[6] Enthalpies of reaction calculated using $\Delta_{\mathrm{f}}H_{298}^{\ominus}$(1-$C_5H_{11}$) = 61.0± 3.8 kJ mol^{-1}, $\Delta_{\mathrm{f}}H_{298}^{\ominus}$(2-$C_5H_{11}$) = 46.8± 3.7 kJ mol^{-1} and $\Delta_{\mathrm{f}}H_{298}^{\ominus}$(3-$C_5H_{11}$) = 46.8± 3.6 kJ mol^{-1} [232].

gether owing to their indistinguishable exothermicities and that they both represent secondary H atom abstraction. The experimental data were fitted using forward convolution simulations by decomposing the CM angular and translational energy distributions into two components. One component (channel A) was found to be strongly forward scattered with a high kinetic energy release ($\sim$ 92% of the available energy), whilst the other (channel B) was seen to show more isotropic, but backwards peaking scattering with the much lower kinetic energy release of $\sim$ 65% of the available energy. The branching ratio was determined to be 58% for the first channel and 38% for the second channel.[7] It should be noted that decomposition of the CM distributions into two components using the forward convolution method, especially for the forward scattered products, was somewhat arbitrary [223]. Assignment of the two components of the CM distributions to abstraction of hydrogen atoms from primary and secondary carbon sites was performed on the basis of the translational energies, with abstraction of secondary H atoms proposed to correspond to channel A and abstraction of primary H atoms therefore associated with channel B. The validity of the separation of the CM distributions into two components in the analysis of the results of this experiment, and therefore the assignments of the reaction pathways, has been brought into question by a more recent crossed molecular beam imaging experiment by Suits and co-workers [247]. These experiments use 157 nm laser radiation to selectively ionise the 2- and 3-pentyl radicals only and are insensitive to the *n*-pentyl products. Products were clearly seen to be backwards scattered and, since these can correspond to the abstraction of hydrogen atoms from secondary carbon sites only, the earlier assignments were concluded to be erroneous.

Cl + *c*-C_6D_{12}

The dynamics of the reaction between chlorine and deuterated cyclohexane, where abstraction of a D atom from a secondary carbon site is the only available pathway, have been investigated by Flynn and co-workers using time-resolved infrared

---

[7] Note that, as in Ref. [223], these branching fractions do not sum to 100%.

laser absorption spectroscopy to probe the DCl products [248]. In these experiments, c-C_6D_{12} and either NOCl or S_2Cl_2 were premixed and flowed through a 2 m cell. Reaction was initiated by photodissociation of NOCl at 193 nm and S_2Cl_2 at 248 nm to produce Cl atoms and give reasonably well-defined collision energies of 0.62 ± 0.09 eV and 0.23 ± 0.03 eV, respectively. DCl products were monitored rovibrational state selectively at wavelengths around 4.9 μm through infrared absorption changes. The enthalpy of reaction, $\Delta_r H_0^{\ominus}$, was estimated to be -33.3 ± 8 kJ mol^{-1}. At the lower collision energy, around 95% of the DCl products were found to be formed in the ground vibrational state, with the Boltzmann rotational temperature of the ground and first vibrationally excited states both measured to be ~ 150 K. Higher levels of vibrational excitation were observed for the DCl products of reaction using NOCl as the chlorine atom precursor; the rotational temperature for the DCl($v' = 0$) products at this collision energy was measured to be ~ 200 K. Around 60% and 37% of the available energy was seen to be deposited into the internal modes of the cyclohexyl radicals at the lower and higher collision energies, respectively. The DCl products were found to have translational energies approaching those of the reactant Cl atoms. It was thus suggested that the reaction proceeds with direct transfer of the D atom from the c-C_6D_{12} to the chlorine, in accord with a simple 'spectator' model [2]. The cold DCl rotational energy was speculated to result from D atom abstraction with a collinear Cl–D–C recoil configuration. QCT calculations on an empirical three-body London–Eyring–Polanyi–Sato surface, where the c-C_6D_{11} fragment was treated as a structureless particle, were consistent with the experimental observations and suggested a direct abstraction mechanism with a collinear Cl–D–C recoil geometry [248].

5.2.4 Summary

The previous work on the reactions of chlorine atoms with saturated alkanes can be summarised as follows: (i) *ab initio* calculations on the transition state geometries of the Cl + C_3H_8 and Br + C_3H_8 and n-C_4H_{10} reactions at both primary and secondary carbon sites show a near collinear X–H–C arrangement, suggesting that the Cl + n-C_4H_{10} reaction is also likely to be characterised by a near-linear transition state; (ii) the HCl products are found predominantly in the ground vibrational state and are rotationally cold, with the products of abstraction from a secondary or tertiary carbon atom being more rotationally excited than those formed by abstraction from a primary carbon site; (iii) at collision energies similar to those employed in the current study, abstraction from the secondary and tertiary carbon atoms in C_3H_8 and i-C_4H_{10} is favoured by a factor of 2–3 over the statistical ratio of primary to secondary or tertiary atoms at collision; (iv) the analysis of photoloc experiments, and several theoretical treatments of the dynamics of the reactions, have assumed that the systems may be approximated to three-body reactions, where internal modes of the alkyl fragments are not excited; (v) within this approximation, the products of abstraction from primary carbon sites are seen to be more forward scattered than the products of abstraction from secondary or tertiary sites; (vi) in light of recent studies, the results of crossed molecular beam experiments now also find the products of abstraction from primary carbon sites to be forward scattered, whilst secondary hydrogen atom abstraction gives sideways and backwards scattered products; and, (vii) these crossed molecular beams studies suggest that the alkyl fragments are internally excited and therefore cannot be considered as spectators in the reactions.

5.3 Results

5.3.1 Images and Legendre Moments

Representative velocity-map ion images and the corresponding zeroth, second and fourth order Legendre moments are shown in Figure 5.4 for HCl($v' = 0$,$j' = 1$, 3 and 6). The images have been background-subtracted and quadrant-averaged for clarity; the Legendre moments were obtained from the raw images as described in Chapter 3. It can be seen clearly in the images, and especially in the zeroth order moments, that the intensity is shifted towards the centre of the images with

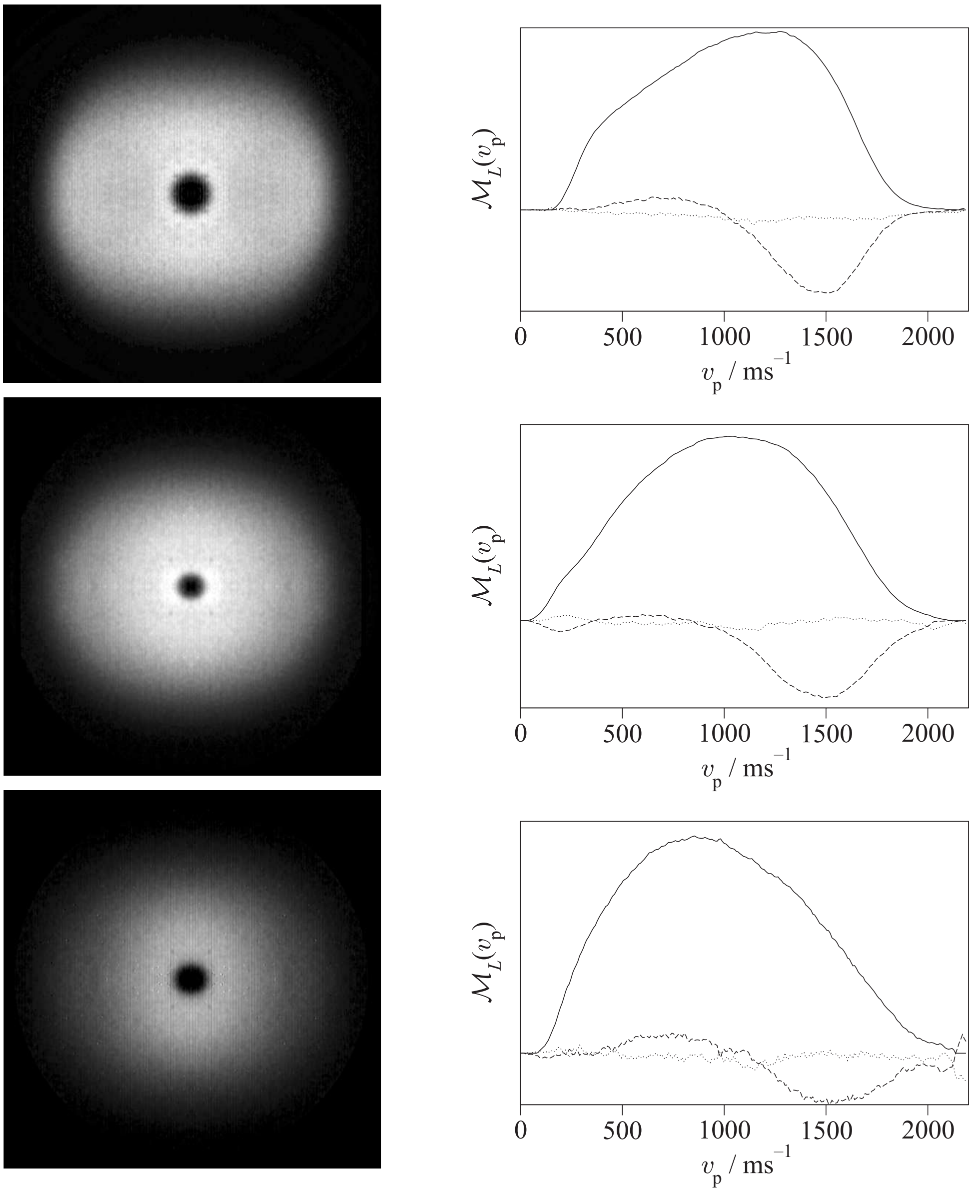

Figure 5.4: Background subtracted images and Legendre moments of order 0 (—), 2 (- - -) and 4 ($\cdots$) for HCl($v' = 0$,$j' = 1$ (top), 3 (middle) and 6 (bottom)).

increasing HCl rotational state, a similar trend to that seen for the Cl + C_2H_6 reaction in Chapter 4. This change in the intensity distribution could reflect either more backwards scattering or lower kinetic energy releases associated with the HCl products formed in higher rotational states. It should also be noted that, within the experimental signal-to-noise ratio of the data, the 4th order Legendre moments are very close to zero. The experimental data are therefore consistent with the description of the LAB scattering distribution used in Chapter 3, in which the only non-zero image moments are those for which $L = 0$ and 2.

Owing to the arrangement of the experimental apparatus used, it was not possible to scan the probe laser reliably over the extended range of wavelengths required to obtain the full rotational structure of the REMPI spectrum of the nascent HCl reaction products, and therefore the rotational population distribution was not determined. However, on the basis of the observed signal intensities for each transition studied and using the linestrength factors determined experimentally by Rohlfing *et al.* [244], the rotational Boltzmann temperature was estimated qualitatively to be ~ 180 K. The rotational population distribution at this temperature peaks quite narrowly at $j' = 2$, with a short tail extending to $j' = 9$. This product HCl rotational population distribution is in good agreement with that obtained for the Cl + C_3H_8 reaction by Varley and Dagdigian [215], but is slightly hotter than those found for the Cl + $CH_3CD_2CH_3/CD_3CH_2CD_3$ reactions ($\sim$ 70–100 K) studied by Koplitz and co-workers [224] and the Cl + *i*-C_4H_{10} reaction (~ 120 K) investigated by Varley and Dagdigian [216]. The low populations in the higher rotational states studied are reflected in the lower signal-to-noise ratios seen in the experimental images and Legendre moments obtained for these states.

5.3.2 Legendre Moment Fitting Analysis

The experimental data were analysed using the basis function fitting method (see Chapter 3), rather than by attempting the direct inversion of the data performed previously for the Cl + $CD_3CH_2CD_3$ and Cl + $(CH_3)_3CD$ reactions by Varley and

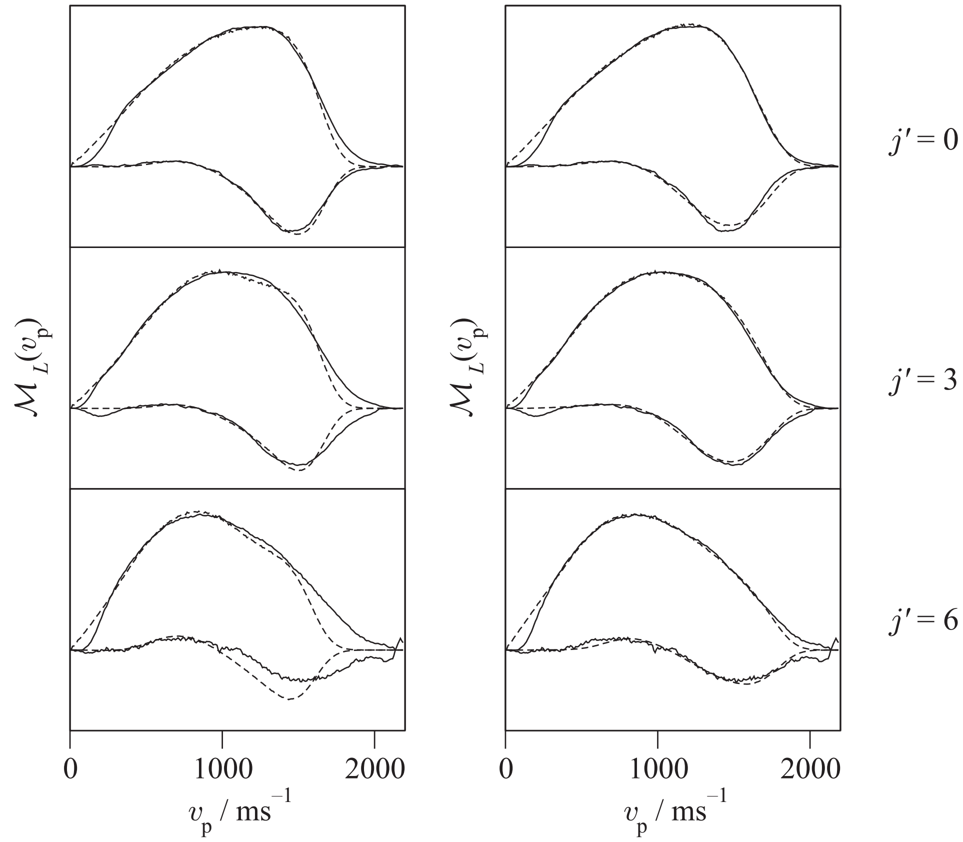

Figure 5.5: Zeroth and second order Legendre moments (—), and fits to those moments (- - -), assuming H atom abstraction from either only primary (left) or only secondary (right) carbon atoms. From top to bottom, data are shown for HCl($v' = 0$), products born in $j' = 0$, 3 and 6. The fits were performed using basis function sets with four moments each in the CM angular scattering distribution and the kinetic energy release distribution.

Dagdigian [215, 216]. The basis function sets used in all of the fits allow for the finite instrument resolution and the molecular beam temperature (see Section 2.10.4), and were generated in moments of the CM angular scattering and fractional kinetic energy release ($P(f_t)$) distributions. Fits were performed simultaneously to the zeroth and second order Legendre moments of the experimental images.

Initial fits to the data were attempted on the assumption that the HCl product signal arose exclusively from hydrogen atom abstraction at *either* primary *or* secondary carbon sites. The resulting fits to the data are shown in Figure 5.5 for HCl($v' = 0, j' = 0$, 3 and 6). In the case of abstraction occurring from primary carbon atoms only, the quality of the fits is seen to decrease drastically with increasing HCl rotational excitation. The high velocity sections of the experimental moments for the three rotational states are seen to be poorly reproduced by the fits. In addition, the fits to the second order Legendre moments, which are sensitive to the velocity-dependent translational anisotropy, show structure sharper than that seen in the experimental data. The fits obtained using basis sets calculated assuming product formation exclusively through abstraction from secondary carbon atoms, although much better than those for abstraction from just primary carbon atoms, are seen to show the opposite trends, with the fits increasing in quality for products formed in higher rotational states. This is particularly evident for the $L = 2$ moments, with the best fits at low j' being noticeably broader than those determined experimentally. A qualitative trend that may be drawn from these observations is that more of the HCl products born with low rotational energies are formed from abstraction of primary hydrogen atoms, whilst a greater fraction of those formed in the highest rotational quantum states investigated are the products of secondary hydrogen abstraction.

A more complete analysis, allowing for the participation of both reaction pathways and the determination of the relative contribution of each to the total signal, yields the more satisfactory fits shown in Figure 5.6. Within the framework of this analysis, the CM angular scattering and fractional kinetic energy release distributions are constrained to take the same form for reactions involving abstraction of either a primary or secondary hydrogen atom. This approach allows the relative contribution of each reaction channel to be determined. The relative χ^2 values returned from these fits are compared with those obtained from the fits assuming abstraction of hydrogen atoms takes place from either exclusively primary or exclusively secondary carbon sites (see Figure 5.5) in Table 5.1. Inclusion of both reaction pathways is seen to improve the quality of the fits for the HCl($v' = 0$) products formed in low rotational states. For the HCl($v' = 0$,$j' = 6$) products, the value of χ^2 obtained from the fit assuming hydrogen atom abstraction takes place only from

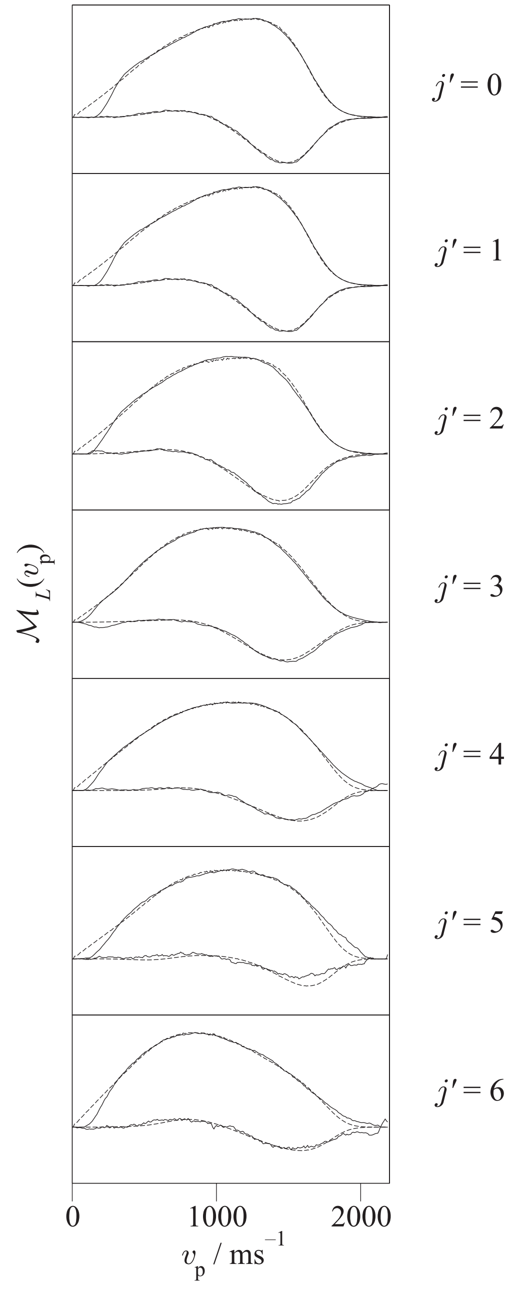

Figure 5.6: Zeroth and second order Legendre moments (—), and fits to those moments (- - -) for HCl($v' = 0$,$j' = 0$) (top) through to HCl($v' = 0$,$j' = 6$) (bottom). The fits were performed using basis function sets with four moments each in the CM angular scattering distribution and the kinetic energy release distribution. The very low speed section of the moments ($v_p < 255\,\mathrm{ms}^{-1}$) was not included in the fits, as discussed in Section 2.10.3.

Table 5.1: The returned relative χ^2 values from the fits to the experimental data assuming H atom abstraction from only primary, only secondary, and both primary and secondary carbon atom sites (see Figures 5.5 and 5.6). The χ^2 values returned assuming 1° only or 2° only abstraction have been normalised to those obtained allowing for 1° and 2° abstraction for each HCl($v' = 0$) rotational quantum state.

	Relative χ^2		
HCl($v' = 0,j'$)	1° only	2° only	1° and 2°
0	4	3	1
3	7	2	1
6	10	1	1

secondary carbon sites is seen to be unchanged by inclusion of the primary hydrogen atom abstraction channel, reflecting the fact that hydrogen atom abstraction from a secondary carbon atom is the dominant pathway leading to HCl($v' = 0$) products in this rotational state (see below).

The overall angular and energy resolutions of the current study are governed by the number of moments in CM angular scattering and kinetic energy release required to fit the Legendre moments of the experimental images. To gain an appreciation of the level of dynamical detail inherent in the data, it is necessary to investigate the dependence of the returned CM angular scattering and kinetic energy release distributions, and the relative weighting of the primary and secondary abstraction channels, on the number of moments employed for each distribution. This dependence is shown in Figure 5.7 for HCl($v' = 0,j' = 0$, 3 and 6), together with Monte Carlo error limits determined as outlined in Section 3.4.7. The error bars shown on the data are the result of the Monte Carlo analysis detailed in Section 3.4.7, and reflect the uncertainties in the fitting procedure. The truncation point for the number of basis functions used was determined by observing the dependence of χ^2 on the number of fitting coefficients employed. In the present case, χ^2 did not decrease by a significant amount with inclusion of more than four moments in either the CM

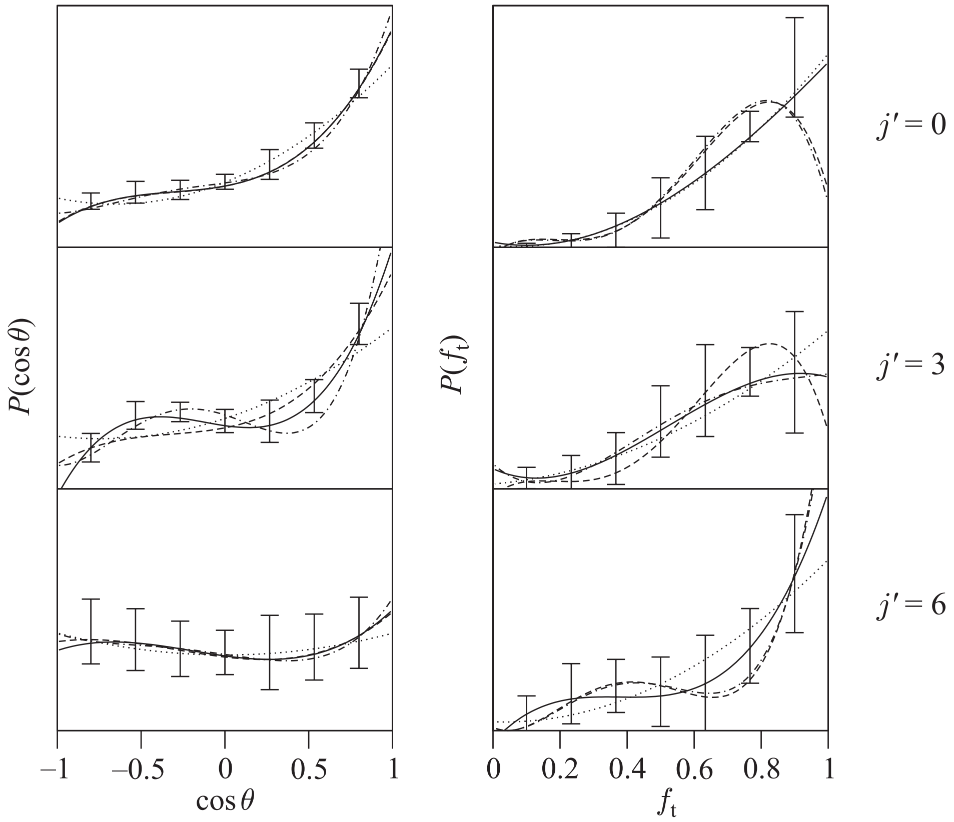

Figure 5.7: The dependence of the returned CM angular scattering (left) and kinetic energy release (right) distributions on the number of moments employed. From the top, the data are for HCl ($v' = 0$,$j' = 0$, 3 and 6). The solid lines represent fits to the data using four moments in the CM angular scattering distribution and four moments in the kinetic energy release distribution. The other lines are fits with basis sets of dimension (n,m)=(3,3) (···), (4,5) (---) and (5,5) (— · — ·). The relative weighting between the two reaction channels for each rotational state are within the error limits shown in Figure 5.9 (see Table 5.2).

angular scattering distribution or the kinetic energy release distribution. The returned distributions and the relative weighting between the two reaction pathways are, however, noticeably consistent as the number of moments used is varied. The relative contributions of the two reaction channels associated with the distributions shown in Figure 5.7 are given in Table 5.2 and are all seen to lie with the 2σ error bounds shown in Figure 5.9. These measurements thus confirm that the branching ratios for the reaction channels are reliably returned.

Fits to the experimental Legendre moments were also carried out allowing different CM angular scattering and fractional kinetic energy release distributions to be

Table 5.2: Relative contributions of the reaction pathways involving abstraction of a hydrogen atom from primary (1°) and secondary (2°) carbons sites determined from fits using basis sets generated with n Legendre moments in the CM angular scattering distribution and m Legendre moments in the kinetic energy release distribution. The CM distributions returned from these fits are shown in Figure 5.7. Error limits for the optimum (4,4) fit represent 2σ errors resulting from statistical errors in the fit; these data are shown in Figure 5.9.

	HCl($v' = 0$,j')					
	0		3		6	
(n, m)	1°	2°	1°	2°	1°	2°
(3,3)	0.70	0.30	0.42	0.58	0.00	1.00
(4,5)	0.61	0.39	0.44	0.56	0.03	0.97
(5,5)	0.61	0.39	0.43	0.57	0.03	0.97
(4,4)	0.73 (±0.16)	0.27 (±0.16)	0.47 (±0.15)	0.53 (±0.15)	0.00 (±0.23)	1.00 (±0.23)

associated with each channel. The χ^2 values returned from these fits were not found to be significantly lowered with respect to those obtained from the more constrained fits performed above, despite requiring almost double the number of fitting parameters. After appropriate averaging, the CM angular scattering and kinetic energy release distributions for each reaction pathway returned from these fits were seen to be in very good agreement with those obtained when the distributions are constrained to be the same for each reaction channel. The branching ratios determined in these fits were also seen to show the same trends as those obtained from the more constrained fits. Although the results of this analysis present a sensible and appealing alternative to the more constrained analysis outlined above, the insignificant improvement in the fits demonstrates that the returned CM angular scattering and kinetic energy release distributions and the branching ratios are insensitive to whether or not the CM distributions for the two pathways are separated. It is therefore believed that constraining the CM angular scattering and fractional kinetic energy release distributions to be the same for reactions involving abstraction of either a primary or secondary hydrogen atom is justified.

The set of CM angular scattering and kinetic energy release distributions returned from the fits for HCl($v' = 0$,$j' = 0$–6) using the current analysis method are shown in Figure 5.8. A steady trend is clearly seen in the CM angular scattering distributions, with the predominantly forward scattering of HCl products formed in low rotational states shifting to more isotropic scattering for the HCl products formed in the highest rotational states. The kinetic energy release distributions are insensitive to HCl rotational state, with only a minor trend towards higher kinetic energy release with higher HCl rotational excitation. Note that the f_{t} values shown on the x axes in Figure 5.8 refer to the fractional energy release for the specific HCl quantum state in question.

The relative contributions from pathways 5.1 and 5.2 are plotted against rotational state in Figure 5.9. In general, primary H atom abstraction is seen to be largely associated with low rotational excitation of the HCl($v' = 0$) products, while abstraction of a secondary hydrogen atom dominates for HCl($v' = 0$) products produced with higher rotational energies; this is in good agreement with the qualitative results drawn from the single channel fits. The nascent HCl product rotational population distributions for the two pathways may be calculated using the Boltzmann rotational temperature of 180 K estimated in the previous Section for the total HCl($v' = 0$) signal, in conjunction with the relative contributions of each reaction pathway (see Figure 5.10). The rotational population distributions obtained in this way show the HCl products of secondary hydrogen atom abstraction to be significantly rotationally hotter than those of primary hydrogen atom abstraction. The overall branching ratios determined from the rotational population distributions for the Cl + n-C_4H_{10} reaction show that $52 \pm 6\%$ of products are formed by abstraction of hydrogen from primary carbon atoms, whilst $48 \pm 6\%$ are the products of secondary hydrogen atom abstraction.

The mean values obtained from the fractional kinetic energy release distributions

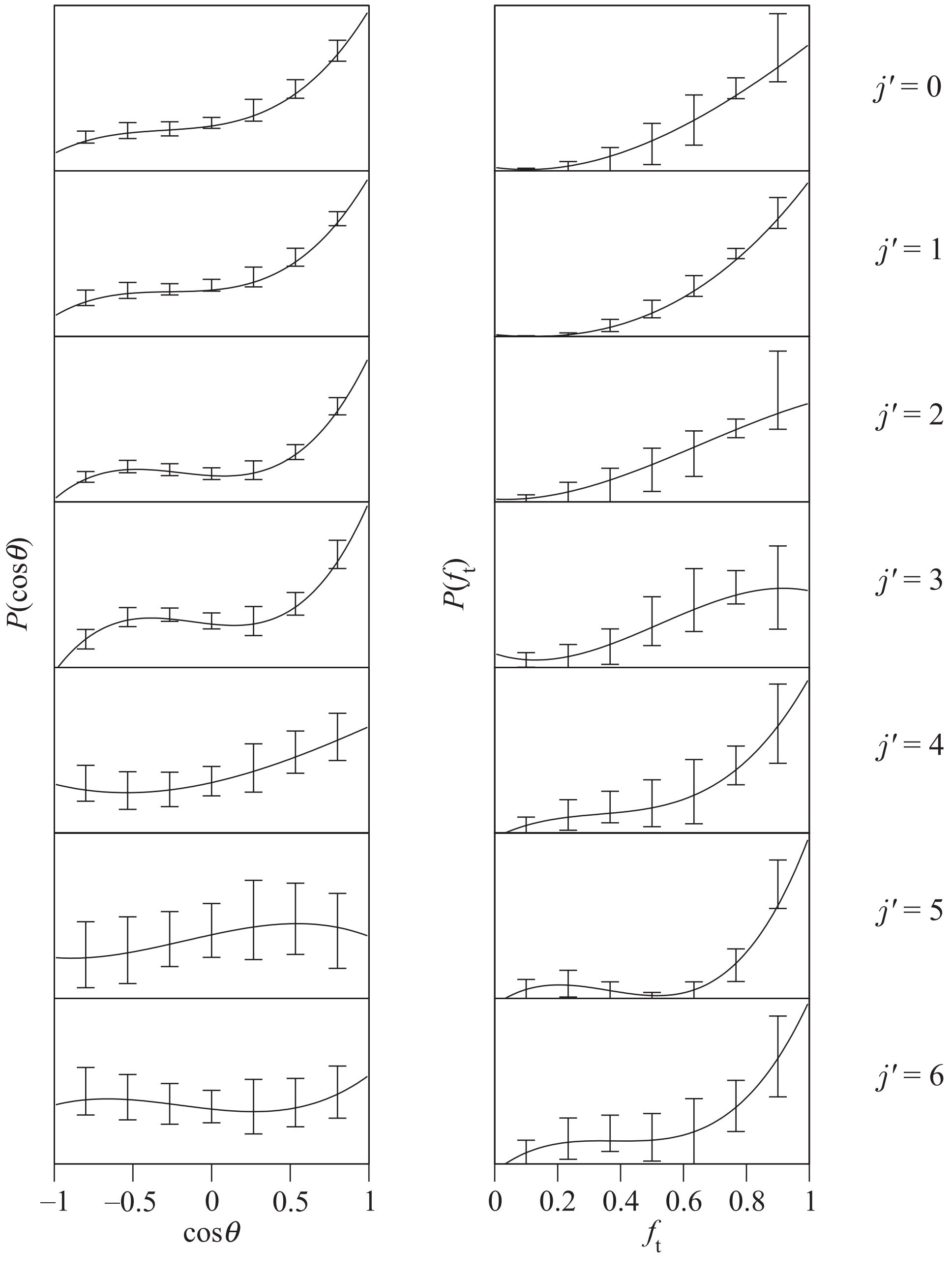

Figure 5.8: Returned CM angular scattering (left) and kinetic energy release (right) distributions for HCl($v' = 0$,$j' = 0$) (top) through to HCl($v' = 0$,$j' = 6$) (bottom). Optimum fits to the data were obtained with four moments in both the CM angular scattering distribution and the kinetic energy release distribution. Error bars represent 2σ errors resulting from statistical errors in the fits. Note that in the right-hand panels, the $f_{\rm t}$ scale refers to the state-specific fractional kinetic energy release, which does not include the rotational energy in the HCl product (see Table 5.3).

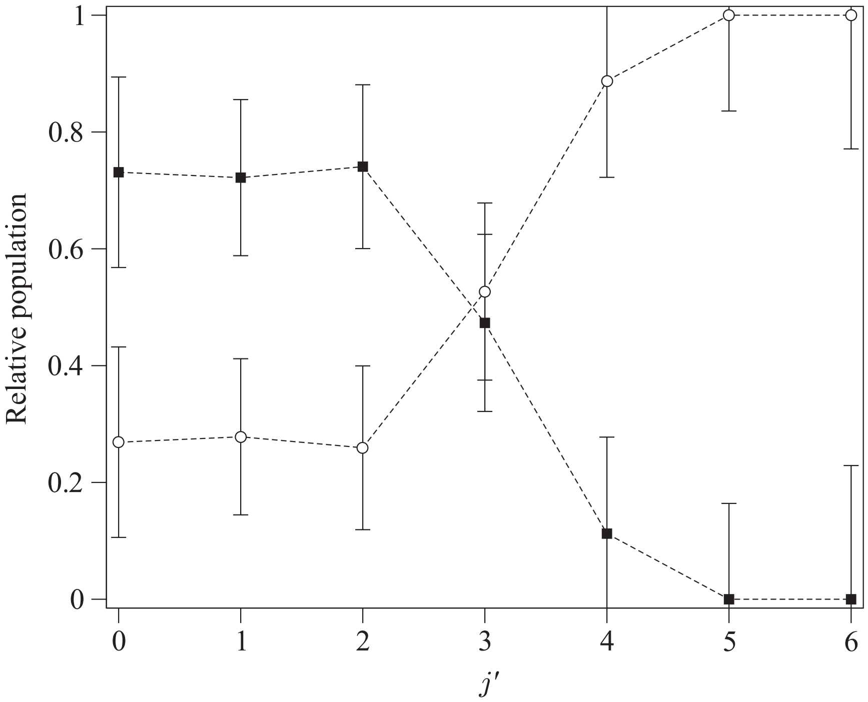

Figure 5.9: The relative contributions to the HCl($v' = 0$,j') products by abstraction of hydrogen atoms from primary carbon atoms (- - ■ - -) and secondary carbon atoms (- - ○ - -). Error bars represent 2σ errors resulting from statistical errors in the fits.

shown in Figure 5.8, $\langle f_\mathrm{t} \rangle$, are corrected for the HCl($v' = 0$,j') rotational energy and given in Table 5.3. The mean internal energies in the butyl fragments are seen to remain fairly constant with HCl rotational state for both reaction pathways. A weighted mean over the HCl rotational quantum states investigated for each reaction channel gives the overall average fraction of available energy in internal excitation of the n- and s-butyl radicals, $\overline{\langle f_\mathrm{int}(n\text{-}\mathrm{C_4H_9})\rangle}$ and $\overline{\langle f_\mathrm{int}(s\text{-}\mathrm{C_4H_9})\rangle}$, to be $\sim$0.3 in both cases. The weights for each quantum state for each channel used in calculating this average were taken from the HCl($v' = 0$,j') rotational populations shown in Figure 5.10.

The data shown in Figures 5.8 and 5.10 may be used to create 2D contour maps and the corresponding 3D 'wireframe' plots of the product flux as a function of HCl speed and CM scattering angle, $P(w, \theta_\mathrm{t})$. Plots are shown for the products of hydrogen atom abstraction from primary only, secondary only and both carbon

Table 5.3: HCl($v' = 0,j'$) state-resolved, and state-averaged energy disposal data for the two pathways in the Cl + n-C_4H_{10} reaction. The data have been obtained assuming mean available energies of 3280 cm^{-1} for primary H atom abstraction and 4510 cm^{-1} for secondary H atom abstraction. The errors on the state-resolved $\langle f_t \rangle$ values are typically ±0.05. The averaging over rotational state was performed using a Boltzmann rotational population distribution calculated at 180 K for the HCl($v' = 0$) products, weighted by the contribution of each pathway for the rotational state in question. HCl($v' = 1$) has been shown to be produced in negligible quantities in the reactions of Cl with both C_3H_8 and i-C_4H_{10} at similar collision energies [215, 216], and is thus neglected, despite being energetically accessible in both reaction pathways.

	$Cl + n\text{-}C_4H_{10} \longrightarrow HCl + n\text{-}C_4H_9$			$Cl + n\text{-}C_4H_{10} \longrightarrow HCl + s\text{-}C_4H_9$		
HCl($v' = 0,j'$)	f_{rot}(HCl)	$\langle f_t \rangle$	$\langle f_{\mathrm{int}}(n\text{-}C_4H_9) \rangle$	f_{rot}(HCl)	$\langle f_t \rangle$	$\langle f_{\mathrm{int}}(s\text{-}C_4H_9) \rangle$
0	0.00	0.72	0.28	0.00	0.73	0.27
1	0.01	0.75	0.24	0.00	0.76	0.24
2	0.02	0.67	0.31	0.01	0.68	0.31
3	0.04	0.62	0.34	0.03	0.64	0.33
4	0.06	0.66	0.28	0.05	0.68	0.28
5	0.10	0.68	0.23	0.07	0.70	0.22
6	0.14	0.59	0.27	0.10	0.62	0.28
Average	0.02	0.69	0.29	0.04	0.68	0.28

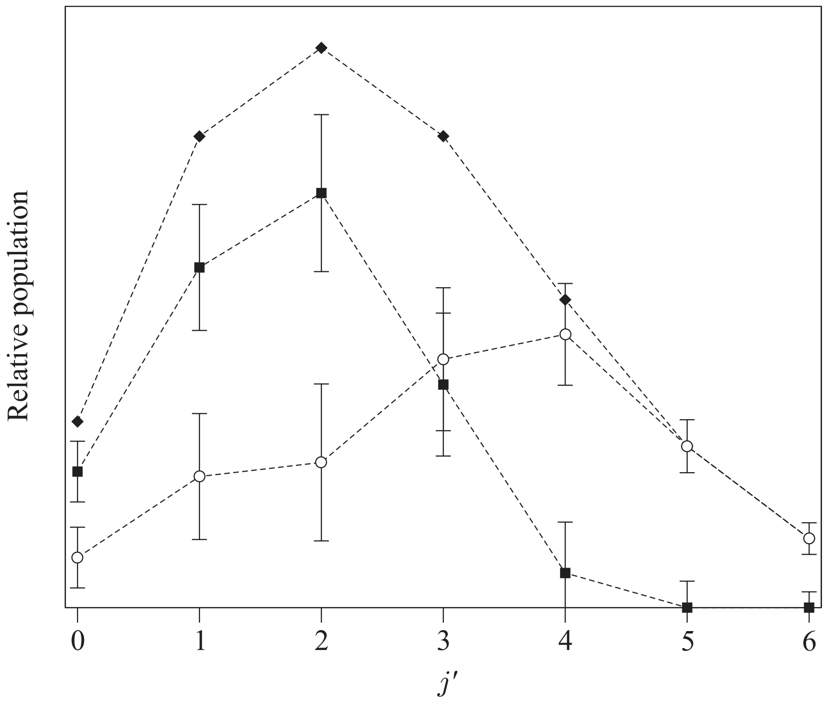

Figure 5.10: The rotational population distributions for the HCl($v' = 0$,j') products formed by abstraction of hydrogen atoms from primary carbon atoms (- - ■ - -) and secondary carbon atoms (- - ○ - -), calculated using the relative contributions of each channel determined from the fits (see Figure 5.9) and assuming a Boltzmann distribution for the total rotational population characterised by a rotational temperature of 180 K (- - ◆ - -). Error bars represent 2σ errors resulting from statistical errors in the fits.

sites in Figure 5.11. In generating these plots, the CM angular scattering and kinetic energy release distributions for the individual HCl rotational states have been averaged using the same weighting factors as above. The contour map for primary hydrogen atom abstraction is seen to have a smaller radius than that for secondary hydrogen atom abstraction, reflecting the lower exothermicity of this reaction pathway. The broader angular scattering distribution seen for secondary hydrogen atom abstraction results from the greater contribution to rotationally excited HCl($v' = 0$) products from this reaction pathway. The contour map calculated for the overall reaction including both pathways mimics the results that would be obtained from a crossed molecular beam experiment without product quantum state resolution.

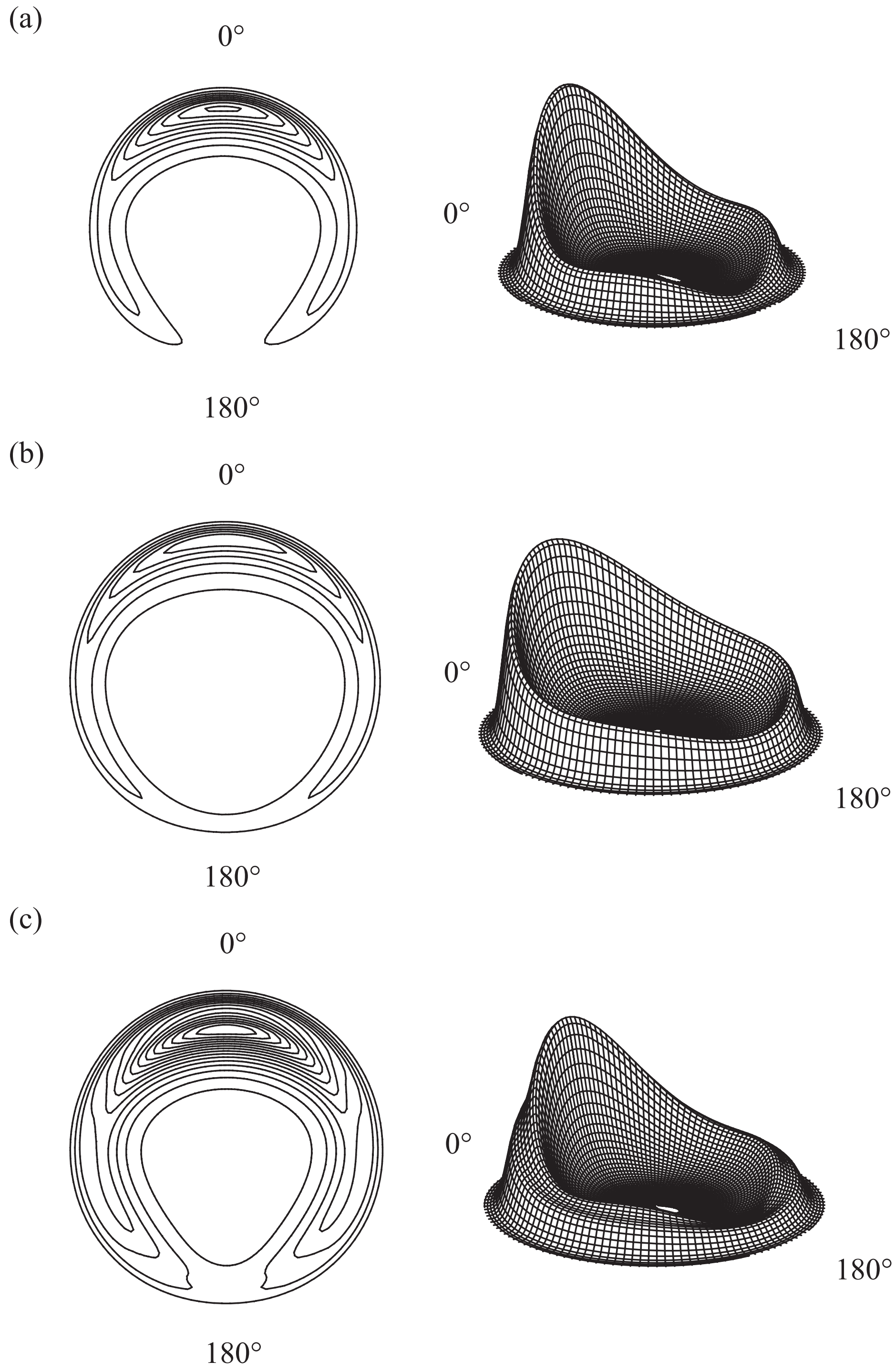

Figure 5.11: Contour map and 'wireframe' plots of the product velocity-angle flux averaged over HCl rotational state for abstraction of hydrogen atoms from (a) primary and (b) secondary carbon sites. Plots (c) correspond to the *total* flux for the reaction, where both primary and secondary hydrogen atoms are abstracted. The plots were obtained using the results shown in Figures 5.8 and 5.10.

5.4 Discussion

As discussed in the previous Section, new results on the reaction of atomic chlorine with *n*-butane have been obtained using photoloc velocity-map ion imaging. Product rotational state resolved CM angular scattering distributions, kinetic energy release distributions and the relative contributions of hydrogen atom abstraction from primary and secondary carbon sites to the total were obtained for HCl($v' = 0$,$j' = 0$–6) using a basis function fitting analysis of the Legendre moments of the ion images.

5.4.1 Rotational Population Distribution

Based on the observed relative signal intensities for the transitions studied, the total nascent HCl rotational population distribution for both reaction channels was estimated to be described by a rotational Boltzmann temperature of around 180 K. This rotational Boltzmann temperature is higher than the $\sim$70–100 K estimated by Koplitz and co-workers for both the HCl and DCl products of the reactions of atomic chlorine with the selectively deuterated propanes $CH_3CD_2CH_3$ and $CD_3CH_2CD_3$ [224]. The HCl products of the Cl + *n*-C_4H_{10} reaction in the current study were also found to be slightly rotationally hotter than those of the Cl + *i*-C_4H_{10} reaction studied by Varley and Dagdigian [216]. The difference is thought to arise from the differing contributions made by the primary, secondary and tertiary hydrogen atoms to the reactivities of the two systems (there are six primary and four secondary hydrogen atoms in *n*-C_4H_{10}, whilst there are nine primary hydrogen atoms and only one tertiary hydrogen atom in *i*-C_4H_{10}). The higher exothermicity associated with secondary and tertiary hydrogen atom abstraction may be linked to higher rotational excitation of the HCl products, as shown in the previous Section. The product HCl rotational population distribution determined by Varley and Dagdigian for the reaction of atomic chlorine with propane [215] and that returned for the HCl products from the reaction of chlorine atoms with *n*-butane using the rotational Boltzmann temperature of $\sim$180 K are shown in Figure 5.12. The strong similarity between the rotational population distributions for the two reactions is

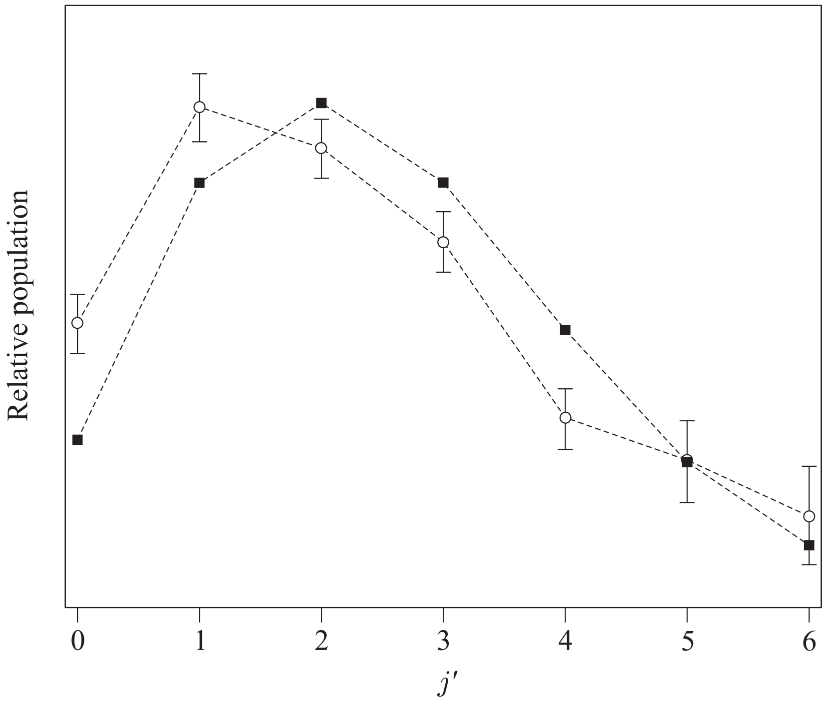

Figure 5.12: The rotational population distribution for the HCl($v' = 0$,j') products of the Cl + *n*-C_4H_{10} reaction calculated using a Boltzmann rotational temperature of 180 K (--■--) and the HCl($v' = 0$,j') rotational population distribution measured by Varley and Dagdigian for the Cl + C_3H_8 reaction (--○--) [215].

thought to be a reflection of the comparable ratios of primary to secondary hydrogen atoms in propane and n-butane (3:1 and 3:2, respectively), and the similar exothermicities of the respective channels in the two reactions.

From the rotational population distributions shown in Figure 5.10, the HCl products of abstraction of primary hydrogen atoms are found to be formed with an average rotational energy of around 60 cm^{-1}, while secondary hydrogen atom abstraction is found to yield HCl products with an average rotational energy of around 170 cm^{-1}. This degree of rotational excitation in the products of the two reaction pathways is in good agreement with the results of Varley and Dagdigian for the Cl + $CD_3CH_2CD_3$ and Cl + $(CH_3)_3CD$ reactions, where in the former the average rotational energies were found to be 84 cm^{-1} and 110 cm^{-1} for the DCl and HCl products respectively [215], while in the latter the HCl and DCl products were found to have average rotational energies of 50 cm^{-1} and 100 cm^{-1}, respectively [216].

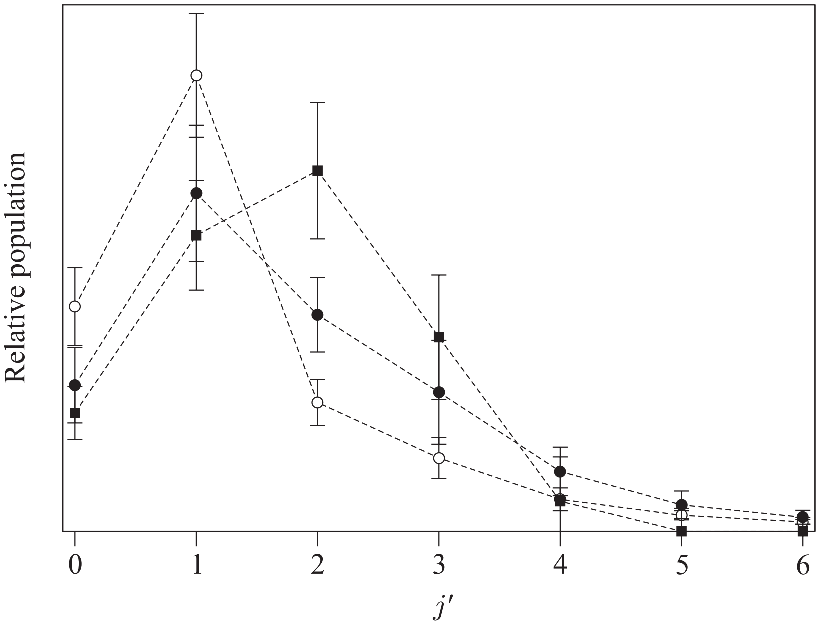

Figure 5.13: A comparison of the rotational quantum state population distribution for the HCl($v' = 0, j'$) products formed by abstraction of hydrogen atoms from primary carbon atoms in the Cl + *n*-C_4H_{10} reaction (--■--) (as shown in Figure 5.10) with the experimental nascent rotational quantum state population distributions for the HCl($v' = 0, j'$) products of the Cl + C_2H_6 reaction measured by Zare and co-workers (--○--) [151] and by Orr-Ewing and co-workers (--●--) [207]. The error bars represent 2σ confidence limits; each distribution has been normalised in the j' range shown.

As can be seen in Figure 5.13, the rotational population distribution determined for the primary abstraction channel is very similar to those measured by Zare and co-workers [151] and Orr-Ewing and co-workers [207] for the Cl + C_2H_6 reaction, in which hydrogen atoms are available for abstraction from primary carbon sites only. This suggests that the dynamics observed for primary hydrogen atom abstraction may arise from a similar mechanism operating in both reactions.

5.4.2 Branching Ratio

Closely related to the rotational population distributions for the two reaction channels is the branching ratio between them. Overall, $52 \pm 6\%$ of products are found to be formed by abstraction of hydrogen from primary carbon atoms, whilst 48±6% are the products of secondary hydrogen atom abstraction. Expressed in terms of the relative reactivity of the primary and secondary carbon sites, where the 3:2 statistical abundance of primary to secondary H atoms has been allowed for, this corresponds to abstraction of an atom in the secondary position being favoured by a factor of 1.4 ± 0.2 over that of abstraction of an atom in the primary position. The value determined here shows the same, albeit rather lower, propensity as that obtained from the kinetics studies by Tyndall *et al.* [191] and Sarzynksi and Sztuba [184], where, allowing for the statistical abundances, secondary H atom abstraction was seen to be favoured by a factor of 3.7 over primary H atom abstraction. This difference may originate from the significantly lower collision energies sampled in the thermal kinetic study compared to the collision energy provided by the fast-moving chlorine atoms in the current photoloc study and also from the different activation energies for the two reaction pathways. The positive activation energy for abstraction of hydrogen from primary carbon sites indicates a barrier in this reaction pathway, whilst no such barrier is present for secondary hydrogen atom abstraction, where the 'effective' activation energy is found to be negative [184]. The thermalized Cl atoms used in the kinetic studies provided the low mean collision energy of $\sim$0.03 eV, with the result that the barrierless abstraction of hydrogen atoms from secondary carbon sites is thus favoured over abstraction of hydrogen atoms from primary carbon sites. The much higher collision energies of around 0.32 eV afforded by Cl_2 photolysis, however, lie well above the barrier to primary H atom abstraction, resulting in the lower enhancement in the reactivity of the secondary carbon atom site obtained from the current study. The reactivity enhancement for the secondary hydrogen atom abstraction pathway seen in the present experiment is also lower in comparison with that seen in propane: allowing for the 3:1 statistical abundance of primary to secondary H(D) atoms, Koplitz and co-workers found abstraction of hydrogen and deuterium atoms from the secondary carbon site to be favoured by a factor of 2–3 over abstraction from a primary carbon site in the Cl + $CH_3CD_2CH_3$ and Cl

+ $CD_3CH_2CD_3$ reactions [224]; while Varley and Dagdigian found abstraction from the secondary carbon site to be favoured by a factor of 2.7 ± 0.5 over that from the primary site in the Cl + $CD_3CH_2CD_3$ reaction. Varley and Dagdigian also found abstraction of the deuterium atom from the tertiary carbon site in $(CH_3)_3CD$ to demonstrate a greater enhanced reactivity over the primary carbon sites, for which, allowing for the 9:1 statistical abundance of primary H to tertiary D atoms, the factor was determined to be 2.7 ± 0.3 [216].

5.4.3 Angular Scattering Distributions

A steady trend with HCl product rotational quantum state is seen in the CM angular scattering distributions returned from the Legendre moment fitting analysis: products formed in low rotational levels are seen to be predominantly forward scattered, with the relative intensity of the forward peak reducing with increasing rotational excitation, such that the CM scattering distribution for products in the highest probed rotational quantum state is seen to be almost isotropic.

Following completion of the work presented here, Toomes and Kitsopoulos reported CM angular scattering distributions for the Cl + *n*-C_4H_{10} reaction at a collision energy of 0.32 eV obtained using the ‘crossed’ parallel beam technique discussed in Section 4.4.1 [77]. Angular scattering distributions were extracted from the experimental images by direct integration of the raw data over velocity. As was noted previously, unlike forward convolution methods, this approach does not take into account the differing sensitivities to forward and backward scattered products or the speed distribution of the Cl atoms. An additional shortcoming of the direct inversion technique is that differentiation between the two available reaction pathways was not possible. The CM angular scattering distributions obtained from the experiments of Toomes and Kitsopoulos are compared with the results of the present investigation in Figure 5.14. The distributions obtained from the two experiments are seen to be in very good agreement, providing strong support for the credibility of both sets of results.

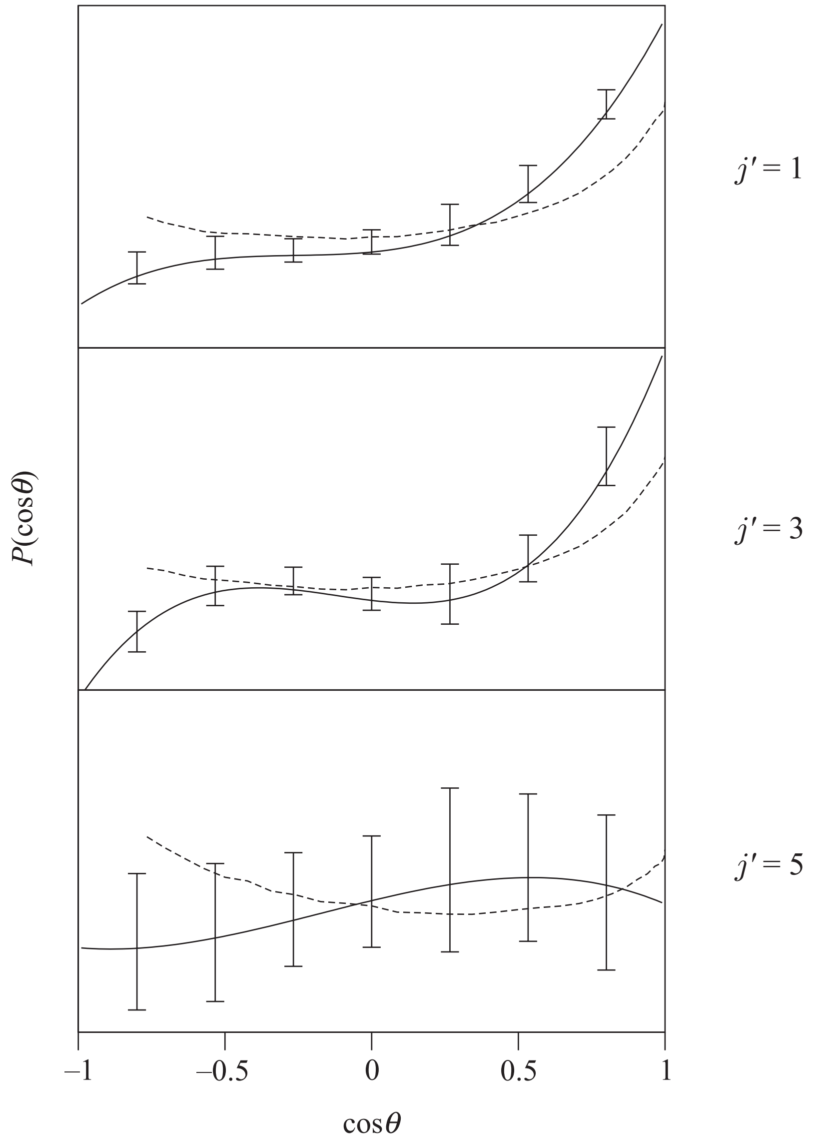

Figure 5.14: Comparison between the CM angular scattering distributions obtained in the present study (—) and those obtained from the 'crossed' parallel beam experiments of Toomes and Kitsopoulos (- - -) [77, 218]. From top to bottom, data are shown for HCl($v' = 0$,$j' = 1$, 3 and 5).

Comparison of the total CM velocity-angle flux map for the Cl + *n*-C_4H_{10} reaction shown in Figure 5.11 with that obtained by Suits and co-workers for the Cl + C_3H_8 reaction (see Figure 5.2) reveals that, overall, a greater degree of forward scattering is seen in the current photoloc study than in the crossed molecular beam experiment. Abstraction of a hydrogen atom from a primary carbon site is seen from the present results to be associated with predominantly forward scattering, while more isotropic and less forward peaked scattering is seen for the products of secondary hydrogen atom abstraction. The results of the crossed molecular beam experiments by Suits and co-workers on the Cl + C_3H_8 and Cl + *n*-C_5H_{12} reactions initially suggested the opposite assignment, namely that hydrogen atom abstraction from a primary carbon site was associated with backward scattering of the products, while abstraction of hydrogen atoms from secondary carbon sites yielded forward scattered products [222, 223]. This assignment was later brought into question by the results of the Cl + C_2H_6 reaction presented in Chapter 4, in which only primary hydrogen atoms were available for abstraction and the products were seen to be predominantly forward scattered. Re-assignment of the results of the crossed molecular beam experiments on the Cl + C_3H_8 and Cl + *n*-C_5H_{12} reactions in the light of these new results brings them into agreement with the assignment for the Cl + *n*-C_4H_{10} reaction presented here [222, 223, 247].

The differing propensities in the CM angular scattering of the products formed *via* the two abstraction pathways, and the different HCl product rotational excitation associated with each, suggests that two reaction mechanisms may be needed to explain the dynamics of the Cl + *n*-butane system. Consider first the mildly exothermic primary hydrogen atom abstraction channel, producing forward scattered HCl products formed in low rotational states. The dynamical characteristics of this abstraction pathway appear to match strongly those of a peripheral chemical reaction, in which abstraction of an atom at the periphery of a reagent [220] leads to forward scattering of the products of a direct exoergic atom transfer reaction. As was mentioned in Section 5.2.2, transition state calculations on the Cl + C_3H_8

and Br + n-C_4H_{10} systems suggest that the optimum geometry for both abstraction channels in the Cl + n-butane reaction is likely to be that in which the Cl–H–C atoms are arranged collinearly. In this arrangement, the impact parameter, b, for the abstraction of a hydrogen atom from a primary carbon site is necessarily non-zero and relatively large. This corresponds to an opacity function, $P(b)$, for this reaction pathway which is zero (or very small) at low b and which peaks at impact parameters on the order of the distance from the centre-of-mass of the n-butane molecule to the chlorine atom in the transition state, $\sim$4 Å (i.e., the periphery of the n-C_4H_{10} molecule). A similar mechanism, albeit less extreme than that considered here, was also suggested for the Cl + C_2H_6 reaction (where abstraction can take place only from primary carbon sites) in Section 4.4.1, for which the HCl($v' = 0$,j') rotational population distribution and rotational state resolved CM angular scattering distributions are seen to be very similar to those determined for the primary abstraction pathway here. Owing to the smaller overall size of ethane compared to n-butane, however, the opacity function for the reaction of chlorine with ethane is likely to be non-zero at much lower impact parameters and extend to significantly smaller values of b. This may be the origin of the slightly greater amount of backward scattering seen in the Cl + C_2H_6 reaction when compared to abstraction of hydrogen from a primary carbon site in n-butane.

The more exothermic abstraction of a hydrogen atom from a secondary carbon site produces more isotropically, but forward peaking, scattered HCl products that are (relatively) rotationally excited. As for abstraction of a hydrogen atom from a primary carbon site, this reaction pathway is expected to be direct and to have a collinear transition state. From similar considerations to those used in the primary reaction channel, the estimated range of impact parameters over which the opacity function for this reaction pathway is expected to be non-zero extends from $b = 0$ to approximately 2.5 Å. For a direct reaction occurring primarily at low impact parameters, products are expected to be predominantly backward scattered. Whilst the observed scattering is not as extreme as this, greater backwards and sideways scattering is seen for this reaction pathway than for abstraction of a hydrogen atom from a primary carbon site, and a more rebound-type mechanism is thus suggested for this reaction channel. This is consistent with the higher rotational excitation found for the HCl products formed in this reaction pathway. Forward scattering of the products of secondary hydrogen atom abstraction may be taken as an indication of a wide cone of acceptance, for which the approach of the chlorine atom is not tightly constrained to be collinear with the breaking C–H bond. Release of energy along the axis of the C–H bond for these slightly bent transition states yields rotational excitation of the HCl products, as observed for this reaction pathway. The observed scattering dynamics can thus be well accounted for through this interplay between the impact parameter and the angle of approach of the reactants.

Proposed schematic opacity functions for the two abstraction pathways are shown in Figure 5.15. The reaction cross-section, σ_r, may be written in terms of the opacity function as

$$\sigma_\mathrm{r} = \int_0^\infty 2\pi b P(b)\,\mathrm{d}b, \tag{5.10}$$

where $2\pi b\,\mathrm{d}b$ is the element of the total collision cross-section and $P(b)$ is the fraction of collisions at an impact parameter b that leads to reaction. The opacity functions for the two reaction channels have been scaled such that the reaction cross-sections returned from them using Equation 5.10 reflect the degree to which abstraction from a secondary carbon site is favoured over that from a primary carbon site, allowing for the 3:2 statistical abundance of primary to secondary H atoms. The thermal rate constant, $k(T)$, given by the average $\langle v\sigma_\mathrm{r}\rangle$, where v is the relative speed of the reagents, derived from these opacity functions is in broad agreement with the kinetic data obtained by Sarzynski and Sztuba [184].

5.4.4 Energy Partitioning

On average, just under 30% of the available energy is seen to be channelled into the internal modes of both the *n*- and *s*-butyl radical co-products. Owing to the different exothermicities for the two reaction pathways, this corresponds to energies

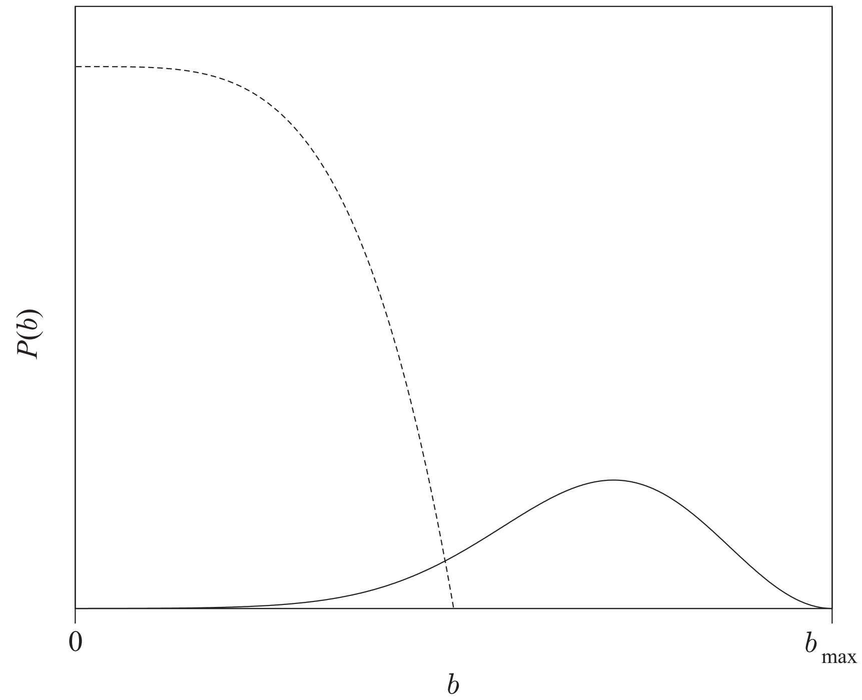

Figure 5.15: Schematic opacity functions for abstraction of hydrogen atoms from primary (—) and secondary(- - -) carbon sites in the Cl + *n*-butane reaction. The two distributions have been scaled relative to each other such that the reaction cross-sections, σ_r, obtained from them using Equation 5.10 reflect the differing reactivities determined for the two abstraction sites.

of around 950 cm^{-1} and 1260 cm^{-1} being partitioned into internal excitation of the *n*-butyl and *s*-butyl co-fragments, respectively. The HCl rotational state resolved product speed distributions obtained from the 'crossed' parallel beams experiments by Toomes and Kitsopoulos described in the previous Section suggest a similar level of excitation of the internal modes in the butyl co-products, despite differentiation between the two reaction pathways not being possible in their study [77]. The mean fractions of the total available energy found in internal excitation of the *n*-butyl and *s*-butyl co-fragments in the present investigation are slightly higher than the 22% found for the ethyl radical products of the Cl + C_2H_6 reaction (see Section 4.4.2). This may be a reflection of both the higher collision energy employed in the Cl + *n*-C_4H_{10} reaction and of the greater number of low energy internal modes in the butyl radical compared with the ethyl radical. The level of rotational excitation of the HCl products is very similar in the two reaction systems.

In their crossed molecular beam study on the reaction of chlorine with propane, Suits and co-workers found that 40–50% of the available energy was deposited into the internal modes of the HCl and propyl products, with most of this energy concluded to be directed into the propyl radicals [222]. This is significantly greater internal excitation of the alkyl co-fragment than found here for either the Cl + *n*-C_4H_{10} or Cl + C_2H_6 reactions. Also note that more backward scattering was seen in the Cl + C_3H_8 crossed molecular beam study than in the current photoloc investigations into the reactions of chlorine with *n*-butane and ethane. It is possible that these two observations may be linked and could, perhaps, be symptomatic of a systematic error in the crossed molecular beam experiments of Suits and co-workers. In these experiments, the alkyl fragments are detected using vacuum ultraviolet synchrotron radiation to effect photoionisation of the alkyl radicals, with the resulting ions detected mass spectrometrically. If alkyl radical products in which the internal modes are excited are preferentially ionised (and therefore detected), then the overall energy disposal obtained from the resulting data will be biased towards greater internal excitation of the alkyl products. Furthermore, alkyl products that are backwards scattered are generally likely to be more internally excited than those that are forward scattered, and thus there will also be a bias towards the detection of backwards scattered products. A similar difference between the results of crossed molecular beam experiments using photoionisation of alkyl products by Suits and co-workers and those from photoloc studies of the co-fragments has been seen in the reactions of O(^{3}P) with saturated hydrocarbons [74–76]. Bulb experiments carried out by Kajimoto and co-workers with Doppler-resolved laser induced fluorescence detection of the OH fragments find the products of the reactions of O(^{3}P) with isobutane and cyclohexane to be almost isotropically scattered [249, 250]. In the case of the O(^{3}P) + *c*-C_6D_{12} reaction, around 60% of the available energy was seen to be deposited into the cyclohexyl products. At similar collision energies, however, Suits and co-workers find the *i*-C_4H_9 and *c*-C_6D_{11} fragments to be strongly backward scattered, with a slightly greater fraction of the available energy found as internal excitation of the alkyl products [75].

5.4.5 Internal Excitation of the Butyl

Two possible sources of the butyl product internal excitation yield n-butyl and s-butyl radicals which are either predominantly rotationally, or predominantly vibrationally, excited. The internal excitations of the two butyl radicals will be considered separately due to the differing mechanisms and exothermicities associated with the two reaction pathways.

n-Butyl Products

Consider first the abstraction of a hydrogen atom from a primary carbon site in n-butane. Assuming that the product n-butyl radical is well approximated as a rigid prolate near-symmetric top with a rigid carbon frame, the rotational levels are given approximately by

$$F(J, K) \simeq \bar{B}J(J+1) + (A - \bar{B})K^2, \tag{5.11}$$

where, assuming the n-butyl radical takes on the lowest energy conformation, the average rotational constant about the b or c axes, $\bar{B} = 0.5(B + C)$, is calculated to be ~ 0.123 cm^{-1}, and the rotational constant about the a axis, A, is calculated to be ~ 0.827 cm^{-1} [251]. If all the energy observed to be channelled into internal excitation of the n-butyl radicals was rotational in origin, in the two extreme cases this would correspond to end-over-end rotational excitation of n-butyl to $F(J \simeq 88, K = 0)$, or rotational excitation about the a axis to $F(J = K \simeq 34)$. Similar considerations to those used in the discussion of the internal excitation of the ethyl product of the Cl + C_2H_6 reaction in Section 4.4.3, where an impulsive release of the reaction exothermicity along the breaking C–H bond in the transition state geometry was seen to impart a torque on the alkyl fragment, lead to the generation of

n-butyl rotational angular momenta of $\sim 40\hbar$ for end-over-end rotation, or of $\sim 25\hbar$ for rotation about the a axis. This estimate is a lower limit since, experimentally, the energy partitioned into the n-butyl radical is found to be rather greater than the reaction exoergicity of ~ 700 cm^{-1}. In a peripheral mechanism, higher torques may be expected to be imparted on the n-butyl radical from abstraction of the hydrogen atom by a fast moving chlorine atom. Note that the actual rotation is likely to be about all three axes with intermediate values of J and K, since the breaking C–H bond is not necessarily in the plane of the carbon backbone. End-over-end rotation is expected to dominate, however, due to the larger torque exerted for this motion.

Energy release into the vibrational modes of the n-butyl products may be associated with relaxation of the –CH_2 moiety in the nascent radical from the pyramidal geometry expected to be adopted in the transition state, to the near planar arrangement in the free n-butyl radical [252]. This change in geometry could give rise to excitation of the out-of-plane –CH_2 rocking mode;[8] the frequency of this mode has been measured to be 520 cm^{-1} and its motion is thought to be almost independent of the non-radical portion of the hydrocarbon chain [252–255]. From the similarities in the vibrational frequencies of the radical rocking modes and the transition state geometries between this abstraction pathway and the Cl + C_2H_6 reaction, one would expect a similar vibrational state distribution to be predicted by the Franck–Condon overlap model for primary hydrogen abstraction from n-butane to that calculated for the Cl + C_2H_6 reaction in Section 4.4.3. The vibrational state distribution returned from this analysis was seen to be very broad with a peak at $v' = 4$. As found for the reaction of chlorine with ethane, the level of vibrational excitation predicted by this model for the n-butyl radical is unrealistically high. However, lower levels of excitation could be generated if there was a more gradual relaxation of the geometry of the CH_2 moiety from the transition state to the products.

---

[8] This vibrational mode is referred to as the 'radical umbrella' mode in Refs. [253] and [254], and as the 'radical bend' in Ref. [252].

s-Butyl Products

Assuming that the *s*-butyl radical formed by abstraction of a hydrogen atom from a secondary carbon site in *n*-butane may also be well approximated to a rigid prolate near-symmetric top with a rigid carbon frame that has energy levels given by Equation 5.11, the average rotational constant about the *b* or *c* axes, $\bar{B} = 0.5(B + C)$, is calculated to be ~ 0.118 cm^{-1}, while the rotational constant about the *a* axis, A, is calculated to be ~ 0.891 cm^{-1} [251]. The maximum rotational state accessible if all the observed available energy deposited into internal modes of the *s*-butyl is found as end-over-end rotation is $F(J \simeq 104, K = 0)$, or for rotational excitation about the *a* axis, $F(J = K \simeq 38)$. Impulsive release of the reaction exothermicity along the breaking C–H bond in the transition state is not expected to yield such high levels of end-over-end rotation, but is more likely to excite rotation about the *a* axis. The axis of the breaking bond passes very close to the centre-of-mass of the *s*-butyl, thus such an impulse will exert only a very small torque on the nascent molecule, and owing to the high moments of inertia about the *b* and *c* axes, the components of the impulse about these axes will yield only modest levels of end-over-end rotational excitation. Using a transition state geometry based on the structure of *n*-butane, this is indeed seen to be the case, with end-over-end rotational angular momenta of only $\sim 34\hbar$ (~ 140 cm^{-1}) found to be generated. The moment of inertia about the *a* axis is much lower, however, and the component of the impulse about this axis is thus expected to induce higher levels of rotation about this axis. Rotational angular momenta of $\sim 28\hbar$ (~ 710 cm^{-1}) are calculated to be generated for rotation about the *a* axis. The principal rotational motion of the *s*-butyl products is thus thought to be around the *a* axis. As in the case of the *n*-butyl radical, the actual rotation will be about all three axes, with lower values for J and K than predicted from the extremes presented here.

Very little is known about the vibrational modes of the *s*-butyl radical, and thus discussion about energy release into these modes will be limited. Relaxation of the >C–H moiety from the expected pyramidal geometry of the transition state to the more planar equilibrium geometry in the free *s*-butyl radical is likely to excite the out-of-plane rocking mode. The frequency of the out-of-plane >C–H rocking mode in *s*-butyl is likely to be similar to that in isopropyl, $\sim 364\ \mathrm{cm^{-1}}$ [255]; the next lowest vibrational mode in the isopropyl radical is the C–C stretch with a frequency of $\sim 880\ \mathrm{cm^{-1}}$ [255]. The lower frequency of the out-of-plane >C–H rocking mode in *s*-butyl compared to the out-of-plane –CH_2 rocking mode in *n*-butyl, suggests a smaller force constant for this mode. One would therefore expect, for a similar change in the dihedral angle on going from the transition state to the *s*-butyl radical, the Franck–Condon model to predict vibrational excitement to a greater extent in the *s*-butyl fragment than was found in either the ethyl or *n*-butyl radicals. The predicted vibrational excitation was seen to be unreasonably high in these previous cases, so a greater vibrational excitation of the rocking mode for the *s*-butyl radical is also expected to be unreasonable. Note that excitation of the C–C stretching modes in the carbon backbone is also energetically allowed and cannot be ruled out as being associated with the internal excitation of the *s*-butyl fragment.

5.5 Summary

Using the Legendre moment analysis method, rotational state resolved CM angular scattering and kinetic energy release distributions have been determined from experimental velocity-map ion images of the HCl($v' = 0, j = 0$–6) products of the reaction of chlorine with *n*-C_4H_{10}. The relative contributions of the two abstraction pathways in the reaction have been obtained for each HCl($v' = 0$) rotational state investigated. Abstraction of a hydrogen atom from a primary carbon site is seen to produce rotationally very cold HCl($v' = 0$) products that are forward scattered, whereas abstraction of a hydrogen atom from a secondary carbon site yields more isotropically scattered HCl($v' = 0$) products formed with higher rotational excitation. The reaction is believed to proceed *via* two simultaneously mechanisms: a peripheral reaction mechanism is thought to operate for the primary hydrogen atom abstraction channel, whilst a more rebound-type mechanism is seen to account for the dynamics of the secondary abstraction channel. The returned kinetic energy release distributions show that around 30% of the available energy is found as internal excitation of the *n*-butyl and *s*-butyl products. Possible sources of this excitation have been discussed.

Chapter 6

The Dynamics of the Cl + CH_4 Reaction

6.1 Introduction

Abstraction of a hydrogen atom from methane by chlorine represents the simplest of the reactions of chlorine atoms with saturated hydrocarbons and as such provides a good test of both experiment and theory. The methyl radical products are amenable to direct rovibrational state selective detection *via* (2+1) REMPI, allowing the experimental difficulties associated with the high levels of background HCl signal encountered for the Cl + C_2H_6 and Cl + n-C_4H_{10} reactions to be avoided. Through investigation of the reactions[1]

$$\begin{aligned} \mathrm{Cl} + \mathrm{CH_4} &\longrightarrow \mathrm{HCl} + \mathrm{CH_3} & \Delta_\mathrm{r} H_0^{\ominus} &= -5.0\,\mathrm{kJ\,mol^{-1}} & (6.1)\\ \mathrm{Cl} + \mathrm{CD_4} &\longrightarrow \mathrm{DCl} + \mathrm{CD_3} & \Delta_\mathrm{r} H_0^{\ominus} &= -11.5\,\mathrm{kJ\,mol^{-1}} & (6.2)\\ \mathrm{Cl} + \mathrm{CH_3D} &\longrightarrow \mathrm{HCl} + \mathrm{CH_2D} & \Delta_\mathrm{r} H_0^{\ominus} &= -5.5\,\mathrm{kJ\,mol^{-1}} & (6.3)\\ &\longrightarrow \mathrm{DCl} + \mathrm{CH_3}, & & & (6.4) \end{aligned}$$

the aim of the current study is to clarify and explain some of the discrepancies that have arisen from the various experimental and theoretical studies carried out pre-

---

[1] Enthalpies of reaction calculated using D_0^0(H–Cl) = 427.64 ± 0.02 kJ mol^{-1} [177, 178] and D_0^0(H–CH_3) = 432.64 ± 0.29 kJ mol^{-1} [256]. The thermochemistry for the reactions with CD_4 and CH_3D were calculated from zero point energy differences based on vibrational frequencies [255] and using D_0^0(D–Cl) = 432.59 ± 0.01 kJ mol^{-1} [257]. In these calculations, the CH_2D vibrational frequencies were taken as those evaluated in Ref. [258].

viously and to provide a framework within which the origin of these inconsistencies may be understood. A brief overview of these previous investigations is provided in the following section, with the aim of placing the current work in context.

6.2 Previous Work on the Cl + CH_4 Reaction

6.2.1 Kinetics Studies

Owing to its importance in both atmospheric and combustion chemistry, the kinetics of the Cl + CH_4 reaction have been the subject of study for almost fifty years. Kinetic work to date has spanned the wide temperature range of 181–1104 K [185, 189, 190, 200, 259–272], with particularly good agreement between the results obtained by both direct and relative rate methods at the lower end of this temperature range. The direct measurements, which yield the absolute rate constant, have generally employed similar techniques to those used in the kinetic studies of the Cl + C_2H_6 reaction that were outlined in Section 4.2.1. Reviews of the resulting rate constants can be found, for example, in Refs. [195–199, 271]. The recommended value of the absolute rate coefficient, k, given by these reviews is 1.0×10^{-13} $\text{cm}^3\,\text{molecule}^{-1}\,\text{s}^{-1}$ at 298 K. Of particular relevance to the present study is that the reaction is seen to exhibit pronounced non-Arrhenius behaviour at both low and high temperatures. A variety of factors have been proposed to account for this behaviour. Heneghan *et al.* [273] showed that the estimated temperature dependence of the transition state heat capacity can lead to non-Arrhenius behaviour at high temperatures. Several studies have indicated that quantum mechanical tunnelling contributes to the curvature in the Arrhenius plots at low temperatures [198, 199, 263, 267, 274–277]. Ravishankara and Wine [200] suggested that the non-Arrhenius behaviour and the large variability in the low temperature measurements could be attributed to differential reactivity between the thermally populated ground state Cl($^2P_{3/2}$) and spin-orbit excited Cl($^2P_{1/2}$) atoms. However, the electronic quenching rates on which this analysis was based have since been demonstrated to be inaccurate [190, 278], with recent studies indicating that the reaction of CH_4 with Cl($^2P_{1/2}$) is not significantly faster than that with Cl($^2P_{3/2}$) [270, 279]. The enhanced reactivity of thermally populated vibrationally excited methane molecules has also been investigated as a source of curvature in the Arrhenius plots. An enhancement of the reaction probability through excitation of the CH_4 stretching modes was concluded to influence the rate of reaction at high temperatures strongly [198, 199]. Very recently, Bryukov *et al.* [272] combined new absolute experimental rate constants for the Cl + CH_4 reaction, measured using the discharge flow/resonance fluorescence technique over the temperature range of 295–1104 K, with those determined in the previous studies. A good fit to the resulting data set was achieved using the modified Arrhenius expression

$$k = (5.69 \times 10^{-19})\, T^{2.49}\, \mathrm{e}^{-609/T}\ \ \mathrm{cm^3\, molecule^{-1}\, s^{-1}}\ (200\text{–}1104\,\mathrm{K}). \tag{6.5}$$

In the narrower temperature range of 200–300 K, however, the data are seen to be reproduced reasonably well using the simple Arrhenius expression, $k = A\,\mathrm{e}^{-E_\mathrm{a}/RT}$, with pre-exponential factor, $A = 6.6 \times 10^{-12}\ \mathrm{cm^3\, molecule^{-1}\, s^{-1}}$, and an activation energy of $E_\mathrm{a}/R = -1240\,(\pm 200)\,\mathrm{K}$ [195].

Although there have been several measurements of the kinetic isotope effects for the reaction of chlorine atoms with the complete set of deuterated methanes, disagreement over some of the reported values remains. This has been discussed in detail by Boone *et al.* in light of further experiments and theoretical calculations [280]. An average of the results of direct and indirect measurements yields the rate constants $k(\mathrm{Cl{+}CH_3D}) = (6.2{\pm}0.2) \times 10^{-14}\ \mathrm{cm^3\, molecule^{-1}\, s^{-1}}$ [260, 270, 280–283] and $k(\mathrm{Cl} + \mathrm{CD_4}) = (6.72 \pm 0.02) \times 10^{-15}\ \mathrm{cm^3\, molecule^{-1}\, s^{-1}}$ [280, 283–285] in the temperature range 295–305 K. The rate constants are seen to decrease with increasing deuteration due to a primary kinetic isotope effect, i.e., the activation energy for breaking a C–D bond is greater than that for a C–H bond due to the lower zero point energy of the more deuterated methane.

6.2.2 Dynamical Studies

In addition to the kinetic studies, there have been numerous experimental attempts to elucidate the dynamics of the reaction of atomic chlorine with methane [109, 111, 208, 210, 214, 258, 279, 286–293]. Much of the work has been performed by Zare and co-workers, and has mainly addressed the enhancement and control of the reaction cross-section by vibrational excitation of the methane reactants [109, 111, 208, 210, 279, 286–291]. The Cl atom reactions with CH_4 and CHD_3 excited by one quantum in the antisymmetric stretching modes, $\nu_3 = 1$ and $\nu_1 = 1$ respectively, were seen to yield HCl products with similar rovibrational state resolved CM angular scattering distributions. The HCl($v' = 1$,j') products of both reactions, accounting for $\sim 30\%$ of those observed in each case, were found to be formed rotationally cold and were seen to be predominantly forward scattered with a backward peak that was seen to increase with increasing j'. A hotter rotational population distribution was determined in both reactions for the HCl($v' = 0$,j') products, which were seen to be scattered in the backwards and sideways directions. By comparison with the reactivity of methane in the absence of infrared excitation, a vibrational enhancement for excitation of the antisymmetric stretch in CH_4 of 30 ± 15 was obtained at a mean collision energy of 0.16 eV [208]. This value is strongly supported by recent calculations based on the non-Arrhenius behaviour seen in the kinetics experiments by Michelson and Simpson, from which a vibrational enhancement factor of 36 was determined [198, 199]. This enhancement was envisaged as arising from a lowering of the reaction barrier and a corresponding opening of the cone of acceptance of the reaction upon vibrational excitation of the methane reactant. These studies were extended to the excitation of two quanta of stretch in CH_4 and its isotopomers [288–290]. The results indicated that the methyl products were formed without significant energy redistribution of the initially prepared vibrational state [289] and, furthermore, that the reaction can be controlled to achieve both selective bond breaking and a specific vibrational mode population distribution in the products [289, 290]. The data support the view that the reaction with vibrationally excited methane remains direct [289] and that the CH_3 moiety behaves essentially as a spectator [290].

A particularly interesting and controversial aspect of the dynamics of the title reaction has been the role played by the low frequency torsional (ν_2) and/or umbrella bending (ν_4) modes of CH_4 in promoting reaction. Kandel and Zare were the first to note that the CH_3 products of the Cl + CH_4 reaction are born with too much kinetic energy for them to have been produced exclusively by reaction of Cl($^2P_{3/2}$) with ground vibrational state CH_4 [287]. The LAB frame velocity distribution of the CH_3 products was interpreted in terms of the competing reactivity of Cl with ground state and with torsion- and bend-excited methane. Subsequent experiments by Zare and co-workers demonstrated that the product velocity distribution was incompatible with reaction of methane with spin-orbit excited Cl($^2P_{1/2}$) atoms [279], which could have been another possible source of the high kinetic energy products [208], and that the reaction of Cl($^2P_{1/2}$) with CH_4 near threshold was insignificant. Note that Cl($^2P_{1/2}$) atoms are not produced in significant quantities by photolysis of Cl_2 at wavelengths between $\sim$300 nm and 375 nm [128], the source of Cl originally employed by Zare and co-workers [208, 287]. The experiments also confirmed that reactions of spin-orbit excited Cl($^2P_{1/2}$) atoms could be ruled out as an explanation for the non-Arrhenius behaviour of the thermal rate coefficient [288], as had been proposed previously by Ravishankara and Wine [200]. Zare and co-workers instead suggested that the low frequency, thermally populated vibrational states (i.e., the ν_2 torsional mode and the ν_4 umbrella mode) of methane could enhance the reactivity by factors as high as 200 and 400 for the Cl + CH_4 reaction at collision energies of 0.24 eV and 0.16 eV respectively, and by a factor of 80 for the reaction of Cl with CD_4 at a collision energy of 0.28 eV [279, 287]. Note that for the Cl + CH_4 reaction, these vibrational enhancement factors for excitation of the umbrella bending or torsional modes are much larger than that determined for excitation of the antisymmetric stretching mode. This very high level of umbrella bending (or torsional) mode enhancement was found to be inconsistent with a subsequent analysis of the non-Arrhenius behaviour of the reaction rate by Michelson and Simpson [198]. The CH_3

products of the reaction of Cl atoms with ground vibrational state CH_4 at a collision energy of 0.24 eV were seen to be predominantly sideways scattered, whereas the CD_3 products of the reaction of chlorine with ground state CD_4 at a collision energy of 0.28 eV were seen to be more backward scattered. Note that almost all of the methyl products were found to be formed in the lowest vibrational level, with only a very small amount of umbrella bending (ν_2) excitation observed.

The issues of vibrational enhancement and mode selectivity have also been investigated by Crim and co-workers [258, 292, 293]. Excitation of the symmetric stretch-umbrella bend combination (ν_1+ν_4) of CH_4 was seen to promote reaction with atomic chlorine more efficiently than excitation of the antisymmetric stretch-umbrella bend combination ($\nu_3 + \nu_4$) by a factor of 1.9 ± 0.5. The reaction cross-section of the Cl atom reaction with $CH_4(\nu_1 + \nu_4)$ was found to be 19 ± 5 times larger than that with methane in the ground or thermally populated states [292]. The fact that the vibrational population distribution of the CH_3 product was found to be similar for both vibrationally excited reactions was interpreted as an indication that the influence of excitation of the ν_4 umbrella bending mode was the same in both cases. A similar study, in which CH_3D reactants were employed, indicated that excitation of the symmetric C–H stretch yields methane that is 7.1 ± 0.6 times more reactive than that obtained by excitation of the antisymmetric stretch. Two quanta excitation of the ν_2 C–D stretch was found to promote reaction at the C–D bond, while excitation of the ($\nu_4 + \nu_3$) combination (involving the C–H stretch and CH_3 umbrella bending modes) was seen to promote hydrogen atom abstraction. The difference in reactivity of the symmetric and antisymmetric stretching modes of CH_3D has recently been explained in terms of differences in the localisation of the vibrational motion as the reactants approach one another [258].

The most recent experimental development has been made by Liu and co-workers, who have studied the Cl + CH_4 and Cl + CD_4 reactions at collision energies of 0.20 eV and 0.21 eV respectively, by employing the crossed-molecular beam technique, coupled with methyl radical detection using REMPI and time-sliced ion velocity imaging [88]. The returned CM angular scattering distributions are in qualitative agreement with the previous single beam experiments of Zare and co-workers [208, 279, 287], but are of significantly higher resolution. The experiments of Liu and co-workers, however, find only very modest cross-section enhancements (~ 3) with torsional/bending mode excitation. The contribution from vibrationally excited methane reactants is clearly resolved in the ion images and becomes more visible when the nozzle temperature is increased above ambient. The level of vibrational enhancement found by Liu and co-workers is in excellent agreement with an analysis of kinetic data by Michelson and Simpson, in which excitation of the methane umbrella bending mode was calculated to enhance the reaction probability by a factor of ≤ 2 [198, 199]. The origin of the discrepancy between these new experiments performed by Liu and co-workers and the previous work of Zare and co-workers is at present unclear and is one of the principal issues addressed in the present work.

6.2.3 Theoretical Studies

Despite the relative complexity of the Cl + CH_4 system, many theoretical calculations have been performed using various levels of approximation and theory [201, 274, 275, 294–299]. Several *ab initio* studies of the structures and energetics of the reactants, transition state and products have been undertaken. The transition state was found to be collinear along Cl–H–C and located near the product channel [294, 295]. A direct dynamics approach, together with variational transition state theory (VTST) including multidimensional semi-classical tunnelling corrections, was used by Duncan and Truong to calculate both thermal and vibrationally state-selected rate constants in the temperature range 200–1000 K [274]. These calculations, in which the motional character of the vibrational modes was assumed to be preserved along the reaction coordinate, suggested that excitation of the symmetric stretching and umbrella bending modes could enhance reactivity by factors of 1600 and 52 respectively, at a temperature of 200 K. Based on analytical functions for the potential energy surface of the analogous H + $CH_4 \longrightarrow CH_3 + H_2$ reaction devised by Joseph *et al.* [300] and Jordan and Gilbert [301], Corchado and co-workers developed two new empirical potential energy surfaces for the Cl + CH_4 system [275, 297]. Canonical variational transition state theory (CVT) calculations, which included tunnelling corrections, were performed on these potential energy surfaces and yielded rate constants and kinetic isotope effects in good agreement with experimental values. State-selected rate constants at 200 K obtained on the most recent of the two potential energy surfaces [297] indicated vibrational enhancements in the range of 400–500 and 50–240 for excitation of the C–H stretching and umbrella bending modes respectively. Troya *et al.* have recently reported excellent agreement with the experimental kinetic data in the 200–500 K temperature range using the variational transition state approach, which again included tunnelling corrections, on a full-dimensional *ab initio* potential energy surface [299]. The same authors also performed quasi-classical trajectory calculations on a reduced dimensionality (triatomic) potential energy surface and obtained state-selected CM angular scattering distributions in qualitative agreement with experiments [299]. Very recently, Rudić *et al.* [205] estimated the HCl and CH_3 product rovibrational excitations using the on-the-fly *ab initio* trajectory approach described previously (see Section 4.4.2). The HCl($v' = 0,j'$) rotational population distribution derived from these calculations is compared with that determined by Troya *et al.* [299] using quasi-classical trajectory calculations and the distributions obtained experimentally by Varley and Dagdigian [214] and by Zare and co-workers [208] in Figure 6.1. The on-the-fly *ab initio* trajectory results obtained by Rudić *et al.* [205] are seen to be in good agreement with those of the quasi-classical trajectory calculations by Troya *et al.* [299], although both are found to give hotter HCl rotational distributions than those determined from the experiments. The rotational state distribution of the CH_3 radical fragments determined from the calculations of Rudić *et al.* [205] was also seen to be cold, peaking at $J' = 2$ and gradually decreasing to $J' = 8$ (see Section 6.3.1), in agreement with the cold rotational distribution observed by Kandel and Zare [287].

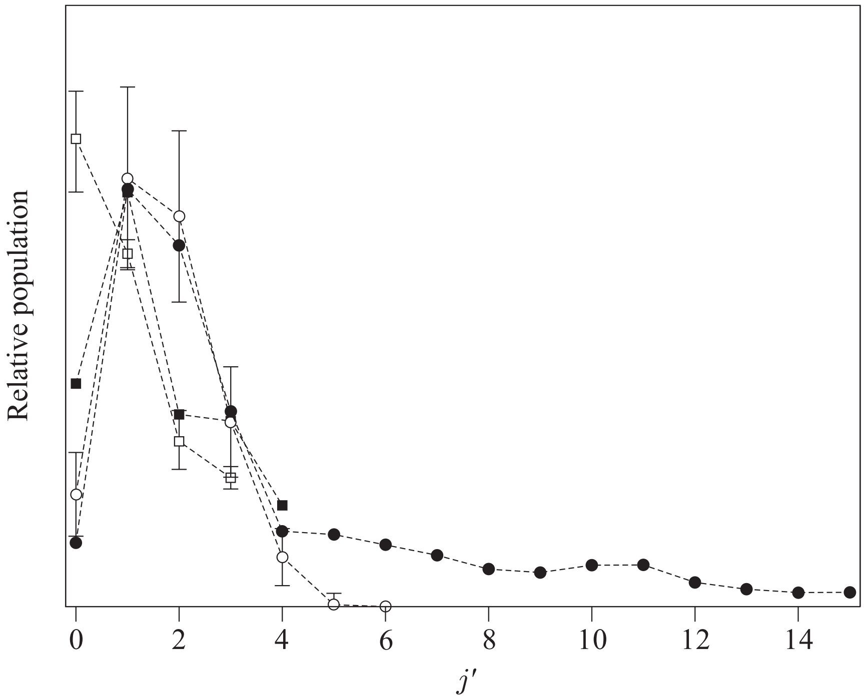

Figure 6.1: A comparison of the nascent rotational quantum state population distributions for the HCl($v' = 0$,j') products of the reaction of Cl with CH$_4$ obtained experimentally by Varley and Dagdigian (--■--) [214] and by Zare and co-workers (--□--) [208], with those determined from theoretical calculations by Troya *et al.* (--○--) [299] and by Rudić *et al.* (--●--) [205]. The error bars represent 1σ confidence limits; the distributions have been normalised in the j' range shown.

To date, few quantum mechanical scattering calculations on the title reaction have been performed, all of which have been of reduced dimensionality [276, 302–305]. Nyman and co-workers first reported calculations employing the 2D rotating bond approximation [302], which were subsequently extended to 3D [303] and 4D calculations [276, 304], with the most recent treatment including both the umbrella bending mode and an approximation for CH$_3$ rotation [304]. Rate constants obtained using the J-shifting approximation were found to be smaller than those determined experimentally and exhibited significant tunnelling effects. The vibrational enhancements predicted by the calculations [303] were consistent with those predicted by Duncan and Truong [274], but were of much smaller magnitude than estimated in the experiments of Zare and co-workers [279, 287]. Qualitative agreement was seen between the state-specific CM angular scattering distributions obtained from the theoretical calculations of Nyman and co-workers [276, 304] and those determined experimentally by Zare and co-workers [109, 111, 208, 210, 279, 286–291]. For reactions involving CH_4 reactants in which the symmetric stretching mode was excited, the presence of umbrella bending mode excitation in the methyl products was predicted by the calculations. This is inconsistent with the experimental measurements, which suggest that there is only a small level of excitation of the umbrella bending mode in the methyl products [287]. A more accurate potential energy surface was developed by Yu and Nyman [304] to reinvestigate this last issue, and also to explore the dynamics of the reaction with CD_4. Vibrational excitation of the umbrella mode of the CH_3 product of the reaction of Cl with vibrationally excited CH_4 was also observed in the new calculations, although the CD_3 product of the Cl atom reaction with CD_4 was produced preferentially in the ground vibrational state, in better agreement with the experimental measurements [287]. The most recent quantum mechanical calculation, reported by Skokov and Bowman [305], involved a reduced dimensionality wave packet calculation on the effect of bend excitation of CH_4 on the HCl co-product rotational population distribution. A multi-modal HCl rotational population distribution was observed to correlate with the presence of umbrella bending mode vibrational excitation in the CH_4 reactant and was rationalised in terms of a simple Franck–Condon-type model, in which the bending eigenstates of the transition state were projected onto the rotational states of the product HCl.

6.2.4 Summary

The previous work on the reactions of atomic chlorine with methane and its deuterated analogues can be summarised as follows: (i) the HCl and DCl products of reaction with ground vibrational state CH_4 and CD_4, respectively, are found from both theory [205, 299] and experiment [208, 214] to be formed in very low rotational states of the ground vibrational state; (ii) the methyl radical products of the reaction with ground vibrational state CH_4 and CD_4 are also seen from theory [205, 276] and experiment [287] to be formed predominantly in low rotational levels of the ground vibrational state; (iii) Zare and co-workers [287] and Liu and co-workers [88] found the CH_3 products of the Cl + CH_4 reaction to be predominantly scattered in the sideways direction, whereas the CD_3 products of the Cl + CD_4 reaction were found to be more strongly backward scattered; (iv) controversy remains over the level of vibrational enhancement yielded by excitation of the umbrella bending mode in the methane reactants, with Zare and co-workers [287] suggesting far higher enhancement factors than obtained by either Michelson and Simpson [198] or Liu and co-workers [88].

6.3 Results

6.3.1 REMPI Spectra

Cl + CD_4

A (2+1) REMPI spectrum of the 0_0^0 band of the CD_3 products of the Cl + CD_4 reaction is shown in the upper panel of Figure 6.2. A similar spectrum was recorded by Kandel and Zare for the reaction at a comparable collision energy [287]. The best fit to the data was provided by a spectrum simulated [306] using a single rotational temperature of 80 K. This simulation, also shown in Figure 6.2, employed the spectroscopic constants, line strength factors and predissociation rates reported in Refs. [135, 307, 308]. Note that the fit implies that the high K' rotational states, which lie lower in energy for an oblate top, are more highly populated than the low K' rotational states. This is at variance with the results of an empirical comparison of the S and R branch transitions and symmetric top two-photon linestrength factors by Kandel and Zare, from which they concluded that the methyl radical products were formed preferentially in the lower K' rotational states [287]. In order to investigate this apparent difference, further simulations were performed in which the K' and J' rotational state 'temperatures' were allowed to differ [134]. The qual-

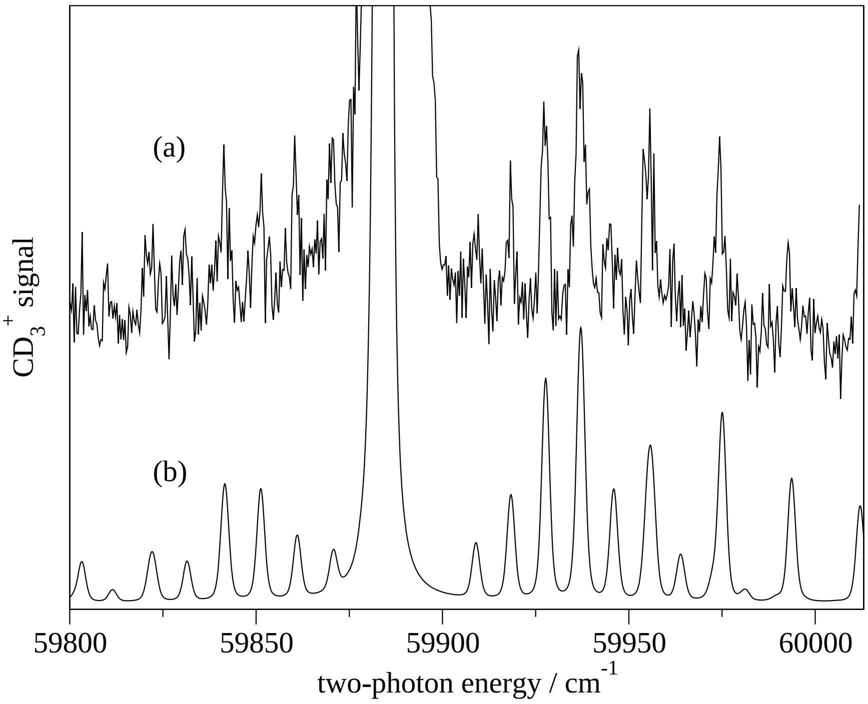

Figure 6.2: (2+1) REMPI spectrum of the CD_3 product of the Cl + CD_4 reaction in the region of the 0_0^0 vibronic band: (a) experimental spectrum, (b) simulated spectrum using a single J',K' temperature of 80 K [306]. The dominant feature in the spectrum is the Q branch.

ity of the fit to the present experimental REMPI spectrum obtained using these simulations was found to be rather insensitive to the assumptions made about the K' state populations. In addition, a good fit to the REMPI spectrum recorded by Kandel and Zare [287] was obtained using the same model as that for the simulation of the present REMPI spectrum when a single J',K' rotational temperature of between 20 and 25 K was employed. The difference in the methyl radical rotational temperatures derived from the two experiments is thought to arise primarily from the differing temperatures of the molecular beams employed, which have been measured as 15 K and 50 K for the experiments in Stanford [287] and Oxford (see Section 2.6) respectively. It is interesting to note that these results suggest that a significant fraction of the rotational excitation observed in the CD_3 products of the Cl + CD_4 reaction arises from excited rotational states of the CD_4 reactant. Similar conclusions have been drawn for the H + H_2O reaction, where a Franck–Condon

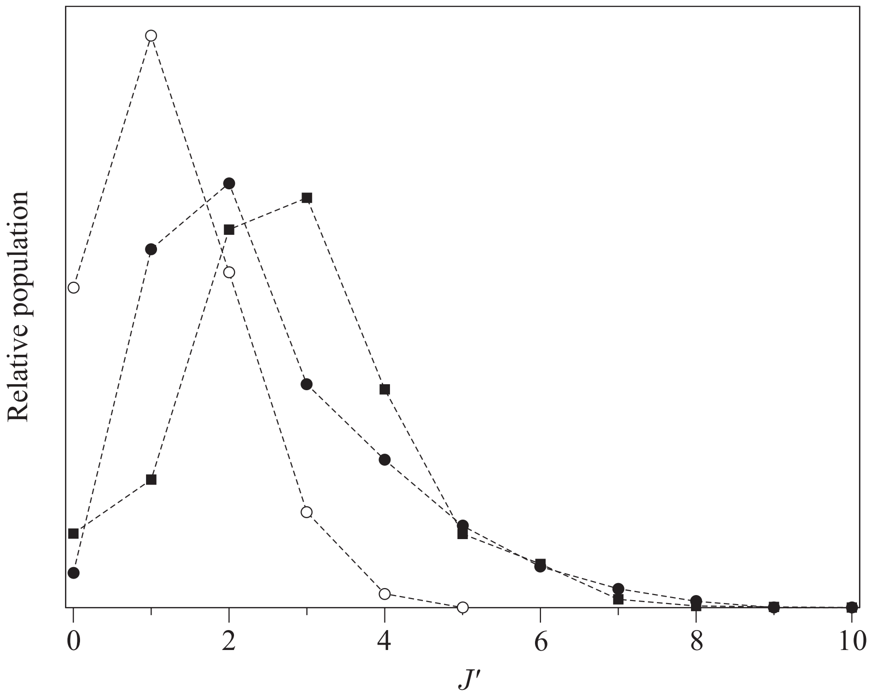

Figure 6.3: A comparison of the rotational quantum state population distributions for the CH_3 radical products of the reaction of Cl with CH_4 obtained from a simulation using a single J',K' rotational temperature of 80 K (- - ■ - -) with the results obtained by Yu and Nyman from 4D quantum mechanical scattering calculations (- - ○ - -) [276] and by Rudić *et al.* from on-the-fly *ab initio* quasi-classical trajectory calculations (- - ● - -) [205]. The distributions have been normalised in the J' range shown.

model can be used to explain the OH product rotational population distribution at low collision energy [309–314].

Despite the uncertainties in the simulations, it is clear that the CD_3 products of the Cl + CD_4 reaction, and presumably the methyl radical products of the Cl + CH_4 and Cl + CH_3D reactions, are formed in low rotational levels. This result is in agreement with the quantum mechanical scattering calculations of Yu and Nyman [276] and the on-the-fly *ab initio* quasi-classical trajectory calculations of Rudić *et al.* [205]. The CH_3 radical product rotational quantum state population distribution obtained from the simulation using a J',K' rotational temperature of 80 K is compared with the theoretical distributions of Yu and Nyman [276] and Rudić *et al.* [205] in Figure 6.3. The slightly higher rotational excitation of the

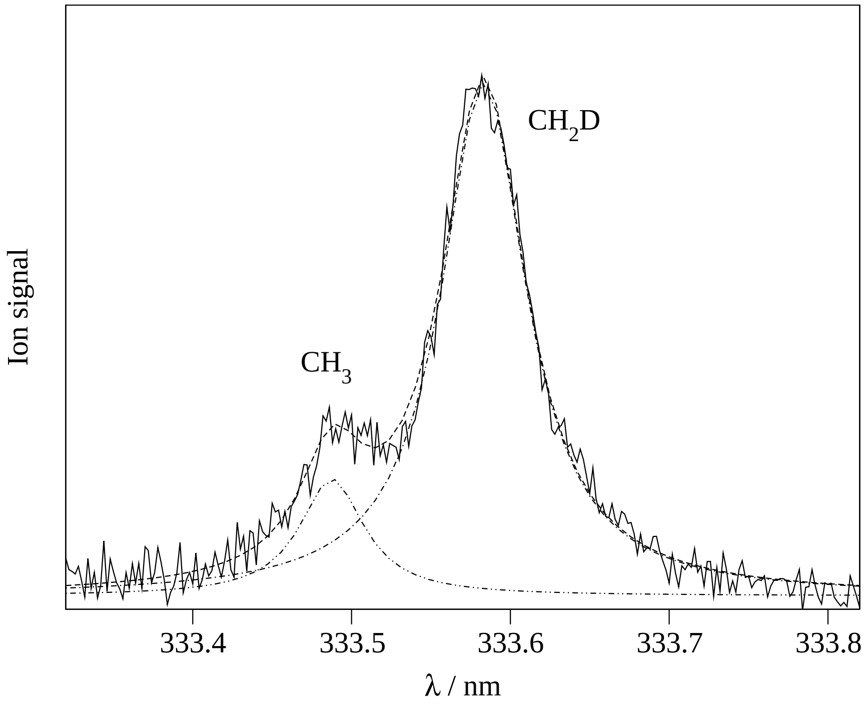

Figure 6.4: (2+1) REMPI spectrum of the CH$_3$ and CH$_2$D radical products of the Cl + CH$_3$D reaction. The dominant peaks are the Q branches of the 0_0^0 vibronic bands. Also shown is a fit to the spectrum assuming Lorenztian Q branch lineshape functions (- - -), yielding relative signals for the two products, CH$_3$:CH$_2$D, of 1:6. The separate contributions derived from the fit from CH$_3$ (— · · — · ·) and CH$_2$D (— · — ·) are also shown.

methyl radical obtained in the current experiments is thought to reflect the higher collision energy employed in the present study, compared with those used in the theoretical calculations. Note that Kandel and Zare also found the CD$_3$ radical products to be formed vibrationally cold [287], a result which is again supported by quantum mechanical scattering calculations by Yu and Nyman [304].

Cl + CH$_3$D

The (2+1) REMPI spectrum of the methyl radical products of the two pathways for the Cl + CH$_3$D reaction, CH$_3$ and CH$_2$D, is shown in Figure 6.4. The spectrum was obtained with the time-of-flight detection gate set to collect both product masses. The two observed peaks correspond to the Q branches of the 0_0^0 bands of CH$_3$ and

CH_2D.[2] No other rotational structure can be resolved within the signal-to-noise ratio of the data due to efficient predissociation in the excited electronic states of the two radicals [135, 293, 315–317]. A fit to the spectrum assuming a Lorentzian lineshape function for the Q branches is also shown in Figure 6.4. The CH_3:CH_2D intensity ratio of 1:6 obtained from the fit is in excellent agreement with the recent study by Crim and co-workers [293]. The difference in the intensities of the two peaks in the REMPI spectrum is thought to reflect the different barrier heights for the reactions [280, 293] and also the statistical abundance of H to D atoms available for abstraction. Although quantitative interpretation of the ratio is complicated by lack of information on the relative Franck–Condon factors and predissociation rates for the CH_3/CH_2D detection, the ratio suggests that the rate of D atom abstraction is lower than that of H atom abstraction, consistent with the primary kinetic isotope effect.

6.3.2 Images and Legendre Moments

Velocity-map ion images and the corresponding zeroth, second and fourth order Legendre moments are shown in Figure 6.5 for the CH_3 products of the Cl + CH_4 reaction, the CH_2D products of the Cl + CH_3D reaction and the CD_3 products of the Cl + CD_4 reaction. The data were obtained by probing the methyl radical products on the maxima of the Q branch REMPI transitions. In the case of the CD_3 products, for which predissociation is much slower than for CH_3 or CH_2D, images were also obtained on the peak of an R branch transition with $J' = 3$. The images are all shown on the same velocity scale and have been quadrant averaged for clarity. The Legendre moments were extracted from the raw images using the procedure described in Chapter 3. A small amount of background signal that was not removed by the background subtraction procedure can be seen in the centre of the image of the CD_3 products detected *via* the $R(3)$ transition and is thought result from imperfect gating of the detector. The correct detection gate position was

---

[2] The observed CH_2D radical peak is assigned to the 0^0_0 band of the $3p\,^2B_1 \leftarrow \tilde{X}\,^2B_1$ Rydberg transition [293, 315].

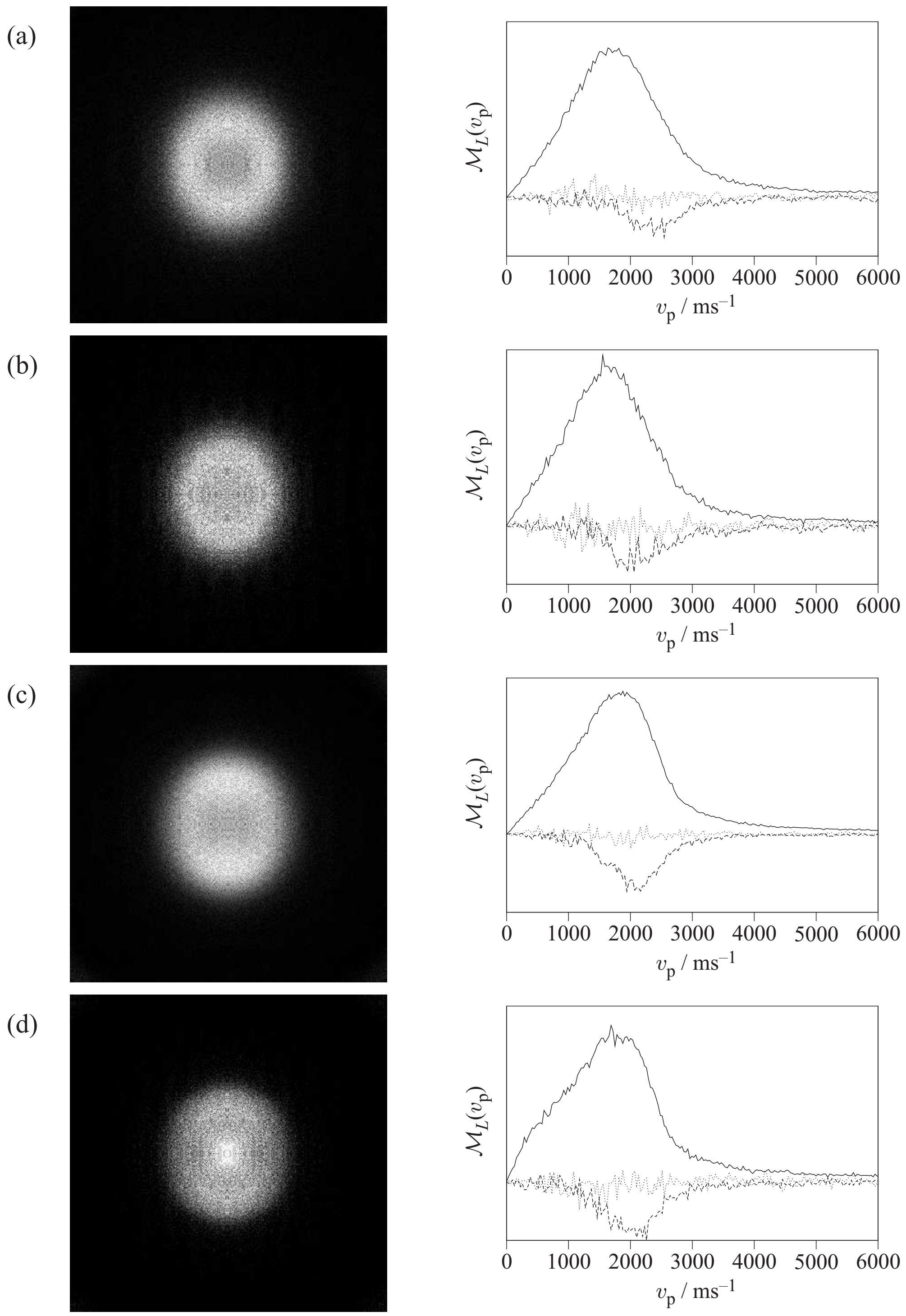

Figure 6.5: Ion images and Legendre moments of order 0 (—), 2(- - -) and 4 (· · ·) of (a) the CH_3 products of the Cl + CH_4 reaction, (b) the CH_2D products of the Cl + CH_3D reaction, (c) the CD_3 products of the Cl + CD_4 reaction detected on the Q branch, and (d) the CD_3 products of the Cl + CD_4 reaction detected on the $R(3)$ transition. All transitions are for the 0^0_0 vibronic band.

difficult to determine accurately due to the extremely low signal intensity yielded on this REMPI transition. The impact of this background signal on the extracted moments, however, was not seen to be significant. Clearly evident from the images, and especially in the Legendre moments, are the similarities between the data obtained for the CH_3 and CH_2D products, and between the data recorded for the CD_3 products detected on the Q branch and on the $R(3)$ transition. This aspect of the experimental data is discussed more fully in Sections 6.3.5 and 6.3.6, in light of the returned CM scattering distributions. Also note that, within the experimental signal-to-noise ratio of the data, the fourth order Legendre moments are very close to zero. The experimental data are therefore consistent with the description of the LAB scattering distribution used in Chapter 3, in which the only non-zero image moments are those for which $L = 0$ and 2. The fact that the fourth order Legendre moments are very close to zero also serves to confirm that the images are not perturbed by fly-out of either the reactant Cl atoms or of the methyl products from the probe region during the delay between photolysis and probe laser pulses.

In the present work, any effects that product rotational angular momentum alignment might have had on the product velocity-map ion images have been neglected. If product rotational alignment were an important effect, the efficiency of the REMPI detection step for the methyl radicals produced in the reactions would depend both on the polarisation of the probe laser and on the product LAB scattering angle, and the zeroth and second order moments of Equation 3.43 would no longer be sufficient to completely describe the product LAB frame scattering distribution. However, since very similar velocity-map ion images were obtained for the Cl + CD_4 reaction on probing the CD_3 products *via* both the Q and R branches, for which the transition dipoles have different correlations with the direction of $\mathbf{J}_{CD_3}$, it appears that alignment effects are not large in this system and neglect of product alignment in any of the following analysis procedures is unlikely to be a significant source of error.

6.3.3 Collision Energy Distributions

A crucial feature of the Legendre moment data analysis method employed in this thesis is the characterisation of the velocity distribution of the translationally 'hot' atoms and the associated distribution of collision energies. In the current experiments, information about these quantities was provided by velocity-map ion images of Cl($^2P_{3/2}$) atoms obtained subsequent to photodissociation of Cl_2 under experimental conditions identical to those used in the study of the reactions. A typical image of the Cl($^2P_{3/2}$) reactants and the corresponding speed distribution have been given previously for the present reactions in Section 2.9.2. The broadening of this distribution relative to that observed under skimmed beam conditions could have several different sources and, reflecting this, the data were analysed in two different ways.

The first procedure was analogous to that adopted by Zare and co-workers [110, 111, 208, 287], in which it was assumed that the inverse Abel transformed image of the Cl($^2P_{3/2}$) products of Cl_2 photolysis represents an instrument function. Note that the expansion conditions and the distance between the interaction region and the nozzle exit employed in the current experiments were both very similar to those used previously in the core-extraction experiments of Zare and co-workers. In the present experiments, the width of this instrument function could reflect, for example, poor velocity mapping across the entire probe volume or possibly secondary collisions of the fast moving product ions with other molecules in the beam. To take these effects into account, the instrument function was used to convolute the basis functions generated to fit the data.

In the second procedure, it was assumed that the inverse Abel transform of the image of the Cl($^2P_{3/2}$) products of photodissociation of Cl_2 provided an accurate map of the reactant Cl atom velocity distribution. Possible explanations proposed to account for the broad chlorine atom speed distribution obtained from the ion image are discussed in Section 6.4. Within this second analysis, the Cl($^2P_{3/2}$) velocity distribution was used directly in generating the basis functions.

In both analyses the CH_4, CD_4 or CH_3D reactant in the molecular beam was assumed to be characterised by a translational temperature of 50 K (see Section 2.6). The results presented here, however, were found to be quite insensitive to the effects of changing the translational temperature over the range 50–300 K. Although this procedure is not exact, the basis functions and fits to the experimental data were found to vary little using temperatures within this range.

The three isotopic reactions studied have slightly different collision energies, owing to the dependence of the collision energy, E_t, on the reduced mass of the reactants (see Equation 3.18). The estimate of the collision energy was seen to depend significantly upon the assumptions made about the Cl atom speed distribution. For the analysis in which the Cl speed distribution was assumed to reflect an instrument function, the mean collision energies for the Cl + CH_4, Cl + CH_3D and Cl + CD_4 reactions were determined to be 0.25 eV, 0.26 eV and 0.29 eV, respectively. The collision energy distributions were seen to have a FWHM of ~0.10 eV, which may be attributed to residual thermal motion of the Cl_2 photolysis precursor and the methane reactant in the free-jet expansion. Since a small barrier to reaction is present in all three systems studied, a simple line-of-centres excitation function, $\sigma_\mathrm{r}(E_\mathrm{t})$, given by

$$\sigma_\mathrm{r}(E_\mathrm{t}) = \begin{cases} 0 & E_\mathrm{t} \le E_0 \\ N(1 - E_0/E_\mathrm{t}) & E_\mathrm{t} > E_0, \end{cases} \tag{6.6}$$

where E_0 is the height of the barrier to reaction and N is a normalisation constant, was used in generating the basis functions for this analysis. The joint CM scattering distribution given by Equation 3.40 was assumed to be independent of the relatively narrow spread of reactant relative velocities. For the second analysis procedure, in which the Cl atom speed distribution was assumed to be a true reflection of the reactant speed distribution in the interaction region, significantly broader collision energy distributions were obtained, all of which had an asymmetric tail at high energies (FWHM ~0.14 eV for the Cl + CH_4 reaction). The collision energy distribution calculated for the Cl + CH_4 reaction using the Cl atom speed distribution discussed above and a CH_4 translational temperature of 50 K is shown in Figure 6.14(a). Thus, while the most probable collision energies were found to be 0.24 eV, 0.25 eV and 0.28 eV for the Cl + CH_4, Cl + CH_3D and Cl + CD_4 reactions respectively, the mean values were seen to be significantly higher: 0.32 eV, 0.33 eV and 0.36 eV. In this analysis method, owing to the wider range of collision energies sampled, it proved important to generate the basis functions in Legendre moments of the collision energy as well as in CM scattering angle. It was then possible to fit the data non-separably, allowing the CM angular scattering distribution to vary with E_t.

6.3.4 The LAB Frame Speed and Anisotropy Distributions

The most direct comparison that can be made between the data obtained in the present experiments and those of the core-extraction REMPI-TOF experiments of Kandel and Zare [287] is through the derived LAB frame distributions. The LAB speed and speed-dependent translational anisotropy distributions for the CH_3 and CD_3 products of the Cl + CH_4 and Cl + CD_4 reactions obtained from the two experiments are compared in Figure 6.6. In both cases, the distributions shown are those for the CH_3 and CD_3 products detected on the Q branch of the 0_0^0 band. The LAB frame distributions from the current experiments were extracted by inverse Abel transformation of images (a) and (c) in Figure 6.5, followed by appropriate integration of the resulting 'slice' through the 3D velocity distribution. The LAB frame distributions of Kandel and Zare were obtained from the core-extracted REMPI-TOF profiles by a basis function fitting analysis, in which an instrument resolution function was included. In order to allow direct comparison, the distributions obtained from the present experiments were deconvoluted with the instrument function described in Section 6.3.3. The LAB frame speed and speed-dependent anisotropy distributions derived from the two experiments are seen to be in excellent agreement.

Rather than attempt a direct inversion of the LAB speed distribution data to obtain the CM angular scattering distributions, as performed previously by Kandel and Zare [287], the images shown in Figure 6.5 were analysed using the basis function

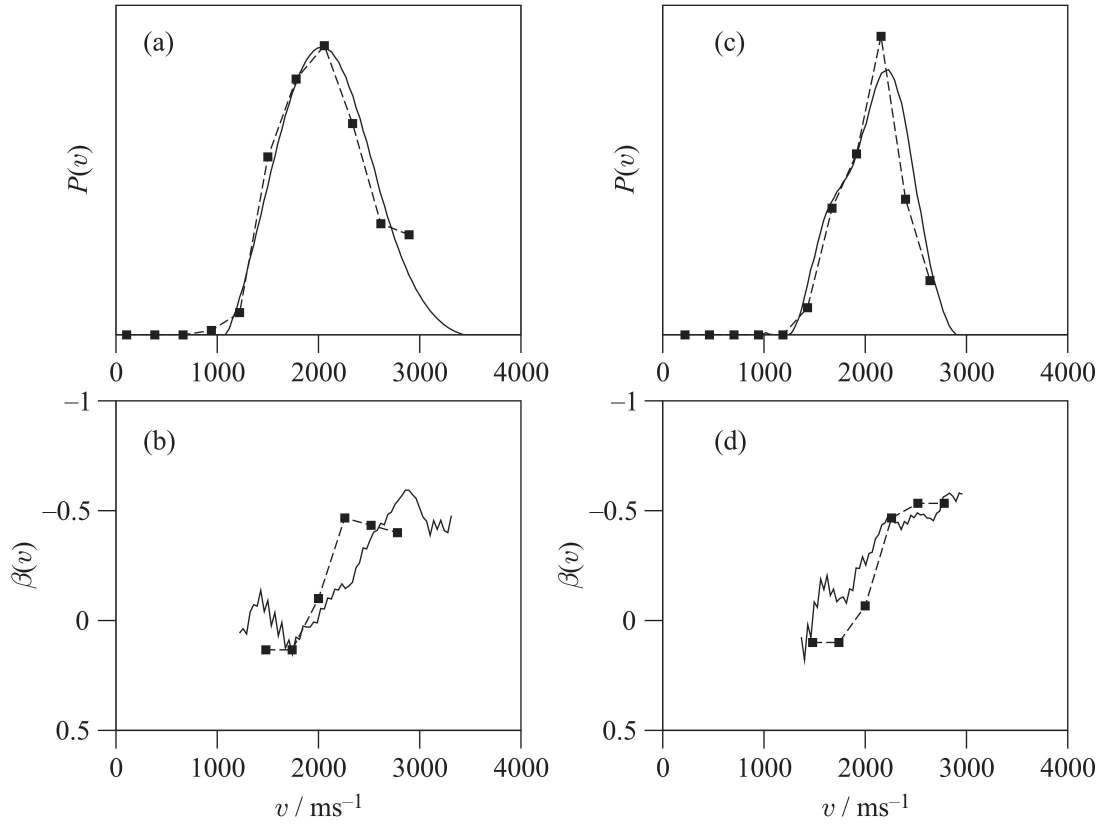

Figure 6.6: The LAB speed distributions (upper panels) and LAB speed-dependent translational anisotropy distributions (lower panels) for the methyl radical products of the reactions of Cl with CH_4 ((a) and (b)) and CD_4 ((c) and (d)). The present results (—), which were obtained from the inverse Abel transforms of images (a) and (c) in Figure 6.5, are compared with the results of Kandel and Zare [287] (--■--), which were obtained from a basis function fit to methyl radical core-extracted REMPI-TOF profiles. Since the analysis of Kandel and Zare employed an instrument resolution function, for comparison, the present data from the inverse Abel transform have been deconvoluted with the instrument function discussed in Section 6.3.3.

fitting method (see Chapter 3), subject to the assumptions made about the collision energy distribution outlined in Section 6.3.3.

6.3.5 Legendre Moment Fitting Analysis: An Instrument Function

The Legendre moment fitting analysis detailed in this Section made use of the first procedure described in Section 6.3.3, in which the $Cl(^2P_{3/2})$ atom speed distribution (see Figure 2.11) was assumed to reflect an instrument resolution function. The basis functions used to fit the data were generated by employing a single Cl atom reactant speed and were then convoluted with the instrument function.

Since in the present reactions only a very small amount of the available energy is seen to be deposited into internal degrees of freedom of the methyl radical products [279, 287] and HCl (or DCl) co-products [208, 214], for a given reaction system it proved sensible to constrain the kinetic energy release distribution, $P(f_t)$, to that determined from the measured rovibrational populations of the two products. The fixed kinetic energy release distributions used in generating the basis sets were calculated by convolution of the known HCl (and DCl) rovibrational population distributions [208, 214] with the methyl radical rotational populations characterised by J',K' temperatures in the range 80–200 K, taking into account the transitions excited within the overlap of the probe laser bandwidth and the Q branch of the CH_3 (CD_3 or CH_2D) REMPI transition. Example kinetic energy release distributions calculated in this way are shown in Figure 6.7 for the CH_3 and CD_3 products of the $Cl + CH_4(v = 0)$ and $Cl + CD_4(v = 0)$ reactions, for which the methyl J',K' rotational temperatures were chosen to be 80 K. Owing to the low internal excitations of both fragments, pair correlations between their internal energies were neglected. The parameters returned by the fit were found to be insensitive to the precise choice of kinetic energy release distribution, provided the latter were sensibly chosen to lie within the aforementioned uncertainties in the methyl radical rotational excitation.

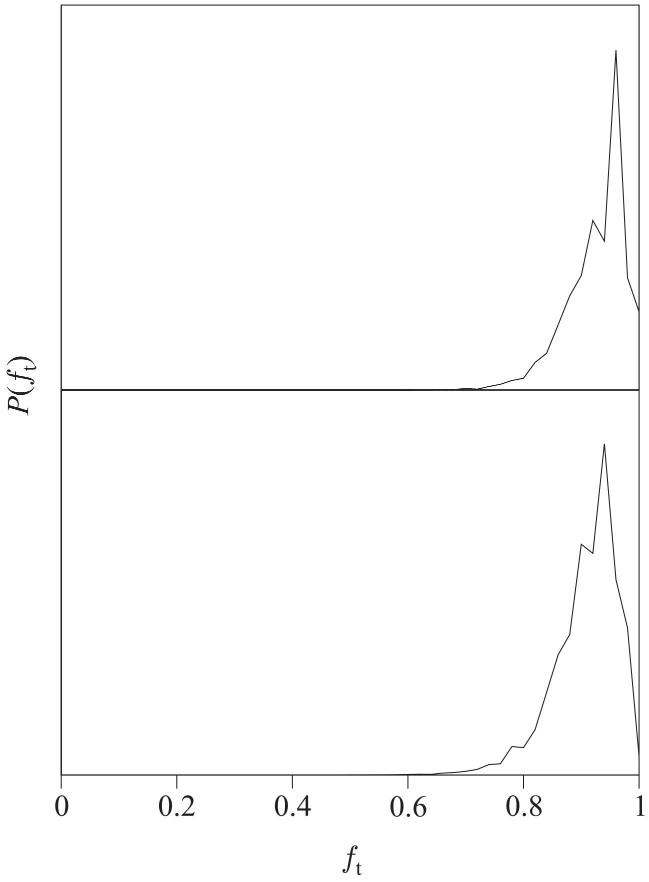

Figure 6.7: Kinetic energy release distributions calculated for the CH$_3$ (upper panel) and CD$_3$ (lower panel) products of the Cl + CH$_4$ and Cl + CD$_4$ reactions. The distributions were obtained by convolution of measured HCl and DCl rotational population distributions [208, 214] with methyl radical rotational population distributions calculated for J',K' temperatures of 80 K.

Cl + CH$_4$

Fits to the data were first attempted assuming that the product methyl signals arose exclusively from the Cl atom reaction with *ground* vibrational state methane molecules. The resulting fits, shown in Figure 6.8, are seen to be totally unsatisfactory. The second Legendre moment of the image, $\mathcal{M}_2(v_\mathrm{p})$, which is sensitive to the LAB frame translational anisotropy (see Equation 3.46), is seen to be particularly poorly fit using the basis functions generated using this assumption. Within this analysis, it is clear that the CH$_3$ signals are incompatible with the reaction of Cl exclusively with CH$_4$ in the ground vibrational state.

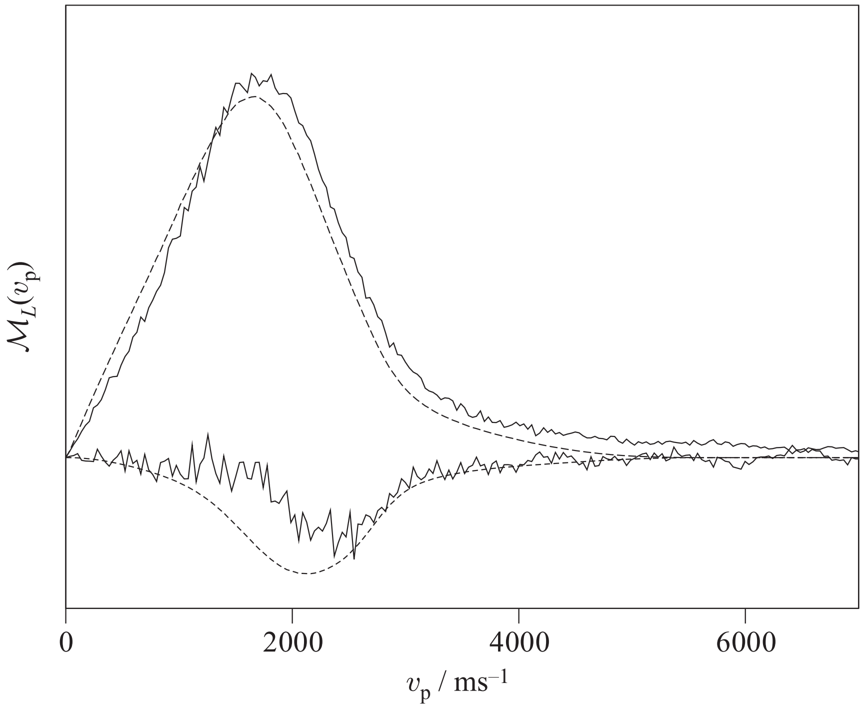

Figure 6.8: Zeroth and second order Legendre moments (—) of the raw CH_3 image shown in Figure 6.5(a), and fits to those moments (- - -), obtained by assuming that the observed signal arose solely from reaction of Cl atoms with CH_4 in the *ground* vibrational state. The fits were performed using five moments in the CM angular scattering distribution.

As was noted in Section 6.2.2, the cross-section of the Cl + CH_4 reaction is thought to be greatly enhanced by vibrational excitation in the CH_4 reactant. Since vibrational cooling of CH_4 in the free-jet expansion is inefficient, the small fraction of bend- and/or torsion-excited molecules remaining in the beam could make a noticeable contribution to the reactive signal. The sufficiently different energetics of the reaction of chlorine with ground and vibrationally excited CH_4 permitted the analysis to be extended to allow two basis sets to be used to fit the data, with an extra fitting coefficient employed to determine the relative contribution to the signal from each of the two reaction channels. Note that a very similar methodology was used in the analysis of the images of the Cl + n-butane reaction in Chapter 5. In the present case, however, the kinetic energy release distributions were fixed for both reaction pathways, while the two CM angular scattering distributions were

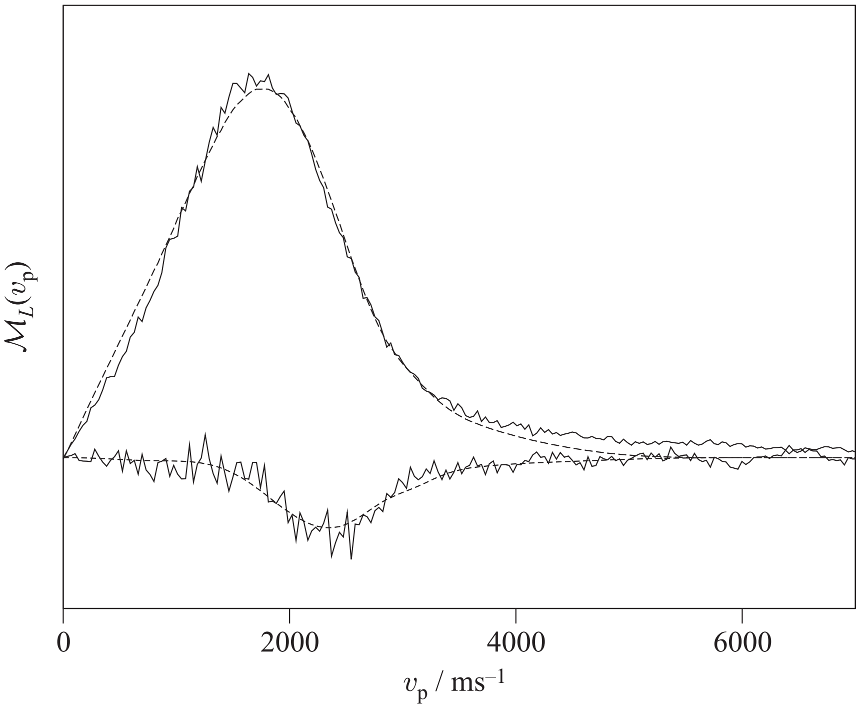

Figure 6.9: As for Figure 6.8, but showing the fits to the Legendre moments of the CH_3 image obtained by assuming that both ground state, $CH_4(v = 0)$, and vibrationally excited, $CH_4(\nu_4 = 1)$, methane reactants contribute to the REMPI signal. The fits were performed using five moments in the CM angular scattering distribution for each reaction pathway.

allowed to vary independently. Fits to the experimental data, in which the active vibrational mode in the methane molecule was assumed to be the lowest-lying ν_4 umbrella bending mode, are shown in Figure 6.9. The fits using this more involved analysis are seen to be a significant improvement on those shown in Figure 6.8, in which only ground vibrational state methane was considered. Owing to the similar vibrational energies of the ν_4 umbrella bending mode (1306 cm^{-1}) and the ν_2 torsional mode (1534 cm^{-1}) [255], almost indistinguishable results were obtained for fits in which the ν_2 mode was assumed to be active.

CM angular scattering distributions for the Cl + CH_4 reaction returned from the more complete analysis are shown in Figure 6.10. The error bars shown on the data are the result of the Monte Carlo analysis detailed in Section 3.4.7 and reflect generous uncertainties in the fitting procedure. The truncation point for the number

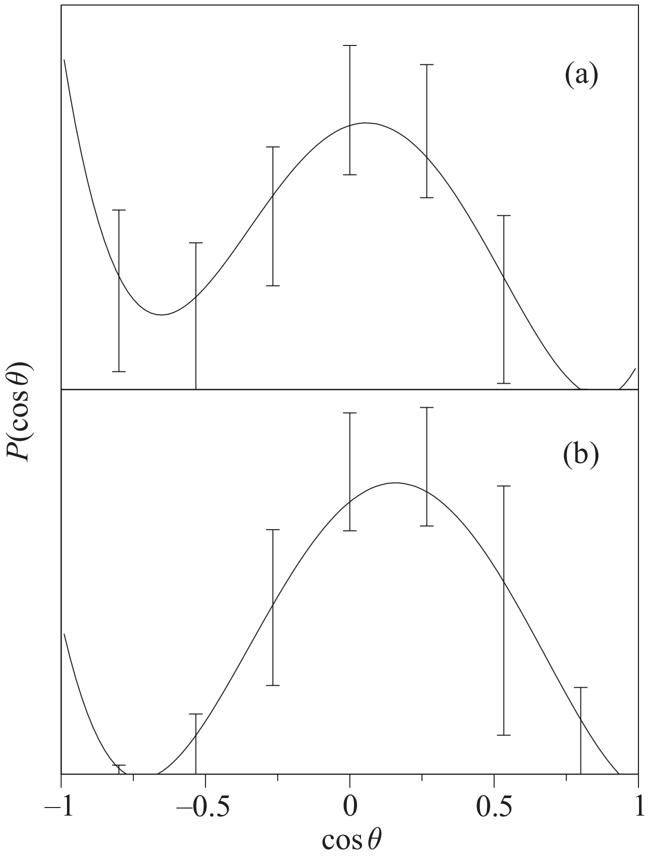

Figure 6.10: CM angular scattering distributions returned from the fits shown in Figure 6.9 (obtained using basis function sets convoluted with an instrument function), for the Cl + CH$_4$ reaction with (a) ground vibrational state methane reactants, and (b) vibrationally excited methane reactants. In the latter case, the active vibrational mode is assumed to be the CH$_4$ ν_4 umbrella bending mode. The CM scattering angle, θ, refers to the scattering of CH$_3$ with respect to the CH$_4$ reactant, such that rebound dynamics correspond to scattering through 180°. The fits were performed using five moments in the CM angular scattering distribution for each reaction pathway. Error bars represent 1σ errors resulting from statistical errors in the fits.

of basis functions required to fit the data was determined using a procedure similar to that used for the Cl + n-butane reaction (see Section 5.3.2). In the present case, the fits did not improve by a significant amount with inclusion of more than five moments in the CM angular scattering distribution for each reaction pathway. The returned distributions and the relative weighting between the two reaction pathways were, however, remarkably consistent as the number of moments used was varied. The data are in good agreement with the previous results of Kandel and Zare [287]. The CM angular scattering distributions for ground and vibrationally excited methane both appear to have dominant peaks in the sideways direction, but scattering for the vibrationally excited methane reactants is more forward than that for ground state reactants. The change in the CM angular scattering distribution with reactant vibrational excitation is perhaps not unexpected, given that the cross-section of the reaction is enhanced by a large extent through low-frequency vibrational excitation of the reactants (see below). The result is consistent with reactive collisions proceeding from a wider range of reactant phase-space than for the reaction with unexcited methane molecules, or, equivalently, with an opening of the cone of acceptance and consequent reaction over a wider range of impact parameters with vibrational excitation of the reagents [208].

Cl + CD_4

The Legendre moment fitting analysis allowing for both ground state and vibrationally excited CD_4 yielded the CM angular scattering distributions shown in Figure 6.11 for the CD_4 products detected on the maximum of the Q branch and on the $R(3)$ transition of the 0_0^0 band. The CM angular scattering distributions obtained on the two branches (which sample subsets of radical products with somewhat different values of J',K') are almost identical, suggesting that the dynamics are insensitive to the internal rotational state of the CD_3 radical (or to alignment of the rotational angular momentum). The excellent agreement between the two sets of data also provides some measure of the reproducibility of the experiment. Similarly to the Cl

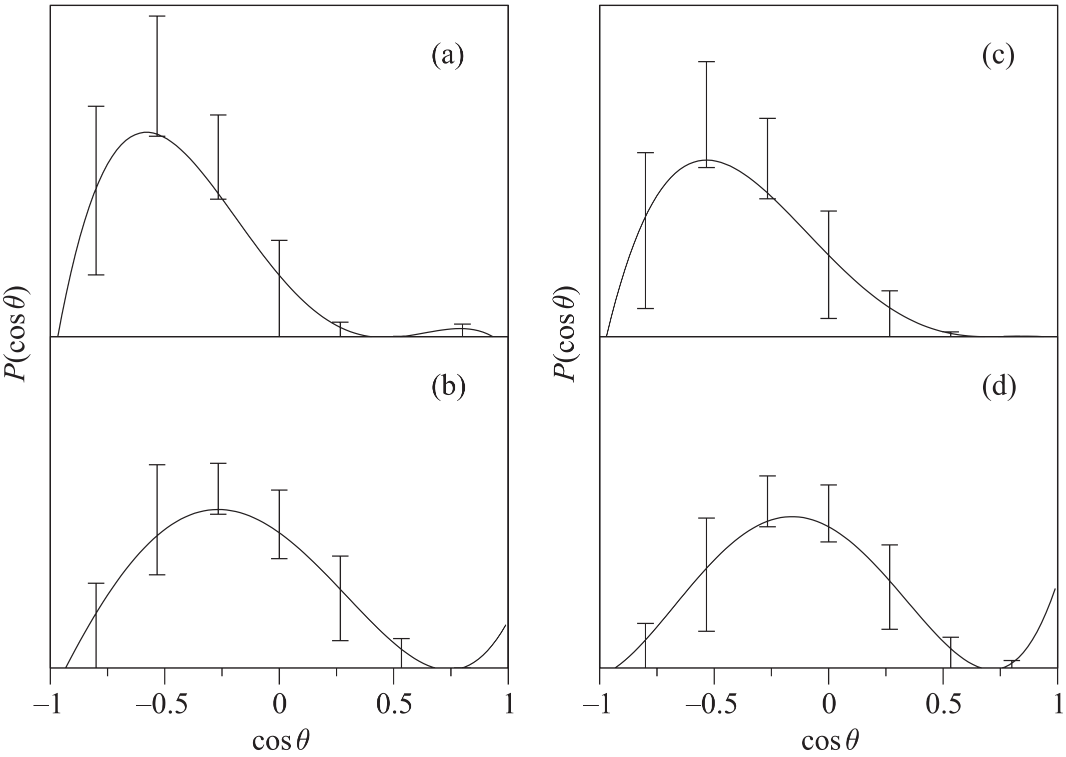

Figure 6.11: As for Figure 6.10, but showing CM angular scattering distributions for the Cl + CD_4 reaction for ground vibrational state methane reactants ((a) and (c)), and vibrationally excited methane reactants ((b) and (d)). The data shown in the left column were obtained by probing the CD_3 products on the maximum of the Q branch, while that on the right was obtained by probing the CD_3 products on the $R(3)$ transition. The fits were performed using five moments in the CM angular scattering distribution for each reaction pathway. Error bars represent 1σ errors resulting from statistical errors in the fits.

+ CH_4 reaction, the CM angular scattering distributions for the products of reaction with vibrationally excited CD_4 are peaked more towards the sideways/forwards direction compared with those for the vibrationally unexcited reactants. Note that the CM angular scattering distributions for the reaction of chlorine with perdeuterated methane are more strongly peaked in the backwards hemisphere than that for the reaction of chlorine with CH_4. This is consistent with the reaction with the perdeuterated methane occurring lower on the potential energy surface due to a reduction in zero-point energy, and therefore with a reduced cone of acceptance. Similar behaviour has been observed in the reaction of H atoms with protonated

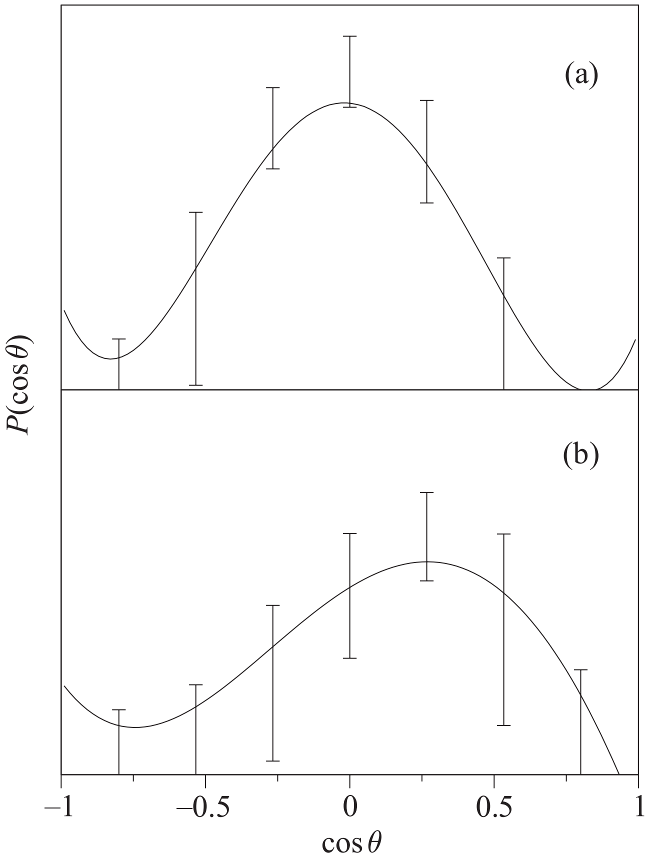

Figure 6.12: CM angular scattering distributions for the CH_3D products of the Cl + CH_3D reaction for (a) ground vibrational state methane reactants and (b) vibrationally excited methane reactants. In the latter case, the active vibrational mode is assumed to be the CH_3D ν_6 CH_3 rocking mode. The CM scattering angle, θ, refers to the scattering of CH_3 with respect to the CH_4 reactant, such that rebound dynamics correspond to scattering through 180°. The fits were performed using five moments in the CM angular scattering distribution for each reaction pathway. Error bars represent 1σ errors resulting from statistical errors in the fits.

and deuterated water [314, 318].

Cl + CH_3D

The Legendre moment fitting analysis allowing for both ground state and vibrationally excited CH_3D, in which the active vibrational mode in the CH_3D molecule was assumed to be the lowest-lying ν_6 CH_3 rocking mode [255], yielded the CM angular scattering distributions shown in Figure 6.12 for the CH_3D products. Owing to the similar vibrational energies of the ν_6 CH_3 rocking mode (1155 cm^{-1}) and the ν_3 umbrella bending (1300 cm^{-1}) and ν_5 CH bending (1471 cm^{-1}) modes [255], almost indistinguishable results were obtained for fits in which either the ν_3 mode or the ν_5 mode were assumed to be active. The distributions shown in Figure 6.12 follow the same trends with vibrational excitation of the CH_3D reactant as noted above for the other reactant species. Once again, reaction of chlorine with vibrationally excited reactants is seen to yield methyl products that are more forward scattered than those of the reaction of chlorine with ground vibrational state reactants. It is interesting to note that the CM angular scattering distributions are much more similar to those for the reaction of chlorine with CH_4 than for those for the reaction with CD_4, which are more backward scattered. The data suggest that the cone of acceptance for the two isotopic reaction channels is influenced significantly by whether a hydrogen or a deuterium atom is abstracted.

Vibrational Enhancement

The relative contributions to the total signal from methane molecules in the ground and first vibrational states are given in Table 6.1 for the methyl products of the Cl + CH_4, Cl + CD_4 and Cl + CH_3D reactions. The analysis suggests that about half of the CH_3 signal originates from reaction with vibrationally excited methane, in good agreement with the value originally estimated by Kandel and Zare [279, 287]. Also shown in the table are the vibrational enhancements in the reaction cross-section calculated on the assumption that the vibrational temperature of the methane molecules in the molecular beam is 300 K. For the Cl + CH_4 and Cl + CD_4 reactions, the ν_4 umbrella bending mode is assumed to be the active vibrational mode, as indicated by theory [274, 276, 297]. Similar values are obtained, however, if the ν_2 torsional mode is assumed to be active instead. In the case of the Cl + CH_3D reaction, the ν_6 CH_3 rocking mode is assumed to be the active vibrational mode. Greater enhancements are seen if either the ν_3 umbrella bending or the ν_5 CH bending modes are assumed to be active. Note that the calculated cross-section

Table 6.1: Results from the first analysis procedure, in which the basis functions used to fit the data were convoluted with an instrument function obtained from the Cl atom speed distribution. Relative signals (S) from, and populations (P) and reactivities (σ) of, vibrationally excited ($v = 1$) and ground state ($v = 0$) methane are shown for the reactions given. The vibrational mode assumed to be active for CH_4 and CD_4 is the ν_4 umbrella mode, although similar results are obtained if the ν_2 torsional mode is assumed to be the active vibrational mode. The populations have been estimated on the assumption that the vibrational temperature of the methane molecules in the molecular beam is 300 K. In the case of CH_3D, the results are quoted for the excitation of the ν_6 CH_3 rocking mode. If the ν_3 or ν_5 modes are assumed to be active, the calculated reaction cross-section enhancements are 290 and 280 respectively. The data for the Cl + CD_4 reaction has been averaged over the data obtained from the two CD_3 probe transitions employed.

	$S_{v=1}/S_{v=0}$	$P_{v=1}/P_{v=0}$	$\sigma_{v=1}/\sigma_{v=0}$
$Cl + CH_4 \longrightarrow HCl + CH_3$	1.2 ± 0.3	5.7×10^{-3}	210 ± 50
$Cl + CD_4 \longrightarrow HCl + CD_3$	5.1 ± 2.3	2.5×10^{-2}	200 ± 90
$Cl + CH_3D \longrightarrow HCl + CH_2D$	0.75 ± 0.39	7.9×10^{-3}	100 ± 50

enhancements are very large for all three reaction systems. If the assumptions made in performing this analysis are correct, it is hard to reconcile these measurements with the rather modest enhancements estimated by Michelson and Simpson, based on a line-of-centres analysis of the temperature dependence of the thermal rate constant [198], or with the new imaging experiments of Liu and co-workers [88]. More modest cross-section enhancements with excitation of the ν_4 umbrella mode of CH_4 have also been predicted by Yu and Nyman [276, 303, 304] in their 4D quantum scattering calculations, and by Palma and Clary following a similar quantal study of the analogous $O(^3P)$ + CH_4 reaction [319].

6.3.6 Legendre Moment Fitting Analysis: A Collision Energy Distribution

While the results of the analysis in the previous Section are in excellent agreement with the photoloc studies of Zare and co-workers [279, 287], given the very large vibrational enhancements obtained with this analysis method, and the disagreement with the findings of Liu and co-workers [88], it was important to establish whether or not the data were amenable to another interpretation. To this end, a second Legendre moment fitting analysis was performed, in which use was made of the second procedure described in Section 6.3.3. Within this analysis, the $\mathrm{Cl}(^2\mathrm{P}_{3/2})$ atom speed distribution shown in Figure 2.11 was assumed to give an accurate map of the reactant Cl atom velocity distribution, and was used directly in the generation of the basis sets. The kinetic energy release distributions were again constrained to be those evaluated by convolution of the known HCl and DCl rovibrational population distributions [208, 214] with the calculated methyl radical rotational populations. In addition, owing to the much broader collision energy distributions arising from the present analysis (see Section 6.3.3), it was necessary to determine the excitation function, $\sigma_{\mathrm{r}}(E_{\mathrm{t}})$, describing the collision energy dependence of the reaction cross-section. The CM scattering distribution in this case, $P(\theta, E_{\mathrm{t}})$, was expressed as a double expansion of Legendre polynomials

$$P(\theta, E_{\mathrm{t}}) = \frac{1}{4}\sum_{n,m} a_{nm} P_n(\cos\theta) P_m(\varepsilon_{\mathrm{t}}), \tag{6.7}$$

where

$$\varepsilon_{\mathrm{t}} = \left[2\left(\frac{E_{\mathrm{t}}}{E_{\mathrm{t,max}}}\right) - 1\right], \tag{6.8}$$

and $E_{\mathrm{t,max}}$ is the maximum collision energy. Basis functions were therefore generated in Legendre moments of both the collision energy and CM scattering angle, and the data fitted non-separably in order to allow the CM angular scattering distribution to vary with collision energy.

Cl + CH_4

The fits to the experimental Legendre moments for the CH_3 products of the Cl + CH_4 reaction obtained using the alternative analysis method described above are shown in Figure 6.13. It is noteworthy that these alternative basis functions provide a good

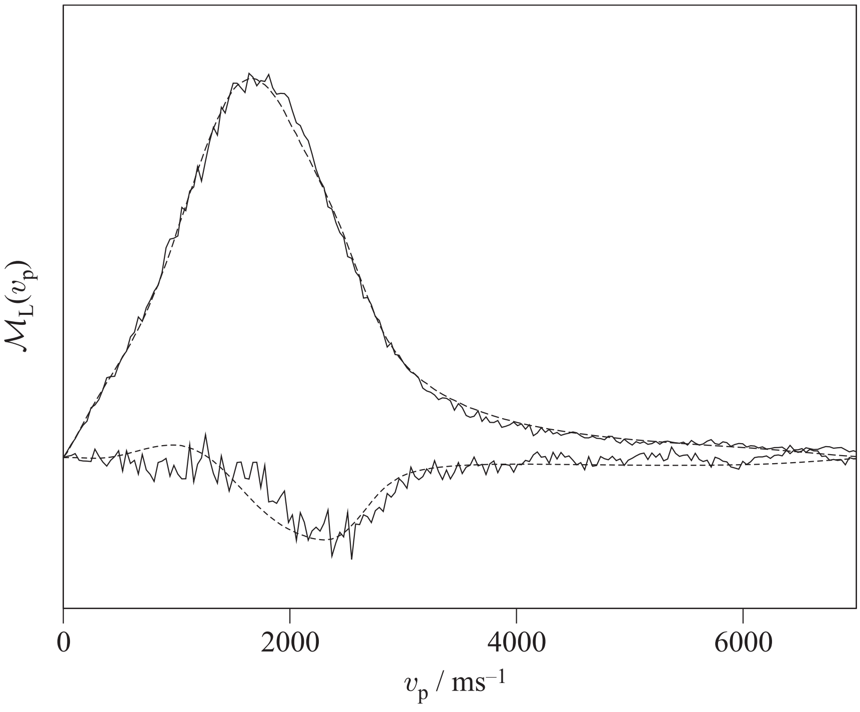

Figure 6.13: Zeroth and second order Legendre moments (—) of the raw CH$_3$ image shown in Figure 6.5(a), and fits to those moments (- - -), obtained by assuming that the observed signal arose solely from reaction of Cl atoms with CH$_4$ in the ground vibrational state. The basis functions were generated using the Cl atom speed distribution shown in Figure 2.12 directly. The fits were performed using five moments in the CM angular scattering distribution and three moments in the excitation function.

fit to the experimental moments even at very high speeds, a region where the basis functions assuming an instrument function have little amplitude (see Figure 6.9). It should be stressed that in the current method the chlorine atom reaction is assumed to take place *exclusively* with CH$_4$ in the ground vibrational state. It is possible that some small contribution from vibrationally excited methane would improve the quality of the fit still further, but such an elaborate fit was not attempted. It is also important to note that the two different interpretations of the Cl reactant ion images employed here and in the previous Section both yield quite satisfactory fits to the data, but lead to very different conclusions regarding the activity of vibrationally excited reactants.

The excitation function and the collision energy averaged CM angular scattering distribution for the Cl + CH_4 reaction returned by the current analysis are shown in Figure 6.14. Note that the excitation function was set to zero below the barrier to reaction (0.11 eV). While the reaction cross-section was found to vary only slightly with collision energy above this value, it was found that significantly improved fits were obtained by allowing the CM angular scattering distribution to vary with collision energy. The peaks in the resulting CM angular scattering distributions were seen to shift sensibly from about 130° to around 60° as the collision energy was increased from the barrier height to 1 eV. The collision energy averaged CM angular scattering distribution determined from the current analysis procedure, although demonstrating slightly more backward scattering, is seen to be in qualitative agreement with that determined very recently by Liu and co-workers [88] at a collision energy of around 0.20 eV using the crossed molecular beam time-sliced ion velocity imaging technique. Also note that the CM angular scattering distribution for the reaction with ground state methane is in qualitative agreement with that obtained using the first analysis procedure (see Figure 6.10), although it is again shifted somewhat towards the backwards direction. The collision energy averaged CM angular scattering distribution is also seen to be in good qualitative agreement with that obtained from the 4D quantum scattering calculations of Yu and Nyman [276] at a collision energy of 0.16 eV, as shown in Figure 6.13.

Cl + CD_4

The collision energy averaged CM angular scattering distributions returned from the fits using the second Legendre moment analysis procedure are shown in Figure 6.15 for the CD_3 products of the Cl + CD_4 reaction, detected on the maximum of the Q branch and on the $R(3)$ transition. As was seen for the previous analysis procedure, the CM angular scattering distributions obtained from the data on the two transitions are almost identical. Excellent agreement is seen between the results of the current analysis procedure and those of Liu and co-workers at a collision energy of around 0.21 eV using the crossed molecular beam time-sliced ion velocity imaging

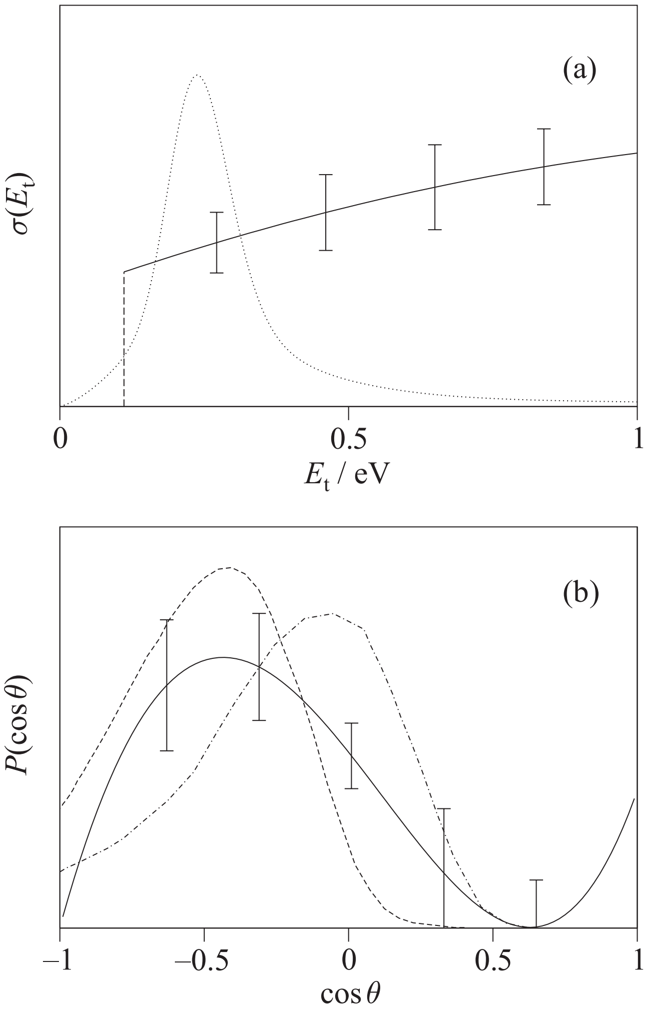

Figure 6.14: (a) The excitation function (—) for the Cl + $CH_4(v = 0)$ reaction as determined using the second analysis procedure. Note that below the barrier of $\sim$0.1 eV, indicated by the dashed line, the reaction cross-section is assumed to be zero. The collision energy distribution ($\cdots$) was calculated using the Cl atom speed distribution and by assuming a CH_4 translational temperature of 50 K. (b) The collision energy averaged CM angular scattering distribution for the Cl + $CH_4(v = 0)$ reaction. The present results are compared with those of Liu and co-workers determined using the crossed molecular beam imaging technique determined at a collision energy of around 0.20 eV [88] ($- \cdot - \cdot$). Also shown are the results of the 4D quantum scattering calculations by Yu and Nyman at a collision energy of 0.159 eV [276] (---).

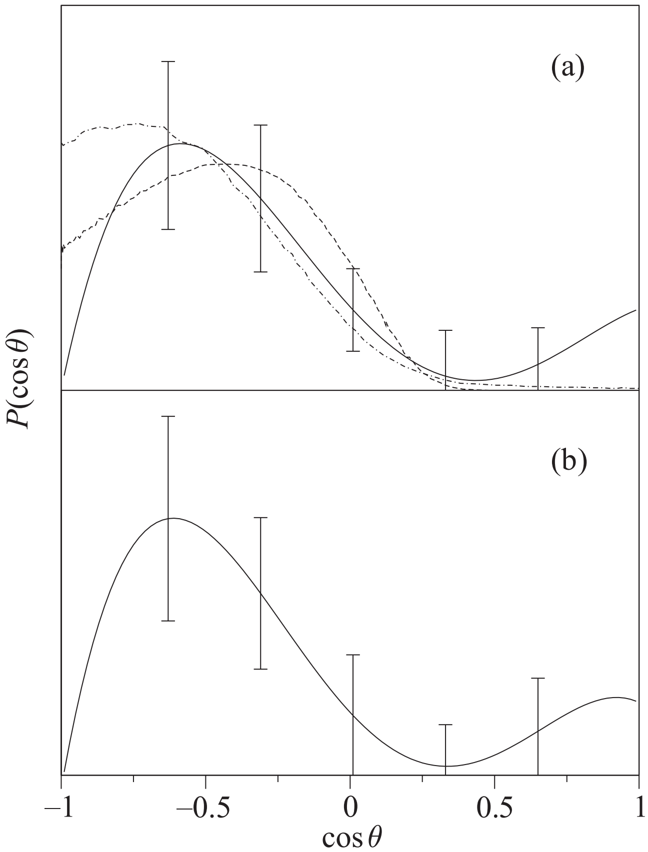

Figure 6.15: As for Figure 6.13, but showing the collision energy averaged CM angular scattering distributions for the Cl + $CD_4(v = 0)$ reaction determined using the second analysis procedure outlined in Section 6.3.3. Distributions are shown for the CD_3 products detected on (a) the maximum of the Q branch, and (b) on the $R(3)$ transition. The results in panel (a) are compared with those of Liu and co-workers determined using the crossed molecular beam imaging technique determined at a collision energy of around 0.21 eV [88] (— · — ·). Also shown in (a) are the results of the 4D quantum scattering calculations by Yu and Nyman at a collision energy of 0.25 eV [304] (- - -).

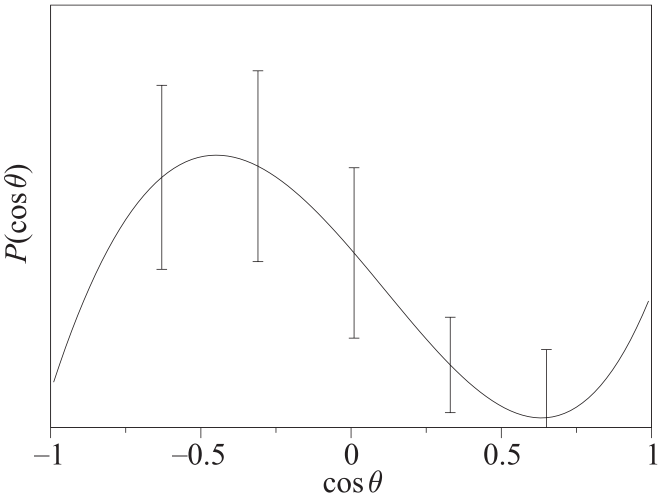

Figure 6.16: The collision energy averaged CM angular scattering distribution for the CH_2D products of the Cl + CH_3D reaction determined using the second analysis procedure. Note that the angular scattering distribution is very similar to that derived for the Cl + CH_4 reaction shown in Figure 6.13(b).

technique, in which the CD_3 products were also detected on the maximum of the *Q* branch [88]. Note that, in the case of chlorine atom reactions with deuterated methane in the vibrational ground state, very similar CM angular scattering distributions were obtained using the first and second analysis procedures. The results of the current analysis are seen to be in excellent agreement with the most recent quantum scattering calculations of Yu and Nyman [304]. The theoretical data were obtained at a collision energy of 0.25 eV, quite close to the most probable collision energy of 0.28 eV sampled in the current experiments.

Cl + CH_3D

Analysis using the current procedure yielded the collision energy averaged CM angular scattering distribution shown in Figure 6.16. As was found using the previous analysis procedure, the CM angular scattering distribution is more similar to that for the Cl + CH_4 reaction than for the Cl + CD_4 reaction, which shows enhanced backward scattering. Further experiments, either on the CH_3 products of the Cl + CH_3D reaction, or on the products of the reactions with other isotopomers, may help to clarify how the cone of acceptance is controlled by whether an H or a D atom is abstracted.

6.4 Discussion

The results of new velocity-map ion imaging experiments on the reaction of atomic chlorine with CH_4, CD_4 and CH_3D were presented in the previous Section. The data were analysed in two separate ways using the Legendre moment fitting procedure, based on two limiting assumptions about the nature of the relatively broad Cl atom speed distribution observed. The CM angular scattering distributions obtained using both of these methods were seen to be in agreement with one another, the previous experimental work of Liu and co-workers [88], and theoretical calculations by Yu and Nyman [276, 304]. The various levels of vibrational enhancement determined from the present and previous studies are discussed here.

In the first procedure, the real Cl atom speed distribution was assumed to have a width due only to thermal motion of the Cl_2 precursor, so that the spread in the measured Cl atom speed distribution (shown in Figure 2.12) allowed an instrument function to be estimated. Using this analysis, the data could not be accurately reproduced by reaction of chlorine atoms with ground vibrational state methane molecules alone. By inclusion of methane molecules in the first vibrational state of either the torsional or umbrella bending mode in the analysis, however, it was possible to produce satisfactory fits to the experimental data. Although vibrational cooling of methane in the molecular beam is inefficient, even by assuming a methane vibrational temperature of 300 K, vibrational enhancements of the reaction cross-section of 100–210 were required to explain the contribution to the observed signal of umbrella bend or torsion mode excitation in the methane that was determined. Despite the good agreement between these results and those of Kandel and Zare [287], such a high level of vibrational enhancement for either the ν_2 or the ν_4 mode seems unlikely to be correct. Note that, in contrast, owing to the late barrier in the reaction [294, 295], excitation of the methane stretching modes would be expected to yield a significant reaction cross-section enhancement, as observed experimentally by Zare and co-workers [208, 287] and Crim and co-workers [258, 292], and predicted theoretically by Duncan and Truong [274] and Corchado an co-workers [297].

The second analysis procedure, in which the measured Cl atom speed distribution was assumed to accurately reflect the true Cl atom reactant speed distribution in the free-jet expansion, represents the limit in which there is no detector function. Satisfactory fits to the data were obtained using this analysis by including only contributions from methane molecules in the ground vibrational state. The reaction cross-section enhancement through vibrational excitation of the low frequency modes in the methane reactants determined from this analysis might therefore be small. This would be in broad agreement with the findings of the previous studies by Michelson and Simpson [198] and Liu and co-workers [88], in which the umbrella bending mode vibrational enhancement was estimated to be ≤ 2 and ~ 3 respectively.

The principal question raised by the second analysis procedure concerns the origin of the broad chlorine atom reactant speed distribution necessary to fit the data. One possible explanation could be that the interaction region was larger than expected, owing to the finite photolysis laser focal region and the use of a free-jet expansion rather than a skimmed molecular beam. Under these conditions, the precursor and target reactant molecules might have possessed significant velocity components perpendicular to the molecular beam/time-of-flight axis. If this were the case, the width of both the Cl reactant and CH_3 product velocity distributions would have been increased. Simulations were performed in order to determine the effect on the Cl atom speed distribution of these simple geometric arguments. A Cl atom image returned by this simulation is compared with a typical experimental image (shown previously in Section 2.9.2) in Figure 6.17. In these simulations, the angular dependence of the free-jet expansion was assumed to be well approximated by a $\cos^2\theta$ distribution, where θ is the angle of deviation from the propagation direction of the molecular beam. A translational temperature of 50 K and a 9 mm^3

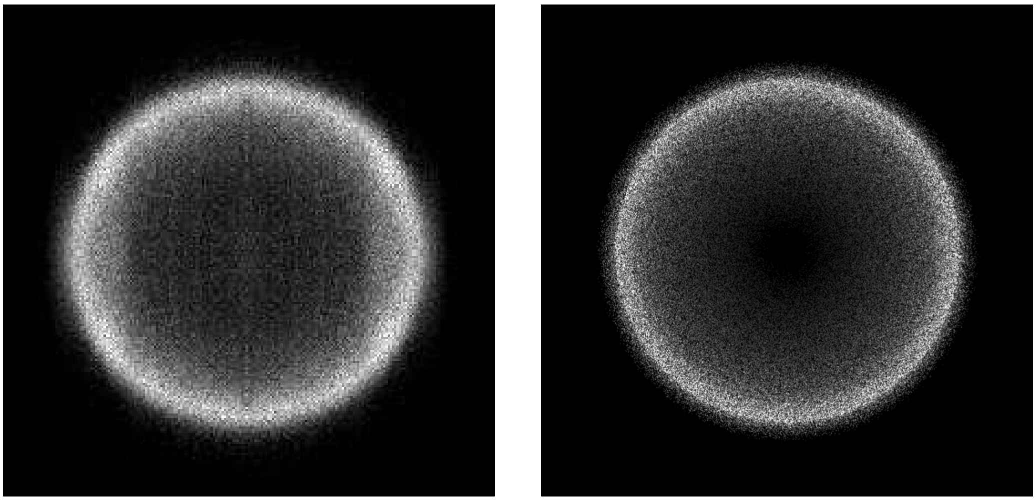

Figure 6.17: Comparison of the experimentally determined ion image (left) with the ion image returned by simulation (right) of the Cl(^{2}P$_{3/2}$) atom products of photodissociation of Cl$_2$. The simulated image was generated assuming a $\cos^2\theta$ angular dependence of the free-jet expansion, with a 50 K translational temperature and a 9 mm^3 interaction volume.

interaction volume were used in the simulation. The chlorine atom speed distribution obtained from the simulated image is compared to that determined from the experimental ion image in Figure 6.18. The simulated speed distribution is seen to reproduce accurately the width of the peak at the most probable speed in the experimental image. The low and high velocity 'wings' on the experimentally determined distribution, however, are not accounted for by the simulation and an alternative explanation for the existence of chlorine atoms with these speeds is required.

One further possible explanation exists to account for both the broad chlorine atom speed distribution observed and the presence of methyl radical products formed with high speeds, which were accounted for in the first analysis procedure by inclusion of vibrationally excited methane reactants. Secondary collisions between both the Cl$^+$ and CH$_3^+$ *ions* and other gases present may have taken place as the ions were accelerated towards the detector. Since the Cl$^+$ and CH$_3^+$ ions travelled along the flight tube with different velocities due to their different masses, they may have been scattered to different extents. The instrument function determined from the ion images of chlorine atom products of Cl$_2$ photodissociation will, therefore, not necessarily be applicable to the methyl radical products of the reaction. Use of an

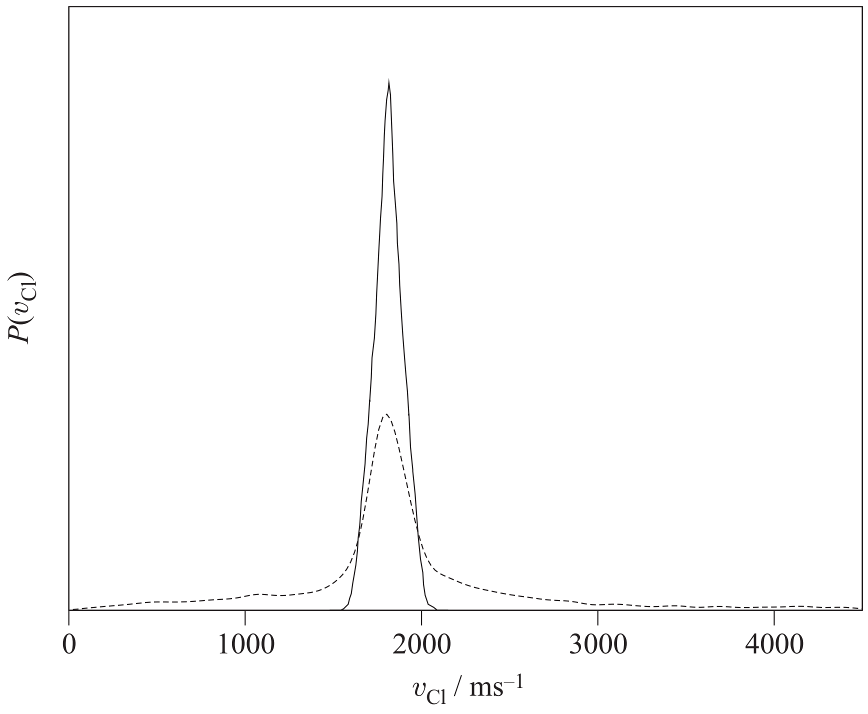

Figure 6.18: Comparison of the Cl($^2P_{3/2}$) atom speed distributions obtained from the simulated (—) and experimental (- - -) ion images in Figure 6.17.

alternative instrument function for the methyl products could thus yield sensible results from analysis of the observed experimental data employing the first Legendre moment fitting procedure. Owing to the very similar conditions employed in the current study and the previous work by Zare and co-workers [111, 287], the hypothesis presented here might provide an explanation for the apparent vibrational enhancement seen in these earlier experiments and may go some way to reconciling the differences between the results obtained by Zare and co-workers [287] and Liu and co-workers [88]. Further experimental work to investigate the various points raised here is therefore required.

6.5 Conclusions and Future Work

New experiments on the H and D atom abstraction reactions between atomic chlorine and CH_4, CD_4 and CH_3D, in which the methyl radical products were detected *via*

REMPI coupled with velocity-map ion imaging, have been performed. For the Cl + CH_4 and Cl + CD_4 reactions, the LAB frame velocity and speed-dependent translational anisotropy distributions are in excellent agreement with the previous REMPI-TOF core-extraction work of Kandel and Zare [287]. A Legendre moment fitting analysis of the methyl radical ion images following procedures analogous to those employed in the core-extraction experiments [110, 111, 287], in which an instrument function is estimated from ion images of the Cl atom reactants, suggests that a significant fraction of the observed signal originates from reaction of Cl atoms with vibrationally excited methane molecules. Both the CM angular scattering distributions derived using this method and the estimated reaction cross-section enhancements for one quantum of vibrational excitation are in excellent agreement with the previous findings from Kandel and Zare [287].

However, it has also been shown that the present velocity-map ion imaging data are amenable to an alternative interpretation, one which is consistent with the new crossed-molecular beam data obtained by Liu and co-workers [88]. A second Legendre moment analysis procedure, in which the chlorine atom ion images are used to provide a direct indication of the Cl atom speed distribution in the free-jet expansion, is seen to provide a satisfactory fit to the experimental data, without the consideration of reaction of chlorine atoms with vibrationally excited methane being required. Allowing for the comparatively broad range of collision energies, the dependence of the CM angular scattering distribution on collision energy is found to be an important factor in determining the quality of the fit. The CM angular scattering distributions thereby derived for the reactions with ground state methane show peaks in the sideways/backwards directions, that shift towards the forwards hemisphere with increasing collision energy. The methyl radical products of the Cl + CD_4 reaction are seen to be more backward scattered than those for the H atom abstraction reactions with CH_4 or CH_3D. The CM angular scattering distributions for the reactions with ground vibrational state CH_4 and CD_4 appear to be in good agreement with the most recent quantum mechanical scattering calculations of Yu and Nyman [276, 304]. Given the differences in collision energy conditions, the results of this analysis are also found to be in good agreement with those from the latest crossed molecular beam time-sliced ion velocity imaging study of Liu and co-workers [88].

Assumptions made here about the reactant velocity distribution in the unskimmed molecular beam have been shown to have a profound effect on the interpretation of the experimental data. However, provided that the reactant velocity distributions can be well characterised, the photoloc method coupled with velocity-map ion imaging can yield reliable information about the scattering dynamics. Furthermore, it should be possible to make significant improvements to the resolution of the photoloc/velocity-map ion imaging technique used in the experiments presented here. Work to address this issue is currently underway in the Brouard group. New molecular beam source and scattering chambers are presently being designed and constructed to accommodate both a new pulsed valve and a new turbo-molecular pump, with the overall aim of improving the quality of the molecular beam produced. It is hoped that in future experiments it will therefore be possible to form a skimmed, or at least collimated, molecular beam suitable for use in the study of photon-initiated reactions, and thereby eliminate many of the uncertainties concerning the velocity distribution of the atomic reactants. Note that there will be an associated decrease in the number density in the interaction region and thus the signal levels attainable with formation of a skimmed molecular beam. However, a recently purchased Nd:YAG pumped dye laser system and a new imaging detector are thought to have improved the product detection efficiency by a sufficient degree to overcome this potential difficulty. It is hoped that further work on the reaction of atomic chlorine with methane using this new apparatus will shed additional light on the precise levels of reaction cross-section enhancement yielded by excitation of the vibrational modes in the methane reactant.

References

[1] F. London, *Z. Elektrochem.*, **35**, 552 (1929).

[2] R.D. Levine and R.B. Bernstein, *Molecular Reaction Dynamics and Chemical Reactivity*, Oxford University Press, 1987.

[3] S.C. Althorpe and D.C. Clary, *Annu. Rev. Phys. Chem.*, **54**, 493 (2003).

[4] L. Bañares, F.J. Aoiz, P. Honvault, and J-M. Launay, *J. Chem. Phys.*, **118**, 565 (2003).

[5] M.G. Evans and M. Polanyi, *Trans. Faraday Soc.*, **35**, 178 (1939).

[6] G.M. McClelland and D.R. Herschbach, *Mol. Phys.*, **30**, 1537 (1975).

[7] D.A. Case, G.M. McClelland, and D.R. Herschbach, *Mol. Phys.*, **35**, 541 (1978).

[8] G.M. McClelland and D.R. Herschbach, *J. Phys. Chem.*, **83**, 1445 (1979).

[9] J.D. Barnwell, J.G. Loeser, and D.R. Herschabach, *J. Phys. Chem.*, **87**, 2781 (1983).

[10] A. Sinha, M.C. Hsiao, and F.F. Crim, *J. Chem. Phys.*, **92**, 6333 (1990).

[11] A. Sinha, *J. Phys. Chem.*, **94**, 4391 (1990).

[12] A. Sinha, M.C. Hsiao, and F.F. Crim, *J. Chem. Phys.*, **94**, 4928 (1991).

[13] M.C. Hsiao, A. Sinha, and F.F. Crim, *J. Phys. Chem.*, **95**, 8263 (1991).

[14] R.B. Metz, J.D. Thoemke, J.M. Pfeiffer, and F.F. Crim, *J. Chem. Phys.*, **94**, 4391 (1993).

[15] M.J. Bronikowski, W.R. Simpson, and R.N. Zare, *J. Phys. Chem.*, **97**, 2194 (1993).

[16] M.J. Bronikowski, W.R. Simpson, and R.N. Zare, *J. Phys. Chem.*, **97**, 2204 (1993).

[17] P.W. Barnes, I.R. Sims, I.W.M. Smith, G. Lendway, and G.C. Schatz, *J. Chem. Phys.*, **115**, 4586 (2001).

[18] J.C. Polanyi and W.H. Wong, *J. Chem. Phys.*, **51**, 1439 (1969).

[19] M.H. Mok and J.C. Polanyi, *J. Chem. Phys.*, **51**, 1451 (1969).

[20] J.C. Polanyi, *Acc. Chem. Res.*, **5**, 161 (1972).

[21] S.E. Bradforth, D.W. Arnold, D.M. Neumark, and D.E. Manolopoulos, *J. Chem. Phys.*, **99**, 6345 (1993).

[22] D.E. Manolopoulos, K. Stark, H-J. Werner, D.W. Arnold, S.E. Bradforth, and D.E. Neumark, *Science*, **262**, 1852 (1993).

[23] R.A. Loomis and M.I. Lester, *J. Chem. Phys.*, **103**, 4371 (1995).

[24] A.H. Zewail, *J. Phys. Chem. A*, **104**, 5660 (2000).

[25] Y.T. Lee, J.D. McDonald, P.R. LeBreton, and D.R. Herschbach, *Rev. Sci. Instrum.*, **40**, 1402 (1969).

[26] P. Casavecchia, *Rep. Prog. Phys.*, **63**, 355 (1999).

[27] K. Liu, *Annu. Rev. Phys. Chem.*, **52**, 139 (2001).

[28] J.J. Valentini, *Annu. Rev. Phys. Chem.*, **52**, 15 (2001).

[29] P.R. Brooks, *Int. Rev. Phys. Chem.*, **14**, 327 (1995).

[30] H.J. Loesch, *Ann. Rev. Phys. Chem.*, **46**, 555 (1995).

[31] H.J. Loesch, *J. Phys. Chem. A*, **101**, 7461 (1997).

[32] G. Scoles (Ed.), *Atomic and Molecular Beam Methods Volume I*, Oxford University Press, 1988.

[33] D.M. Neumark, A.M. Wodtke, G.N. Robinson, C.C. Hayden, and Y.T. Lee, *J. Chem. Phys.*, **82**, 3045 (1985).

[34] D.M. Neumark, A.M. Wodtke, G.N. Robinson, C.C. Hayden, K. Shobatake, R.K. Sparks, and Y.T. Lee, *J. Chem. Phys.*, **82**, 3067 (1985).

[35] M. Faubel, B. Martínez-Haya, L.Y. Rusin, U. Tappe, J.P. Toennies, F.J. Aoiz, and L. Bañares, *J. Phys. Chem. A*, **102**, 8695 (1998).

[36] M. Baer, M. Faubel, B. Martínez-Haya, L. Rusin, U. Tappe, and J.P. Toennies, *J. Chem. Phys.*, **108**, 9694 (1998).

[37] M. Baer, M. Faubel, B. Martínez-Haya, L. Rusin, U. Tappe, and J.P. Toennies, *J. Chem. Phys.*, **110**, 10231 (1999).

[38] L.Y. Rusin and J.P. Toennies, *Phys. Chem. Chem. Phys.*, **2**, 501 (2000).

[39] L. Schnieder, K. Seekamp-Rahn, J. Borokowski, E. Wrede, K.H. Welge, F.J. Aoiz, L. Bañares, M.J. D'Mello, V.J. Herrero, V. Sáez Rábanos, and R.E. Wyatt, *Science*, **269**, 207 (1995).

[40] L. Schnieder, K. Seekamp-Rahn, E. Wrede, and K.H. Welge, *J. Chem. Phys.*, **107**, 6175 (1997).

[41] E. Wrede and L. Schnieder, *J. Chem. Phys.*, **107**, 786 (1997).

[42] E. Wrede, L. Schnieder, K.H. Welge, F.J. Aoiz, L. Bañares, V.J. Herrero, B. Martínez-Haya, and V. Sáez-Rábanos, *J. Chem. Phys.*, **110**, 9971 (1999).

[43] L. Bañares, F.J. Aoiz, V.J. Herrero, M.J. D'Mello, B. Niederjohann, K. Seekamp-Rahn, E. Wrede, and L. Schneider, *J. Chem. Phys.*, **108**, 6160 (1998).

[44] E. Wrede, L. Schnieder, K.H. Welge, F.J. Aoiz, L. Bañares, J.F. Castillo, B. Martínez-Haya, and V.J. Herrero, *J. Chem. Phys.*, **110**, 9971 (1999).

[45] Z. Liu, J.J. Lin, S.A. Harich, G.C. Schatz, and X. Yang, *Science*, **289**, 1536 (2000).

[46] Z. Liu, J.J. Lin, S.A. Harich, and X. Yang, *Phys. Rev. Lett.*, **86**, 408 (2001).

[47] Z. Liu, J.J. Lin, S.A. Harich, and X. Yang, *J. Chem. Phys.*, **113**, 1325 (2000).

[48] B.R. Strazisar, C. Lin, and H.F. Davis, *Science*, **290**, 958 (2000).

[49] L.H. Lai, D.C. Che, and K. Liu, *J. Phys. Chem.*, **100**, 6376 (1996).

[50] Y.T. Hsu and K. Liu, *J. Chem. Phys.*, **107**, 1664 (1997).

[51] Y.T. Hsu, K. Liu, L.A. Pederson, and G.C. Schatz, *J. Chem. Phys.*, **111**, 7921 (1999).

[52] Y.T. Hsu, K. Liu, L.A. Pederson, and G.C. Schatz, *J. Chem. Phys.*, **111**, 7931 (1999).

[53] S.H. Lee and K. Liu, *J. Phys. Chem. A*, **102**, 8637 (1998).

[54] S.H. Lee and K. Liu, *Chem. Phys. Lett.*, **290**, 323 (1998).

[55] S.H. Lee and K. Liu, *J. Chem. Phys.*, **111**, 6253 (1999).

[56] J.H. Wang, K. Liu, G.C. Schatz, and M. ter Horst, *J. Chem. Phys.*, **107**, 7869 (1997).

[57] D.W. Chandler and P.L. Houston, *J. Chem. Phys.*, **87**, 1445 (1987).

[58] B.J. Whitaker, in *Research in Chemical Kinetics*, R.G. Compton and G. Hancock (Eds.), Elsevier, Amsterdam, 1993.

[59] A.J.R. Heck and D.W. Chandler, *Ann. Rev. Phys. Chem.*, **46**, 335 (1995).

[60] P.L. Houston, *Acc. Chem. Res.*, **28**, 453 (1995).

[61] P.L. Houston, *J. Phys. Chem.*, **100**, 12757 (1997).

[62] L. McDonnell and A.J.R Heck, *J. Mass Spectrom.*, **33**, 425 (1998).

[63] A.G. Suits, L.S. Bontuyan, P.L. Houston, and B.J. Whitaker, *J. Chem. Phys.*, **96**, 8618 (1992).

[64] L.S. Bontuyan, A.G. Suits, P.L. Houston, and B.J. Whitaker, *J. Phys. Chem.*, **97**, 6342 (1993).

[65] T.N. Kitsopoulos, M.A. Buntine, D.P. Baldwin, R.N. Zare, and D.W. Chandler, *Science*, **260**, 1605 (1993).

[66] M. Ahmed, D.S. Peterka, and A.G. Suits, *Phys. Chem. Chem. Phys.*, **2**, 861 (2000).

[67] A.T.J.B. Eppink and D.H. Parker, *Rev. Sci. Instrum.*, **68**, 3477 (1997).

[68] M.S. Westley, K.T. Lorenz, D.W. Chandler, and P.L. Houston, *J. Chem. Phys.*, **114**, 2669 (2001).

[69] K.T. Lorenz, M.S. Westley, and D.W. Chandler, *Phys. Chem. Chem. Phys.*, **2**, 481 (2000).

[70] A.G. Suits and R.E. Continetti (Eds.), *Imaging in Chemical Dynamics*, ACS Symposium Series Vol. 770, American Chemical Society, Washington, DC, 2001.

[71] K.T. Lorenz, D.W. Chandler, J.W. Barr, W. Chen, G.L. Barnes, and J.I. Cline, *Science*, **293**, 2063 (2001).

[72] M. Ahmed, D.S. Peterka, and A.G. Suits, *Chem. Phys. Lett.*, **301**, 372 (1999).

[73] M. Ahmed, D.S. Peterka, and A.G. Suits, *Chem. Phys. Lett.*, **317**, 264 (2000).

[74] X. Liu, R.L. Gross, and A.G. Suits, *J. Chem. Phys.*, **116**, 5341 (2002).

[75] X. Liu, R.L. Gross, G.E. Hall, J.T. Muckerman, and A.G. Suits, *J. Chem. Phys.*, **117**, 7947 (2002).

[76] R.L. Gross, X. Liu, and A.G. Suits, *Chem. Phys. Lett.*, **376**, 710 (2003).

[77] R.L. Toomes and T.N. Kitsopoulos, *Phys. Chem. Chem. Phys.*, **5**, 2481 (2003).

[78] C. Murray, A.J. Orr-Ewing, R.L. Toomes, and T.N. Kitsopoulos, *J. Chem. Phys.*, **120**, 2230 (2004).

[79] R.L. Toomes, A.J. van den Brom, T.N. Kitsopoulos, C. Murray, and A.J. Orr-Ewing, *J. Phys. Chem. A* (ASAP Article, 2004).

[80] J.J. Lin, J. Zhou, W. Shiu, and K. Liu, *Rev. Sci. Instrum.*, **74**, 2495 (2003).

[81] K. Tonokura and T. Suzuki, *Chem. Phys. Lett.*, **224**, 1 (1994).

[82] C.R. Gebhardt, T.P. Rakitzis, P.C. Samartzis, V. Ladopoulos, and T.N. Kitsopoulos, *Rev. Sci. Instrum.*, **72**, 3848 (2001).

[83] L. Dinu, A.T.B.J. Eppink, F. Rosca-Pruna, H.L. Offerhaus, W.J. van der Zande, and M.J.J. Vrakking, *Rev. Sci. Instrum.*, **73**, 4206 (2002).

[84] D. Townsend, M.P. Minitti, and A.G. Suits, *Rev. Sci. Instrum.*, **74**, 2530 (2003).

[85] D.A. Chestakov, S-M. Wu, G. Wu, D.H. Parker, A.T.J.B. Eppink, and T.N. Kitsopoulos, *J. Phys. Chem. A* (ASAP Article, 2004).

[86] J.J. Lin, J. Zhou, W. Shiu, and K. Liu, *Science*, **300**, 966 (2003).

[87] W. Shiu, J.J. Lin, K. Liu, M. Wu, and D.H. Parker, *J. Chem. Phys.*, **120**, 117 (2004).

[88] J. Zhou, J.J. Lin, B. Zhang, and K. Liu, *J. Phys. Chem. A* (ASAP Article, 2004).

[89] J. Solomon, *J. Chem. Phys.*, **47**, 889 (1967).

[90] J. Solomon, C. Jonah, P. Chandra, and R. Bersohn, *J. Chem. Phys.*, **55**, 1908 (1971).

[91] R.N. Zare and D.R. Herschbach, *Proc. IEEE*, **51**, 173 (1963).

[92] R.N. Zare, *Mol. Photochem.*, **4**, 1 (1972).

[93] F. Green, G. Hancock, A.J. Orr-Ewing, M. Brouard, S.P. Duxon, P.A. Enriquez, R. Sayos, and J.P. Simons, *Chem. Phys. Lett.*, **182**, 568 (1991).

[94] F.J. Aoiz, M. Brouard, P.A. Enriquez, and R. Sayos, *J. Chem. Soc., Faraday Trans.*, **89**, 1427 (1993).

[95] N.E. Shafer, A.J. Orr-Ewing, W.R. Simpson, H. Xu, and R.N. Zare, *Chem. Phys. Lett.*, **212**, 155 (1993).

[96] N.E. Shafer-Ray, A.J. Orr-Ewing, and R.N. Zare, *J. Phys. Chem.*, **99**, 7591 (1995).

[97] F.J. Aoiz, M. Brouard, and P.A. Enriquez, *J. Chem. Phys.*, **105**, 4964 (1996).

[98] E.J. Murphy, J.H. Brophy, G.S. Arnold, W.L. Dimpfl, and J.L. Kinsey, *J. Chem. Phys.*, **70**, 5910 (1979).

[99] M. Brouard and J.P. Simons, in *The Chemical Dynamics and Kinetics of Small Radicals*, K. Lui and A. Wagner (Eds.), World Scientific, Singapore, 1995.

[100] A.J. Alexander, M. Brouard, K.S. Kalogerakis, and J.P. Simons, *Chem. Soc. Rev.*, **27**, 405 (1998).

[101] M. Brouard, I. Burak, S.D. Gatenby, and G.A.J. Markillie, *Chem. Phys. Lett.*, **287**, 682 (1998).

[102] J.P. Simons, *Faraday Discuss.*, **113**, 1 (1999).

[103] M. Brouard, I. Burak, S.D. Gatenby, D. Hart, and D. Minayev, *J. Chem. Phys.*, **110**, 11335 (1999).

[104] M. Brouard, I. Burak, and S.D. Gatenby, *Phys. Chem. Chem. Phys.*, **2**, 715 (2000).

[105] M. Brouard, S.D. Gatenby, D.M. Joseph, and C. Vallance, *J. Chem. Phys.*, **113**, 3162 (2000).

[106] M. Brouard, P. O'Keeffe, and C. Vallance, *J. Phys. Chem. A*, **106**, 3629 (2002).

[107] J.P. Simons, *J. Chem. Soc., Faraday Trans.*, **93**, 4095 (1997).

[108] W.C. Wiley and I.H. McLaren, *Rev. Sci. Instrum.*, **26**, 1150 (1955).

[109] W.R. Simpson, A.J. Orr-Ewing, and R.N. Zare, *Chem. Phys. Lett.*, **212**, 163 (1993).

[110] W.R. Simpson, A.J. Orr-Ewing, T.P. Rakitzis, S.A. Kandel, and R.N. Zare, *J. Chem. Phys.*, **103**, 7299 (1995).

[111] W.R. Simpson, T.P. Rakitzis, S.A. Kandel, A.J. Orr-Ewing, and R.N. Zare, *J. Chem. Phys.*, **103**, 7313 (1995).

[112] F. Fernández-Alonso, B.D. Bean, and R.N. Zare, *J. Chem. Phys.*, **111**, 1022 (1999).

[113] F. Fernández-Alonso, B.D. Bean, and R.N. Zare, *J. Chem. Phys.*, **111**, 1035 (1999).

[114] S.C. Althorpe, F. Fernández-Alonso, B.D. Bean, J.D. Ayers, A.E. Pomerantz, R.N. Zare, and E. Wrede, *Nature*, **416**, 67 (2002).

[115] A.E. Pomerantz, F. Ausfelder, R.N. Zare, S.C. Althorpe, F.J. Aoiz, L. Bañares, and J.F. Castillo, *J. Chem. Phys.*, **120**, 3244 (2004).

[116] J.D. Ayers, A.E. Pomerantz, F. Fernández-Alonso, F. Ausfelder, B.D. Bean, and R.N. Zare, *J. Chem. Phys.*, **119**, 4662 (2003).

[117] F. Ausfelder, A.E. Pomerantz, R.N. Zare, S.C. Althorpe, F.J. Aoiz, L. Bañares, and J.F. Castillo, *J. Chem. Phys.*, **120**, 3255 (2004).

[118] F. Fernández-Alonso and R.N. Zare, *Annu. Rev. Phys. Chem.*, **53**, 67 (2002).

[119] B.D. Bean, J.D. Ayers, F. Fernández-Alonso, and R.N. Zare, *J. Chem. Phys.*, **116**, 6634 (2002).

[120] F. Fernández-Alonso, B.D. Bean, R.N. Zare, F.J. Aoiz, L. Bañares, and J.F. Castillo, *J. Chem. Phys.*, **115**, 4534 (2001).

[121] B.D. Bean, F. Fernández-Alonso, and R.N. Zare, *J. Phys. Chem. A*, **105**, 2228 (2001).

[122] D.H. Parker, R.F. Delmdahl, B.L.G. Bakker, and H-P. Loock, *J. Chin. Chem. Soc.*, **48**, 327 (2001).

[123] B-Y. Chang, R.C. Hoetzlein, J.A. Mueller, J.D. Geiser, and P.L. Houston, *Rev. Sci. Instrum.*, **69**, 1665 (1998).

[124] B. Martínez-Haya, M.J. Bass, M. Brouard, C. Vallance, I. Torres, and J. Barr, *J. Chem. Phys.*, **120**, 11042 (2004).

[125] NIST Atomic Spectra Database, NIST Standard Reference Data, No. 78, `http://physics.nist.gov/cgi-bin/AtData/main_asd`.

[126] J. Luque and D.R. Crossley, *LIFBASE: Database and Spectral Simulation Program (Version 1.5)*, SRI International Report MP 99-009, 1999.

[127] G. Herzberg, *Molecular Spectra and Molecular Structre I. Spectra of Diatomic Molecules*, D. Van Nostrand Company Inc., 2nd ed., 1950.

[128] P.C. Samartzis, B.L.G. Bakker, T.P. Rakitzis, D.H. Parker, and T.N. Kitsopoulos, *J. Chem. Phys.*, **110**, 5201 (1999).

[129] B. Buijsse, W.J. van der Zande, A.T.J.B. Eppink, D.H. Parker, B.R. Lewis, and S.T. Gibson, *J. Chem. Phys.*, **108**, 7229 (1998).

[130] S. Rudić, C. Murray, D. Ascenzi, H. Anderson, J.N. Harvey, and A.J. Orr-Ewing, *J. Chem. Phys.*, **117**, 5692 (2002).

[131] P.C. Samartzis, D.J. Smith, T.P. Rakitzis, and T.N. Kitsopoulos, *Chem. Phys. Lett.*, **324**, 337 (2000).

[132] J.W. Hudgens, T.G. DiGiuseppe, and M.C. Lin, *J. Chem. Phys.*, **79**, 571 (1983).

[133] D.H. Parker, Z.W. Wang, M.H.M Janssen, and D.W. Chandler, *J. Chem. Phys.*, **90**, 60 (1988).

[134] D.W. Chandler, M.H.M. Janssen, S. Stolte, R.N. Strickland, J.W. Thoman Jr., and D.H. Parker, *J. Phys. Chem.*, **94**, 4839 (1990).

[135] J. Heinze, N. Heberle, and K. Kohnse-Höinghaus, *Chem. Phys. Lett.*, **223**, 305 (1994).

[136] H. Dickinson, T. Chelmick, and T.P. Softley, *Chem. Phys. Lett.*, **338**, 37 (2001).

[137] Y. Matsumi, M. Kawaska, T. Sato, T. Kinugawa, and T. Arikawa, *Chem. Phys. Lett.*, **155**, 486 (1989).

[138] Y. Matsumi, K. Tonokura, and M. Kawasaki, *J. Chem. Phys.*, **97**, 1065 (1992).

[139] P.C. Samartzis, I. Sakellariou, T. Gougousi, and T.N. Kitsopoulos, *J. Chem. Phys.*, **107**, 43 (1997).

[140] P.C. Samartzis, T. Gougousi, and T.N. Kitsopoulos, *Laser Chem.*, **17**, 185 (1998).

[141] M.J. Bass, M. Brouard, A.P. Clark, C. Vallance, and B. Martínez-Haya, *Phys. Chem. Chem. Phys.*, **5**, 856 (2003).

[142] D. Proch and T. Trickl, *Rev. Sci. Instrum.*, **60**, 12757 (1989).

[143] D.S. Green, G.A. Bickel, and S.C. Wallace, *J. Mol. Spectros.*, **150**, 303 (1991).

[144] D.S. Green, G.A. Bickel, and S.C. Wallace, *J. Mol. Spectros.*, **150**, 354 (1991).

[145] D.S. Green, G.A. Bickel, and S.C. Wallace, *J. Mol. Spectros.*, **150**, 388 (1991).

[146] R.W. Diesen, J.C. Wahr, and S.E. Adler, *J. Chem. Phys.*, **50**, 3635 (1969).

[147] G.E. Busch, R.T. Mahoney, R.I. Morse, and K.R. Wilson, *J. Chem. Phys.*, **51**, 449 (1969).

[148] Y. Wang, H-P. Loock, J. Cao, and C.X.W. Qian, *J. Chem. Phys.*, **102**, 808 (1994).

[149] A.S. Bracker, E.R. Wouters, A.G. Suits, and O.S. Vasyutinskii, *J. Chem. Phys.*, **110**, 6749 (1999).

[150] T.P. Rakitzis and T.N. Kitsopoulos, *J. Chem. Phys.*, **116**, 9228 (2002).

[151] S.A. Kandel, T.P. Rakitzis, T. Lev-On, and R.N. Zare, *J. Chem. Phys.*, **105**, 7550 (1996).

[152] S.A. Kandel, T.P. Rakitzis, T. Lev-On, and R.N. Zare, *Chem. Phys. Lett.*, **1265**, 121 (1997).

[153] B.J. Whitaker (Ed.), *Imaging in Molecular Dynamics: Technology and Applications*, Cambridge University Press, 2003.

[154] N.H. Abel, *J. Reine Angew. Math.*, **1**, 153 (1826).

[155] K.R. Castleman, *Digital Image Processing*, Prentice–Hall, Englewood Cliffs, New Jersey, 1996.

[156] R.N. Bracewell, *The Fourier Transform and its Applications*, McGraw–Hill, New York, London, 2nd ed., 1986.

[157] C.J. Dasch, *Applied Optics*, **31**, 1146 (1992).

[158] L.M. Smith, D.R. Keefer, and S.I. Sudharsanan, *J. Quant. Spectrosc. Radiat. Transfer*, **39**, 367 (1988).

[159] W.H. Press, S.A. Teukolsky, W.T. Vetterling, and B.P. Flannery, *Numerical Recipies in FORTRAN 77: The Art of Scientific Computing*, Cambridge University Press, 2nd ed., 1992.

[160] L.M. Smith, *IEEE Trans. Inf. Theory*, **IT-34**, 158 (1988).

[161] M.J. Bass, M. Brouard, A.P. Clark, and C. Vallance, *J. Chem. Phys.*, **117**, 8723 (2002).

[162] M.J.J. Vrakking, *Rev. Sci. Instrum.*, **72**, 4084 (2001).

[163] V. Dribinski, A. Ossadtchi, V.A. Mandelshtam, and H. Reisler, *Rev. Sci. Instrum.*, **73**, 2634 (2002).

[164] R.N. Zare, *Angular Momentum: Understanding spatial aspects in chemsitry and physics*, John Wiley & Sons Inc., 1988.

[165] D.A. Case and D.R. Herschbach, *J. Chem. Phys.*, **64**, 4212 (1976).

[166] M.G. Prisant, C.T. Rettner, and R.N. Zare, *J. Chem. Phys.*, **75**, 2222 (1981).

[167] C. Jonah, *J. Chem. Phys.*, **55**, 1915 (1971).

[168] G.E. Busch and K.R. Wilson, *J. Chem. Phys.*, **56**, 3638 (1972).

[169] M.J. Bass, M. Brouard, C. Vallance, T.N. Kitsopoulos, P.C. Samartzis, and R.L. Toomes, *J. Chem. Phys.*, **119**, 7168 (2003).

[170] M. Brouard, A.P. Clark, C. Vallance, and O.S. Vasyutinskii, *J. Chem. Phys.*, **119**, 771 (2003).

[171] M. Brouard, R. Cireasa, A.P. Clark, T.J. Preston, C. Vallance, G.C. Goenenboom, and O.S. Vasyutinskii, *J. Phys. Chem. A* (ASAP Article, 2004).

[172] M. Brouard, I. Burak, G.A.J. Markillie, K. McGrath, and C. Vallance, *Chem. Phys. Lett.*, **281**, 97 (1997).

[173] S.D. Gatenby, D.Phil. thesis, Oxford University (1999).

[174] S.J. Greenland, Part II thesis, Oxford University (1997).

[175] E.E. Marinero, R. Vasudev, and R.N. Zare, *J. Chem. Phys.*, **78**, 692 (1983).

[176] L. Bañares, personal communication (2001).

[177] J.D.D. Martin and J.W. Hepburn, *J. Chem. Phys.*, **109**, 8139 (1998).

[178] M. Michel, M.V. Korolkov, and K-M. Weitzel, *Phys. Chem. Chem. Phys.*, **4**, 4083 (2002).

[179] P. Marshall, *J. Phys. Chem. A*, **103**, 4560 (1999).

[180] P. McLoughlin, R. Kane, and I. Shannan, *Int. J. Chem. Kinet.*, **25**, 137 (1993).

[181] C. Ferronato, J.J. Orlando, and G.S. Tyndall, *J. Geophys. Res.-Atmos.*, **103**, 25579 (1998).

[182] B.J. Finlayson-Pitts, C.J. Keoshian, B. Buehler, and A.A. Ezell, *Int. J. Chem. Kinet.*, **31**, 491 (1999).

[183] Y. Nakano, M. Kawasaki, D.A. Ponomarev, M.D. Hurley, and T.J. Wallington, *Chem. Phys. Lett.*, **353**, 77 (2002).

[184] D. Sarzynksi and B. Sztuba, *Int. J. Chem. Kinet.*, **34**, 651 (2002).

[185] R.G. Manning and M.J. Kurylo, *J. Phys. Chem.*, **81**, 291 (1977).

[186] R.S. Lewis, S.P. Sander, S. Wagner, and R.T. Watson, *J. Phys. Chem.*, **84**, 2009 (1980).

[187] O. Dobis and S.W. Benson, *J. Am. Chem. Soc.*, **113**, 6377 (1991).

[188] E.W. Kaiser, L. Rimai, E. Schwab, and E.C. Lim, *J. Phys. Chem.*, **96**, 303 (1992).

[189] P. Beichert, L. Wingen, J. Lee, R. Vogt, M.J. Ezell, M. Ragains, R. Neavyn, and B.J. Finlayson-Pitts, *J. Phys. Chem.*, **99**, 13156 (1995).

[190] J.S. Pilgrim, A. McIlroy, and C.A. Taatjes, *J. Phys. Chem. A*, **101**, 1873 (1997).

[191] G.S. Tyndall, J.J. Orlando, T.J. Wallington, M. Dill, and E.W. Kaiser, *Int. J. Chem. Kinet.*, **29**, 43 (1997).

[192] K. Hitsuda, K. Takahashi, Y. Matsumi, and T.J. Wallington, *J. Phys. Chem. A*, **105**, 5131 (2001).

[193] M.G. Bryukov, I.R. Slagle, and V.D. Knyazev, *J. Phys. Chem. A*, **107**, 6565 (2003).

[194] K. Takahashi, O. Yamamoto, and T. Inomata, *Proc. Combust. Inst.*, **29**, 2447 (2003).

[195] IUPAC Subcommittee for Gas Kinetic Data Evaluation (2002), `http://www.iupac-kinetic.ch.cam.ac.uk`.

[196] R. Atkinson, D.L. Baulch, R.A. Cox, R.F. Hampson Jr., J.A. Kerr, M.J. Rossi, and J. Troe, *J. Phys. Chem. Ref. Data*, **26**, 521 (1997).

[197] S.P. Sander, R.R. Friedl, D.M. Golden, M.J. Kurylo, R.E. Huie, V.L. Orkin, G.K. Moortgat, A.R. Ravishankara, C.E. Kolb, M.J. Molina, and B.J. Finlayson-Pitts, *Chemical Kinetics and Photochemical Data for Use in Stratospheric Modeling, Evaluation number 14*, JPL publication 02-25, Jet Propulsion Laboratory, Pasadena, CA, 2003.

[198] H.A. Michelson and W.R. Simpson, *J. Phys. Chem. A*, **105**, 1476 (2001).

[199] H.A. Michelson, *Acc. Chem. Res.*, **34**, 331 (2001).

[200] A.R. Ravishankara and P.H. Wine, *J. Chem. Phys.*, **72**, 25 (1980).

[201] A. Gonzalez-Lafont, T.N. Truong, and D.G. Truhlar, *J. Chem. Phys.*, **95**, 8875 (1991).

[202] O. Roberto-Neto and F.B.C. Machado, *J. Mol. Struct.: THEOCHEM*, **580**, 161 (2002).

[203] A. Fernández-Ramos, E. Martínez-Núñez, J.M.C Marques, and S.A. Vázquez, *J. Chem. Phys.*, **118**, 6280 (2003).

[204] A. Bottoni and G. Poggi, *J. Mol. Struct.: THEOCHEM*, **337**, 161 (1995).

[205] S. Rudić, C. Murray, J.N. Harvey, and A.J. Orr-Ewing, *J. Chem. Phys.*, **120**, 186 (2004).

[206] S.A. Kandel, T.P. Rakitzis, T. Lev-On, and R.N. Zare, *J. Phys. Chem. A*, **105**, 2270 (1998).

[207] S. Rudić, D. Ascenzi, and A.J. Orr-Ewing, *Chem. Phys. Lett.*, **332**, 487 (2000).

[208] W.R. Simpson, T.P. Rakitzis, S.A. Kandel, T. Lev-On, and R.N. Zare, *J. Phys. Chem.*, **100**, 7938 (1996).

[209] I.W.M. Smith, *J. Chem. Educ.*, **59**, 9 (1982).

[210] T.P. Rakitzis, S.A. Kandel, T. Lev-On, and R.N. Zare, *J. Chem. Phys.*, **107**, 9392 (1997).

[211] S.S. Parmar and S.W. Benson, *J. Am. Chem. Soc.*, **111**, 57 (1989).

[212] T.P. Rakitzis, S.A. Kandel, and R.N. Zare, *J. Chem. Phys.*, **107**, 9382 (1997).

[213] L.J. Xu, X.B. Wang, J.M. Yan, and F. Kong, *Acta Physico-Chimica Sinica (Chinese)*, **14**, 158 (1998).

[214] D.F. Varley and P.J. Dagdigian, *J. Phys. Chem.*, **99**, 9843 (1995).

[215] D.F. Varley and P.J. Dagdigian, *Chem. Phys. Lett.*, **255**, 393 (1996).

[216] D.F. Varley and P.J. Dagdigian, *J. Phys. Chem.*, **100**, 4365 (1996).

[217] L. Schnieder, K. Seekamp-Rahn, F. Liedeker, H. Steuwe, and K.H. Welge, *Faraday Discuss. Chem. Soc.*, **91**, 259 (1991).

[218] R.L. Toomes and T.N. Kitsopoulos, personal communication (2003).

[219] D. Skouteris, D.E. Manolopoulos, W.S. Bian, H-J. Werner, L-H. Lai, and K. Liu, *Science*, **286**, 1713 (1999).

[220] M. Ben-Nun, M. Brouard, J.P. Simons, and R.D Levine, *Chem. Phys. Lett.*, **210**, 423 (1993).

[221] A.J. Orr-Ewing, *J. Chem. Soc., Faraday Trans.*, **92**, 881 (1996).

[222] D.A. Blank, N. Hemmi, A.G. Suits, and Y.T. Lee, *Chem. Phys.*, **231**, 261 (1998).

[223] N. Hemmi and A.G. Suits, *J. Chem. Phys.*, **109**, 5338 (1998).

[224] Y-F. Yen, Z. Wang, B. Xue, and B. Koplitz, *J. Phys. Chem.*, **98**, 4 (1994).

[225] A.L.L. East and P.R. Bunker, *Chem. Phys. Lett.*, **282**, 49 (1998).

[226] T.J. Sears, P.M. Johnson, and J. BeeBe-Wang, *J. Chem. Phys.*, **111**, 9213 (1999).

[227] W.L. Hase, H.B. Schlagel, V. Balbyshev, and M. Page, *J. Phys. Chem.*, **100**, 5354 (1996).

[228] P.M. Johnson and T.J. Sears, *J. Chem. Phys.*, **111**, 9222 (1999).

[229] T.J. Sears, P.M. Johnson, P. Jin, and S. Oatis, *J. Chem. Phys.*, **104**, 781 (1996).

[230] E. Kim and S. Yamamoto, *J. Chem. Phys.*, **120**, 3265 (2004).

[231] S. Davis, D. Uy, and D.J. Nesbitt, *J. Chem. Phys.*, **112**, 1823 (2000).

[232] J.A. Seetula and I.R. Slagle, *J. Chem. Soc., Faraday Trans.*, **93**, 1709 (1997).

[233] Calculated using $D_0^0(\mathrm{H–R}) = D_{298}^0(\mathrm{H–R}) - 5R/2$ (see Ref. [234]).

[234] J. Berkowitz, G.B. Ellison, and D. Gutman, *J. Phys. Chem.*, **98**, 2744 (1994).

[235] R. Atkinson and S.M. Aschmann, *Int. J. Chem. Kinet.*, **17**, 33 (1985).

[236] T.J. Wallington, L.M. Skewes, W.O. Siegl, C-H. Wu, and S.M. Japar, *Int. J. Chem. Kinet.*, **20**, 867 (1988).

[237] S.M. Aschmann and R. Atkinson, *Int. J. Chem. Kinet.*, **27**, 613 (1995).

[238] P.A. Hooshiyar and H. Niki, *Int. J. Chem. Kinet.*, **27**, 1197 (1995).

[239] M. Ragains and B.J. Finlayson-Pitts, *J. Phys. Chem. A*, **101**, 1509 (1997).

[240] W.H. Wang, M.J. Ezell, G. Soskin, and B.J. Finlayson-Pitts, *Phys. Chem. Chem. Phys.*, **4**, 1824 (2002).

[241] M.J. Ezell, W.H. Wang, A.A. Ezell, G. Soskin, and B.J. Finlayson-Pitts, *Phys. Chem. Chem. Phys.*, **4**, 5813 (2002).

[242] H-B. Qian, D. Turton, P.W. Seakins, and M.J. Pilling, *Int. J. Chem. Kinet.*, **34**, 86 (2002).

[243] J.A. Seetula, *Phys. Chem. Chem. Phys.*, **2**, 3807 (2000).

[244] E.A. Rohlfing, D.W. Chandler, and D.H. Parker, *J. Chem. Phys.*, **87**, 5229 (1987).

[245] Y. Xie, P.T.A. Reilly, S. Chilukuri, and R.J. Gordon, *J. Chem. Phys.*, **95**, 854 (1991).

[246] R. Atkinson, D.L. Baulch, R.A. Cox, R.F. Hampson Jr., J.A. Kerr, and J. Troe, *J. Phys. Chem. Ref. Data*, **21**, 1125 (1992).

[247] X. Liu and A.G. Suits, in *Modern Trends in Chemical Reaction Dynamics: Experiment and Theory (Part I)*, X. Yang and K. Lui (Eds.), Advanced Series in Physical Chemistry Vol. 14, World Scientific, Singapore, 2004.

[248] J. Park, Y. Lee, J.F. Hershberger, J.M. Hossenlopp, and G.W. Flynn, *J. Am. Chem. Soc.*, **114**, 58 (1992).

[249] H. Tsurumaki, Y. Fujimura, and O. Kajimoto, *J. Chem. Phys.*, **112**, 8338 (2000).

[250] Y. Fujimura, H. Tsurumaki, and O. Kajimoto, *Bull. Chem. Soc. Jpn.*, **75**, 2309 (2002).

[251] C. Vallance, personal communication (2004).

[252] J. Pacansky, R.J. Waltman, and L.A. Barnes, *J. Phys. Chem.*, **100**, 16828 (1996).

[253] J. Pacansky, D.E. Horne, G.P. Gardini, and J. Bargon, *J. Phys. Chem.*, **81**, 2149 (1977).

[254] J. Pacansky and A. Gutierrez, *J. Phys. Chem.*, **87**, 3074 (1983).

[255] NIST Chemistry WebBook, NIST Standard Reference Data, No. 69, `http://webbook.nist.gov/chemistry/`.

[256] M. Litorja and B. Ruscic, *J. Chem. Phys.*, **107**, 9852 (1997).

[257] Q.J. Hu, T.C. Melville, and J.W. Hepburn, *J. Chem. Phys.*, **119**, 8938 (2003).

[258] S. Yoon, R.J. Holiday, E.L. Sibert III, and F.F. Crim, *J. Chem. Phys.*, **119**, 9568 (2003).

[259] H.O. Pritchard, J.B. Pyke, and A.F. Trotman-Dickenson, *J. Am. Chem. Soc.*, **76**, 1201 (1954).

[260] M.A.A. Clyne and R.F. Walker, *J. Chem. Soc., Faraday Trans.*, **69**, 1547 (1973).

[261] G. Poulet, G. Le Bras, and J. Combourieu, *J. Chim. Phys.*, **71**, 101 (1974).

[262] R. Watson, G. Machado, S. Fischer, and D.D. Davis, *J. Chem. Phys.*, **65**, 2126 (1976).

[263] D.A. Whytock, J.H. Lee, J.V. Michael, W.A. Payne, and L.J. Stief, *J. Chem. Phys.*, **66**, 2690 (1977).

[264] M.H. Baghal-Vayjooee, A.J. Colussi, and S.W. Benson, *J. Am. Chem. Soc.*, **100**, 3214 (1978).

[265] L.F. Keyser, *J. Chem. Phys.*, **69**, 214 (1978).

[266] C.L. Lin, M.T. Leu, and W.B. DeMore, *J. Phys. Chem.*, **82**, 1772 (1978).

[267] M.S. Zahniser, B.M. Berquist, and F. Kaufman, *Int. J. Chem. Kinet.*, **10**, 15 (1978).

[268] O. Dobis and S.W. Benson, *Int. J. Chem. Kinet.*, **19**, 691 (1987).

[269] J.V. Seeley, J.T. Jayne, and M.J. Molina, *J. Phys. Chem.*, **100**, 4019 (1996).

[270] Y. Matsumi, K. Izumi, V. Skorokhodov, M. Kawasaki, and N. Tanaka, *J. Phys. Chem. A*, **101**, 1216 (1997).

[271] J.J. Wang and L.F. Keyser, *J. Phys. Chem. A*, **103**, 7460 (1999).

[272] M.G. Bryukov, I.R. Slagle, and V.D. Knyazev, *J. Phys. Chem. A*, **106**, 10532 (2002).

[273] S.P. Heneghan, P.A. Knoot, and S.W. Benson, *Int. J. Chem. Kinet.*, **13**, 677 (1981).

[274] W.T. Duncan and T.N. Truong, *J. Chem. Phys.*, **103**, 9642 (1995).

[275] J. Espinosa-García and J.C. Corchado, *J. Chem. Phys.*, **105**, 3517 (1996).

[276] H.G. Yu and G. Nyman, *J. Chem. Phys.*, **110**, 7233 (1999).

[277] N.M. Donahue, *J. Phys. Chem. A*, **105**, 1489 (2001).

[278] G.S. Tyndall, J.J. Orlando, and C.S. Kegley-Owen, *J. Chem. Soc., Faraday Trans.*, **91**, 3055 (1995).

[279] Z.H. Kim, A.J. Alexander, H.A. Bechtel, and R.N. Zare, *J. Chem. Phys.*, **115**, 179 (2001).

[280] G.D. Boone, F. Agyin, D.J. Robichaud, F-M. Tao, and S.A. Hewitt, *J. Phys. Chem. A*, **105**, 1456 (2001).

[281] G. Chiltz, R. Eckling, P. Goldfinger, G. Huybrechts, H.S. Johnston, L. Meyers, and G. Verbeke, *J. Chem. Phys.*, **38**, 1053 (1963).

[282] V.P. Strunin, N.K. Serdyuk, E.N. Chesnokov, and V.N. Panfilov, *React. Kinet. Catal. Lett.*, **3**, 97 (1975).

[283] T.J. Wallington and M.D. Hurley, *Chem. Phys. Lett.*, **189**, 437 (1992).

[284] G. Saueressig, P. Bergamaschi, J.N. Crowley, H. Fischer, and G.W. Harris, *Geophys. Res. Lett.*, **23**, 3619 (1996).

[285] S.C. Tyler, H.O. Ajie, A.L. Rice, R.J. Cicerone, and E.C. Tuazon, *Geophys. Res. Lett.*, **27**, 1715 (2000).

[286] A.J. Orr-Ewing, W.R. Simpson, T.P. Rakitzis, S.A. Kandel, and R.N. Zare, *J. Chem. Phys.*, **106**, 5961 (1997).

[287] S.A. Kandel and R.N. Zare, *J. Chem. Phys.*, **109**, 9719 (1998).

[288] Z.H. Kim, H.A. Bechtel, and R.N. Zare, *J. Am. Chem. Soc.*, **123**, 12714 (2001).

[289] Z.H. Kim, H.A. Bechtel, and R.N. Zare, *J. Chem. Phys.*, **117**, 3232 (2002).

[290] H.A. Bechtel, Z.H. Kim, J.P. Camden, and R.N. Zare, *J. Chem. Phys.*, **120**, 791 (2004).

[291] H.A. Bechtel, J.P. Camden, D.J. Ankeny Brown, and R.N. Zare, *J. Chem. Phys.*, **120**, 5096 (2004).

[292] S. Yoon, S. Henton, A.N. Zivkovic, and F.F. Crim, *J. Chem. Phys.*, **116**, 10744 (2002).

[293] S. Yoon, R.J. Holiday, and F.F. Crim, *J. Chem. Phys.*, **119**, 4755 (2003).

[294] T.N. Truong, D.G. Truhlar, K.K. Baldridge, M.S. Gordon, and R. Steckler, *J. Chem. Phys.*, **90**, 7137 (1989).

[295] K.D. Dobbs and D.A. Dixon, *J. Phys. Chem.*, **98**, 12584 (1994).

[296] O. Roberto-Neto, E.L. Coitiño, and D.G. Truhlar, *J. Phys. Chem. A*, **102**, 4568 (1998).

[297] J.C. Corchado, D.G. Truhlar, and J. Espinosa-García, *J. Chem. Phys.*, **112**, 9375 (2000).

[298] E. Martínez-Núñez, A. Fernández-Ramos, S.A. Vázquez, and M.A. Ríos, *Chem. Phys. Lett.*, **360**, 59 (2002).

[299] D. Troya, J. Millán, I. Baños, and M. González, *J. Chem. Phys.*, **117**, 5730 (2002).

[300] T. Joseph, R. Steckler, and D.G. Truhlar, *J. Chem. Phys.*, **87**, 7036 (1987).

[301] M.J.T. Jordan and R.G. Gilbert, *J. Chem. Phys.*, **102**, 5669 (1995).

[302] G. Nyman, H.G. Yu, and R.B. Walker, *J. Chem. Phys.*, **109**, 5896 (1998).

[303] H.G. Yu and G. Nyman, *Phys. Chem. Chem. Phys.*, **1**, 1181 (1999).

[304] H.G. Yu and G. Nyman, *J. Chem. Phys.*, **111**, 6693 (1999).

[305] S. Skokov and J.M. Bowman, *J. Chem. Phys.*, **113**, 4495 (2000).

[306] F.J. Aoiz and B. Martínez-Haya, personal communication (2003).

[307] K.M. Chen and E.S. Yeung, *J. Chem. Phys.*, **69**, 43 (1978).

[308] J.F. Black and I. Powis, *J. Chem. Phys.*, **89**, 3986 (1988).

[309] G.G. Balint-Kurti, *J. Chem. Phys.*, **84**, 4443 (1986).

[310] D.C. Clary, *J. Chem. Phys.*, **95**, 7298 (1991).

[311] G. Nyman and D.C. Clary, *J. Chem. Phys.*, **99**, 7774 (1993).

[312] D. Wang and J.M. Bowman, *Chem. Phys. Lett.*, **207**, 227 (1993).

[313] D.C. Clary, *J. Chem. Phys.*, **96**, 3656 (1994).

[314] M. Brouard I. Burak, D.M. Jospeh, G.A.J. Markillie, D. Minayev, P. O'Keeffe, and C. Vallance, *J. Chem. Phys.*, **114**, 6690 (2001).

[315] J.L. Brum, R.D. Johnson III, and J.W. Hudgens, *J. Chem. Phys.*, **98**, 3732 (1993).

[316] P. Chen, S.D. Colson, W.A. Chupka, and J.A. Berson, *J. Phys. Chem.*, **90**, 2319 (1986).

[317] D.W. Chandler, J.W. Thoman Jr., M.H.M. Janssen, and D.H. Parker, *Chem. Phys. Lett.*, **156**, 151 (1989).

[318] M. Brouard, I. Burak, D. Minayev, P. O'Keeffe, C. Vallance, F.J. Aoiz, L. Bañares, J.F. Castillo, D.H. Zhang, and M.A. Collins, *J. Chem. Phys.*, **118**, 1162 (2003).

[319] J. Palma and D.C. Clary, *J. Chem. Phys.*, **115**, 2188 (2001).